# Manipulating Exfoliated 2D Materials at the Air-Water Interface: Towards Large-area Coatings and Applications

by

**Luzhu Xu**

A thesis
presented to the University of Waterloo
in fulfillment of the
thesis requirement for the degree of
Doctor of Philosophy
in
Chemical Engineering (Nanotechnology)

Waterloo, Ontario, Canada, 2023

© Luzhu Xu 2023

# Examining Committee Membership

The following served on the Examining Committee for this thesis. The decision of the Examining Committee is by majority vote.

| | | |
|---|---|---|
| External Examiner | NAME: | Michael S. Arnold |
| | Title: Professor | |
| Supervisor | NAME: | Michael A. Pope |
| | Title: Associate Professor | |
| Internal Member | NAME: | Mario Ioannidis |
| | Title: Professor | |
| Internal Member | NAME: | Boxin Zhao |
| | Title: Professor | |
| Internal-external Member | NAME: | Shawn D. Wettig |
| | Title: Professor | |

# Author's Declaration

This thesis consists of material all of which I authored or co-authored: see Statement of Contributions included in the thesis. This is a true copy of the thesis, including any required final revisions, as accepted by my examiners.

I understand that my thesis may be made electronically available to the public.

# Statement of Contributions

This thesis was written solely by myself and edited mainly by my supervisor. It is comprised of published and unpublished work as listed below.

***Chapter 3:***

This chapter is adapted from my MASc thesis and my published work: **Xu L.**, Tetreault A., Khaligh H., *et al*., *Langmuir*, (2019), 51-59, 35(1). Even though most of the experimental work were conducted and published in my MASc, during the 1st year of my PhD, we went through serval rounds of revisions and carried out further work including studies of 'ionic strength effect on the behavior of GO sheets' and 'spreading pressure and film deposition related to chloroform'. I conducted all experimental planning, developed all methodologies, carried out all experiments, data collection and formal data analysis. I also drafted and finalized the manuscript. Adam R. Tetreault assisted on data collection with regards to spreading pressure measurements as well as review & editing of the manuscript.

***Chapter 4:***

This chapter is adapted from one of my published work: **Xu L.**, Tetreault A., Pope M., *Chemistry of Materials*, (2020), 148-156, 32(1). I conducted all experimental planning, developed all methodologies, carried out all experiments, data collection and formal data analysis. I also drafted and finalized the manuscript; Adam R. Tetreault assisted on data collection with regards to UV-Vis spectra, FTIR and Raman measurements of samples during initial investigation and help with review & editing of the manuscript. The work related to 'improved spreading dispersion of *ce*-$MoS_2$' has been not published.

***Chapter 5:***

This chapter is adapted from one of my published work: **Xu L.**, Chekini M., Wilson N., *et al*., *Journal of Colloid and Interface Science*, (2023), 129-140, 648**.** I conducted all experimental planning, developed all methodologies, carried out all experiments, data collection and formal data analysis. I also drafted and finalized the manuscript. Mahshid Chekini conducted GO synthesis and performed concentration measurements of GO stock dispersions. She also helped with review & editing of the manuscript; Nicholas D. Wilson assisted with review & editing of the manuscript;

Ryan J. Zamperoni modified and finalized the custom python codes for applying multi-Gaussian fits on the height profiles obtained by AFM.

***Chapter 6:***

The work in this chapter is unpublished. I conducted all experimental planning, developed all methodologies, carried out almost all experiments, data collection and formal data analysis. Nicholas D. Wilson helped with the upgrade of the Langmuir-Adam balance and data collection with regards to spreading profiles. Azam Nasr Esfahani conducted data collection with regards to 'Impact on Langmuir film phase transition'; Lauren Prophet assisted with data collection related to the multi-dripper system and R2R coatings of graphene films

***Chapter 7:***

The work in this chapter is unpublished. I conducted most of the experimental planning and production of the hole transporting layer composed of $MoS_2$ Langmuir films. I also performed the formal analysis. Saikiran Khamgaonkar developed methodologies and designs of the perovskite solar cell, assembled the cells and performed data collection. Charlotte Burmeister also assembled the cells and performed data collection.

# Abstract

The aim of this thesis is to develop a versatile, large-area coating process for two-dimensional (2D) materials which preserves single-layer or exfoliated sheets and provides comprehensive investigation of the controlling factors for the deposition process. Compared to other approaches, traditional Langmuir film methods not only are economically suitable for transition to large-scale manufacturing but also permit retention of the exfoliated form and freedom of sheet rearrangements. However, challenges remain in existing Langmuir film-based traditional and continuous coating process: 1). Significant material loss due to water-miscible solvent; 2). External forces required for film densification and transfer. In this thesis, we expand upon my MASc work which focuses on the development of a solvent-spreading assisted Langmuir film method which enables large batch film transfer process or a continuous one for monolayer graphene-based materials. With the goal of applying the coating process for films in flexible, optoelectronic devices such as in solar cells, we refined the procedure for preparing spreading dispersion of exfoliated molybdenum disulfide ($MoS_2$). During investigation of the chemical and colloidal stability of the precursor, chemically exfoliated $MoS_2$ (*ce*-$MoS_2$) dispersions in water, we found that *ce*-$MoS_2$ degrades rapidly to form soluble molybdates under alkaline conditions and exposure to both light and air. Building upon this fundamental study, the modified spreading dispersion retains almost 100% of metallic $MoS_2$ and contains ~40% increase in single-layer content. Then, we investigated the structure of the aggregates formed upon spreading each drop of the ink on the air-water interface. We observed cluster structure transitions from island-like domains to more linear networks in three different nanosheets as dispersion concentration is reduced. Regardless of assembly method, we found that cluster structure impacts the attainable density of transferred Langmuir films. Finally, since the spreading pressure of solvent provides the driving force for film assembly and transfer, we evaluated the spreading profiles of various combinations of organic solvents and their impacts on Langmuir film formation. We uncover that the formulation of mixing polar and water-immiscible solvents not only largely reduces the loss of materials into the subphase water but also induces a sharp increase in spreading pressure which facilities the formation of a solid film as well as further densification and transfer of the floating film to substrates in a R2R deposition system. We also develop a multi-dripper system to showcase the strategy of coating films with arbitrary widths. When conducting the R2R deposition, we unveil the importance of using wetting substrate to maximize the effectiveness from the spreading

pressure for achieving continuous, uniform coatings. In the end, we attempt to utilize the Langmuir film of *ce*-$MoS_2$ in the perovskite solar cell to demonstrate the potential use of our coating process.

# Acknowledgments

Firstly, I would like to thank my supervisor, Professor Michael Pope, for his continuous support and invaluable advice throughout my graduate school studies. His patience, encouragement and honest feedback have not only enhanced my ability for critical-thinking and problem-solving, but also set a great model for me to follow when I started supervising others. His hard-working nature and evolving effects on improving himself have motivated me to constantly develop and become a better version of myself. I could not imagine going through this challenging but rewarding PhD journey without Prof. Pope's enlightening guidance.

I am also thankful for Prof. Ioannidis, Prof. Zhao, Prof. Wettig and Prof. Arnold for serving on my thesis committee. Special thanks to Prof. Wettig, who always provided detailed and instructive feedbacks on my manuscript and reports. His practical advice and encouragement have helped tremendously on my scientific writing.

Furthermore, I am grateful for all of the support I received from my collaborators, group members and friends. Special thanks to Gillian who is always ready to listen and help with my problems, who constantly inspires me to continue my journey in conducting research; to Azam who is always so kind to me and gives me the strength to overcome challenges; to Mahshid who generously taught me all of the hands-on tips and tricks when working in the lab and provided me with valuable feedback on my manuscripts; to Ryan who inspired me to pursue a better work-life balance and always stay positive; to Nich and Adam for their contributions and suggestions to my PhD projects; to my collaborator Sai and his coop, Charlotte, for helping me realize my vision of using my films in photovoltaic application.

I would also like to thank the Evercloak team for their support throughout my part-time PhD journey, particularly to Evelyn for her tremendous understanding and encouragement, and to Ted for his invaluable mentorship providing me with wise guidance and constructive feedback.

Additionally, I would like to express my gratitude to my families and my in-law families. Both my parents and my in-laws have been so supportive during my graduate school studies. I feel very fortunate to have two sets of families who are both very understanding and encouraging.

Lastly, I owe many thanks to my husband, Nate, who is more patient with me than himself. He never stops encouraging me to pursue my dreams and building my professional career. He has

supported me through all the ups and downs during my graduate studies. I am amazed by his willingness to proofread all my drafts and listen to my project obstacles. I would have never been able to achieve this far without Nate’s support and company.

# Table of Contents

**Statement of Contributions** ..... **iv**

**Abstract** ..... **vi**

**Acknowledgments** ..... **viii**

**List of Figures** ..... **xv**

**List of Tables** ..... **xviii**

**List of Abbreviations** ..... **xix**

**Chapter 1: Introduction** ..... **1**

1.1 Overview of the Thesis ..... 1

1.2 Objectives of the Thesis ..... 3

**Chapter 2: Literature Review** ..... **4**

2.1 Introduction ..... 4

2.2 Traditional and Modified Langmuir Film Deposition ..... 4

2.2.1 Early history of insoluble films (Langmuir films) at the air-water interface ..... 4

2.2.2 Mechanism of substance trapping at the water surface ..... 7

2.2.3 Langmuir film of 0D, 1D and 2D materials ..... 8

2.2.4 Thermodynamics of Langmuir film ..... 13

2.2.5 Modified Langmuir film deposition – Towards R2R process ..... 18

2.3 Two-dimensional (2D) Materials ..... 20

2.3.1 Graphene-based materials ..... 20

2.3.2 Molybdenum disulfide ..... 21

2.4 Spontaneous Clustering of Nanomaterials at the Air-water Interface ..... 24

2.4.1 Cluster formation of 0D and 1D materials ..... 24

2.4.2 Cluster formation of 2D materials ..... 26

2.4.3 Colloidal Forces ..... 27

2.4.4 Mechanism of 2D clustering at the air-water interface ..... 28

2.5 Liquid Spreading at the Air-water Interface ..... 30

2.5.1 Thermodynamics of liquid spreads upon the surface of another ..... 30

2.5.2 Kinetics and dynamics of liquid spreading upon the surface of another ..... 31

2.6 Layout of the Thesis ..... 36

**Chapter 3: Continuous Langmuir Film Deposition and Transfer by Controlled Edge-to-Edge Assembly of Graphene-Based Materials ..... 39**

3.1 Introduction ..... 39

3.2 Experimental Methods ..... 40

3.2.1 Graphene oxide (GO) synthesis ..... 40

3.2.2 Thermally reduced graphene oxide (rGO) ..... 41

3.2.3 GO spreading dispersion ..... 41

3.2.4 Thermally reduced graphite oxide (rGO) spreading suspension: ..... 42

3.2.5 Barrier-free, spreading-assisted deposition ..... 42

3.2.6 Solvent spreading-assisted deposition on commercial LB trough with fixed barriers ..... 43

3.2.7 Compression-expansion isotherm experiment on commercial LB trough ..... 44

3.2.8 Characterization ..... 44

3.3 Results and Discussion ..... 47

3.3.1 Ink formulation and development of large-area Langmuir film ..... 47

3.3.2 Aggregation mechanism of GO nanosheets ..... 52

3.3.3 Solvent spreading-induced film densification ..... 55

3.3.4 Continuous coating of rGO film ..... 58

3.4 Conclusion ..... 60

**Chapter 4: Aging Spreading Dispersion of 1T-$MoS_2$ – Aging Effect and Improved Processing Method ..... 61**

4.1 Introduction ..... 61

4.2 Experimental Methods ..... 63

4.2.1 Chemical exfoliation of $MoS_2$ using n-butyllithium ..... 63

4.2.2 Sample preparation for degradation studies ..... 63

4.2.3 Solvent exchange of *ce*-$MoS_2$ aqueous dispersion ..... 64

4.2.4 Preparation of stock and spreading dispersion of 1T-$MoS_2$ nanosheets ..... 65

4.2.5 *SSaL* deposition of 1T-$MoS_2$ nanosheets ..... 65

4.2.6 Characterization ..... 66

4.3 Results and Discussion ..... 69

4.3.1 Effect of pH on 1T-$MoS_2$ stability. ..... 69

4.3.2 Ambient light-accelerated degradation ..... 72

4.3.3 Influence of oxygen on degradation process. ..... 76

4.3.4 Insights on the enhanced degradation of 1T-$MoS_2$ dispersion by alkaline media and ambient light irradiation. ..... 78

4.3.5 The improved spreading dispersion of *ce*-$MoS_2$ – Maximizing yields of monolayer sheets and 1T polymorph contents ..... 87

4.4 Conclusions ..... 89

**Chapter 5: Spontaneous Clustering of Exfoliated Two-dimensional Materials at the Air-Water Interface ..... 91**

5.1 Introduction ..... 91

5.2 Materials and Methods ..... 93

5.2.1 Materials ..... 93

5.2.2 Experimental methods ..... 93

5.2.3 Characterization methods ..... 101

5.2.4 Data analysis methods ..... 102

5.3 Results and Discussion ..... 109

5.3.1 Surface tension measurements of various solvents ..... 109

5.3.2 Spontaneous cluster formation and concentration effect ..... 109

5.3.3 Global trend in 2D materials ..... 112

5.3.4 Clustering mechanism ..... 116

5.3.5 Impact of cluster structure on Langmuir film assembly ..... 123

5.4 Conclusions ..... 128

**Chapter 6: Study of Solvent Spreading and its Application in Roll-to-roll processing of 2D Langmuir film ..... 130**

6.1 Introduction ..... 130

6.2 Materials and Methods ..... 131

6.2.1 Materials and spreading dispersions ..... 131

6.2.2 Instrumentation ..... 132

6.3 Results and Discussion ..... 133

6.3.1 Upgrade of Custom-designed Langmuir-Adam Balance ..... 133

6.3.2 Study of the driving force of solvent spreading-assisted Langmuir film assembly (*SSaL*) ..... 134

6.3.3 Impact of spreading profile on film assembly ..... 140

6.3.4 R2R Coatings of 2D Langmuir films ..... 144

6.4 Conclusion ..... 148

**Chapter 7: $MoS_2$ Langmuir film for perovskite solar cell ..... 150**

7.1 Introduction ..... 150

7.2 Experimental Methods ..... 151

7.2.1 Preparation of FTO substrate ..... 151

7.2.2 *SSaL* deposition of *ce*-$MoS_2$ and annealing treatment ..... 151

7.2.3 Fabrication of perovskite solar cells ..... 152

7.2.4 Characterization ..... 152

7.3 Results and Discussion ..... 153

7.4 Conclusion ..... 154

**Chapter 8: Summary and Recommendations for Future Studies ..... 155**

8.1 Summary of Main Conclusions ..... 155

8.2 Recommendations for Future Studies ..... 156

8.2.1 $MoS_2$ HTL based large-area PSC ..... 156

8.2.2 Expanding the ink library ..... 156

8.2.3 Developing method to 'connect' sheets ..... 157

8.2.4 Further investigation: Aggregation mechanism of 2D sheets at the air-water interface ..... 157

**References ..... 158**

# List of Figures

**Figure 2.1 Early history of insoluble films (Langmuir films) at the air-water interface..... 5**
**Figure 2.2 Schematics of commonly used Langmuir film deposition methods ..... 6**
**Figure 2.3 Langmuir film of 0D materials. ..... 9**
**Figure 2.4 Langmuir film of aligned 1D nanorods. ..... 10**
**Figure 2.5 Langmuir film of GO monolayers and film applications ..... 11**
**Figure 2.6 Langmuir film of exfoliated 2D nanosheets other than graphene-based nanomaterials ..... 13**
**Figure 2.7 An ideal surface pressure−area ($\Pi - A$) isotherm obtained from Langmuir film of lipids ..... 15**
**Figure 2.8 Examples of elastic modulus ($K$) plots ..... 16**
**Figure 2.9 Modified LB methods - Towards R2R processing ..... 19**
**Figure 2.10 1T and 2H $MoS_2$ and their application in photovoltaics. ..... 22**
**Figure 2.11 Spontaneous cluster formation of 0D and 1D materials at the air-water interface..... 26**
**Figure 2.12 Spontaneous cluster formation of 2D materials at the air-water interface ..... 27**
**Figure 2.13 Gold nanoparticles at the air-water interface. ..... 30**
**Figure 2.14 Profiles of one liquid spreading on another. ..... 32**
**Figure 2.15 Liquid behavior at the spreading boundary ..... 34**
**Figure 2.16 Occurrence of solutal Marangoni flows when IPA spreads on water surface. ..... 35**
**Figure 3.1 Analysis of Langmuir films deposited from the traditional and improved spreading solvent systems. ..... 48**
**Figure 3.2 Solvent spreading-assisted deposition of GO. ..... 49**
**Figure 3.3 Morphology of GO films prepared by barrier-free deposition ..... 51**
**Figure 3.4 Two times Langmuir specific surface area ($LSSA$) of GO Langmuir films as a function of the deposition dispersion concentration ..... 52**
**Figure 3.5 Impact of subphase pH on GO aggregation ..... 53**
**Figure 3.6 Impact of subphase ionic strength on GO aggregation ..... 54**
**Figure 3.7 Probing the liquid-liquid spreading pressure acting on the Langmuir film ..... 56**
**Figure 3.8 Morphology of GO films by using chloroform/ethanol (v:v = 1:13) as the spreading solvent ..... 57**
**Figure 3.9 Barrier-free deposition and continuous film coating of rGO ..... 59**
**Figure 4.1 Study of pH effect. ..... 70**
**Figure 4.2 UV-Vis spectra of two-weeks aged Milli-Q samples when stored in air and under light ..... 71**
**Figure 4.3 Impact of dispersion concentration of the fresh samples. ..... 72**
**Figure 4.4 Light-induced rapid degradation of 1T dominated $MoS_2$ in basic aqueous dispersion ..... 73**
**Figure 4.5 XPS results of fresh, LiOH/light and LiOH/dark samples ..... 74**
**Figure 4.6 XPS results of bulk $MoS_2$ powder ..... 75**

**Figure 4.7 Settlement of nanosheets in diluted 1T-$MoS_2$ dispersion facilitated by light exposure ..... 76**
**Figure 4.8 Influence of oxygen on degradation process – $O_2$ environment ..... 77**
**Figure 4.9 Influence of oxygen on degradation process – $N_2$ environment ..... 77**
**Figure 4.10 Analysis of the solid and soluble degradation products and comparison of degradation rates ..... 79**
**Figure 4.11 Morphology changes in 1T-$MoS_2$ sheets after degradation ..... 80**
**Figure 4.12 Mechanism study of light-accelerated degradation of 1T-$MoS_2$ aqueous dispersion ..... 82**
**Figure 4.13 Degradation of supernatant samples ..... 83**
**Figure 4.14 Kinetic study of 1T-$MoS_2$ aqueous degradation in air ..... 85**
**Figure 4.15 Proposed mechanism of photo accelerated degradation in 1T dominated $MoS_2$ aqueous dispersion ..... 87**
**Figure 4.16 Improved spreading dispersion of *ce*-$MoS_2$ ..... 88**
**Figure 5.1 Surface pressure measurement during cluster deposition of *ce*-$MoS_2$ ..... 100**
**Figure 5.2 Examples of fractal dimension characterization ..... 104**
**Figure 5.3 Investigation on the purity of reagent alcohol ..... 109**
**Figure 5.4 Fractal clusters and island-like domains formed by various nanosheets ..... 110**
**Figure 5.5 Material characterization of *ce*-$MoS_2$ and rGO nanosheets ..... 111**
**Figure 5.6 Global trend of 2D nanosheets clustering at the air-water interface ..... 113**
**Figure 5.7 SEM image of cluster formed from re-stacked *ce*-$MoS_2$ dispersion in RA/DCE ..... 116**
**Figure 5.8 Study of clustering mechanism stage 1 ..... 117**
**Figure 5.9 Impact of dipping rate on concentration of droplet ..... 118**
**Figure 5.10 2D materials gathering in the spreading reservoir ..... 120**
**Figure 5.11 Study of clustering mechanism stage 2 ..... 122**
**Figure 5.12 Impact of cluster structure on packing density in the final Langmuir film of *ce*-$MoS_2$ ..... 125**
**Figure 5.13 Compression-expansion isotherms of GO nanosheets prepared from clusters of (a) island-like domains (0.025 mg/mL) and (b) linear networks (0.00625 mg/mL) ..... 125**
**Figure 5.14 Impact of cluster structure on the final Langmuir film of *ce*-$MoS_2$ (high compression) ..... 127**
**Figure 5.15 Buckling shown in Langmuir films of *ce*-$MoS_2$ nanosheets when surface pressure reaches plateau. ..... 128**
**Figure 6.1 Custom-made Langmuir-Adam balance ..... 133**
**Figure 6.2 Upgraded Custom-designed Langmuir-Adam Balance ..... 134**
**Figure 6.3 Spreading profile of various polar and water-immiscible solvent mixtures ..... 136**
**Figure 6.4 Impact of polar solvent on spreading profile ..... 137**
**Figure 6.5 Impact of water-immiscible solvent on spreading profile ..... 138**
**Figure 6.6 Summary plot of spreading pressure measured at 4-6 cm away from the dripping position. ..... 138**
**Figure 6.7 Correlation between spreading profile and mixture physical properties ..... 139**
**Figure 6.8 Impact of spreading pressure on film packing density ..... 141**
**Figure 6.9 Impact of spreading pressure on Langmuir film phase transition ..... 142**

**Figure 6.10 Impact of number of drippers on wider film assembly ..... 143**
**Figure 6.11 Impact of substrate wettability by water on film quality prepared using R2R processing. ..... 145**
**Figure 6.12 Resulting 2D films by *SSaL*-R2R processing..... 147**
**Figure 6.13 Resulting 2D films by *SSaL*-R2R processing on wider trough ..... 148**
**Figure 7.1 Forward-bias *J – V* characteristics of PSC with and without $MoS_2$ film as HTL. ..... 153**

# List of Tables

**Table 4.1 Summary of fitting constrains for XPS analysis. ..... 67**
**Table 4.2 Changes in 2H/(2H+1T) with time estimated by UV-Vis (and XPS) ..... 71**
**Table 4.3 Percentage of the individual component estimated by the integrated areas of the fitted Mo 3d core level spectra. ..... 75**
**Table 4.4 Kinetic parameters extracted from first-order rate law ..... 85**
**Table 5.1 Recipes of spreading dispersion of *ce*-$MoS_2$ used in this work in an example of 1.4 mL spreading dispersion ..... 97**
**Table 5.2 Recipes of spreading dispersion of GO used in this work in an example of 1.4 mL spreading dispersion ..... 98**
**Table 5.3 Recipes of spreading dispersion of rGO used in this work in an example of 1.4 mL spreading dispersion ..... 98**
**Table 5.4 Parameters for estimating van der Waals (vdW) potential. ..... 106**
**Table 5.5 Parameters for estimating long-range capillary potential. ..... 107**
**Table 5.6 Parameters for estimating hydrophobic potential/area. ..... 108**
**Table 5.7 Surface tension of pure and mixed solvents used in this work. ..... 109**
**Table 5.8 Uncorrected vs. corrected *LSSA* using microscopic packing density. ..... 114**
**Table 6.1 Physical properties of pure solvents and their mixtures ..... 135**
**Table 6.2 Summary of *SSaL*-R2R coating speed ..... 146**

# List of Abbreviations

| | |
|---|---|
| 0D | zero-dimensional |
| 1D | one-dimensional |
| 2D | two-dimensional |
| BtOH | 1-butanol |
| t-BtOH | t-butanol |
| DCE | 1,2-dichloroethane |
| DCM | dichloromethane |
| IPA | 2-propanol, isopropanol |
| n-BuLi | n-butyllithium |
| BCP | bathocuproine |
| DMF | dimethylformamide |
| NMP | *N*-Methyl-2-pyrrolidone |
| RA | reagent alcohol |
| DMSO | dimethyl sulfoxide |
| GO | graphene oxide |
| rGO | (thermally) reduced graphene oxide |
| 1T-$MoS_2$ (Chapter 4); *ce*-$MoS_2$ (rest of the thesis) | chemically exfoliated $MoS_2$ |
| TMD | transition metal dichalcogenides |
| hBN | hexagonal boron nitride |
| FTO | fluorine-doped tin oxide |
| PEDOT:PSS | poly(3,4-ethylenedioxythiophene) polystyrene sulfonate |
| PTAA | poly(triaryl amine) |

| | |
|---|---|
| PET | polyethylene terephthalate |
| PES | polyethersulfone |
| ROS | reactive oxygen species |
| AFM | atomic force microscopy |
| BAM | Brewster angle microscope |
| SEM | scanning electron microscopy |
| FTIR | Fourier-transform infrared |
| XPS | X-ray photoelectron spectroscopies |
| PL | photoluminescence |
| CVD | chemical vapor deposition |
| DLCA | diffusion-limited cluster aggregation |
| RLCA | reaction-limited cluster aggregation |
| LB | Langmuir-Blodgett |
| LS | Langmuir-Schaefer |
| vdW | van der Waals |
| EDL | electrical double layer |
| PCE | power conversion efficiency |
| PSC | perovskite solar cell |
| HTL | hole transporting layer |
| ETL | electron-transporting layer |
| *LSSA* | Langmuir specific surface area |
| *SSA* | specific surface area |
| *SSaL* | Solvent-spreading assisted Langmuir film method |

| | |
|---|---|
| *BCL* | Barrier-compressed Langmuir film |
| *SP* | spreading pressure |
| R2R | roll-to-roll |
| *SSaL*-R2R | Solvent-spreading assisted Langmuir film method-based roll-to-roll processing |

# Chapter 1: Introduction

## 1.1 Overview of the Thesis

Atomically thin two-dimensional (2D) materials have emerged as promising candidates in various applications including not only flexible electronics,[1,2] energy storage devices and sensors,[3–5] but also as functional coatings in water-purification,[6] anti-corrosion[7] and anti-microbial protection [8]. Compared to their bulk counterparts, the uniqueness of 2D materials is unlocked only when they are exfoliated into monolayer or few-layers nanosheets. Historically, these materials have been produced and investigated by mechanical exfoliation (Scotch® tape) of bulk synthetic crystals. However, this method is not scalable. Fortunately, there has been extensive research on refining exfoliation methods (both physically and chemically) and identifying advantageous applications. However, challenges remain in developing versatile, large-area coatings that are at the level of a single layer or exfoliated sheet. Trapping 2D materials at the air-water interface forms so-called Langmuir films, which provides an interesting platform for manipulating and assembling any type of exfoliated 2D material if it is water stable.[4,9–22] It is more versatile than high vacuum, high temperature vapor deposition methods (e.g. chemical vapor deposition) and provides remarkable uniformity in coverage and thickness than common solution processing techniques does such as vacuum-filtration, spay-coating, spin coating or electrophoretic deposition. No matter if it is traditional or modified Langmuir film methods, the deposition process can be broken down into four steps: 1) Formulation of a dispersion (i.e., ink) of 2D material to be spread onto the air-water interface; 2) The spreading of a singular drop of the ink over part of the air-water interface. This occurs concurrently with evaporation of the solvent or mixing with the water. 3) Repetitive dripping deploying the desired amount of materials floating on the water surface; 4) Densification of the film followed by transfer to the substrate.

As for step 1), alcohol solutions are predominately chosen for the dispersion of 2D materials, since it is a preferable solvent to eliminate restacking of exfoliated sheets and, in some cases, can also be used to perform the liquid-exfoliation procedure.[9,23–25] However, when transferring materials onto the water surface, the mixing of the carrier solvent and subphase water causes significant loss of materials into the subphase water, especially for hydrophilic or

amphiphilic materials such as chemically exfoliated $MoS_2$ (*ce*-$MoS_2$) and graphene oxide (GO).[25] Therefore, new formulation is required, which ideally is suitable for different types of 2D materials. Additionally, since exfoliated materials contain defects which are prone to degradation, fundamental studies on material degradation is crucial to form stable, low-impurity 2D materials inks.

In step 2), 2D aggregates/clusters can form and become the 'building blocks' of the Langmuir film. The spontaneous clustering of 0D and 1D materials at the air-water interface has been commonly reported in previous literatures, along with the controlling factors on cluster structure.[26,27] Despite that, contradictory observations are revealed in the case of 2D materials involving the formation of island-like domains[28] vs. fractal clusters[22] vs. isolated sheets[9,29]. To our knowledge, there is not yet a way to control the formation of clusters of 2D materials on the water surface, let alone studying their impact on the quality of the resulting Langmuir film.

Moving on to step 3) and 4), existing Langmuir film-based roll-to-roll (R2R) processing separates these two processes. As materials are continuously deployed upon the water surface, the densification and transfer of films rely on external forces such as barrier/paddle or flowing subphase water.[30–36] However, by utilizing the lateral pressure exerted from the spreading of each droplet, step 3) and 4) can be combined which results in an efficient R2R processing. Furthermore, unlike the existing R2R methods where the surface pressure of the film is not monitored, we could measure the spreading pressure and use it to estimate the compression stage of the film.

As for the application of the Langmuir film of 2D materials, researchers have demonstrated considerable applications not only including electronic devices such as (transparent) conductors,[9,22,37,38] sensors,[12] optoelectronics,[19,39] and batteries[4,40] but also in anti-microbial coatings,[16,21,41] and being used as platforms for fundamental studies.[11,13,14,17,18,42] Molybdenum disulfide ($MoS_2$), a 2D material in the Transition metal dichalcogenides (TMD) family, has recently been utilized as an ultrathin hole transporting layer and interfacial layer in perovskite solar cells. The results present enhancement in both device efficiency and long-term stability, especially in the large-area devices.[43–48] However, current deposition methods such as spray- and spin-coating forms patchy coverage and non-uniform thickness. Therefore, Langmuir film method will likely be a better alternative for depositing precisely controlled $MoS_2$ film to achieve consistent

improvements in performance and a transitioned roll-to-roll process would benefit the development of flexible, large-scale photovoltaics.

## 1.2 Objectives of the Thesis

The main goal of this thesis is to develop a coating method capable of depositing single layers of exfoliated 2D materials (i.e., flake) onto large-area substrates (e.g., silicon wafers or continuous films) for applications in optoelectronics. To do so, we aim to not only transition the traditional Langmuir-Blodgett coating approach, that uses barriers to densify single layers, into a barrier-free method that uses solvent spreading or Marangoni flows to densify and direct film growth, but also seek to understand how to control the 'building blocks' (i.e. cluster/aggregation) and 'driving force' (i.e. spreading pressure) for film formation and transfer. This is achieved through the following specific aims:

***Specific aim 1*** – Develop stable, exfoliated 2D materials ink formulations that are suitable for both hydrophilic and hydrophobic 2D materials and capable of being spread at the air-water interface with high yield of material transfer

***Specific aim 2*** – Understand how to control the 2D aggregate structure after droplet spreading and their impact on the properties of resulting film.

***Specific aim 3*** – Elucidate the role of the spreading solvent properties on directing film densification and formation

***Specific aim 4*** – Showcase the R2R processing powered by solvent spreading and application of Langmuir film in perovskite solar cell

# Chapter 2: Literature Review

## 2.1 Introduction

This chapter presents a review of the literature relevant to the understanding of the research contained in this thesis.

## 2.2 Traditional and Modified Langmuir Film Deposition

### 2.2.1 Early history of insoluble films (Langmuir films) at the air-water interface

In 1774, Dr. Franklin conducted an experiment on the pond at Clapham, where he placed less than a teaspoon of oil and observed that the oil immediately spread into a thin film covering over serval square yards of the water surface.[49] Little did he know that the thickness of this film could uncover the size of one single molecule. Two hundred years later, a surface chemist – Professor Charles Giles, identified the pond at Clapham Common and reproduced Franklin's experiment. This time the evidence was captured by photography, as shown in Figure 2.1a.[50] In 1891, Miss Pockels built one of the first surface balances by using parts in her kitchen and conducted experiments to measure the surface tension of water and unveiled behaviors of contaminated water surface. The value of these studies was recognized by Dr. Rayleigh and published in Nature in 1891.[51] In 1917, Irving Langmuir systematically studied the thermodynamic behavior of oil films (insoluble films) on the water surface. In a typical experiment, after spreading a very small amount of oil on the water surface, the surface pressure, which is determined as the surface tension difference between pristine and contaminated water surface, was measured to be zero. By sliding the barrier along the tray (trough), the surface pressure was first increased slowly in which case molecules could still move around freely (gas phase). After further compression, the film entered into a 'liquid' phase where it transitioned from 'liquid-expanded' phase to 'liquid-condensed' phase and the molecules became immobile. As the surface pressure started escalating, the film remained solid until it collapsed to release the compression stress. The critical surface area at the collapse determined the minimum area per molecule which was utilized as evidence by Langmuir to prove a particular hypothesis of molecule composition over another. In 1935, Katherine Blodgett worked with Langmuir and successfully transferred insoluble films (Langmuir

films) onto glass substrates for anti-reflective application.[52] Figure 2.1b displays a schematic illustration of the deposition apparatus. The final thickness of the coating can be precisely controlled via layer-by-layer deposition. The process required great care for subphase pH and pre-treatment on the glass substrates for successful deposition. During the process, the surface pressure of the film held constant by spreading a piston-oil, such as oleic acid, on the other side of the string, as shown in Figure 2.1c. Prior to the Wilhelmy plate and electronic tensiometer being introduced to the Langmuir film system to monitor the surface tension, piston-oil was often used to maintain an constant surface pressure at any given water surface area (e.g. 30 mN/m for oleic acid), since it spreads into a monolayer film holding at an equilibrium pressure with excess liquid forming a lens (**Section 2.5.1**, Liquid type 2).

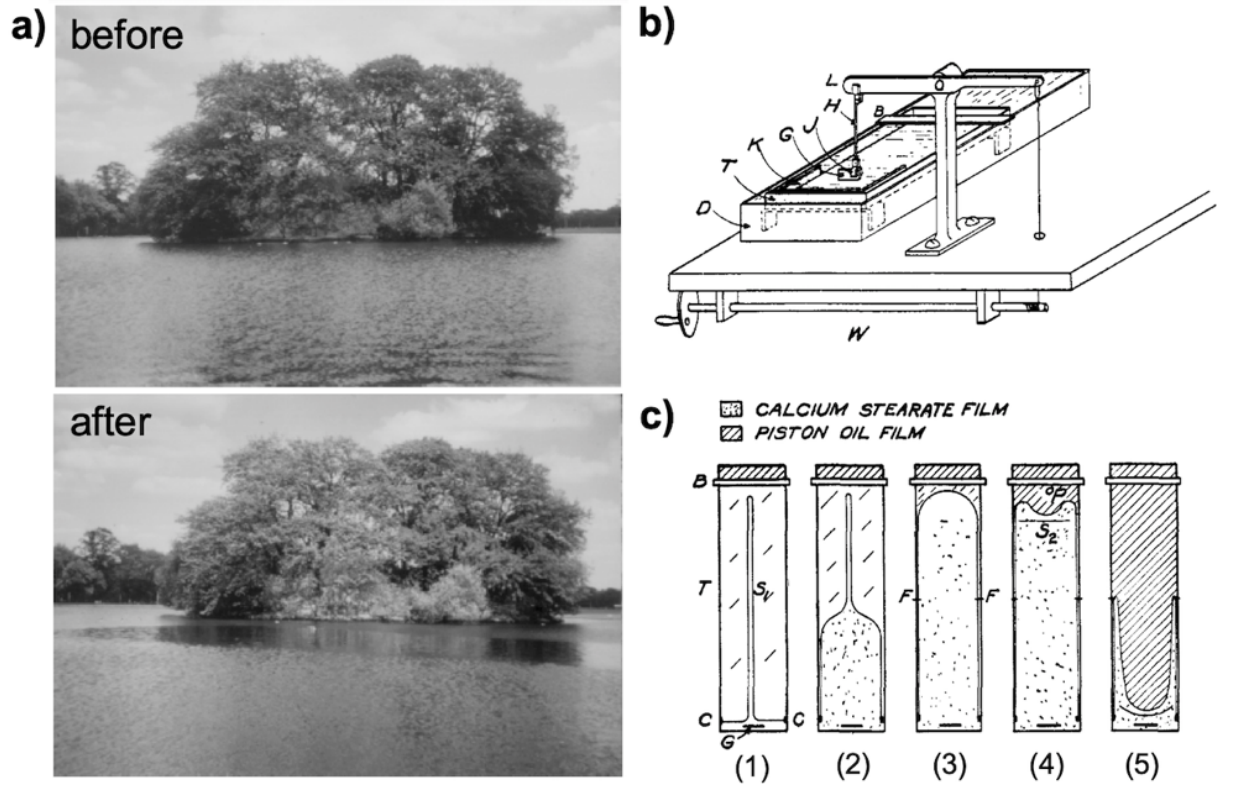



**Figure 2.1 Early history of insoluble films (Langmuir films) at the air-water interface.** (a) photographs of Clapham pond before and after spreading less than a teaspoon of oil. Reproduced from Ref.[50] (b) Schematic illustration of apparatus for transferring Langmuir film from the water surface to a solid substrate. (c) Deposition of calcium stearate surface film at the equilibrium pressure provide by spreading of piston oil. (b) and (c) are reproduced from ref.[52]

As technology evolved, tensiometers and Wilhelmy plate were used to monitor surface tension changes, which allows continuous measurements of surface pressure during compression

and deposition. Besides the vertical deposition (Langmuir-Blodgett, LB) method used by Blodgett, Langmuir-Schaefer (LS) method is a popular alternative where a substrate is placed parallel to the water surface and comes in contact with the film from the air side. Another alternative is horizontal-precipitation method where the substrate is placed underneath the subphase water prior to film formation, and the film is transferred onto the substrates by reducing the water level below the substrate surface. Figure 2.2 presented schematic diagrams for all three deposition methods.

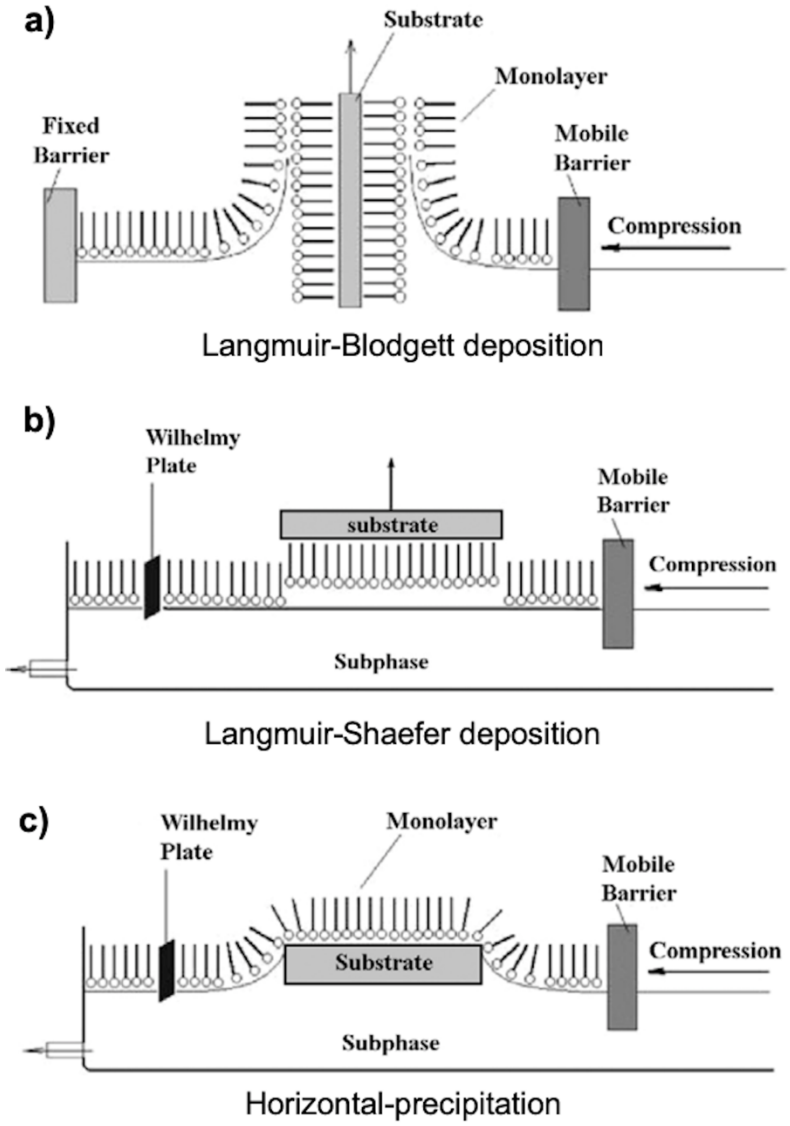



**Figure 2.2 Schematics of commonly used Langmuir film deposition methods**: (a) Langmuir-Blodgett, (b) Langmuir-Schaefer and (c) Horizontal-precipitation. Reproduced from ref.[34]

### 2.2.2 Mechanism of substance trapping at the water surface

Surface tension is a measurement of the cohesive energy present at an interface. Considering water as an example, two water molecules attract each other via hydrogen bonds. As for a molecule in the bulk of water, the attractive forces from other molecules located at all directions form a balanced interaction, whereas molecules located at the surface of water experience imbalanced forces, pulling them towards the bulk of the liquid. Amphiphilic molecules consist of two parts: a hydrophilic 'head' and hydrophobic 'tail'. When introduced into the bulk of water, they usually form micelles. However, they can also be trapped at the water surface via the spreading of a volatile solvent. Chloroform and toluene are typically used as the spreading solvent for lipids because: 1) They are water-immiscible and thus will prevent the loss of lipids into the bulk of subphase water forming micelles; 2) They are volatile and have little affinity with the lipids and are therefore unlikely to contaminate the resulting film. A positive spreading coefficient, *S*, is the thermodynamic requirement for spontaneous spreading, otherwise the spreading liquid will pool and form a lens instead. More information regarding *S* and solvent spreading can be found in **section 2.5**. Both chloroform and toluene on their do not spread well on the air-water interface. However, when amphiphilic lipids are dissolved, they can aid in spreading by enabling Marangoni flows.[53] After solvent evaporates, the amphiphilic molecule will be anchored at the air-water interface with the hydrophilic 'head' immersing in the water due to strong attraction with water molecules, while hydrophobic 'tail' experiencing repulsive interactions with the water and pointing towards the air. On the other hand, as for non-typical amphiphiles, such as nanoparticles, they can be trapped at the water surface using the same method (solvent spreading and evaporation) due to the high surface tension of water. Chloroform is also used for transferring 0D and 1D nanoparticles such as Au nanoparticles and carbon nanotubes, since these particles are often decorated with amphiphilic molecules. However, as for 2D nanosheets, typical spreading solvents can easily cause colloidal instability and their poor spreading behavior could unlikely be improved by the nanosheets. In the case of graphene oxide, a water-alcohol mixture is used instead. Unfortunately, it results in significant loss of material (~ 99% loss) into the subphase water.[25] We developed a new strategy to formulate spreading solvent (mixture) for 2D materials which not only provides high yield but also ensure uniform spreading. More discussions about this can be found

in **Chapter 3**. In the following section, we will demonstrate the applications of Langmuir film method on 0D, 1D and 2D materials, respectively.

### 2.2.3 Langmuir film of 0D, 1D and 2D materials

As nanotechnology started blooming in the 20th Century, Langmuir film technology falls perfectly in place for assembling nanoparticles into one-atom thick films. In the case of nanoparticles and nanorods, it is recognized as a powerful tool to precisely control the interparticle distance and resulting structure. Collier *et al*. used LB technology to manipulate organically functionalized silver quantum nanodots into a quasi-ordered monolayer.[54] During compression, once the interparticle distance was reduced below ~12 angstroms (Figure 2.3a), the electronic wave function started overlapping between adjacent particles resulting in the tunable electronic band structure. This was the first experimental evidence that revealed quantum mechanical couplings between adjacent silver nanocrystals. Further compression below 5 angstroms led to a reversible transition from insulator to metal. In 2001, Kim *et al*. reported the Langmuir film assembly of 1D nanorods.[55] Unlike super structures formed by nanoparticles, as for short nanorods, increasing the film density resulted in transition from 2D isotropic to nematic, and then to smectic (Figure 2.3b1-b4). Further compression eventually led to burst from 2D monolayer to multilayers. This precisely controlled transition is suggested to potentially facilitate discovery on new optical, magnetic and electrical properties resulting from tunable structures engineered by sizes and dimensions. On the other hand, nanorods with larger aspect ratio (~ 150:1) exhibited difficulties in assembling into organized structures. They instead formed nematic layers, where the long nanorods pointed roughly towards the same direction. Lateral capillary force and van der Waals attractions were suggested to be responsible for the side-by-side arrangements. Apart from size and aspect ratio, surface functionality also played an important role in regulating the interactions between the particles when forming Langmuir films for use in high density logic and memory devices. Paul. *et al*. built a metal-insulator-semiconductor (MIS) based electronic memory structure by incorporating LB monolayers of densely-packed organically passivated gold nanoparticles (Figure 2.3c1) onto silicon oxide/silicon substrate prior to depositing layers of fatty acid salt.[56] By performing capacitance-voltage sweeps, the device showed unexpected hysteresis effect during the reverse scan (Figure 2.3c2), which could result from the storage of charges in the monolayers of organically passivated gold nanoparticles.

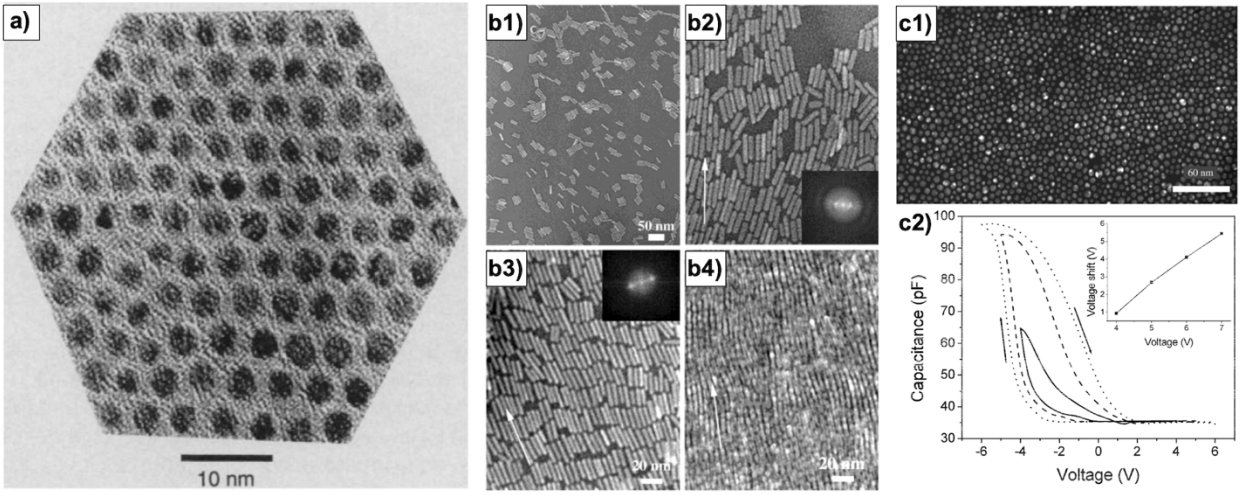



**Figure 2.3 Langmuir film of 0D materials**. (a) Transmission electron microscopy (TEM) images of compressed films consisting of decanethiol-capped Ag particles separated by ~12 Å. Reproduced from ref. [54] (b1-b4) TEM images of pressure-induced phase transition in film composed of BaCrO4 from (b1) isotopic to (b2) 2D nematic, (b3) 2D smectic and eventually to multilayer 3D nematic. Reproduced from ref.[55] (c1) TEM images of compressed Au nanoparticles. (c2) Current-voltage sweeps measured on MIS structures incorporating film of Au nanoparticles shown in (c1) Reproduced from ref. [56]

As for 1D nanowires, LB assembly method has emerged as a popular approach to achieve uniform, directional alignment. Tao *et al*. assembled LB monolayer of aligned silver nanowires.[57] The compression forced the nanowires to align in parallel to the barriers and pack densely (Figure 2.4a). The resulting film presented promising results in sensing molecules in air-borne and solution environment. The detection on 1-hexadecanethiol, Rhodamine 6G and 2,4-dinitrotoluene (2,4-DNT) showed large enhancement factors as well as remarkable precision on the detection of 2,4-DNT achieving a sensitivity as high as 0.7 pg. Li *et al*. also formed parallel arrays of closely-packed single wall carbon nanotubes (SWNTs) via LB assembly on oxide substrate (Figure 2.4b) for evaluating electronic properties of two types of SWNTs.[58] Devices composed of small carbon nanotubes were 25 times more resistive and exhibited a higher degree of nonlinearity in the I-V characteristic, possibly due to high contact resistance. Moreover, Wang *et al*. simplified the method to synthesize gram qualities of Ge nanowires (GeNWs) and used LB technology to prepare an ultra-thin film of GeNWs.[59] As shown in Figure 2.4c, the resulting film consisted of highly aligned nanowires after compression. Interestingly, 5% of ethanol in subphase water appeared to be a key factor to obtain monolayers of GeNWs. Without the ethanol, hydrophobic interactions between functionalized nanowires appeared to be so strong that overlaps and bundles of nanowires formed instead. It is suggested that the GeNWs LB film could be used in field effect transistors.

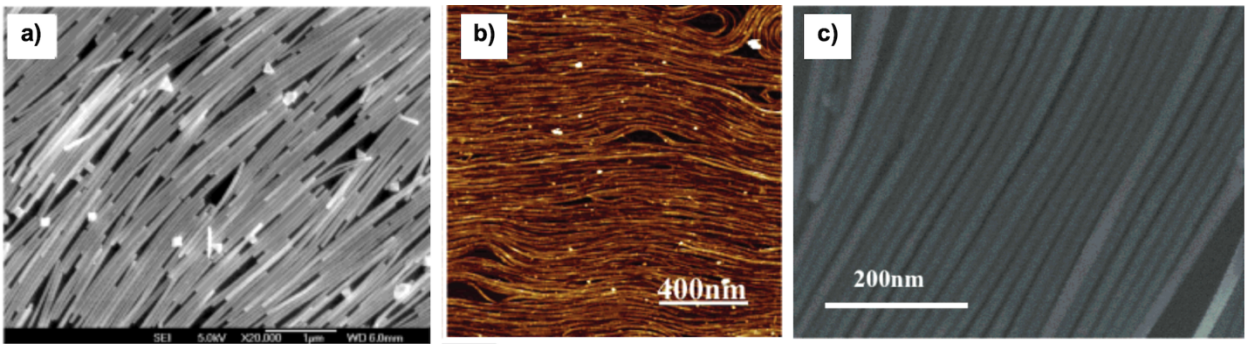



**Figure 2.4 Langmuir film of aligned 1D nanorods**. (a) SEM image of Langmuir-Blodgett (LB) film of aligned silver nanowires. Reproduced from ref. [57] (b) AFM image of LB film of aligned SWNTs. Reproduced from ref. [58] (c) SEM image of Langmuir-Blodgett (LB) film of aligned GeNW. Reproduced from ref. [59]

In 2009, Cote *et al*. initiated the studies of assembling Langmuir film of 2D nanosheets at the air-water interface. In their work, individual GO sheets were transferred onto the water surface. After compression, the GO sheets became interconnected at the edges to form wrinkles. Further compression resulted in sheets sliding over each other and formed interlocking overlaps. The densification of GO LB film and corresponding isotherm are presented in Figure 2.5a. The final film composed of interlocking sheets were collected on solid substrate and reduced to graphene via exposure to hydrazine vapor. The monolayer graphene exhibited transmission of 95.4% and sheet resistance of $1.9 \times 10^7 \Omega$ (Figure 2.5b1).[9] Since then, several research groups explored method to enhanced electrical properties of as-prepared graphene film. Zheng *et al*. demonstrates that sheet size plays a crucial role in the conductivity, as does the after-treatment.[10,60] By using GO sheets with lateral size of ~ 200 μm, the author obtained almost 8 times higher conductivity yielding ~600 Ω/sq compared to the films composed of sheets that are 10 – 50 times smaller. The after-treatment using thermal annealing and chemical doping further enhanced the performance to 459 Ω/sq without affecting the transmittance. The performance of these films is summarized in Figure 2.5b2.[10]

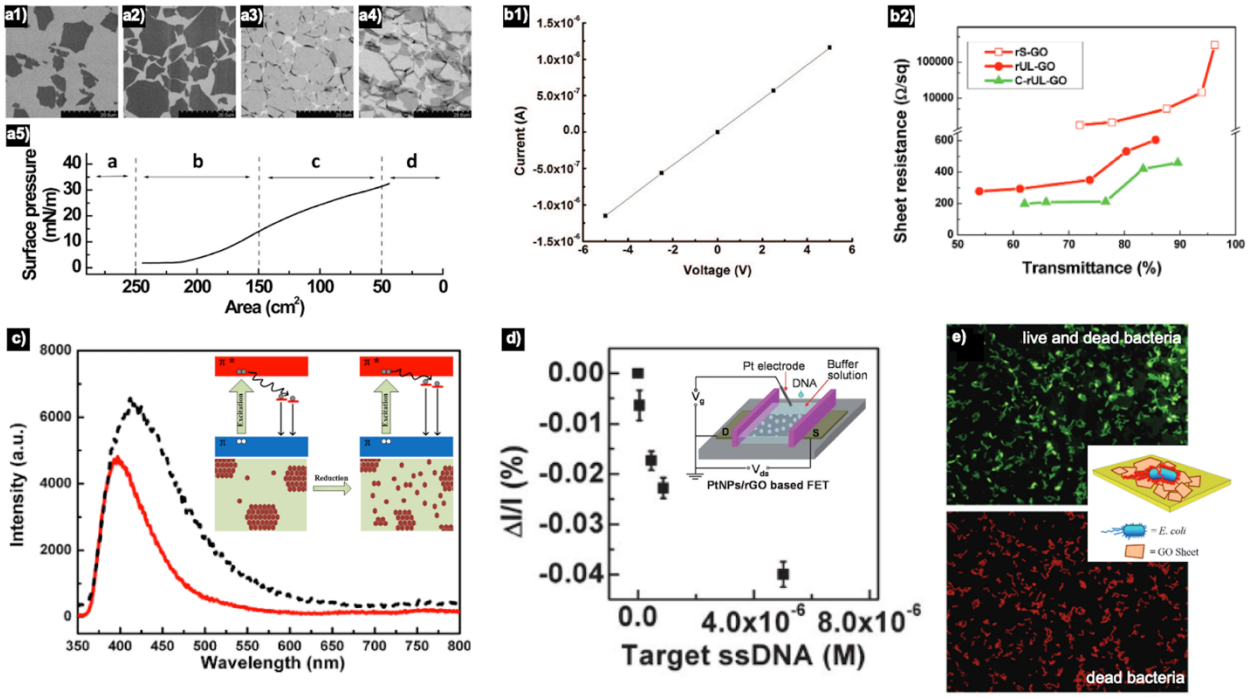



**Figure 2.5 Langmuir film of GO monolayers and film applications**. (a) LB assembly of single-layer GO sheets. (a1-a4) SEM images of the GO film collected at different compression stages resulting in surface pressure from low (a) to high (d) indicated in the (a5) isothermal surface pressure vs. area plot. Reproduced from ref.[9] (b1) Current-voltage plot of over-packed GO monolayers LB film measured using four-point probe. Reproduced from ref.[9] (b2) sheet resistance and transmittance measured at 550 nm for transparent conductors prepared from LB films of close-packed reduced small graphene oxide (rS-GO), reduced ultralarge graphene oxide (rUL-GO), and chemically doped, reduced ultralarge graphene oxide (C-rUL-GO). Reproduced from ref.[10] (c) Photoluminescence spectra of GO (red solid-line) and GO annealed at 800 °C (black dashed-line) LB films with the model of back structure for each case presented in the inset. Reproduced from ref.[14] (d) Conductance change vs. concentration of target DNA plot with the schematic illustration of the Pt nanoparticles/rGO LB films based DNA detection device shown in the inset. Reproduced from ref.[12] (e) Representative fluorescence images of Escherichia coli (E.coli) on double depositions of GO LB films. The inset displays the schematic illustration of the antibacterial mechanism at the basal plane of GO monolayers. Reproduced from ref.[16]

Compared to other cost-effective coating methods such as vacuum filtration, spin-coating and spray-coating, LB technology allows precise control on thickness and uniformity. Therefore, researchers used GO Langmuir film as a platform to perform fundamental studies. Han *et al*. investigated the photoluminescence (PL) properties of graphene sheets by altering $sp^2$ to $sp^3$ ratio via reduction process of GO to rGO (Figure 2.5c).[14] Compared to GO, rGO showed decreased PL and blueshift which is attributed to the newly formed $sp^2$ clusters after thermal reduction. Wang *et al*. separated a batch of single-layer GO sheets into two groups based on their lateral size by using pH-induced sedimentation method.[13] LB film composed of large, small and mixed GO monolayers were prepared followed by hydrazine reduction. After three layer-by-layer deposition, the resulting

film assembled from large sheets exhibits 0.95 MΩ/sq which is 6 times and 10 times less than the ones from mixed and small sheets. Since LB deposition can immobilize the nanosheets and result in exposure of sheet edges when the floating film was collected at early stage of compression, Mangadlao *et al*. used GO LB film to investigate the antibacterial mechanism of the nanosheets. The results suggested that the bacterial inactivation predominately relies on the chemistry of the GO basal plane instead of the physical puncture caused by sharp edges (Figure 2.5e).[16]

Moreover, by taking advantage of the available functional groups on the GO sheets, GO monolayers have also be used as a foundation to implement functional nanomaterials for various applications. Yin *et al*. decorated LB film of rGO monolayers with platinum nanoparticles (PtNPs). The resulting PtNPs/rGO film showed very high sensitivity (2.4 nM) for real-time DNA detection limit (Figure 2.5d).[12] Kumar *et al*. took advantage of the air-water interface and functionalized GO Langmuir film with 4-aminothiophenol modified gold nanoparticles (Au-ATP) by using Au-ATP containing water as the subphase instead of pure water.[15] The amine terminated Au-ATP bonded to the GO nanosheets via the edge carboxyl groups. The resulting composite films showed two-fold enhanced photocatalytic performance upon degradation of methylene blue dye as compared to earlier reports.

In 2017, Zhang (Xu) *et al*. produced a large-area, uniform coating of chemically-exfoliated $MoS_2$ sheets (*ce*-$MoS_2$), as shown in Figure 2.6a, by using a modified LB technology – the same one used in my Master's and PhD work.[61] Characterization of electrical and optical properties were conducted on the resulting film before and after heat treatment which resulted in polymorph transition of $MoS_2$ from 1T to 2H. This work is the first to apply Langmuir film technology to exfoliated 2D nanosheets other than graphene-based materials (graphene, GO, rGO). In 2019, Kalosi *et al*. prepared Langmuir film of few-layer $MoS_2$ prepared by liquid-phase exfoliation. The resulting film was transferred onto a silicon wafer coated with 500 nm thick thermal oxide via a modified Langmuir-Schaefer deposition method.[22] After thermal annealing treatment, the film achieved a low sheet resistance close to 10 kΩ/sq (Figure 2.6b), which is comparable to the one prepared from chemical vapor deposition (CVD) method. Zheng *et al*. took advantage of the smoothness of a Langmuir film and deposited Langmuir film of $MoS_2$ nanosheets on quartz substrate as a saturable absorber for a high-power Q-switched laser, resulting in high average output power and slope efficiency.[20] Chen (Xu) *et al*. utilized Langmuir film as a platform to

investigate the intrinsic capacitance of several exfoliated 2D materials. The results suggested that the metallic *ce*-$MoS_2$ exhibits over 10-fold the capacitance of the semiconducting 2H polymorph $MoS_2$ (14.9 vs. 1.39 μF/cm$^2$) under negative polarization with little frequency dependence.[42] The author further investigated the restacking effect of exfoliated $MoS_2$ and rGO by assembling multilayers via layer-by-layer deposition. The capacitance of multilayer $MoS_2$ scaled with the increased surface area whereas rGO did not, indicating the feasible ion penetration between stacked $MoS_2$ layers (Figure 2.6c). Nasr (Xu) *et al*. assembled Langmuir films of densely packed hexagonal boron nitride (hBN) nanosheets prepared via liquid-phase exfoliation (Figure 2.6d). A completely pinhole-free film was obtained after four depositions and the resulting break down voltage was measured to be 2.92 ± 0.36 MV/cm, which is close to what was reported for a CVD grown hBN film.[17]

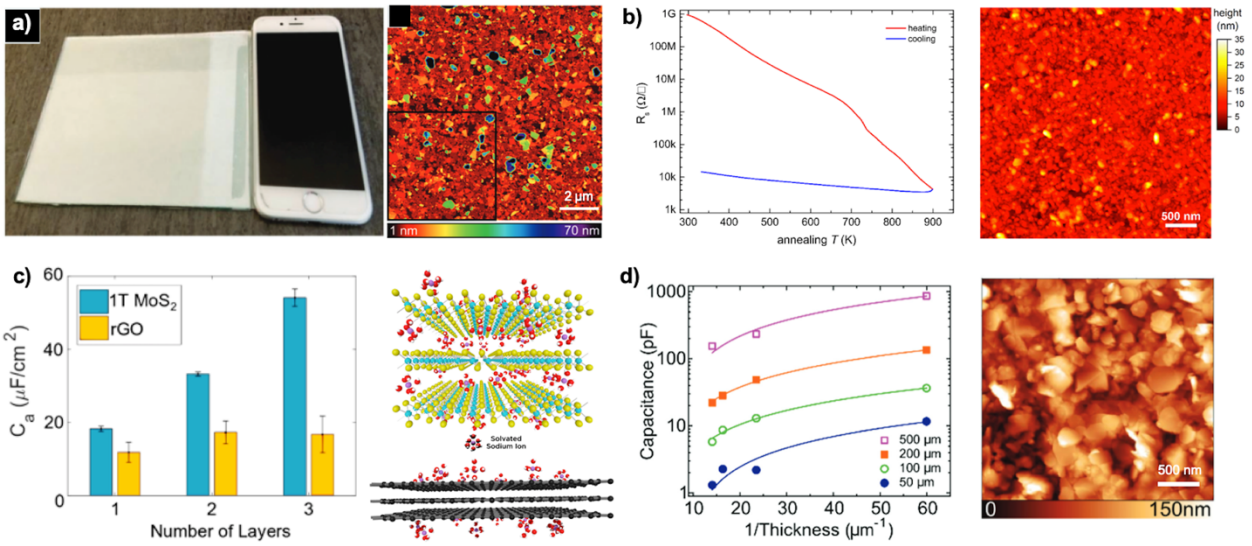



**Figure 2.6 Langmuir film of exfoliated 2D nanosheets other than graphene-based nanomaterials**. (a) A photo of large-area Langmuir film of *ce*-$MoS_2$ coated on glass substrate and AFM images of the resulting film coated on mica substrate. Reproduced from ref.[61] (b) Sheet resistance measured during the heating−cooling cycle on a Langmuir film of close-packed few-layer $MoS_2$ nanosheets. The AFM image of the resulting film is presented on the right. Reproduced from ref.[22] (c) Areal capacitance vs. number of depositions for electrodes prepared from *ce*-$MoS_2$ and rGO Langmuir films with charging mechanisms presented in the schematic diagrams. Reproduced from ref.[42] (c) Capacitance of LB films of exfoliated hBN nanosheets as a function of inverse film thickness. The AFM image of the resulting film is presented on the right. Reproduced from ref. [17]

### 2.2.4 Thermodynamics of Langmuir film

The changes in surface tension of water, defined as surface pressure (Π), is usually monitored while compressing the floating materials at the air-water interface to characterize the

Langmuir film. It is defined that $\Pi = \gamma_0 - \gamma$, where $\gamma_0$ is the surface tension of the pure water and $\gamma$ is the surface tension of the water covered by materials (e.g. lipid). The thermodynamic equation (Eq. 2.1) for a perfect gas in 3D can be easily transposed for a 2D Langmuir film (Eq. 2.2) as expressed here:

$$dG = VdP - SdT \tag{2.1}$$

$$dG = Ad\Pi - SdT \tag{2.2}$$

where $G$ is Gibbs free energy, $V$ is volume, $P$ is pressure, $S$ is entropy, $T$ is temperature and $A$ is the water surface area covered by materials. At a constant temperature, one obtains:

$$dG = Ad\Pi \Rightarrow \Delta G = \int_0^{\Pi} Ad\Pi \tag{2.3}$$

At a given temperature ($T$), one can determine the physical state and transitions in Langmuir film based on the pressure response ($\Delta G$) to the area reduced during compression. This is called elastic modulus ($K$), or surface compressional modulus ($Cs^{-1}$) in some cases and it can be expressed in the following equation:

$$K = -A\frac{d\Pi}{dA} \tag{2.4}$$

which can be approximated, for small changes in area and surface pressure, by:

$$K \cong -\frac{\Pi_1 - \Pi_2}{\ln A_1 - \ln A_2} \tag{2.5}$$

The elastic modulus essentially describes the slope of the $\Pi - A$ isotherms.

Figure 2.7 displays an ideal $\Pi - A$ graph of amphiphilic molecules with indicators of phase transition from gas to solid, in analogy to the three-dimensional (3D) states of matter. In an ideal case, one can easily spot when the slope changes and the typical phase transition including gaseous, low-density liquid phase, liquid-expanded (LE), liquid-condensed (LC) and solid, beyond which the 2D film will collapse and form 3D structure.

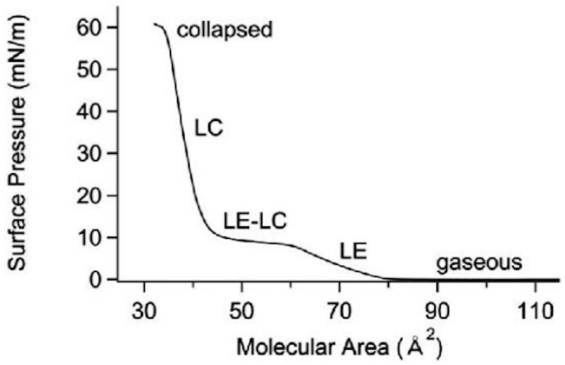



**Figure 2.7 An ideal surface pressure−area ($\Pi - A$) isotherm** obtained from Langmuir film of lipids showing clear phase transitions at two-dimensional air-water interface. Reproduced from ref.[62]

Early studies conducted by Irving Langmuir focused on determining the critical trough area ($A^0$) when the film collapses, which can be used to predict a particular structure of a molecule. Depending on material properties and structures, as well as experimental temperatures, some phases can be missing in an actual measurement and slope changes can be subtle, especially for nontypical amphiphiles such as nanoparticles. Therefore, it becomes crucial to extract elastic modulus, $K$, from $\Pi - A$ isotherms to determine the changes in surface states and phase transitions. He *et al*. collected both elastic modulus vs. area ($K - A$) curves and $\Pi - A$ isotherms for stearic acid monolayer on water and electrolyte solutions. In all three cases, $K - A$ curves captured small peaks which are absent in the $\Pi - A$ isotherm. These peaks suggested that the film experienced discontinuity in phase transition from gas to liquid and then to solid.[63] Ładniak *et al*. used compressive elastic modulus to study the impact of various components in subphase on the behavior of a model biological membrane consisting of 1,2-dipalmitoyl-sn-glycero-3-phosphocholine (DPPC).[64] As shown in Figure 2.8a, the two clear divisions in the graph of compression elastic modulus ($K$) vs. surface pressure ($\Pi$) precisely verified the existence of transition from LE to LC. The higher $K$ value in the case of subphase containing nanoparticles suggested a stiffer structure which implied a stronger interaction between nanoparticles and phosphoric biological membranes. As for Langmuir film of nanoparticles, Poonia *et al*. formed and studied Langmuir film of unfunctionalized single-walled carbon nanotubes (SWNTs) at the air-water interface. Both isotherm and elastic curves are presented in Figure 2.8b. The $K - A$ curve not only clearly presented the transition from gas-like to liquid-like phases but also displayed discontinuity with in the transition.[65] Furthermore, the sharp decrease in $K$ could suggest rapid and significant changes in structure and mechanical properties of the film.

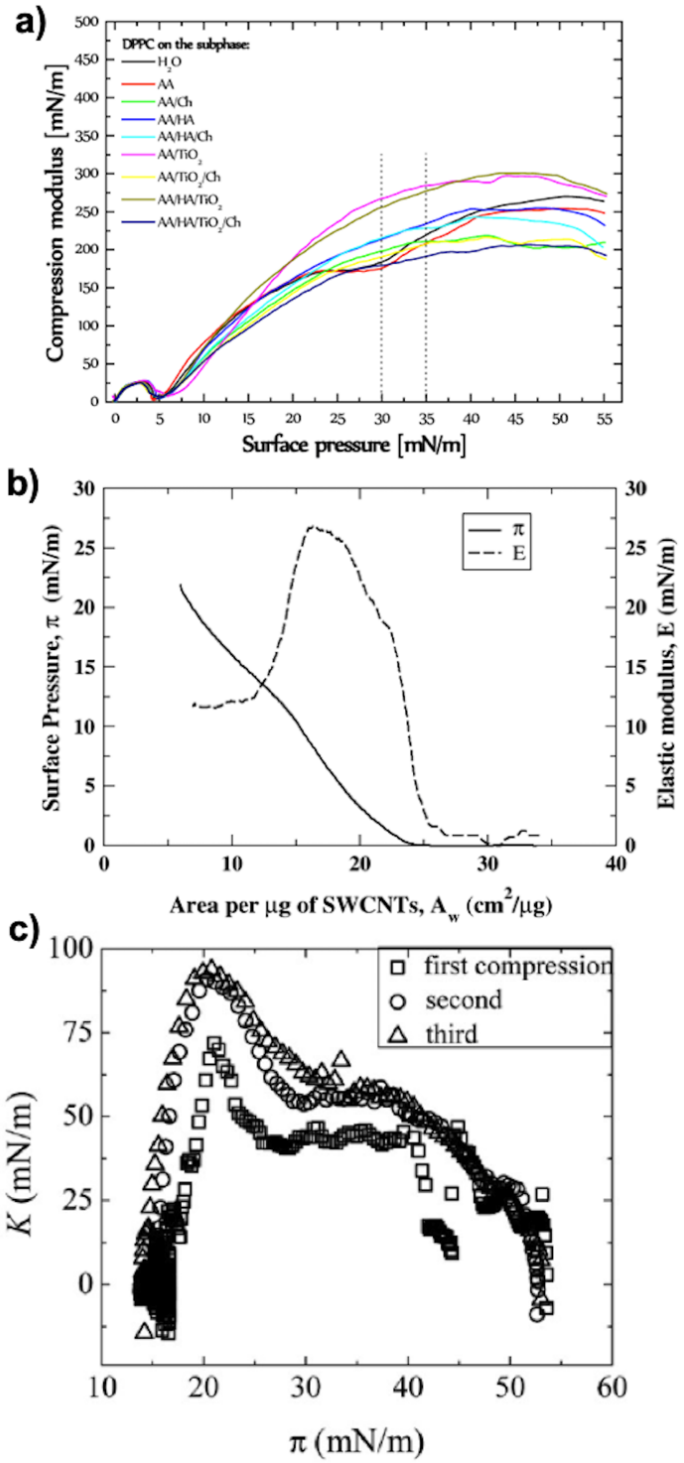



**Figure 2.8 Examples of elastic modulus (*K*) plots**. (a) *K* - Π for DPPC monolayers on various types of subphase. Reproduced from ref. [63] (b) Π - $A_w$ isotherm and *K* - $A_w$ curve of SWNTs Langmuir film. Reproduced from ref. [65] (c) *K* - Π for GO monolayers during the first, second and third cycle of compressions. Reproduced from ref. [28]

López-Díaz *et al*. prepared purified nanofiber graphene oxide (PNGO) by washing the nanofiber graphene oxide (NGO) with alkaline solutions. The resulting PNGO contains similar amounts of oxygen groups and exhibits comparable electric conductivity to the rGO reduced by hydrazine vapor. The researchers then assembled monolayer films from both PNGO and NGO nanosheets and collected $K$ - Π curves. The PNGO film showed almost double the $K$ peak value as NGO did, indicating that it formed a much stiffer film when transitioning from liquid-expand phase to solid phase.[66] Imperiali *et al*. assembled GO nanosheets at the air-water interface and studied the film mechanical property changes between compression-expansion cycles. The $K$ vs. Π curves obtained from each cycle are presented in Figure 2.8c. They shared the same shape – as Π gradually increases, $K$ first increased sharply to a maximum value followed by a rapid decrease to a plateau and further increase in Π eventually caused $K$ to reduce to zero. The increase in $K$ value between the first and second compression suggested that the GO film became significantly stiffer, implying that the nanosheets had aggregated irreversibly after the first compression.[28] Therefore, it is suggested to perform a full cycle of pre-compression in order to obtain the maximum packing density of the Langmuir film.

On the other hand, analysis of isotherms and elasticity should always be coupled with imaging technology to make sound conclusions on the film structure, especially for assembly of nanoparticles where changes in the film are often inhomogeneous. Kalosi *et al*. observed barely any changes in either elastic modulus or isotherms during the initial stage of compressing nanoparticles, however, formation of isolated self-assembled island-like clusters were observed under Brewster angle microscope (BAM).[22] Our recent work also revealed that when clusters with different structures are assembled into Langmuir film, even though elastic modulus vs. surface pressure curves appeared to be similar, evidence of film collapse was observed in the case of dense clusters at the starting of $K$ plateau while in the counterpart it did not occur until reaching the end of the plateau. Note that the film morphology at different stages were evaluated by depositing film at desired target surface pressure followed by characterizing under SEM. More details regarding this work can be found in **Chapter 5**.

### 2.2.5 Modified Langmuir film deposition – Towards R2R process

As early as 2010, Zhavnerko and Marletta have presented a roll-to-roll design of Langmuir film deposition, where a rotating barrier was used to continuously densify the floating molecules.[34] However, the authors did not present any resulting film produced from this pioneer concept. Since 2016, researchers have made considerable efforts to realize the continuous coating of Langmuir films. Depending on the driving force used for film densification and transferring, LB-based R2R processing can be segregated into three main categories. The first one uses a movable barrier to physically compress and transfer the films as shown in Figure 2.9a. By implementing this concept, Parchine *et al*. attempted to conduct R2R coatings of monolayers of silica nanoparticles with diameters of both 250 and 550 nm nanoparticles (Figure 2.9a1).[32] Two years later, the same research group successfully utilized the resulting R2R coatings as an effective light trapping layer in organic photovoltaic (OPV) cells.[33] These 2D coatings resulted in enhanced light intensity entering the photo-active layer in OPV cells, which boosted the generation of photocurrent and thus increased the total power conversion efficiency (PCE) of the device. This anti-reflective coating was also applied onto a commercial, flexible OPV device via the same R2R LB process. Depending on the diameter of silicon sphere used, it can result in up to a 10% increase in photocurrent and 8% in PCE of a whole module. However, in both works, the length of resulting film was limited by the length of the coating trough. In 2019, Wells *et al*. presented large-area Langmuir films deposition of TMD nanoflakes using a multi-barrier assisted R2R processing at a liquid-liquid interface (Figure 2.9a2).[30] Homogeneous $MoS_2$ film can be produced from a dispersion of 1 mg/mL at a material loading rate of 3.3 mg/m$^2$ and a substrate withdrawal/paddle speed of 60 cm/min. The resulting nanoflake films had a loading of 33 mg/m$^2$ and an estimated thickness of ~7 nm. The as-prepared R2R film generated a photocurrent density of 40 μA/cm$^2$ for iodide oxidation (vs. Ag/Ag+ reference) under 1 sun illumination. Moreover, heterostructures of $MoS_2$/$WSe_2$ were also demonstrated via layer-by-layer deposition using the same R2R process. Even though this work resolves the problem of limited coating length, the process did not result in monolayer coatings.

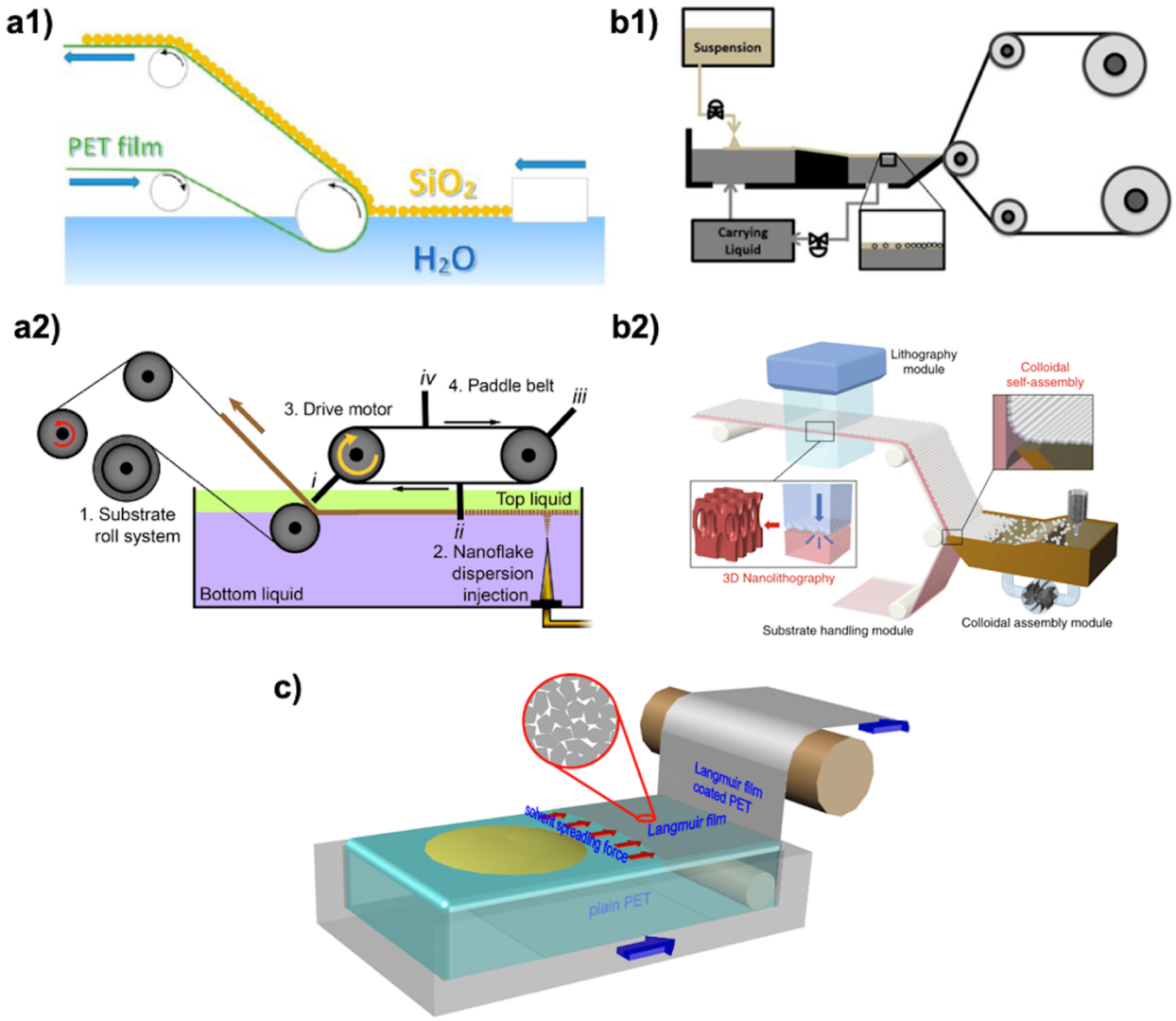



**Figure 2.9 Modified LB methods - Towards R2R processing** (a) Schematic diagrams illustrating continuous coating of (a1) SiO2 nanoparticles and (a2) exfoliated $MoS_2$ nanoflakes using movable barrier. Reproduced from ref.[32] and ref. [30], respectively. (b) Schematic illustration of subphase flow driven R2R processing of Langmuir film of colloidal particles. (b1) and (b2) are reproduced from ref. [36] and ref. [35], respectively. (c) Schematic diagrams illustrating solvent spreading driven continuous coating of Langmuir film of exfoliated 2D nanosheets.

The second type of R2R LB also relies upon external force – the hydrodynamic force generated from a continuously flowing subphase. Li and Gilchrist showcased this concept via R2R deposition of micron-sized silica colloids (Figure 2.9b1).[36] A monolayer deposition of the particles was achieved when the web speed was maintained at 6 cm/min. Faster web speed resulted in coating instability shown as discontinuous and multilayer deposition. Chen *et al*. recently produced R2R LB deposition of silica nanospheres with diameters ranging from 325 - 500 nm. At the air-water interface, these nanospheres self-assembled into hexagonal close-packed lattices on the

moving liquid surface (Figure 2.9b2). The monolayers were then transferred onto a photoresist substrate. By applying the lithography process, the near-field intensity was recorded by the underlying photoresist, resulting in creation of 3D periodic nanostructure. By tuning the coating speed and ink injection speed, the optimal R2R process can coat a rate of 6 cm/min with an assembly yield over 85%.[35] This process presented continuous monolayer depositions. However, the setup is more complex requiring a pumping system to allow continuous flow of carrier liquid.

The R2R processing in the third category takes advantage of the later force from solvent spreading at the air-water interface and the initial development was carried out in my MASc thesis. Solvent spreading appears to not only provide directional flow to gather materials at opposite side of the coating bath but also densify and transfer the film onto a flexible substrate (Figure 2.9c).[67] Results and challenges regarding this method can be found in **Chapter 3**.

## 2.3 Two-dimensional (2D) Materials

### 2.3.1 Graphene-based materials

Graphene is a single atomic layer of $sp^2$ bonded carbon atoms arranged in a hexagonal honeycomb structure. It has known as a 'wonder material' since 2004 and emerged as a promising material for various applications.[68] Graphene was first discovered by using a piece of Scotch® tape via mechanical exfoliation.[69] Later, chemical vapor deposition (CVD) has proven to produce high-quality graphene.[70] However, since this method requires high temperature and high pressure, it is not cost-effective for producing atomically-thin graphene on a large scale. On the other hand, graphene oxide (GO), which can be synthesized by chemically oxidizing graphite flakes, has emerged as a promising and practical alternative for manufacturing graphene-based materials.[71–74] The hydrophilicity imparted by the functional groups on GO allow it to be easily dispersed in water as single-layer sheets,[75] as well as in some polar organic solvents.[76,77] It has been reported that the phenolic hydroxyls and carboxylic acids at the edges can be deprotonated in water, resulting in strong electrostatic repulsions, and thus the most stable dispersions of GO monolayers are in a pH~10 solution where the zeta potential is -40 – -60 mV.[78] The $sp^2$ hybridized network of graphene can be restored from GO by removing the oxygen-containing functional groups via chemical or thermal reduction.[75,79] However, this conversion is often incomplete and results in defects in the graphene lattice, in which case, residual functional groups remain and carbon

vacancies form.[80] Therefore, to differentiate it from the pristine graphene, this new material is referred to as reduced graphene oxide (rGO). The residual functional groups on rGO consist mostly of hydroxyl and epoxide groups on the basal plane and phenolic hydroxyls and carboxylic acid groups at the edges.[81] The presence of these functional groups is validated by the increase in interlayer spacing from 0.335 nm for graphite to more than 0.625 nm for GO.[82] After high-temperature annealing treatment, the resulting rGO can achieve a C/O ratio in a range from ~1.6 for GO to ~400 for rGO,[71,82–84] in which way the conductivity and degree of functionalization can be tuned. rGO has been widely used in applications ranging from electrical/electronic devices, such as energy storage devices, (chemical and bio) sensors and supercapacitors, to membrane technology and environmental applications.[85]

### 2.3.2 Molybdenum disulfide

Molybdenum disulfide ($MoS_2$), a member of the transition metal dichalcogenide (TMD) family, has drawn significant attention due to its fascinating optical,[86,87] electronic,[88,89] and electrochemical properties.[90–93] It has a layered structure of stacked triple planes, in which a hexagonal plane of Mo atoms is sandwiched in-between two hexagonal planes of S atoms. $MoS_2$ exhibits various polymorphs with completely different electronic structures. Figure 2.10a presents the top and side views of 2H and 1T $MoS_2$ structure.[94] Bulk $MoS_2$ is typically found in the 2H polymorph which is a semiconductor possessing an indirect bandgap of ~1.2 eV.[95] By using chemical exfoliation, such as n-butyllithium, 2H $MoS_2$ can be transformed to 1T metallic polymorph[96] which has been reported to be a promising candidate for supercapacitors[96] and an efficient electrocatalyst for the hydrogen evolution reaction (HER).[92] Apart from phase transition, when bulk $MoS_2$ bulk thins down to a single atomic layer, it has a direct bandgap with bandgap energy ~1.9 eV.[97,98]

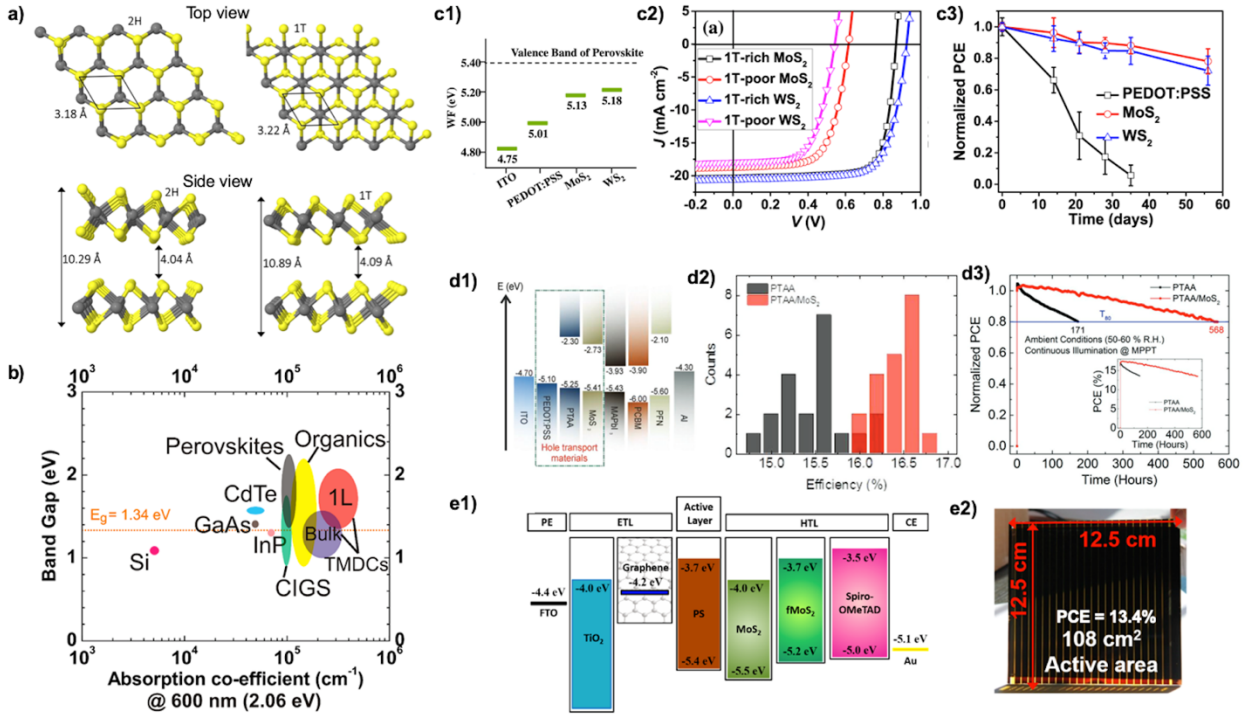



**Figure 2.10 1T and 2H $MoS_2$ and their application in photovoltaics**. (a) top and side view of 1T- and 2H-$MoS_2$ crystal structures. Reproduced from ref.[94]. (b) A graph summarizes energy bandgaps (eV) and corresponding absorption coefficients ($cm^{-1}$) for various semiconductors for use in commercial and research-scale solar cells. Reproduced from ref.[99] (c-e) 1T- or 2H-$MoS_2$ used as HTL in perovskite solar cell. (c1) A graph of valence bends of perovskite, $MoS_2$, $WS_2$, PEDOT:PSS and ITO. (c2) $J-V$ curves of 1T- and 2H- (1T-poor) $MoS_2$ and $WS_2$ (c3) long-term performance of perovskite solar cell using $MoS_2$, $WS_2$, PEDOT:PSS as HTL. The devices were stored in glove box filled with nitrogen. (c1-c3) Reproduced from ref. [48] (d1) energy diagram of the device using a combined HTL of PEDOT:PSS, PTAA and $MoS_2$ (2H) with corresponding PCE distribution and long-term performance shown in (d2) and (d3), respectively. Reproduced from ref.[45] (e1) energy diagram of large-scale perovskite solar cell with a photo of the device shown in (e2). Reproduced from ref.[43]

Thus far, there are four common methods to fabricate monolayer 2H $MoS_2$: 1. Mechanical exfoliation; 2. Chemical vapor deposition (CVD); 3. Liquid exfoliation and 4. Chemical exfoliation. Mechanical exfoliation is not ideal for large-scale production and usually results in limited yield, [100] while CVD provides better precision on controlling layer numbers however it has other drawbacks such as formation of defects, limited substrate types, limited sample size and large energy consumption. [101] As for liquid exfoliation, bulk $MoS_2$ (crystal or powder) is typically ground in an organic solvent, such as dimethylformamide (DMF) or *N*-Methyl-2-pyrrolidone (NMP), and then mixed with water followed by tip-sonication for hour-long periods.[102,103] Although this method is simple to conduct, it usually results in neither high yield of monolayers nor precise control on layer numbers or flake sizes. Lastly, monolayer $MoS_2$ can also be fabricated by chemical[104,105] or electrochemical[106,107] exfoliation. Besides obtaining monolayer $MoS_2$, these

methods are also able to achieve polymorph transition from 2H to 1T. By simply treating 1T-$MoS_2$ under an inert gas at ~150 – 500 ºC, one can achieve complete restoration of 2H polymorph[104,108]. Therefore, 1T monolayer $MoS_2$ is considered as a promising precursor for producing single layer 2H $MoS_2$.

Owing to their highest absorption coefficient (in bulk and monolayer form) among all other photovoltaic materials, TMD materials have emerged as promising candidates for light absorbing layers, especially in 2D solar cells. This is reflected in Figure 2.10b, which shows a graph of bandgap (eV) vs. absorption coefficient ($cm^{-1}$) for major semiconductors used in commercial and research-scale solar cells.[99] The energy bandgap value of TMD materials are very close to the ideal solar band gap of 1.34 eV (labelled in the Figure 2.10b). Moreover, by thinning down the bulk material to a single layer, TMD monolayers transit from indirect to direct bandgap resulting in a higher absorption coefficient ($cm^{-1}$) compared to its bulk material. Wi *et al*. fabricated a PV device with a vertically stacked indium tin oxide electrode (ITO)/multilayer $MoS_2$/metal electrode structure, where the active $MoS_2$ layers are processed using a plasma-assisted p-doping approach to form a p-n junction.[109] The device exhibited a PCE value up to 2.8%, which is reasonable for an ultrathin-film photovoltaic device.

On the other hand, TMD materials have also shown potential to serve as the hole transporting layer (HTL) or interfacial layer in a perovskite solar cell (PSC). Perovskite describes a family of materials that has the same crystallographic structure as calcium titanium oxide mineral ($CaTiO_3$). PSC has shown extraordinary power conversion efficiency (PCE) enhancement to over 25% since 2009.[110–112] A planar PSC usually consists of five main layers: photoanode (FTO or ITO conductive substrate), electron transport layer (ETL), perovskite photoactive layer, hole-transport layer (HTL) and metal electrode (e.g. Au, Ag, Al). The perovskite layer absorbs light and creates electron-hole pairs (excitons). Once the excitons separate, ETL and HTL exact free electrons and holes and transport them towards anode and cathode, respectively. Recently, researchers have used both 1T- and 2H-$MoS_2$ to improve PSC performance. Huang *et al*. implemented an 11 nm thick spin-coated *ce*-$MoS_2$ (predominately 1T-$MoS_2$) and 2H-$MoS_2$ film as the HTL in a p-i-n structured perovskite solar cell (Figure 2.10c1-c2). Compared to devices using poly(3,4-ethylenedioxythiophene) polystyrene sulfonate (PEDOT:PSS) as the HTL, the resulting solar cell not only showed > 2% improvement in power conversion efficiency (PCE) but

also presented significant improvement on long-term stability (Figure 2.10c3).[48] Capasso *et al*. utilized liquid exfoliated 2H $MoS_2$ nanosheets as the interfacial layer between $CH_3NH_3PbI_3$ (perovskite) and Spiro-OMeTAD (HTL). Even though the modified devices did not achieve a PCE increase, the 2H $MoS_2$ interfacial layer showed promising enhancement in cell life-time.[46] The same conclusion was also drawn by Kakavelakis *et al*. when coupling 2H $MoS_2$ with poly(triaryl amine) (PTAA), a popular alternative HTL material (Figure 2.10d1-d3). 2H $MoS_2$ was reported to eliminate the reaction of $CH_3NH_3PbI_3$ with water which eliminated the degradation of perovskite.[45] This improvement became more profound when implemented in large-area devices (Figure 2.10e1 and 2.10e2).[43]

Although exfoliated $MoS_2$ nanosheets show considerable potential, we have encountered serval challenges while working with it: 1). Material stability – regardless of the polymorphs, $MoS_2$ tends to be oxidized in both solid and liquid dispersed forms. 2). Difficulty in generating photoluminescence from thermally converted *ce*-$MoS_2$. Even though several previous literatures have presented successful instances regarding this, we have never been able to produce the same results. We hypothesize that this could be due to the degradation induced by defects and incomplete isolations of single layer nanosheets. The work conducted in Chapter 4 is mainly motivated by these two challenges.

## 2.4 Spontaneous Clustering of Nanomaterials at the Air-water Interface

### 2.4.1 Cluster formation of 0D and 1D materials

Clustering of nanoparticles often occurs at the air-water interface if the subphase water contains electrolytes (i.e. salts). Hu *et al*. unveiled that after silver nanoparticles (AgNPs) were trapped at the surface of potassium chloride solution, AgNPs were first scattered and then over the course of two hours, they gradually collided with one another, forming small fractal clusters which eventually assembled into large networks.[113] Flores-Tandy *et al*. identified that the aspect ratio of particles is one of the controlling factors for the cluster structure. In their study, the aggregation of ellipsoidal colloidal particles with aspect ratio from 1 (sphere) to 6 (rod) at the air-water interface were investigated.[114] The researchers demonstrated that by increasing the aspect ratio, they observed an increase in cluster branches which is in line with the evidence that Fractal dimension ($d_f$) decreased from ~1.8 to ~1.5. The difference in aspect ratio likely resulted in changes in long-

range capillary interaction at various orientations and it was believed that the observed aggregation took place in the DLCA regime even though contradictory results have been presented by others where the shape of particle does not impact the cluster structure. The authors suggested that the conflict might be due to the anisotropy of the particles.

On the other hand, solvent evaporation induced spontaneous clustering of nanomaterials has also been reported. Yang *et al*. observed that $BaCrO_4$ nanorods with small aspect ratio (~3−5:1) formed raft-like clusters (Figure 2.11a).[115] When assembled into Langmuir film, these clusters transitioned from isotropic to 2D nematic followed by formation of 2D smectic before the film was over compressed and formed 3D nematic (Figure 2.11b). In contrast, the nanorods with large aspect ratio dispersed individually at the interface. After compression, a nematic layer was formed with the nanorods aligned towards a similar direction. Spontaneous fractal aggregation of nanoparticles has also been presented previously. Cheng *et al*. presented that cetyltrimethylammonium bromide (CTAB)-capped gold nanoparticles (GNPs) formed fractal clusters with $d_f \sim 1.8$ immediately after chloroform-based dispersion spread and evaporated upon the water (Figure 2.11c).[26] Even after compression to an intermediate surface pressure, this fractal structure still remained, implying the robustness of the original structure (Figure 2.11d). Bai *et al*. found out that the structure of GNPs clusters can be tuned by varying the capping agents, as shown by the difference between Figure 2.11e and 2.11f.[116] Moreover, researchers have also observed nanoparticles forms much denser island-like clusters/domains. Sear *et al*. showed that silver quantum nanodots can form densely packed circular islands (Figure 2.11g) or linear stripes (Figure 2.11h) depending on the concentration used for deploying materials onto the water surface.[27]

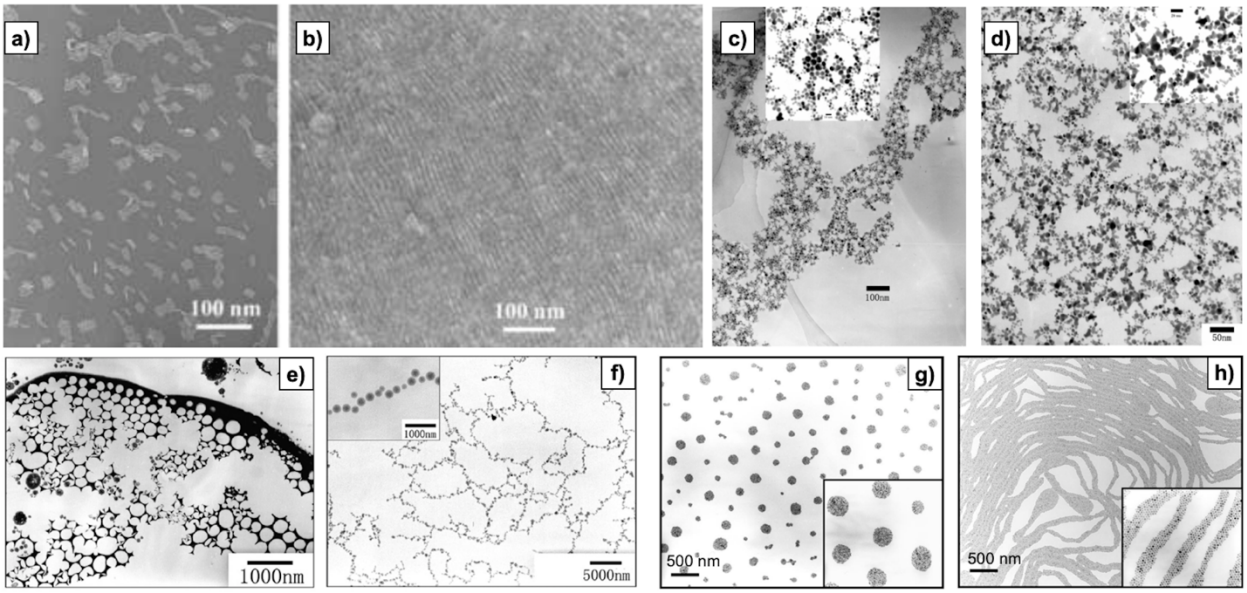



**Figure 2.11 Spontaneous cluster formation of 0D and 1D materials at the air-water interface**. SEM images of (a) raft-like clusters of $BaCrO_4$ nanorods with small aspect ratio (~3−5:1) and (b) densely-packed 3D Nematic formed by rafted-like cluster after compression. (a) and (b) are reproduced from ref. [115] (c) fractal cluster of CTAB-capped Au nanoparticles and (d) Langmuir film that retained fractal structure of Au nanoparticles after moderate compression. (c) and (d) are reproduced from ref.[26] (e) and (f) cluster patterns formed with mixed capping agents of [Camphor$C_2$mim]Cl/[$C_{16}$hmim]Br and [Camphor$C_2$mim]Cl/[$C_{12}$mim]Br, respectively. (e) and (f) are reproduced from ref. [116] (g) and (h) are circular-island shaped and linear-stripe shaped cluster composed of silver quantum nanodots depending upon the concentration used. (g) and (h) are reproduced from ref.[27]

### 2.4.2 Cluster formation of 2D materials

Compared to 0D and 1D materials, there are significantly less studies on manipulating 2D nanosheets at the air-water interface, among which graphene oxide (GO) is the main subject and formation of isolated sheets were reported predominately.[9,37,66,117] This is likely because only 1% of GO can be transferred onto the abundant water surface due to the use of alcohol solution as the spreading solvent. However, Zhang *et al*. reported that GO can aggregate into densely packed clusters/domains at the air-water interface and the domain sizes can be tuned by adjusting the pH value of the subphase water (Figure 2.12a).[118] Silverberg *et al*. presented loosely-connected clusters of photo-reduced GO whose carboxylate groups at the sheet edges remained largely unaffected.[25] As ionic strength was reduced from 0.1 mM to 0.01 mM, the nanosheets approached each other and formed large clusters, however, edge-to-edge contact was absent. It was suggested that the behavior was governed by long-range attractive forces and many-body repulsive forces. On the other hand, as for hydrophobic nanosheets whose transfer rate is largely unaffected by the

spreading solvents, formation of fractal clustering was reported predominately. Kalosi *et al*. presented fractal clusters of liquid-exfoliated, few-layer $MoS_2$ (2H) nanosheets when the film was in gaseous phase (Figure 2.12b).[22] Imperiali *et al*. showed that reduced GO nanosheets can arrange themselves into densely-packed island-like clusters/domains soon after spreading and evaporation of the solvent (Figure 2.12c).[28] In **Chapter 3**, we presented that the aggregation of GO sheets is concentration, pH and ionic strength dependent. In **Chapter 5**, we uncovered that regardless of material properties and morphology, a universal transition from linear fractal cluster to island-like domain was observed by increasing the dispersion concentration.

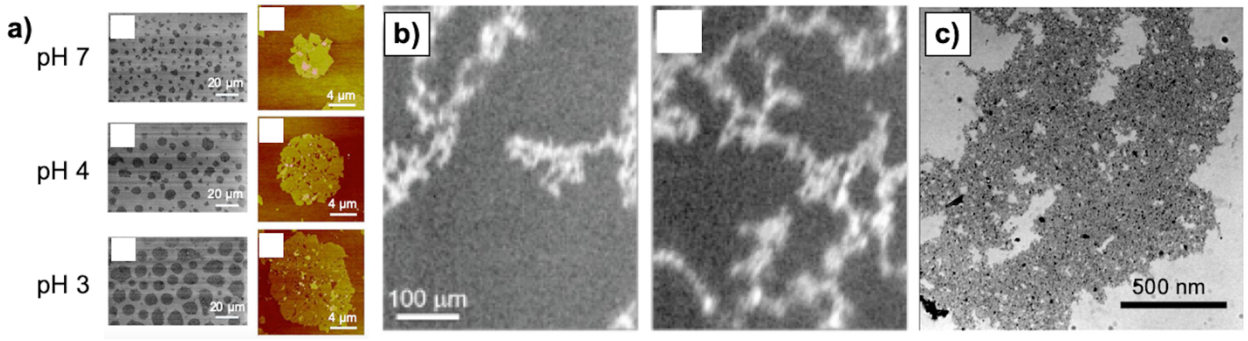



**Figure 2.12 Spontaneous cluster formation of 2D materials at the air-water interface**. (a) SEM and AFM images of domains formed by GO sheets and the domain sizes are pH-dependent. Reproduced from ref.[118] (b) SEM images of fractal clusters formed by few-layer 2H-$MoS_2$ nanosheets. Reproduced from ref.[22] (c) SEM image of aggregation of rGO nanosheets into island-like cluster soon after spreading. Reproduced from ref.[28]

### 2.4.3 Colloidal Forces

Van der Waals (vdW) and electrical double layer (EDL) forces dominate the interactions between particles in the colloidal system. vdW attraction is distance-dependent and it is in the order of a nanometer or less between two atoms or molecules, however, depending on the Hamaker constant and particle size, this distance can be up to hundreds of nanometers for colloidal particles.[119] This is because the atoms of a particle are mutually interactive, and thus the interactions are additive to some extent. More importantly, vdW interaction is also geometry-dependent and the two most commonly discussed configurations are: 1). Sphere and sphere interaction potential: $W(D) = -AR/12D$; and 2). Sphere and plane interaction potential: $W(D) = -AR/6D$, where $D$ is the separation distance; $R$ is the particle radius (assume that two particles share the same radius; $A$ is Hamaker constant. On the other hand, EDL creates electrostatic repulsion between particles in a liquid medium, especially in water. When a particle

is immersed in water, surfaces are often charged either due to adsorption of ions or dissociation of surface groups, thanks to the high dielectric constant of water.[119] The surface charges result in an electric field that attracts counterions via Coulomb force. In an EDL, the first layer describes the surface charges and the second layer (diffusion layer) is the parallel region consisting of distributed counterions, which electrically screens the first layer. Debye length, $\kappa^{-1}$, characterizes the thickness of the diffusion layer. It is largely dependent on the ionic strength of the solution. More specifically, it decreases (increased screening effect) with increasing electrolyte concentration and increasing valence of the ionic species in the electrolyte.

DLVO theory, named after Derjaguin, Landau, Verwey, and Overbeek, is the most celebrated theory that essentially combines the effects of vdW and EDL to explain the stability and aggregation of colloidal dispersion. The total potential is the sum of attractive vdW attraction and repulsive EDL repulsion: i.e. $W_{total} = W_{vdW} + W_{EDL}$. When two particles are very close to each other, vdW dominates the interaction and results in a deep attractive well (primary minimum). However, sufficient EDL can lead to an energy barrier and prevents particles from irreversible aggregation in a colloidal system. Therefore, the height of the energy barrier implies the stability of the colloidal system. More specifically, the maximum of energy barrier should be large than thermal energy (Brownian motion) to create a stable dispersion. At larger distances, the $W_{total}$ profile could also have a secondary minimum, where particles are held together weakly. This aggregation is reversible and can be disrupted easily. DLVO is usually considered as a long-range interaction since both vdW and EDL can act up to hundreds of nanometers between particles.

### 2.4.4 Mechanism of 2D clustering at the air-water interface

After being dispersed in suitable solvents, nanomaterials can be transferred onto the water surface via spreading and evaporation. They then form clusters either immediately after solvent evaporation or due to irreversible self-assembly. The former process takes a few seconds while the latter one takes at least ~5 min to a couple of hours or even serval days. In the 1990s, computational methods were implemented to demonstrate the aggregation theories of self-assembled clusters from 0D and 1D materials, among which diffusion-limited cluster aggregation (DLCA) and Reaction-limited cluster aggregation (RLCA) theories are well-accepted. In DLCA, clusters and particles stick together upon first contact (i.e., the probability of reaction = 1) whereas in RLCA

several potential sticking sites were explored before irreversible aggregation occurred.[120–122] To study the cluster formation, researchers typically carry out time studies regarding changes in fractal dimension to predict the kinetics of cluster formation.

Fractal dimension ($d_f$) is used to characterize a cluster structure. When clusters form at the air-water interface, $d_f$ defines the packing density, or in other words the amount of branching of a cluster. As mentioned above, it is frequently used to determine the aggregation mechanism; when $d_f > 1.5$, it implies a RLCA governed system where the particle sticking probability is less than 1 due to rearrangements resulting from sufficient repulsive forces in the system. However, as early as the 1990s, after conducting detailed studies on the aggregation of spherical particles at the air-water interface from three different aspects: structure ($d_f$), kinetic and dynamic, Robinson and Earnshaw suggested that $d_f$ alone was not sufficient enough to conclude the aggregation mechanism towards one over the other.[120–122] In their studies, polystyrene latex spherical particles (diameter ~1 μm) were transferred onto the water surface via methanol dispersion. The aggregation was induced by adding calcium chloride ($CaCl_2$) electrolyte solution in the subphase water. By decreasing electrolyte concentrations, the diminished screening effect on electrical double layer repulsion resulted in an abrupt transition of aggregation mechanism from DLCA to RLCA, which is in line with the theoretical prediction.[121] However, when the kinetic behavior of clusters were investigated in terms of the cluster size distribution and its time dependence, the results indicated a rather gradual and continuous transition.[122] After further investigation on the dynamics of cluster structure over time, the authors concluded that the cluster formation in various electrolyte molarities followed RLCA at all times and suggested that it could be explained by a scenario where a fraction of the particle surface charge remained unimpacted at all molarities. This implied that one needs to consider both structure and dynamic changes of the clusters to uncover conclusive evidence with regards to the nature of the aggregation process, which is confirmed by later reports. Xiao *et al*. presented direct observation of gold nanoparticles (GNPs) self-assembled at the air-water interface.[123] GNPs were trapped at the air-water interface where the subphase water contained electrolytes. As the water evaporated, the increase in electrolyte concentration resulted in an enhanced screening effect and thus led to clustering of GNPs due to a decrease in repulsive forces between the nanoparticles (Figure 2.13a). The resulting $d_f = 1.36$ was supposed to indicate a DLCA model, however, the real-time videos showed evidence that particles/clusters took time

to rotate locally when approaching and sticking to another particle/cluster, which provides strong evidence for a RLCA model. The authors suggested that the conflict to classical aggregation regime could be explained by the heterogenous environment induced by evaporation, leading to microflow and variations in local diversity of ionic strength and surface tension (Figure 2.13b).

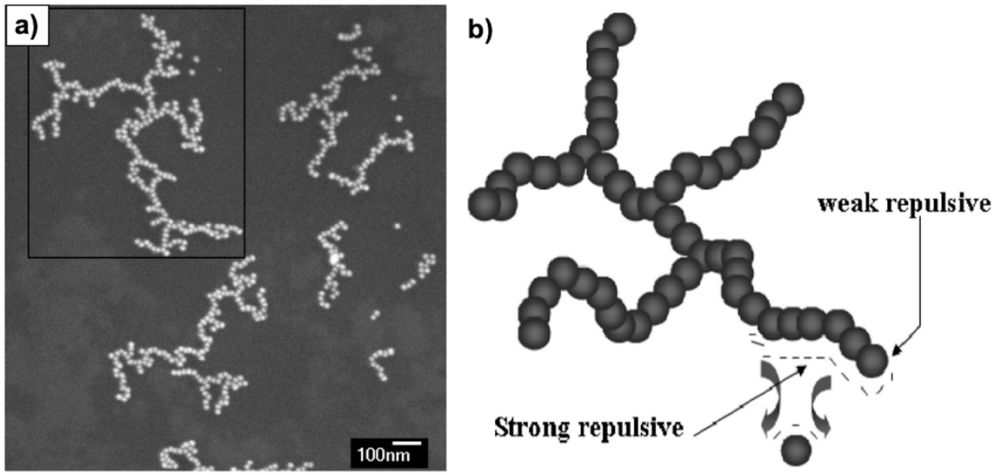



**Figure 2.13 Gold nanoparticles at the air-water interface**. (a) SEM image of dendrite-like cluster of gold nanoparticles. (b) Proposed model: RLCA regime demonstrated by anisotropic particle-cluster interaction.

Although the spontaneous patterning of nanoparticles has been widely reported in zero- and one- dimensional nanomaterials, there is lack of studies that uncover the aggregation mechanism. Cheng *et al*. believed that the fractal structure of GNPs was assembled in the RLCA regime.[26] Bai *et al*. suggested that the tunable cluster structure of GNPs was due to increased hydrophobic interactions.[116] However, both studies were unable to provide any evidence based on either kinetic or dynamic analysis.

## 2.5 Liquid Spreading at the Air-water Interface

### 2.5.1 Thermodynamics of liquid spreads upon the surface of another

In 1922, Harkins and Feldman defined 'spreading coefficient' – *S*, which thermodynamically determines whether or not one liquid spreads on another.[124] This coefficient equals to the difference of the work of cohesion ($W_C$) of the liquid that is about to spread from the work of adhesion ($W_A$) between the two liquids. The equation is shown here:

$$S = W_A - W_C \tag{2.6}$$

where $W_A$ *and* $W_C$ are given by the following two equations:

$$W_A = \gamma_a + \gamma_b - \gamma_{ab} \quad (2.7)$$

$$W_c = 2\gamma_b \quad (2.8)$$

where $\gamma_a$ and $\gamma_b$ represents the surface tension of liquid *a* (top) and *b* (bottom), respectively; $\gamma_{ab}$ represents the interfacial tension between liquid *a* and liquid *b*. By combining equations (2.6) to (2.8), the spreading coefficient (*S*) can also be expressed as:

$$S = \gamma_a - (\gamma_b + \gamma_{ab}) \quad (2.9)$$

When spreading occurs, the top liquid has a positive *S* whereas a negative *S* indicates a non-spreading behavior where the top liquid stays as a lens. The authors verified this concept by evaluating the spreading behavior of ~100 liquids upon clean water surface and recorded their corresponding *S* values. Almost all positive cases were in line with the prediction with only a few exceptions where the magnitude of the positive *S* was so low that the accuracy was uncertain. No case was found where a liquid with a negative spreading coefficient spreads on water. According to the spreading behavior of the investigated liquids, the authors also suggested to divide liquids into 3 types: Type 1. Liquids that spread into a uniform layer but likely not a monomolecular layer, such as most of the paraffin oils; Type 2. Liquids that spread into a monomolecular thick film with excess remaining as a lens or lenses, such as film studied by Rayleigh, Miss Pockels, Langmuir and Adam, which has been discussed in detail in the previous 'Langmuir film' section; Type 3. Liquids that are volatile or soluble in water and spread but disappear eventually due to evaporation or dissolution leaving no visible lenses behind. Understanding the spreading behavior of a solvent is crucial for assembling Langmuir films as it serves as the carrier for transferring materials onto the water surface and may induce cluster formation and impact the quality of the floating film.

### 2.5.2 Kinetics and dynamics of liquid spreading upon the surface of another

Dynamically, the spreading of one liquid onto another is more complicated than just determining the sign of the spreading coefficient, *S*. Studies in this field were driven by the desire to estimate how fast oils would travel during a spill event over an open sea back in 1950s – 1970s. The gain in kinetic energy of a spreading oil is induced by the loss of gravitational energy and surface energy. In terms of forces, gravity and surface tension cause oil to move outwards which is retarded by viscous force from the bottom liquid. Spreading of a non-volatile immiscible liquid, such as silicone oil, onto the water surface was investigated first and researchers discovered that the spreading movement is driven by two forces in sequence: gravity and interfacial tension

(Figure 2.14a). The schematic in Figure 2.14c shows the surface topology (using laser shadowgraphy technique) of silicone oil spreading on a deep layer of water.[125] As the oil contacts the water surface, gravity initially provides the main driving force for thinning the 'reservoir' lens (labelled in Figure 2.14c), and only when $S > 0$ does it spread and continues to the second region, labelled as the interfacial-tension zone in Figure 2.14a. Near the spreading front (labeled as 'leading edge' in Figure 2.14c), gravity is neglected and the movement of spreading is mainly driven by the gradient of interfacial tensions (this phenomenon is known as the Marangoni effect). In this region, depending on the type of the liquids we mentioned earlier, as for liquid type 2 where mono-molecular film was formed due to spreading, the overall surface tension in the region varies with the surface density of the monolayer film. However, if a submicron-thick thin film was produced (liquid type 1), the overall tension varies with the thickness of the film rather than equaling to the sum of the tensions of upper liquid and of the interfacial tension of the two liquids ($\gamma_{A/air} + \gamma_{A/B}$).[126] It is also important to note that the spreading of the upper liquid can cause a flow in the underlying liquid phase (i.e., water), as shown in Figure 2.14b, and that the overall tension gradient may be generated not only by the transport of liquid spreading but also by rapid evaporation (or dissolution) and diffusion through the surrounding environment (or substrates).[126]

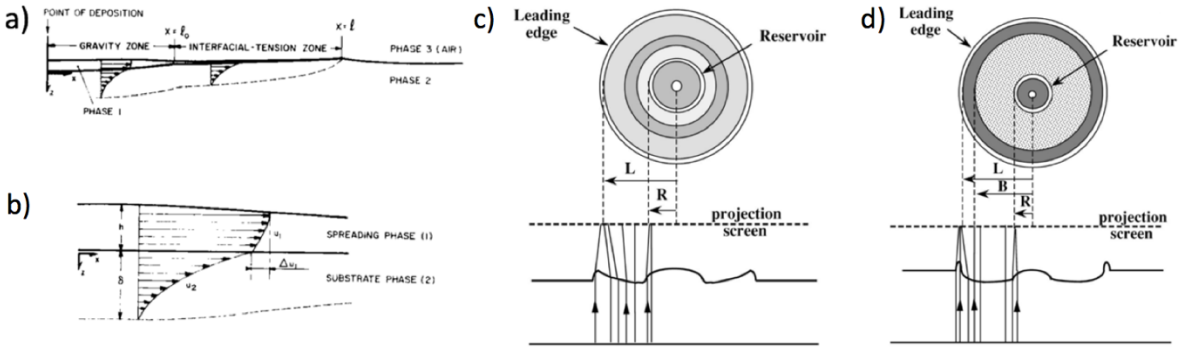



**Figure 2.14 Profiles of one liquid spreading on another**. (a) Schematic diagram of one liquid spreading upon another. Depending on the dominant spreading force in that region, the spreading film is divided into the two zones: gravity and interfacial-tension. (b) Schematic illustration of the spreading film with thin boundary layer of the flow inside the supporting liquid. (a) and (b) are reproduced from Ref. [126]. Diagram of ray tracing and surface profile obtained based on laser shadowgraphy results for depositing (c) ~4 μL sillione oil and (d) ~3 μL tolune over a deep layer of water. Reproduced from Ref. [125]

As early as the 1970s, Fay has presented a step-by-step solution to determine the rate of a volume $V$ of oil spreading on a still water surface into a slick with diameter $l$ and thickness $h$. The

oil spreading can be divided into three phases and the corresponding forces can be expressed by the following equations:

$$\text{Surface tension: } \frac{S}{lh} = \frac{S}{lV} \tag{2.10}$$

$$\text{Gravity: } \frac{\Delta\rho g V}{l^3} \tag{2.11}$$

$$\text{Inertia: } \frac{\rho l}{t^2} \tag{2.12}$$

$$\text{Viscous: } \frac{\rho\nu(l/t)}{\delta h} = \frac{\rho v^{1/2} l^3}{V t^{3/2}} \tag{2.13}$$

$$\text{Gravity – inertia: } l = (\Delta g V)^{1/4} t^{1/2} \tag{2.14}$$

$$\text{Gravity – viscous: } l = (\frac{\Delta g V^2}{\nu^{1/2}})^{1/6} t^{1/4} \tag{2.15}$$

$$\text{Surface tension – viscous: } l = (\frac{S^2}{\rho^2 \nu})^{1/4} t^{3/4} \tag{2.16}$$

where $S$ is spreading coefficient; $l$ and $h$ represent diameter and thickness of an oil slick, respectively, and they change with time $t$; $V$ is the volume of oil and $V = l^2 h$; $\Delta\rho$ is the difference in mass density between water and oil and $g$ is gravitational acceleration; $\rho$ is the oil mass density; $\delta$ is the thickness of the uppermost thin layer of water that is in contact with oil and set into motion by viscous forces with a magnitude of $\delta = \{\nu t\}^{1/2}$ in which $\nu$ is the kinematic viscosity of the water. Note that the dominant force switched from gravity to surface tension at a critical thickness $h_c$, where $h_c = (\frac{S}{\Delta\rho g})^{1/2}$. Since the surface tension term for spreading of low-density, small volume liquids, the correlation of $l \sim S^{1/2} t^{3/4}$ is often used as a standard formulation to compare with when investigating other types of liquids.

Compared to immiscible, non-volatile liquids, dynamics of spontaneous spreading of volatile liquids can be much more complicated due to the presence of evaporation. Dussaud and Troian studied the spreading of several volatile but water-immiscible liquids exhibiting different spreading coefficients and liquid vapor pressures upon a quiescent and deep layer of water.[125] By using laser shadowgraphy, the spreading liquid topology was traced and three distinct regions including reservoir (R), boundary (B) and leading edge (L) are shown in Figure 2.14d. The leading edge is found to advance as a function of a power law in time ($t$), where $L \sim t^{1/2}$. In this case the exponent is significantly smaller than the one for non-volatile films (3/4). This suggests that volatile solvents tend to spread much slower than non-volatile solvents where the solvent does not

dissolve in water in either case. Moreover, the authors also pointed out that the speed of the leading edge is well correlated with the spreading coefficient (*S*), while the speed at the reservoir (Figure 2.14d) is better correlated with the vapor pressure. However, the difference of spreading coefficient and vapor pressure does not affect the spreading exponent. Interestingly, a thickened elevated ridge was observed in both cases, which was identified as a 'Thoreau–Reynolds' ridge,[127] and has been documented since 1971. The authors also reported the observation of an elliptically shaped roll (Figure 2.15b) formed underneath the leading edge and within the boundary layer close to the water surface.[125] They suggested that this radially advancing convective roll is formed due to the temperature gradient at the leading edge, where the solvent experiences the largest cooling effect due to the greatest mass loss by evaporation.

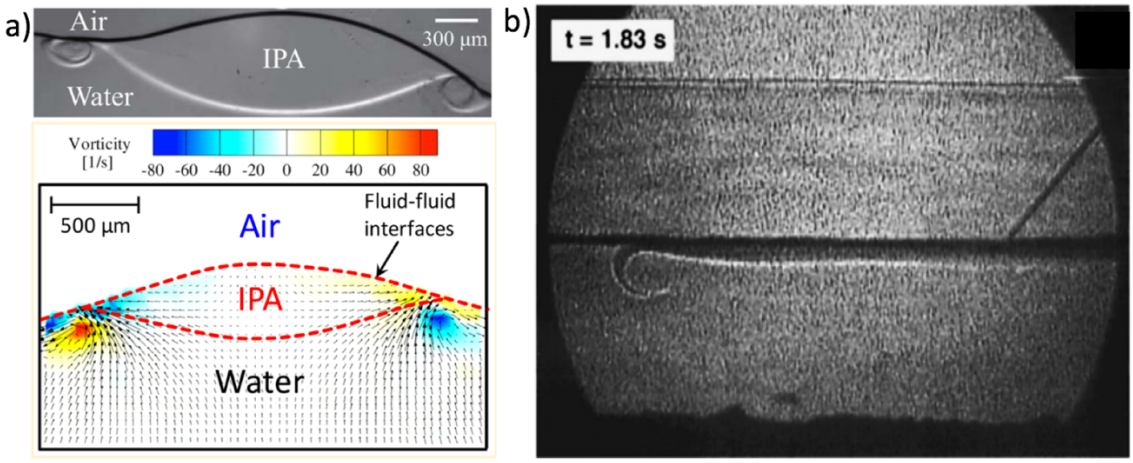



**Figure 2.15 Liquid behavior at the spreading boundary** (a) (Top image) Swirls (Marangoni mixing) generated when a drop of IPA was deposited on the air-water interface in a flow cell with 1 mm gap. The depth of water in the vertical direction is ~ 2 cm. (Bottom image) Particle image velocimetry (PIV) result for depositing a IPA drop upon water surface, where the red dashed lines indicate the interfaces of air−IPA, air−water, and IPA−water. The black arrows represent 2D velocity vectors and the color contours represent vorticity magnitudes. Reproduced from Ref. [128]. (b) Convective roll observed in sideview shadowgraphs for toluene spreading upon water produced by directing a horizontal collimated beam of light near the air–liquid interface. Reproduced from Ref. [125]

As for volatile and water-miscible solvents, investigations have been on-going since the 1960s. Davies and Rideal studied the spreading of acetone and ethanol at the air-water interface and measured a decreased spreading rate which they attributed to the presence of film depletion caused by dissolution and evaporation.[129] More recently, Kim *et al*. studied the spreading of volatile and water-miscible solvent spreading over the surface of water and water/ethanol mixtures. They witnessed spontaneous Marangoni mixing of 2-propanol (IPA) at a water (water/ethanol mixture) – IPA – air contact line (see the swirls shown in Figure 2.15a). The same topic was

revisited with more in-depth studies by the same research group and solute Marangoni flow was concluded to occur when a completely miscible liquid – IPA spreads at the water surface.[130] As a droplet of ~7.2 μL was deployed at the water surface, as shown in Figure 2.16a, the droplet spread quickly and formed a static central lens while the IPA continuously leaks at the boundary (see patterns in the photo in Figure 2.16b). At the edge of the lens, the local spreading coefficient is nearly zero (Figure 2.16b). Within the lens, the interfacial flow velocity rapidly raised to the maximum followed by a gradual decrease as it travelled to the edge of the lens (Figure 2.16c). Even though the diameter of the lens is around 1 cm, the top-view trajectories of seeded particles in IPA suggested that the resulting solutal Marangoni flow can further facilitate outward flow beyond the lens boundary extending the particle movements to at least a few centimeters away from the droplet location.

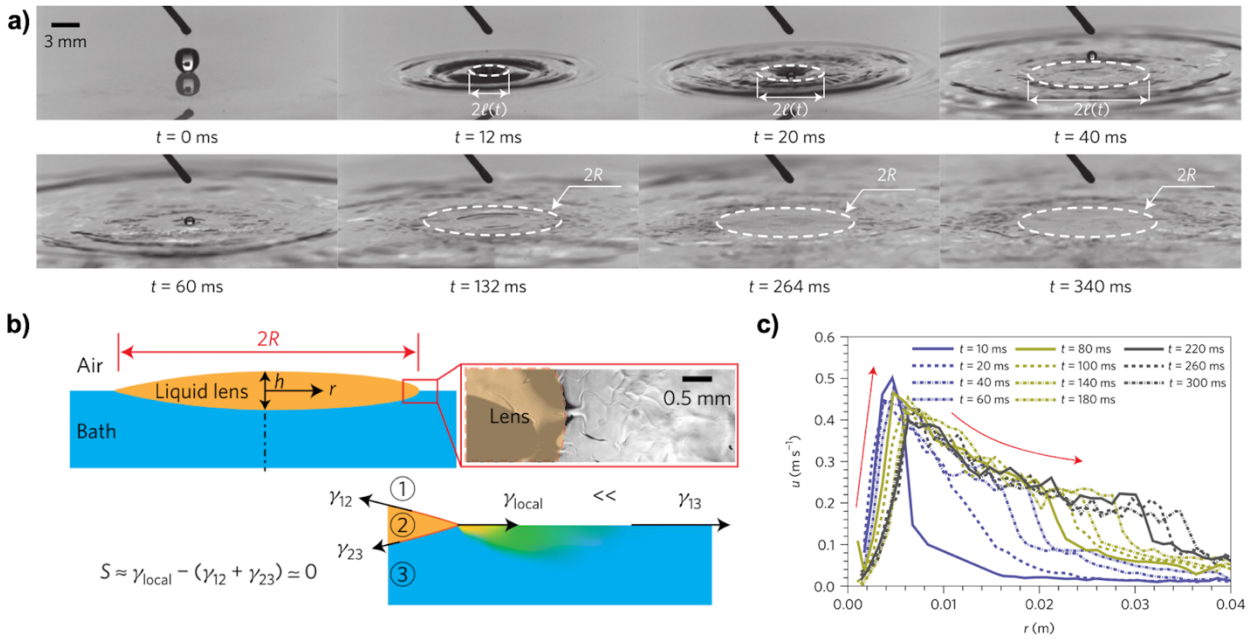



**Figure 2.16 Occurrence of solutal Marangoni flows when IPA spreads on water surface**. (a) Photos of evolutions of a droplet of IPA spreads at the air-water interface. The static central lens is indicated by dashed-line circles. (b) Schematic illustration of the surface and interfacial tensions of a lens of IPA on the water surface where the *S* is nearly zero. (c) Time evolutions of interfacial flow speed profile as a function of spreading distance within a lens of IPA. (a-c) are reproduced from Ref.[130]

The kinetics or dynamics of spreading solvent mixtures has not been investigated in previous literatures. In my PhD work, we employed a custom-made Langmuir-Adam balance to

directly measure the spreading pressure of solvent mixtures. Detailed discussion can be found in **Chapter 6**.

## 2.6 Layout of the Thesis

One of the challenges we aimed to address in our initial work (**Chapter 3**) was to improve the transfer efficiency of GO to the air-water interface by replacing the spreading solvent from a typical methanol or ethanol-based formulation, which causes up to 99% of material to be lost in the subphase, to a majority water-immiscible solvent such as 1,2-dichloroethane (DCE) or chloroform. With this switch, barely any loss of material was detected. While achieving this primary goal, we also studied how GO sheets behaved as a 2D colloidal dispersion at the interface by adjusting the subphase pH and ionic strength as well as the dispersion concentration. Most importantly, to the rest of this thesis, we observed an aggregation process where single-layer GO and other exfoliated materials like reduced graphene oxide (rGO) and chemically exfoliated $MoS_2$ (*ce*-$MoS_2$) aggregated edge-to-edge near the extremities of the Langmuir trough. This directional flow of material and densification during deposition enabled us to either continuously inject material into the trough to fill the entire area and then deposit batch-wise onto large area supports or deploy the spreading dispersion at one end of the trough and collect the dense film continuously from the other side. To understand the densification mechanism, we built our first version of a Langmuir-Adam balance to measure the spreading force acting on the floating, tiled network of sheets during deposition.

At the beginning of my thesis work, we had planned to leverage this process and produce large-area substrates for applications in solar energy conversion. Due to its high optical adsorption and favorable and potentially direct bandgap, we had proposed to study the use of exfoliated molybdenum disulfide as a light absorber. However, while working with *ce*-$MoS_2$ (the precursor), we noticed that the colour of my dispersions rapidly faded when sitting on the lab bench. Thus, in **Chapter 4**, we present the analysis carried out to understand and eliminate this degradation process. we study the degradation kinetics under controlled ambient light conditions, air exposure and dispersion pH and identify the degradation products. we also determine that light and oxygen can cause the formation of superoxide which causes self-degradation of the $MoS_2$. This process is accelerated under basic conditions due to the high solubility of the degradation products. Lastly,

we report on an improved solvent exchange method to obtain a spreading dispersion of *ce*-$MoS_2$ that contains comparably more monolayers while preserving the 1T polymorph. In subsequent chapters, all $MoS_2$ dispersions were kept in dark and solvent exchange was carried out within two days of exfoliation process to minimize aging effects.

In **Chapter 5**, we aim to examine the initial aggregate structure formed after a drop of spreading dispersion is printed onto the air-water interface from the $MoS_2$ dispersion prepared. These were found to form a range of cluster shapes, like that observed for the GO case studied in Chapter 3. Further analysis of different exfoliated flake systems leads to the conclusion of a universal concentration effect on spontaneous clustering of exfoliated 2D nanosheets regardless of material properties and morphology. Since these clusters are the 'building blocks' of the final, densified Langmuir films, we also study the impact of the initial cluster structure on the surface coverage of resulting films and the film collapse behavior. We then discuss the potential clustering mechanism through a combination of experimental observations and known interfacial phenomena in order to estimate the interactions between nanosheets.

In **Chapter 6**, we attempt to elucidate the importance of spreading solvent composition on the film density and transport properties across the coating bath. The custom-made Langmuir-Adam balance was upgraded to achieve a more sensitive response within the lower range of spreading pressure (< 8 mN/m). The upgraded apparatus was used to measure the spreading pressure profiles of various solvent mixtures. We then identify the key factors that govern the profile shape and the maximum spreading pressure by investigating the impact of polar solvents and water-immiscible solvents as well as the physical properties of the mixtures. By selecting several compositions with significantly different spreading profiles, we study the impact of spreading pressure on film formation and packing density, which is compared to the effect of cluster structure. To study how the spreading pressure impacts the ability to form directional aggregates in a roll-to-roll system, we build a coating system with adjustable width and explore the use of a multi-dripper system. We find that the spreading solvent is important for transporting and densifying clusters, but the wettability of the substrate plays a more crucial role in permitting continuous transfer of both hydrophobic and hydrophilic Langmuir films onto moving substrate with minimal macroscopic defects. In the end, we present the R2R coating apparatus and examples of resulting R2R films.

Finally, in **Chapter 7**, we implement the *ce*-$MoS_2$ Langmuir film in a vertically structured device – perovskite solar cell, and present the performance of the initial attempt.

# Chapter 3: Continuous Langmuir Film Deposition and Transfer by Controlled Edge-to-Edge Assembly of Graphene-Based Materials

*Context*: This chapter summarizes the initial work I carried out on the graphene oxide system. The concepts introduced in this chapter provide the basis for the more detailed analysis carried out in Chapters 5 and 6 and motivated our ideas to adapt the coating approach to $MoS_2$. This work is published as *Xu et al.,* Langmuir (2019) (see Statement of Contributions for details). There is partial overlap between this Chapter and my MASc thesis. However, the manuscript was finalized and revised several times during the first year of my PhD work and contains a significant number of new results and analysis which is why we decided to include it here.

## 3.1 Introduction

Since the 1920s, the Langmuir-Blodgett (LB) deposition technique has proven to be one of the most controlled approaches for depositing films that are only one molecular layer thick. Classically, insoluble amphiphiles were used to create these well-ordered thin films, by one or more deposition steps. Nowadays, the technique is being used increasingly to deposit a variety of nanomaterials including graphene and graphene oxide (GO) onto a wide array of substrates.[9,16,131–134] It is more versatile than high vacuum, high temperature vapor deposition methods (e.g. chemical vapor deposition) and provides significantly outstanding uniformity than common solution processing techniques does such as vacuum-filtration, spay-coating, spin coating or electrophoretic deposition.

While typical trough set-ups are only capable of coating substrates with areas on the order of ~$cm^2$, recently trough designs incorporating roll-to-roll coating equipment have been demonstrated.[32] However, at maximum, the continuous films can only be as long as the trough is. Ideally, film transfer would be coupled to continuous material deposition to make the process truly roll-to-roll. Working towards this goal, Kim *et al*. recently presented a Langmuir–Blodgett scooping (LBS) method[40,135] and suggested that the deposition of film on glass slides and membrane supports was driven by the Marangoni-effect caused by the evaporation of ethanol in the water bath. While densely packed monolayers of micron-sized spherical colloids were

demonstrated, films of nanomaterials like carbon nanotubes were uniform but multi-layer in nature as the technique seems limited to films larger than 10-20 nm in thickness.

In this work we first present a dispersion formulation which enables high-yield transfer of GO onto the air-water interface by formulating dispersions in water immiscible solvents, like 1,2-dichloroethane (DCE) and chloroform. We then introduce a barrier-free, solvent spreading-assisted deposition approach which is able to densify large-area monolayer GO films during both batch deposition and by continuous deposition and withdrawal. This allows us to deposit dense monolayer coatings over areas as high as 400 $m^2$ with just one gram of GO material. The mechanism of film densification and edge-to-edge aggregation are also investigated to gain insight as to how to control the film formation process. Lastly, we demonstrate that this approach can be extended to other 2D materials such as thermally reduced graphite oxide (rGO) and showcase a roll-to-roll deposition of rGO film.

## 3.2 Experimental Methods

Please note that batch deposition carried out in this Chapter is on a trough that is twice wider than the one used in **Chapter 5 and Chapter 6**. Moreover, the droplets were deployed at the center of water surface in this work rather than close to one side of the trough in **Chapter 5 and Chapter 6.**

### 3.2.1 Graphene oxide (GO) synthesis

Graphene oxide is synthesized according to Tour's improved hummer's method.[71] In a typical session, 360 mL of sulphuric acid were first mixed with 40 mL of phosphoric acid, and then 9 grams of potassium permanganate ($KMnO_4$) were slowly mixed in. This process will release heat and temperature rises above 30 ºC. Once all clumps of powder disappear, 3 gram of graphite flakes were added in portions over the course of 10 minutes. Then the reaction temperature was increased and kept at 48 – 50 ºC for 16 hrs. The slurry should appear dark green filled with silver shimmery flakes and then turn purple and grainy the next morning. The product can be as thick as toothpaste consistency if reaction temperature is kept on the higher end. Once the reaction is completed, the container was removed from the heating element and set aside to cool down slightly. A 1 L beaker containing 400 grams of ice was placed in an ice water bath and the warm slurry was

mixed in portion by portion slowly and carefully. The temperature of diluted acid mixture should be less than 60 ºC for safety concerns. Once all slurry was mixed in, the beaker was stirred under moderate speed and hydrogen peroxide ($H_2O_2$, 30 wt. %) were added in dropwise. Once enough peroxide was added, the acid slurry changed from dark purple to golden yellow to whiteish color. A few extra drops of peroxide were added to ensure all purple plates disappears. The total amount of peroxide varies from time to time but usually ranging from 12-15 mL. Centrifuging at 3500 rpm (Fisher Scientific accuSpin$^{TM}$ 3) for 20 min was used to separate solid from liquid and the pellets were collected and then purified two times by 10% hydrochloric acid (HCL) followed by 4 times by ethanol (absolute) via centrifuge at 3500 rpm (Fisher Scientific accuSpin$^{TM}$ 3) for 20 min. Each time the liquid was discard and pellets were collected. After purification, the GO was stored in the dark to slow down reduction. Note that the waste collected after each washing step should be segregated properly for safety concerns.

### 3.2.2 Thermally reduced graphene oxide (rGO)

Graphene oxide powder was obtained by spray drying a GO/water dispersion (BUCHI Spray dryer B-290). The GO powder was left to dry under flowing $N_2$ atmosphere overnight to minimize the moisture content before thermal expansion. The dry powder was loaded into quartz tubes and thermally reduced rapidly at 1100ºC for 30s under argon atmosphere in a tube furnace (Thermo Scientific). This process creates a high surface area powder of reduced GO (rGO) which can be effectively dispersed in a variety of non-aqueous solvents by tip ultrasonication. Note that the rGO used in **Chapter 5** and **Chapter 6** was a commercially available product.

### 3.2.3 GO spreading dispersion

The as-prepared GO dispersion in ethanol was diluted (if necessary) and mixed with 1,2-dichloroethane (DCE) (residue-free, electronic grade, Fisher Scientific, 99.9%) or chloroform (Fisher Chemical, HPLC grade) to make a final GO dispersion at the desired concentration with a volume ratio of ethanol/DCE of 1:13. A dilute GO in ethanol dispersion at a concentration of 1.4 mg/mL was prepared from the ethanol stock followed by 5 min of tip ultrasonication. Longer ultrasonication (10 min) would break up the sheets into smaller diameter ones.[67] This ethanol dispersion was then diluted with residue-free DCE or chloroform into the volume ratio mentioned above, final concentrations of 0.1 mg/mL, 0.05 mg/mL, 0.025 mg/mL, 0.00625 mg/mL and 0.003

mg/mL were used in this work. Note that, as for all GO spreading dispersions, after several hours, visible aggregates began to precipitate at the bottom of the vial and could not be effectively re-dispersed by ultrasonication even though sediment in ethanol dispersions could be easily dispersed again by ultrasonication. Thus, ethanol dispersions and DCE or chloroform were mixed just prior to each deposition. Note that an alternative route was also investigated where dried GO powder was dispersed in a mixture of ethanol and DCE with the same volume ratio. Even after a long ultrasonication, preparing Langmuir films from this suspension resulted in films that were significantly wrinkled and overlapping suggesting that this route is not as effective at exfoliating the material into single layers.

The GO in methanol dispersion was prepared via solvent exchange of the GO suspension in ethanol. Typically, the GO dispersion in ethanol was centrifuged at 4000 rpm and the pellet was redispersed with methanol and centrifuged again. This step was repeated twice more. Then, the GO was stored in methanol. A dilute GO in methanol dispersion at a concentration of 1.4 mg/mL was prepared immediately from this methanol stock, followed by 5 min of tip ultrasonication. The final traditional GO spreading dispersion at the concentration of 0.025mg/mL was prepared by diluting this GO in methanol dispersion with water at a volume ratio of 5:1.

### 3.2.4 Thermally reduced graphite oxide (rGO) spreading suspension:

To prepare the rGO spreading dispersion, 2 mg of as-prepared rGO was mixed with 20 mL DCE followed by 30 min tip sonication. The final rGO spreading dispersion was prepared by mixing 714 μL ethanol with 4 times diluted as prepared rGO dispersion in DCE. Note that a modified procedure was used for preparing rGO spreading dispersion used in **Chapter 5 and Chapter 6**.

### 3.2.5 Barrier-free, spreading-assisted deposition

A glass trough with Teflon tape wrapped edges and a fixed barrier was used to carry out the barrier-free deposition of the large area Langmuir film. The trough was cleaned with DCE and rinsed with deionized water (MilliQ) and then filled with MilliQ water until the water surface emerged just passed the trough walls. The air-water interface was cleaned using an aspirator. The cleanliness of the trough was verified by using a filter paper Wilhelmy plate and a balance. The

water surface tension was measured as $72 \pm 0.5$ mN/m. Substrates such as mica, PET and glass slides were placed underneath the water prior to the deposition. A spreading dispersion was prepared according to the procedures discussed above. This was dripped onto the air-water interface using a clean glass syringe and Teflon tubing with inner diameter of 159 μm and outer diameter of 312 μm using a syringe pump (KD Scientific, model 230) at a rate of 0.13 mL/min. As each droplet of the suspension contacted the water surface, the solvent spread spontaneously due to the positive spreading coefficient, and then evaporated, leaving the materials floating at the air-water interface. Dripping was continued until the solvent could no longer spread as indicated by the formation of lens of solvent at the dripping position. The resulting film was then deposited onto arbitrary substrates by the horizontal-precipitation method, as illustrated in Figure 2.2c, which involves slowly draining out the water from the trough, such that the film is lowered onto the substrates placed beneath the sub-phase water. Substrates were air dried prior to collecting them from the trough for further analysis.

### 3.2.6 Solvent spreading-assisted deposition on commercial LB trough with fixed barriers

The Teflon trough (NIMA, KN1006) was carefully cleaned by ethanol and then rinsed with MilliQ water. Then 600 mL of MilliQ water at desired pH was prepared using NaOH solution to adjust the water to pH=10 and HCl solution to adjust to pH=4. Approximately 500 mL of MilliQ (or pH adjusted) water was then added into the trough. Note that due to dissolution of carbon dioxide into water from the atmosphere, the pH = 7 and pH = 10 cases decreased to about 6 and 8, respectively, over the deposition time. The cleanness of water surface was examined by monitoring the changes of surface pressure while the barriers of the trough were being closed. The surface was cleaned by a vacuum aspirator until the surface pressure changed by less than 0.02 mN/m. The barrier on the left was placed 3 cm away from the field of view of the BAM while the other barrier was 14 cm away. Therefore, we could only observe the boundary ~5 cm from the dripping position. The as-prepared GO suspension in DCE/ethanol mixture (v:v = 13:1) was dripped onto the water surface at a speed of 0.13 ml/min. Since the spreading and evaporation disturbs the interface, the dripping had to be paused each time a BAM video recording/snapshot was taken in order to obtain a focused image. The videos were taken after dripping for every 0.5 – 1 min depending on the stage of deposition until the solvent could no longer spread as indicated by pooling of the solvent at the deposition site.

### 3.2.7 Compression-expansion isotherm experiment on commercial LB trough

The Teflon trough (NIMA, KN1006) was carefully cleaned by ethanol and then rinsed with MilliQ water. Approximately 500 mL of MilliQ water was then added into the trough and the cleanness of water surface was examined by monitoring the changes of surface pressure while the barriers of the trough were being closed. The surface was cleaned by a vacuum aspirator until the surface pressure changed by less than 0.02 mN/m and the barriers were then open to the two sides. 3 mL of as-prepared GO suspension in DCE/ethanol mixture (v:v = 13:1) at the concentration of 0.00625 mg/mL was dripped onto the water surface at a speed of 0.13 mL/min. The interface was stabilized for 30 min. Then the isotherm graph was obtained by closing the barriers at a speed of 15 mm/min to achieve the target surface pressure up to 5 mN/m, and opening the barriers at the same speed. This step was repeated to collect the isotherm data for surface pressure up to 10 and 15 mN/m.

As for the experiment of comparing our spreading solvent with the traditional one (methanol and water mixture), the trough was prepared and cleaned as described in last paragraph. Then, 4 mL of as prepared GO suspensions in methanol/water mixture at the concentration of 0.025 mg/mL was dripped onto the water surface at a speed of 0.13 mL/min. The interface was stabilized for 20 min. Then the isotherm graph was obtained by closing the barriers at a speed of 15 mm/min until it reached the smallest surface area. Typical initial and final surface areas were around 760 and 97 $cm^2$. The steps were repeated to obtain isotherm data with as prepared GO suspensions in ethanol/DCE mixture. The BAM videos were taken during both isotherm experiments.

### 3.2.8 Characterization

#### **3.2.8.1** *Atomic force microscopy (AFM)*

Contact mode AFM was carried out on GO films deposited on atomically flat muscovite mica (SPI) substrates using NP-STT10 tips (Bruker) and a Nanoscope MultiMode AFM (Veeco). AFM images were analyzed using Gwyddion software to extract height profiles between the atomically smooth substrate and the GO sheets, and a custom MATLAB code was used to estimate sheet thicknesses from the steps in the height profiles.

**3.2.8.2** *Brewster angle microscopy (BAM)*

BAM from KSV NIMA was used to enable visualization of GO monolayers at the air-water interface. The imaging resolution limit is ~2 μm.

**3.2.8.3** *Calculation of Langmuir specific surface area (LSSA)*

*LSSA* is calculated via this formula: $LSSA = A/m$, where $A$ (in the unit of $m^2$) is the Langmuir surface area that is covered by the nanosheets to naked eyes; $m$ represents the mass of the floating materials (in the unit of g). Unlike what was defined in my MASc thesis and the published paper, here we excluded the factor of 2, therefore, when comparing it to Specific surface area (*SSA*), we need to multiply the *LSSA* by 2, indicating two sides of 2D nanosheets.

**3.2.8.4** *Langmuir-Adam Balance (original)*

Please note that the spreading pressure measurement were carried in the corresponding trough used in this work, which, as mentioned above, is two times wider than the one used in **Chapter 6**.

A Langmuir-Adam balance is used in this work for measuring deflection force of pure solvent spreading as well as spreading pressure exerted by a spreading solvent on a growing film. The force measured was not converted to a spreading pressure value (force/length) in the case of pure solvent spreading because of the uncertainty in the length over which the force acted on the float. Compared to the situation where only solvent spreads at the air-water interface, when there is a network of GO floating on water, this network can transmit a lateral force to the entire barrier. For this reason, we present this data as a spreading pressure by normalizing the force data to the length of the float. The balance operates by measuring the spreading-driven deflection of a lightweight barrier sitting on the water surface. The more typically used Wilhelmy plate method for determining surface pressure cannot be used in this experiment because of the required assumption of zero contact angle and because such a measurement is significantly disturbed by the deployment of a drop on the water surface which causes ripples to propagate across the trough causing the plate/tensiometer to oscillate. Our balance was robust to rippling of water as verified by adding drops of water to the trough which caused changes in the height of the water as the wave propagated over the length of the trough but did not apply any lateral forces on the balance. A

calibration curve was obtained before each measurement and the calibrated balance was validated by measuring the equilibrium spreading pressure of stearic acid and then compared the result with literature value. Note that this apparatus is upgraded when carrying out work in **Chapter 6**.

**Equilibrium spreading pressure measurement with stearic acid**: The trough was first cleaned with DCE and rinsed with MilliQ water. It was then placed under the levelled Langmuir-Adam balance and the floating barrier was placed 17.5 cm away from right edge. A large glass was placed in the trough as it was in a regular deposition. The trough was then filled with MilliQ water. After baseline adjustment and calibration, a droplet of 0.015 M stearic acid in chloroform, prepared freshly before the experiment, was placed on the water surface and the voltage changes was recorded. Typically, a few more droplets were added to ensure the formation of a monolayer film covered the entire air-water interface with excess stearic acid forming a lens. The equilibrium spreading pressure is measured to be 18 ± 0.5 mN/m based on three independent repeats which is in line with the literature value of 18 mN/m[136]. Note that between each measurement, the trough and floating barrier were cleaned to minimize contamination.

**Deflection force measurement of spreading solvent upon the water surface**: The trough was first cleaned by DCE and rinsed with MilliQ water. It was then placed under the levelled Langmuir-Adam balance and the floating barrier was placed 17.5 cm away from right edge. A large glass was placed in the trough as it was in a regular deposition. After baseline adjustment and calibration, ethanol/ DCE mixture (v:v = 1:13) was dripped on the water surface at 2.5, 3, 3.5, 4, 6 ,8 cm from the floating barrier. At each dripping position, over 8 individual deflection force data were collected over a course of 30-sec continuous dripping. The sequence of the measurements was randomized. Then the steps were repeated for measurements of other solvents including ethanol/chloroform mixture (v:v = 1:13), pure DCE and pure chloroform (restarting from cleaning the trough and calibrating the balance).

**Spreading pressure measurements with GO suspension**: After cleaning the trough with DCE and rinsed with MilliQ water, it was then placed under the levelled Langmuir-Adam balance and the floating barrier was placed 17.5 cm away from right edge to form a coating area of 12.5 by 17.5 $cm^2$ which was the same as regular deposition area. A large glass was placed in the trough as it was in a regular deposition. After baseline adjustment and calibration, freshly prepared GO

dispersion in the DCE/ethanol mixture at a concentration of 0.025 mg GO/mL was added onto the water surface area (A) in the same way as was carried out in the regular barrier-free deposition. The photodetector voltage was recorded and plotted as a function of time and curves were processed using a custom MATLAB code. The steps were repeated for the more dilute concentration (0.00625 mg/mL) by restarting from cleaning the trough and calibrating the balance.

## 3.3 Results and Discussion

### 3.3.1 Ink formulation and development of large-area Langmuir film

#### **3.3.1.1** *Traditional vs. improved spreading solvent*

Compare to commonly used spreading solvents - methanol/water mixture, DCE/ethanol-based spreading dispersion offers significantly improved transfer efficiency of GO. Compression isotherms (Figure 3.1a) and *in situ* Brewster angle microscope (BAM) video snapshots (Figure 3.1b-e) are shown for experiments where the same mass and concentration (0.025 mg/mL) of GO was deposited from each spreading solvent system. As for the methanol/water case, compressing the material to an area of ~200 $cm^2$ (point b in Figure 3.1a) barely increased film density and discretely floating sheets and some clusters were observed (Figure 3.1b). Further compression to nearly 100 $cm^2$ (the limit of the trough, point c) resulted in a denser but incomplete coverage (Figure 3.1c). On the other hand, for the DCE dominated case, at 625 $cm^2$, larger mobile clusters are observed (Figure 3.1d). As far as 475 $cm^2$, the surface pressure had increased to ~2 mN/m and BAM imaging shown in Figure 3.1e revealed a fully dense film (at least to the resolution of the BAM, ~2 μm) exhibiting weaker contrast between the water and floating GO because of nearly complete coverage of water surface. To summarize, we come into two conclusions: 1) the transfer efficiency using DCE dominated dispersion (ink) is about five-fold higher than the methanol/water case (compare the final surface pressures in two cases); 2) Large clusters of GO are observed in the DCE case compared to the isolated sheets in the methanol/water case (compare Figure 3.1b and 4.1d).

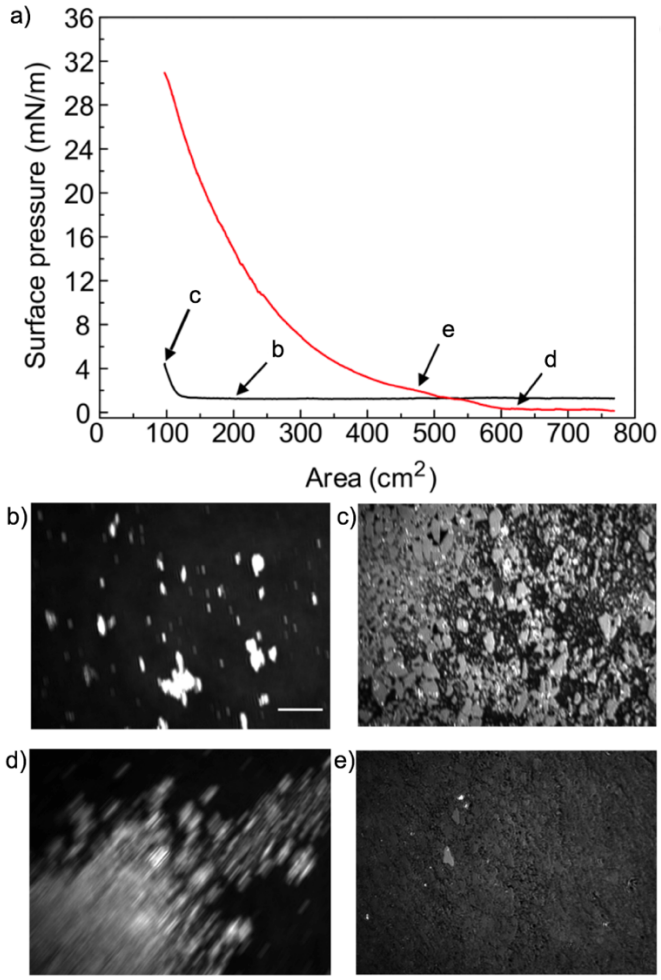



**Figure 3.1 Analysis of Langmuir films deposited from the traditional and improved spreading solvent systems**. a) Isotherms obtained after transferring the same amount of GO onto the air-water interface via two different spreading solvents: the traditional methanol/water (volume ratio of 5:1) system (black curve) and ethanol/DCE (volume ratio of 1:13) (red curve); b-e) *In situ* Brewster angle microscope (BAM) video snapshots of film morphologies with corresponding observation times labelled in (a). Scale bar in (b) is 100 μm. Other images were taken with the same magnification. The dark, nearly black, contrast is the water phase while the brighter contrast corresponds to the GO. Note that compared to (c) where traditional solvent was used, a fully covered dense film was observed in (e) where the DCE/ethanol-based spreading solvent was used. In (e) the contrast is poorer because there was little exposed water surface due to the high density of the GO but the outline of the packed sheets can still be observed.

### **3.3.1.2** *Solvent-spreading assisted Langmuir film Assembly (SSaL)*

The air-water interface was recorded while repetitively dripping a 0.025 mg/mL dispersion at the air-water interface and snapshots are shown in Figure 3.2a-c. Since the snapshots were generated by pausing the video when spreading area was at its maximum, boundary between the evaporating solvent and the adjacent film-covered interface is clearly visible, as marked by red arrows in Figure 3.2b-c. As more materials were transferred onto the water surface, the spreading

area is observed to shrink which implies that the film has grown inwards. Continued dripping leads to a further growth in film coverage until the solvent could no longer spread and forms a liquid lens sitting at the interface which would evaporate once the deposition stops. BAM was used to study the film formation in more detail as shown in Figure 3.2d-f. With each drop, material was observed to move rapidly past the fixed field-of-view but pausing to take a snapshot indicated that the water surface was free of any floating material during the early stages of deposition (Figure 3.2d). After 0.042 mg of GO was deposited, as shown in Figure 3.2e, there was an abrupt transition from a clean interface to a densely tiled film that grew across the field of view with each additional drop. Pausing the dripping to capture a focused image showed that the sheets held a densely tiled arrangement but convection, likely introduced by air-currents above the trough, induced the sheets located at the boundary to move and tumble (in 2D) rapidly passing one another while seeming to maintain some attraction to the growing front (see area within the red dashed-line in Figure 3.2e). Further adding more GO to the trough caused the film boundary to move past the field of view of the BAM. This uniform film composed of densely-packed GO sheets remained solid even after dripping was paused to take a snapshot as shown in Figure 3.2f.

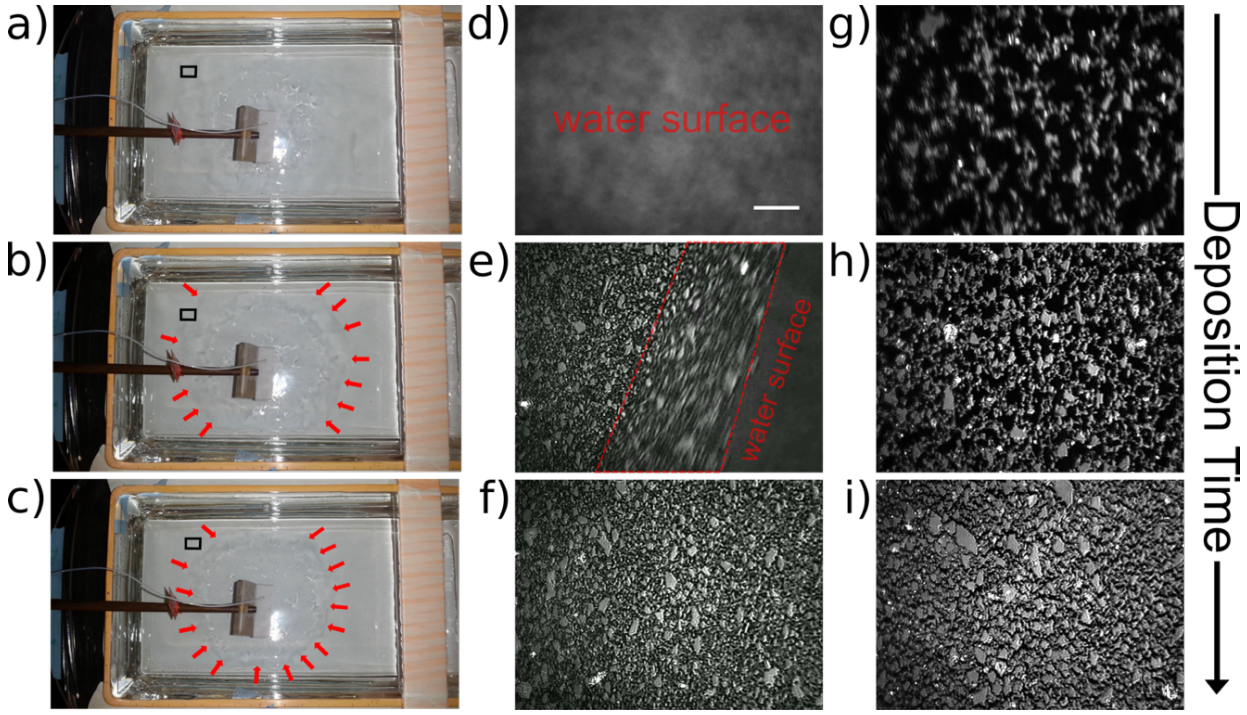



**Figure 3.2 Solvent spreading-assisted deposition of GO**. (a, b, c) Snapshots of videos taken at successive times throughout the process. The interface between growing GO film and solvent spreading is labelled by red arrows in (b) and (c). Note that at the early stage (a) of the deposition, the interface was poorly defined and thus not indicated.

Snapshots of *in situ* BAM videos taken at the interface between the spreading solvent and 'growing' film using a typical concentration of GO dispersions at 0.025 mg/mL (d, e, f) and 0.00625 mg/mL (g, h, i). The position where *in situ* BAM were set is labeled as black squares in (a), (b) and (c). Scale bar in (d), which is effective for all the other BAM images (e-i), is 100 μm. Note that the red dash line in (e) shows the moving sheets at the boundary between film growing front and pure water surface.

On the other hand, if a lower concentration dispersion of GO in DCE/ethanol is used, we observe a different phenomenon. Figure 3.2g-i show snapshots from the BAM when a 0.00625 mg/mL dispersion is continuously dripped onto the trough. After depositing 0.024 mg (Figure 3.2g), a low-density network is observed of what appears to be a mixture of isolated sheets and small clusters of 5-10 sheets aggregated in a branched morphology. As deposition is continued, this network densifies (Figure 3.2h) and eventually yields what appears to be an equivalent packing density as the more concentrated case (Figure 3.2i), although it happens at a relatively later time during the deposition.

As shown in Figure 3.3a and 3.3c, the 0.025 and 0.00625 mg/mL depositions both yield a densely tiled layer of sheets which are 0.7 - 1 nm in thickness, as is known to be the case for single layers of GO, with some wrinkles and occasional overlaps between adjacent sheets. Representative scanning electron microscopy (SEM) images of resulting films are shown in Figure 3.3b and 3.3d. A dense coverage (90-95%) was observed in both cases. In the 0.025 mg/ml case, the sheets are often found to be slightly overlapping at their edges as apparent in Figure 3.3b.

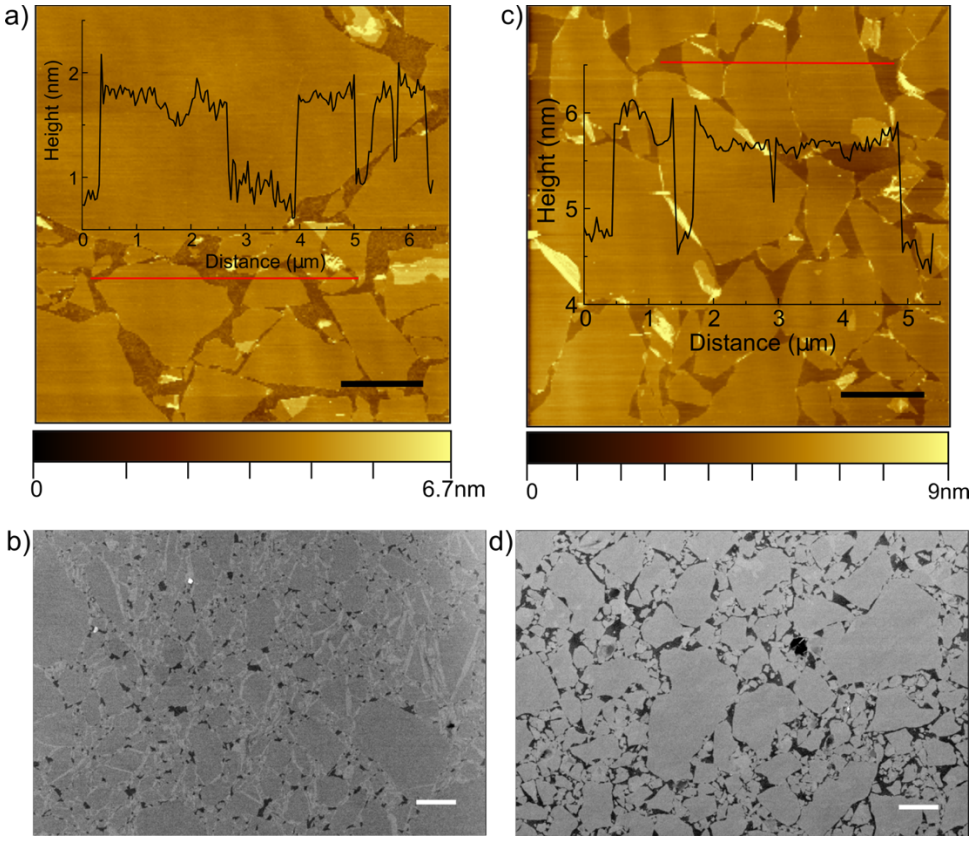



**Figure 3.3 Morphology of GO films prepared by barrier-free deposition**. Representative AFM images of samples coated on mica substrates after filling the trough with different concentrations: 0.025 mg/mL (a), 0.00625 mg/mL (c) of GO in the ethanol/DCE spreading solvent and the corresponding height profile across the red line in the image. The scale bar in (a) and (c) are 2 μm. Representative SEM images of samples coated on highly oriented pyrolytic graphite substrates prepared by barrier-free deposition from GO concentration at 0.025 mg/mL (b) and 0.00625 mg/mL (d). The scale bar in (b) and (d) is 10 μm. In the SEM images, the substrate appears as darker contrast, the GO sheets can be observed as dark grey while the overlaps (observed more so in (b)) at the sheet edges are lighter contrast.

The transfer efficiency of the deposition process can be quantified by the Langmuir specific surface area (*LSSA*, defined in the Characterization section). As shown in Figure 3.4 at dispersion concentrations between 0.003 and 0.025 mg/mL, we reproducibly observe $2 \times LSSA$ of 700 - 800 $m^2/g$. Two times *LSSA* is used to count surface area on both sides of the sheet. Our estimates are close to the highest literature specific surface area (*SSA*) value estimated for GO, determined using the method of methylene blue titration of stable single layer GO dispersions, which is 889 $m^2/g$.[137,138] Therefore, we can conclude that by using our Solvent-spreading assisted Langmuir film method (*SSaL*), we achieve a high efficiency, nearly 100%, in terms of transferring GO single layers onto the air-water interface to assemble into large area monolayer films. However,

the *LSSA* values we estimate begin to drop at higher concentrations which is expected since we observe significant overlapping between sheets at high concentration conditions.

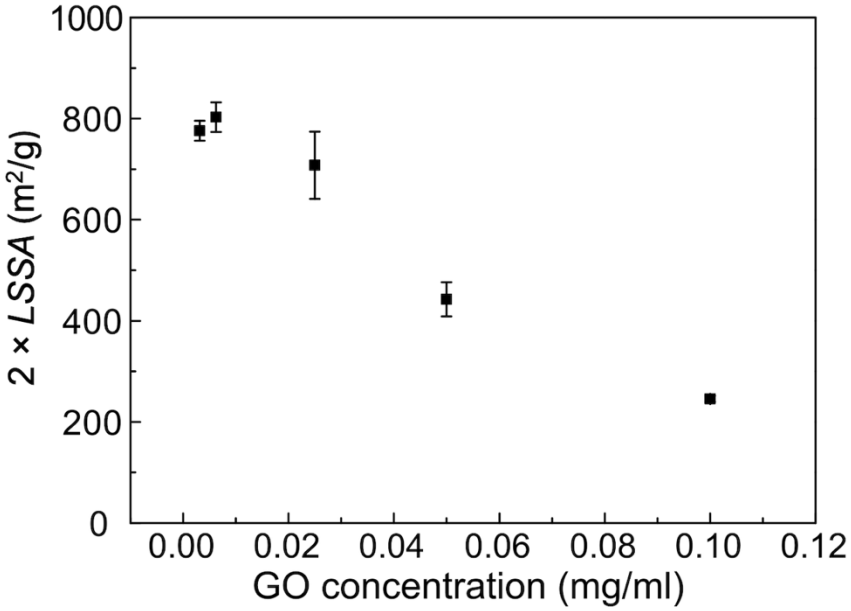



**Figure 3.4 Two times Langmuir specific surface area (*LSSA*) of GO Langmuir films as a function of the deposition dispersion concentration** (i.e., the ethanol/DCE (1:13) mixture). The error was estimated as ± the standard deviation of at least three depositions from freshly prepared GO dispersions. Two times *LSSA* is used for direct comparison with literature *SSA* value.

### 3.3.2 Aggregation mechanism of GO nanosheets

#### **3.3.2.1** *Impact of subphase pH*

As shown in Figure 3.5, the depositions from GO dispersions at 0.025 mg/mL at various sub-phase pH (no additional salt was added) were monitored by *in situ* BAM. In the case of pH = 4, at the early stage of the deposition, when only 0.003 mg GO were transferred onto the water surface, we observed large island-like aggregates of close-packed GO sheets moving rapidly on the water (Figure 3.5a). In contrast, when basic sub-phase water was used, well-dispersed GO sheets were observed on the water surface (Figure 3.5g) even when more GO was deposited (0.013 mg) via the repetitive dripping process. In the case of pH = 7, we observed the formation of a large densely-tiled island of GO when 0.042 mg of GO was deposited. However, as already discussed for the case above, the sheets remain mobile and were observed to tumble past one another under the influence of convection induced by solvent evaporation or air currents flowing over the trough (Figure 3.5d). As more material is added, in all cases, the film is densified

throughout the repetitive dripping process regardless of the sub-phase pH value, as shown in Figure 3.5b-c, e-f, h-i respectively.

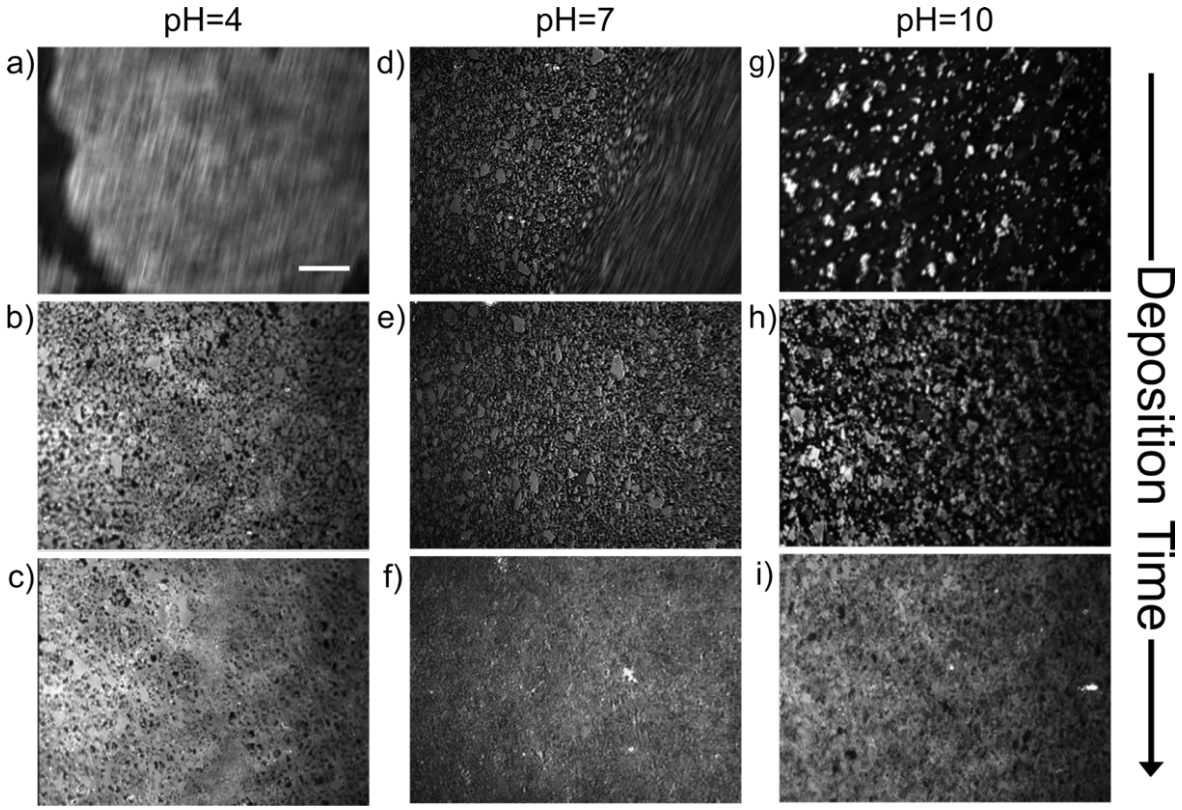



**Figure 3.5 Impact of subphase pH on GO aggregation**. Microscopic observations by *in situ* BAM of GO film formation via repetitive dripping process over subphase water at various pH levels: pH=4 (a-c), PH=7 (d-f), pH=10 (g-i). The scale bar in (a) is 100 μm and is valid for all other images. GO dispersion concentration of 0.025 mg/mL was used in all pH cases.

### **3.3.2.2** *Impact of subphase ionic strength*

In Figure 3.6, we investigate the ionic strength effect on the behavior of GO sheets at 0.025 mg/ml and a sub-phase pH = 10. At the early stage of the deposition, when only 0.007-0.013 mg GO were added onto the water surface, the sheets were observed to be repulsive in the case of 0 mM, 10 mM and 100 mM salt concentration. However, as more material was added we observed the formation of larger aggregates in the case of higher ionic strength. At the end of the deposition, the film achieved a similar density in all cases. When the ionic strength is as high as 1 M, the sheets formed large 3D aggregates from the beginning of the deposition which appeared as bright objects under BAM (Figure 3.6m-p). This is likely due to the significant decrease in electrostatic repulsion between the sheets as this high ionic strength could result in a very strong

screening effect between the sheets. Moreover, this aggregation phenomenon was also supported by the fact that almost twice the amount of GO was required to deposit a film with the same area at pH 10 and 1 M ionic strength. Unfortunately, films from this case could not be deposited on substrates and further characterized by either SEM or AFM, due to the high salt content that caused large crystals to form on top of and around the GO film.

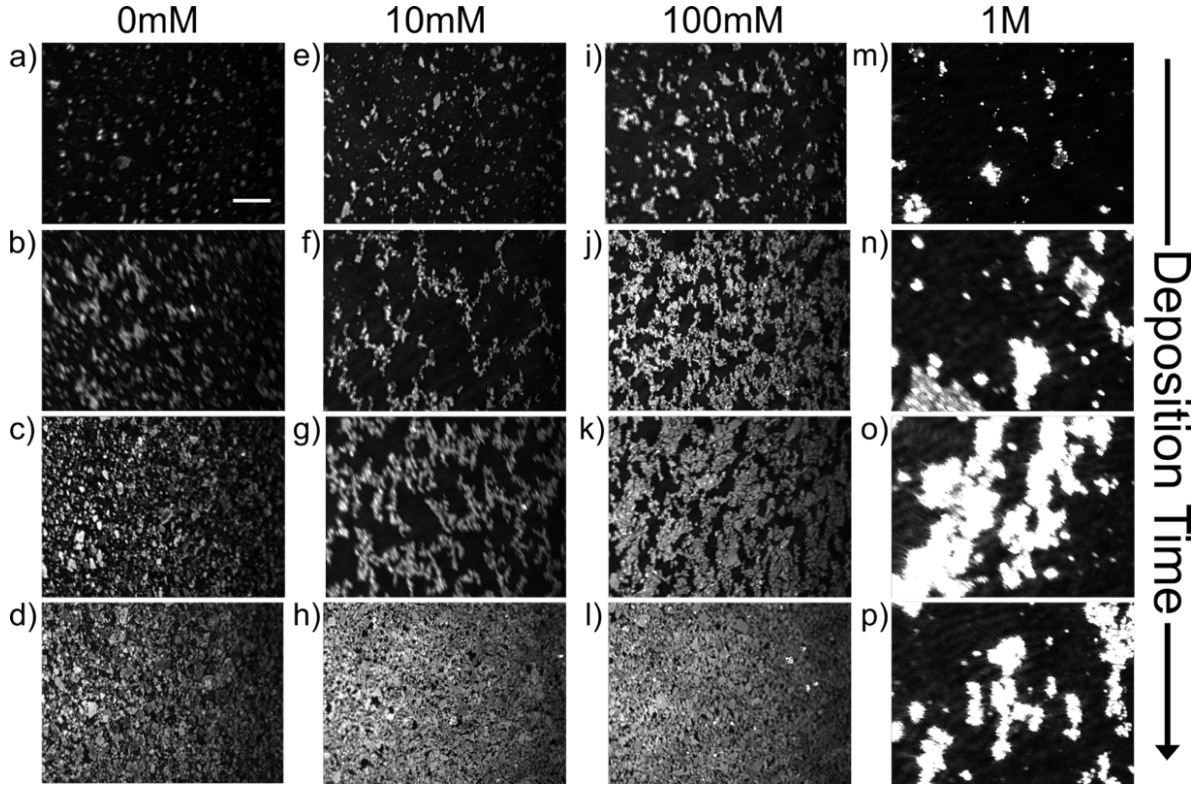



**Figure 3.6 Impact of subphase ionic strength on GO aggregation**. Microscopic observations by *in situ* BAM of GO film formation via a repetitive dripping process over subphase water at pH = 10 but with various ionic strengths: 0 mM (a-d), 10 mM (e-h), 100 mM (i-l), 1 M (m-p). The scale bar in (a) is 100 μm and is valid for all other images. A GO dispersion concentration of 0.025 mg/mL was used in all ionic strength cases.

The observations discussed above suggest that, except at high salt concentrations of ~1 M, at a subphase pH = 10, screening does not play a significant role in the aggregation at early stages of deposition. However, increasing the ionic strength tends to increase the density of 2D clusters as more material is added to the trough. On the other hand, significant changes in cluster structure was observed in Figure 3.2e vs. 3.2g when concentration was reduced. A more universal concentration effect on cluster formation among different types of 2D materials is unveiled in **Chapter 6**, along with the aggregation mechanism.

### 3.3.3 Solvent spreading-induced film densification

As shown schematically in Figure 3.7a, a Langmuir-Adam balance[139] was used to probe the force of the deposition solvent (DCE or chloroform – another common water immiscible spreading solvent) spreading on water and acting at different distances from the dripping position. As shown in Figure 3.7b when pure solvents (DCE and chloroform) were dripped on the water surface, the balance was unable to detect any significant force on the barrier even when drops were deployed 2.5 cm away. When ethanol was added to the solvents (1:13 ratio), the spreading force became significant and rose quickly when the dripping position was closer than 4 cm away from the float. The DCE/ethanol response was felt by the balance at slightly larger distances than the chloroform case. These results indicate that the spreading area prior to solvent evaporation is significantly enhanced with the addition of a small amount of ethanol and that the DCE/ethanol spreads over a larger area than the chloroform/ethanol case. This could be explained by two effects: 1. Adding ethanol will increase the work of adhesion between spreading solvent and sub-phase water and thus increase the spreading coefficient as well as the driving force for spreading; 2. Ethanol is less volatile than chloroform or DCE (vapor pressures are 44.03 mmHg vs. 61.68 mmHg at 20 °C for ethanol vs. DCE).[140] Therefore, their mixture would also be less volatile and could result in a larger spreading area. These observations are also apparent on a macroscopic level as the pure solvent is observed to pool near the deposition point prior to evaporating while mixtures with ethanol clearly spread further and more rapidly across the water surface. In comparing the morphology of the films deposited from the DCE/ethanol vs. chloroform/ethanol cases, the chloroform/ethanol spreading dispersion requires a lower concentration (0.00625 vs. 0.025 mg/ml) to obtain a film with discretely tiled single layers (Figure 3.8) without significant wrinkles and folds. This is likely due to the reduced spreading area that increased the probability of sheet-sheet overlap during deposition.

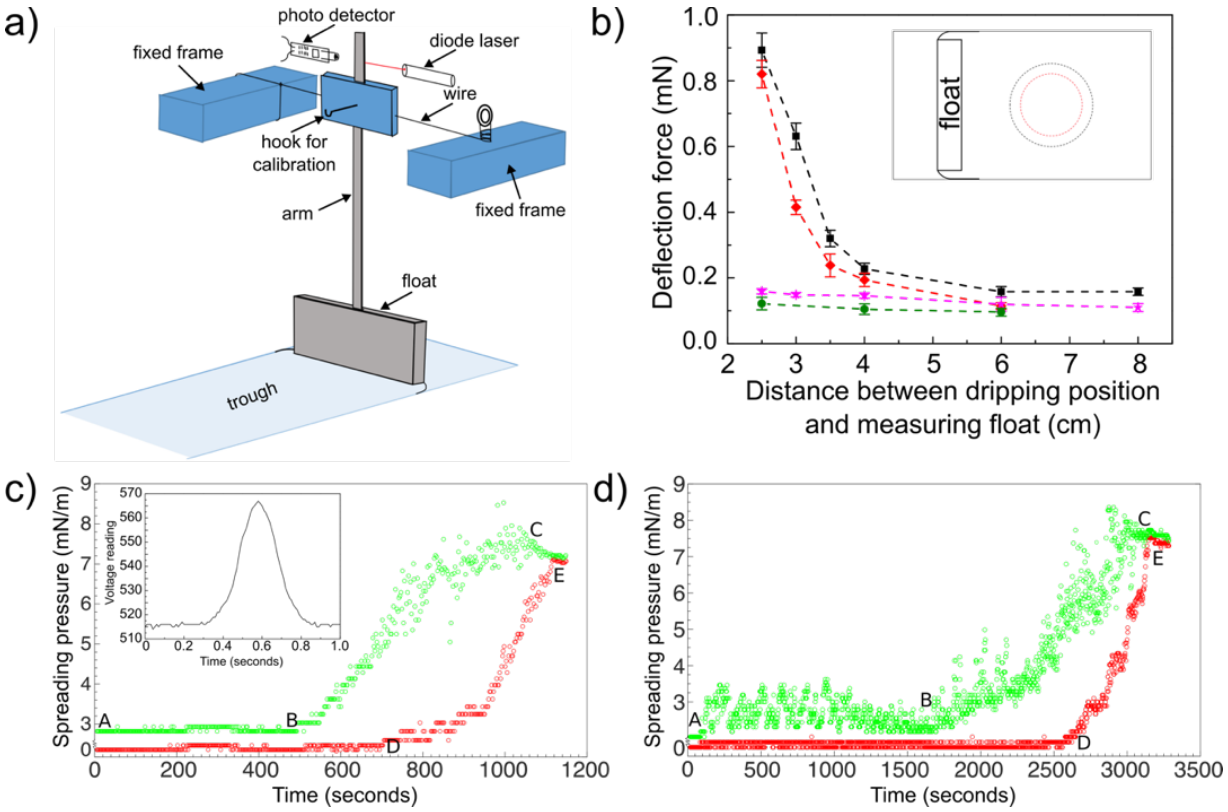



**Figure 3.7 Probing the liquid-liquid spreading pressure acting on the Langmuir film**. (a) Schematic illustration of the Langmuir-Adam balance used. The rigid supporting frame is not shown here. (b) Position-dependent deflection force of deposition solvents: DCE/ethanol (v:v = 13:1) (black, ■), chloroform/ethanol (v:v = 13:1) (red, ◆),pure chloroform (green, ● ) and pure DCE (magenta, ★). The inset shows the position of solvent injection in relation to the float at a distance of 8 cm. It also shows the size scale between the trough area (12 cm by 17 cm) and the approximate solvent spreading areas of DCE/ethanol (outter circle, black dash line, $R_{DCE/EtOH}$ ~ 3.5 cm) and chloroform/ethanol (inner circle, red dash line, $R_{Chl/EtOH}$ ~ 2.6 cm). Error bars indicate the standard deviation of at least 8 measurements. (c, d) Spreading pressure estimated during GO deposition at a concentration of 0.025 mg/mL (c) and 0.00625 mg/mL (d). In both cases the dripping position is the same as the inset indicated in Figure 3.7b. The green and red curves for each concentration show the maximum and minimum pressure, respectively, felt at the float for each drop of spreading solvent as a function of total deposition time. The inset in (c) shows a representative time-dependant voltage change measured by the float during the deployment of one drop of dispersion onto the air-water interface.

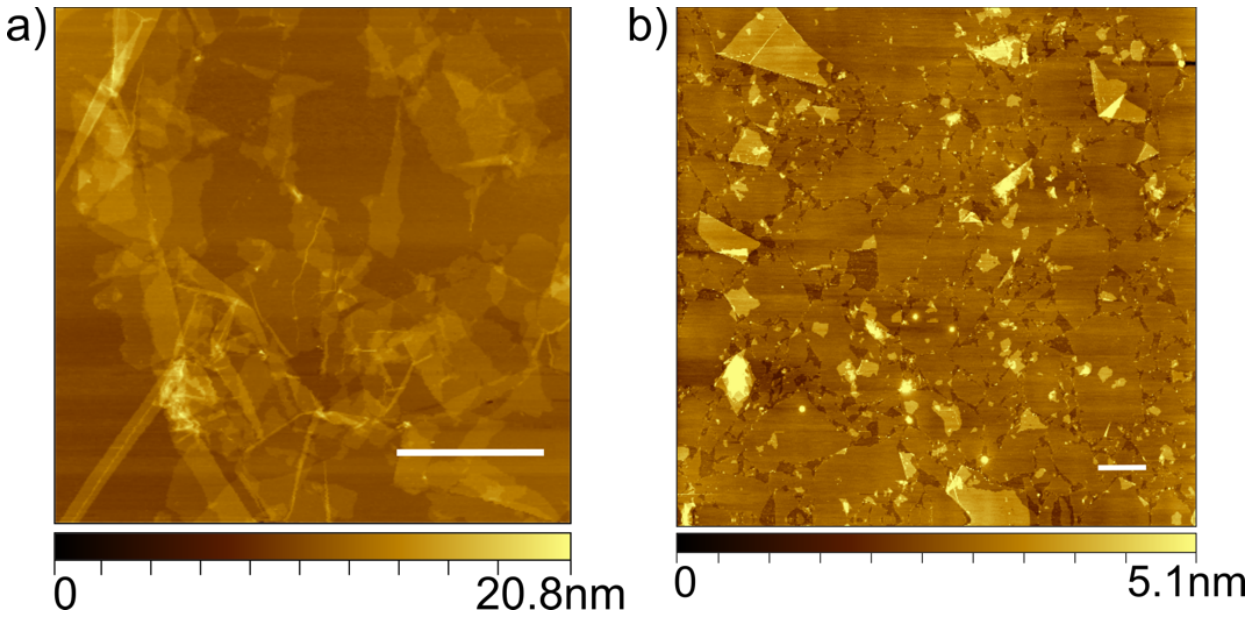



**Figure 3.8 Morphology of GO films by using chloroform/ethanol** (v:v = 1:13) as the spreading solvent: with GO dispersion concentration of 0.025 mg/mL (a) and 0.00625 mg/mL (b). The scale bars in (a) and (b) are 1 μm and 2 μm respectively.

Figure 3.7c and 3.7d show the changes of the maximum and baseline deflection measured after each drop of spreading dispersion (DCE/ethanol now containing GO) was added to the coating bath as a function of extent of deposition for GO dispersions at concentrations of 0.025 mg/mL and 0.00625 mg/mL. At an early stage of the deposition (labelled as A to B in both plots), significant changes in spreading pressure were detected (> 3 mN/m) for the dilute concentration, while no detectable change was recorded in the high concentration case over this range. The low concentration case could be explained by the observation of a repulsive network of branched aggregates as observed by BAM and discussed in the previous section (Figure 3.2g-h). The repulsive network is able to transmit a force to the balance with each drop. In the high concentration case, the aggregated GO are propelled to the extremities of the trough where they form islands that are far from the ~4 cm spreading front and thus no detectable deflection can be transmitted to the barrier. After this initial stage, in both cases, the spreading pressure was observed to increase (stage labelled B to C in plots) as the film grew from the edges of the trough inwards. Furthermore, we observed an increase in the baseline value of spreading pressure measured (in region D to E of the plots) in both concentration cases. The increase in baseline value is indicative of the increase in surface pressure caused by the densely tiled GO film. The early stage of this increase is likely due to GO bridges that form at the growth front as islands growing from both

sides of the trough and begin to merge at the centre. These bridges prevent the film from relaxing from the solid phase. However, approaching the end of the deposition, this increase is likely more related to the spreading pressure of the remaining solvent due to the slower evaporation rate caused by the decrease in spreading area. Near the end of the deposition, the baseline and maximum surface pressure converge when the solvent can no longer spread. This final spreading pressure, measured to be 7.1 and 7.7 mN/m in high and low concentration cases, respectively, might be considered the equilibrium spreading pressure of the solvent acting on the GO. Therefore, the spreading force or pressure exerted by solvent-water interactions act on clustered or isolated sheets, pushing material from high pressure (near the drop deployment site) to low pressure. This acts to compress the dispersion as the film packs and grows closer to the spreading front. The fact that the aggregates rearrange into a more densely tiled configuration during the repetitive dripping process suggests that the edge-to-edge attraction is weak enough to be broken by the force of solvent spreading.

In **Chapter 6**, we evaluated spreading pressure of serval combinations of solvents and conducted studies on interpreting the unique spreading profile of the mixture. Further investigation on how the spreading could impact film formation and densification were also carried out on other 2D materials.

### 3.3.4 Continuous coating of rGO film

To visualize how the solvent spreading process can control film formation (densification) in a macroscopic view, we turn to other materials which are more easily seen by the naked eye as a thin film, like thermally reduced graphene oxide (rGO). Figure 3.9a, shows an example of rGO films deposited from a rGO powder dispersed in the same DCE/ethanol mixture as the GO in the same coating bath configuration at the concentration of 0.025 mg/mL. We observed initial aggregation taking place during evaporation of the thin solvent film that distributes material over the air-water interface. These small islands then coalesced to form larger ones, until a uniform film began to build up from the outside of the trough inwards. The film continued to grow with each additional drop of dispersion until the entire trough was covered as was observed for the GO case above. Similar film growth phenomenon has been recently demonstrated for another 2D material,

chemically-exfoliated $MoS_2$ which suggests that this edge-to-edge aggregation and solvent-driven densification mechanism may be more generally applicable.[141]

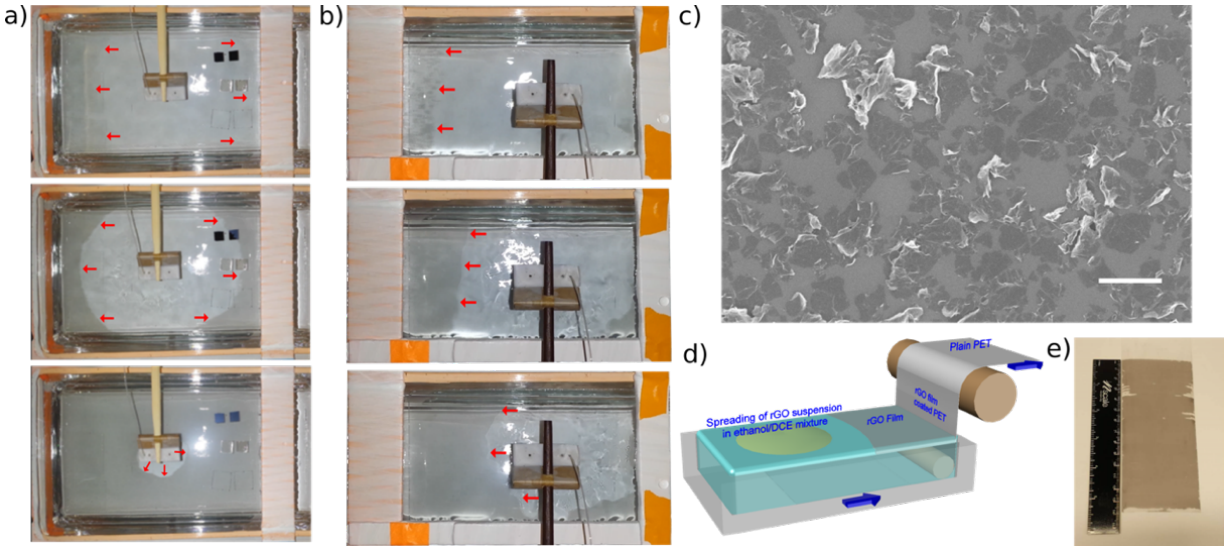



**Figure 3.9 Barrier-free deposition and continuous film coating of rGO**. Snapshots of videos recorded during rGO deposition by setting the dripping position at the center (a) and close to one side of the trough (b) using two typical concentrations: 0.025 mg/mL (a) and 0.1 mg/mL (b). Note that the edges of the growing film are labelled by red arrows in (a) and (b). SEM image of the rGO film coated onto silicon using a concentration of 0.1 mg/mL (c). The scale bar in (c) is 1 µm. In the SEM image, substrate is shown as light grey and rGO sheets are shown as darker contrast with wrinkles shown as white. Schematic illustration of continuous coating setup and operation (d). Resulting PET sample coated with rGO film in a dimension of 6.5 cm by 14 cm using rGO dispersion concentration of 0.1 mg/mL (e).

SEM imaging shown in Figure 3.9c displays that the resulting rGO film is composed of discretely tiled sheets similar to the GO case. However, the sheets appear wrinkled and many aggregated or unexfoliated materials appear to be present within the film. The wrinkling in rGO flakes are frequently observed by others,[142] and are thought to result from the rapid thermal expansion process which produces defects and functional groups as well as by partially exfoliated, stacked materials which are not deaggregated by the ultrasonication procedure used. The $2 \times LSSA$ estimated for this material was typically between 120 - 150 $m^2/g$ which confirms the presence of many aggregates and few layer stacks within the film as the theoretical surface area of a single layer of graphene is 2630 $m^2/g$. While this material is not as well-defined as the mono-dispersed (in the thickness direction) GO films, the material appears to follow the same general behavior as with the GO films. However, the packing density or relative coverage is lower (~80%) compared to the GO films. In a previous work by Pope *et al.*, Langmuir-Blodgett films of rGO were shown to reach a relative coverage of above 90% when barrier compression was used to adjust the surface

pressure to 25-30 mN/m.[143] This is higher than what can be achieved by solvent spreading with the DCE/ethanol system (~8 mN/m as discussed above).

As shown in Figure 3.9b, by changing the position of the dripping closer to one edge and making the bath narrower (6.5 cm) than the spreading front, the film could be selectively assembled from one side of the trough to the other, in contrast to the film growing symmetrically from both sides as for the central injection case. By placing a long piece of clean PET film beneath the sub-phase water, and withdrawing the film at a similar velocity to that of the growing front of rGO film, as the schematic diagram shown in Figure 3.9d, we demonstrate the ability to continuously transfer the rGO film to the PET during the dripping process (Figure 3.9e). More discussion around the coating speed can be found in **Chapter 6 section 6.3.4.2**.

## 3.4 Conclusion

In this Chapter, by replacing the traditional spreading solvent for deploying GO onto the air-water interface with one that is largely water-immiscible, we observe a concentration, sub-phase pH and salt dependant edge-to-edge aggregation behavior that in all cases leads to nearly 100% transfer efficiency. By continuously dripping material onto the interface, we observe that the force of the spreading solvent is capable of densifying the dispersed or aggregated 2D system into a dense layer of single sheets allowing us to measure surface coverages as high as 400 $m^2$ per gram of GO deposited. Using *in situ* Brewster angle microscopy and a Langmuir-Adam balance, we study the aggregation and densification mechanism. Under conditions of weak attraction and by positioning the material injection point appropriately in the bath, we demonstrate that films can be continuously deposited and transferred to substrates such as PET. While the study focuses mainly on GO, other 2D materials such as rGO are shown to yield qualitatively similar aggregation behavior that allow us to paint a mechanistic picture of this new film forming approach.

# Chapter 4: Aging Spreading Dispersion of 1T-$MoS_2$ – Aging Effect and Improved Processing Method *

*Context*: Chemically exfoliated $MoS_2$ has proven to be a promising precursor for producing monolayer 2H $MoS_2$ which shows great potential in photovoltaic applications, as demonstrated in **Chapter 2 section 2.3.2**. While we were working with this precursor, we noticed degradation phenomenon in the dispersion such as rapid color-fading. Therefore, in this chapter, we present the analysis carried out to understand and eliminate this degradation process. We further improve the procedure to prepare spreading dispersion of chemically exfoliated $MoS_2$ with better quality and use it in later studies including clustering formation (**Chapter 5**), solvent spreading (**Chapter 6**) and application in perovskite solar cell (**Chapter 7**).

## 4.1 Introduction

Chemically exfoliated 1T-$MoS_2$ (1T polymorph dominated, denoted as 1T-$MoS_2$ in this chapter and as *ce*-$MoS_2$ in other Chapters) can be readily converted to monolayer 2H $MoS_2$ by thermal treatment in either the solid or solution phase.[23,104,144] 2H $MoS_2$ monolayers possess a direct bandgap with a bandgap energy of 1.8-1.9 eV.[97,98] This makes 1T-$MoS_2$ a precursor to single-layer 2H $MoS_2$, a promising material for semiconducting, photovoltaic, photoelectronic and photoelectrochemical applications.[145–148] Unfortunately, the chemical exfoliation process is known to introduce defects which can significantly impact transport properties and electrochemical reactivity. By varying the intercalation conditions, Knirsch *et al.* showed that the defects, such as sulfur vacancies, can be controlled in the resulting chemically exfoliated 1T-$MoS_2$.[108] However, the introduction of defects in 1T-$MoS_2$ via degradation after chemical exfoliation remains unknown. Thus, it is urgent to identify degradation mechanisms which introduce such defects so that they can be minimized for electronics and optoelectronics applications or controlled for electrochemical applications where some level of defects is known to have a significant impact on performance.[149]

* This chapter is adapted from my published paper: "**Xu, L.**; Tetreault, A. R.; Pope, M. A. Chemical Insights into the Rapid, Light-Induced Auto-Oxidation of Molybdenum Disulfide Aqueous Dispersions. *Chemistry of Materials* **2020**, 32 (1), 148–156. https://doi.org/10.1021/acs.chemmater.9b02987."

Recently, the instability of $MoS_2$, in both the 1T and 2H polymorphs, has drawn attention from the scientific community. Most studies have focused on the degradation of monolayer and bulk 2H $MoS_2$ due to water/moisture,[150,151] ambient air,[152] solution pH as well as light irradiation.[153] On the other hand, little is known regarding the aging effect of 1T-$MoS_2$. In 2015, Knirsch *et al.* reported the observation of $MoO_2$ and $MoO_3$ formed in the 1T-$MoS_2$ dispersion over the course of one to two months, coupled with the phase restoration from 1T to 2H.[108] More recently, Nurdiwijayanto L. *et al.* reported that 1T-$MoS_2$ sheets aggregated and restacked in aged aqueous dispersions where they considered the effect of Li-ion concentration and gaseous environment (oxygenated vs. oxygen-free dispersion).[154] According to their study, the resulting aggregates remained in the 1T polymorph but aggregated due to a continuous reduction in the magnitude of the zeta potential which destabilized the dispersions. The sheets were also found to breakdown into small fragments under long-term ambient air exposure. The authors also pointed out that the dispersion appeared to be a lighter color as a result of the degradation but did not investigate this observation any further.

In this work, we aim to further understand the degradation processes occurring in 1T-$MoS_2$ aqueous dispersions by systematically investigating the chemical changes as a function of common processing conditions including combinations of exposure to ambient light, varying pH and ambient oxygen vs. deoxygenated conditions. The aged products were analyzed over a one to three weeks period using UV-Vis, Fourier-transform infrared (FTIR), Raman and X-ray photoelectron spectroscopies (XPS). Using these results, we identify degradation rates as a function of processing conditions allowing us to highlight conditions where significantly accelerated degradation is observed. This helps us to provide a mechanistic picture of the photoelectrochemical changes occurring in the dispersions over time. The mechanism of the light-accelerated degradation in alkaline solution was also investigated and we proved that the formation of superoxide was involved. In addition, the results also suggest that the degradation is favored by sulfur vacancies as well as edge defects. We believe that the results presented herein will not only serve as a crucial foundational work to develop an improved procedure for preparing the spreading dispersion of 1T-$MoS_2$, but also help guide researchers working on $MoS_2$ to minimize or control degradation and resulting defect formation in this technologically important material.

## 4.2 Experimental Methods

### 4.2.1 Chemical exfoliation of $MoS_2$ using n-butyllithium

In a typical process, 500 mg of $MoS_2$ powder (Aldrich Chemistry) was mixed with 5 mL of 1.6 M n-butyllithium in hexane (Across Organics) for 67 hrs at room temperature in an argon-filled glove box. The resulting lithiated $MoS_2$ ($Li_xMoS_2$, $0 \leq x \leq 1$) flakes were collected and rinsed with 20 mL of hexane (Fisher Scientific) four times. A 1.5 mg/mL stock solution was prepared by transferring this filter cake into Milli-Q water (~18 MΩ·cm) where it spontaneously exfoliates when water infiltration causes the lithiated product to generate $H_2$ gas and LiOH. Both filtration and water-assisted exfoliation were completed under nitrogen atmosphere using a glovebag. The as-prepared stock solution was immediately bath ultrasonicated (360 W, 40 kHz) being careful to prevent the sample from exposure to ambient light. The stock solution was segregated into individual vials for further use within the same day of exfoliation. Please refer to **Chapter 5 section 5.2.2.1** for more details.

### 4.2.2 Sample preparation for degradation studies

In order to minimize the influence of dissolution of carbon dioxide into the samples, for each study, the dispersions were divided into small volume and stored with their caps tightly closed. The vials were only opened for measurements at the designated day. The characterization of freshly prepared sample was carried out one day after exfoliation was carried out. However, in the case of the kinetics studies, defect studies (surfer vacancies and edge defects) and mechanism studies (using superoxide scavenger), the fresh samples were characterized right after the exfoliation.

The sediment in the stock dispersion was discarded and the dispersion was then stirred before being distributed into small vials. Most of the alkaline samples were directly taken from the 1T-$MoS_2$ stock dispersion. They were diluted with Milli-Q water if their counterpart samples (noted as Milli-Q samples in this work) were designed to be diluted, which is noted in the main text. The pH of freshly prepared 1T-$MoS_2$ dispersion was measured to be ~11.5. Samples were prepared at a concentration of ~ 0.5 mg/mL for kinetics studies.

Milli-Q samples were prepared by washing the 1T-$MoS_2$ stock solution using Milli-Q water via filtration until the pH of the filtrate was neutral. Re-dispersion of these samples was assisted by 15 min of additional bath sonication.

To carry out mechanism studies (using superoxide scavenger), 10 mmol/L 1,4-benzoquinone (BQ) in Milli-Q water was prepared and then mixed with stock alkaline dispersion using volume ratio of 1:1. The final concentration is ~ 0.7 mg/mL.

Samples for defect studies (sulfur vacancies in this case) were prepared by preparing the n-BuLi intercalated $MoS_2$ stock dispersions using three different Li/$MoS_2$ molar ratio (Li/$MoS_2$ = 1.28, 2.56 and 5.12). The procedure of exfoliation in water remained the same as did the concentration of stock dispersion (~ 1.5 mg/mL). These stock dispersions were diluted with Milli-Q water to prepare the samples at a concentration of ~ 0.7 mg/mL before they were segregated into individual vials for the study.

As for samples for edge defects studies, a one-step centrifugation-based size selection were conducted at 3000 rpm for 20 min and this was carried out after freshly preparing a batch of chemically exfoliated 1T-$MoS_2$. The supernatant (2/3 of the top layer dispersion) was separated from the sediment or pellet (the leftover 1/3) and then mixed with other supernatant samples. The same merging step was also utilized for preparing pellet samples. Then, 5 min bath sonication (360 W, 40 kHz) was used before distributing then into individual vials for the study.

Ambient light illumination studies were carried out by storing the samples in between two florescence lamps (T5/21W 4100K) in a closed cabinet. All of the samples are placed the same distance from the two lamps. The counterpart samples were stored in a cardboard box with lid on. The box was covered by aluminum foil and stored in the same cabinet.

### 4.2.3 Solvent exchange of *ce*-$MoS_2$ aqueous dispersion

**Neutralization methods:** After intercalated $Li_xMoS_2$ exfoliated in water, the dispersion is basic (pH ~ 10). Two methods were investigated for neutralization: 1). Add desired amount of 10% hydrochloric acid (Sigma Aldrich) solution until pH ~ 7 (determined by pH paper); 2). Dialyzing the basic solution in MilliQ water under dark with continuously purging $N_2$ gas (99.99%, dry) Flocculation method: Add desired amount of 10% hydrochloric acid (Sigma Aldrich) solution

until pH ~ 2, wait overnight until materials settles. Dialysis tubing: Spectrum™ Spectra/Por™ 4 RC Dialysis Membrane Tubing with 12,000 to 14,000 Dalton MWCO.

### 4.2.4 Preparation of stock and spreading dispersion of 1T-$MoS_2$ nanosheets

***ce*-$MoS_2$ in dimethylformamide (DMF) and reagent alcohol (RA)**: Immediately after exfoliation, on the same day, every 50 mL of *ce*-$MoS_2$/LiOH aqueous solution was filtered through a nylon membrane (Millipore, GNWP04700, 0.2 μm pore size) using vacuum filtration. When there was about 5 mL remaining over the filter cake, the remaining dispersion was discarded and the wet filter cake along with the membrane were transferred into 15 mL of dimethylformamide (DMF). The *ce*-$MoS_2$ could be easily redispersed in DMF by shaking the container gently. Then, 6-10 min of bath sonication (VEVOR DIGITAL PRO$^+$, 360 W) was applied to remove material stuck to the filtration membrane, followed by 2 min of probe-sonication (BioLogics, Model 150V/T Ultrasonic Homogenizer 460 W, at 70% max power) to ensure recovery of *ce*-$MoS_2$ monolayers in DMF. For the RA-based dispersions, DMF was simply replaced by RA with the same volume but 6 min of probe-sonication (BioLogics, Model 150V/T Ultrasonic Homogenizer 460 W, at 70% max power) was used instead. Note that we found it difficult to recover single layer sheets from fully dried filter cakes. This is why, wet/moist cakes were used in this work. Note that *ce*-$MoS_2$ stock dispersions in DMF (or RA) were stored at concentrations less than 0.8 mg/mL and new batches were prepared every 1-2 months to limit the impact of aging.

***ce*-$MoS_2$ in DMF/DCE and RA/DCE** The final spreading dispersion of *ce*-$MoS_2$ was prepared by mixing stock dispersions of *ce*-$MoS_2$/DMF or *ce*-$MoS_2$/RA with DCE at a desired concentration with a volume ratio ($V_{DMF/RA}/V_{DCE}$) of 1:6. For example, to prepare 1.4 mL of a final spreading dispersion of *ce*-$MoS_2$ in DMF/DCE (v:v=1:6) at 0.057 mg/mL, 200 μL of 0.4 mg/mL *ce*-$MoS_2$/DMF was diluted by 1.5 g of DCE (the density of DCE is 1.246 g/mL).

### 4.2.5 *SSaL* deposition of 1T-$MoS_2$ nanosheets

Please refer to **Chapter 5 section 5.2.2.5** for experimental details on the preparation of deposition methods.

### 4.2.6 Characterization

#### **4.2.6.1** *UV-Vis Spectrophotometry*

Optical absorption was measured on a UV-Vis spectrometer (Agilent 8453A) using a quartz cuvette.

#### **4.2.6.2** *Fourier-transform infrared spectroscopy (FTIR)*

The FTIR spectra were then acquired using an FTIR spectrometer (Perkin Elmer Spectrum Two$^{TM}$). The $MoS_2$ dispersions were freeze dried to obtain a powder and then mixed with KBr and pressed into pellets. The FTIR spectra were acquired with a resolution of 4 $cm^{-1}$ and averaged three times.

#### **4.2.6.3** *Raman spectra*

Raman spectra were collected using a Horiba HR800 spectrometer operating at $\lambda$ = 532 nm.

#### **4.2.6.4** *Atomic force microscopy (AFM)*

AFM images were taken using NP-STT10 tips (Bruker) and a Nanoscope MultiMode AFM (Veeco) and then analyzed using Gwyddion software.

#### **4.2.6.5** *X-ray photoelectron spectroscopy (XPS)*

X-ray photoelectron spectroscopy (XPS) was performed with a Thermo-VG Scientific ESCALab 250 Microprobe XPS spectrometer. The spectra were acquired using a monochromatic Al $K_\alpha$ X-ray source (1486.6 eV). The curve fitting on core-level spectra was carried out using CasaXPS software. The details of XPS analysis including constraints used for fitting can be found in the following session.

#### **4.2.6.6** *X-ray Photoelectron Spectroscopy (XPS) analysis of Mo 3d core-level peaks*

The deconvolution of Mo 3d spectra has always been challenging since the binding energies of several components are very close to each other. It is even more complicated in our case since the degraded samples consist of a mixture of 1T and 2H polymorph $MoS_2$ as well as

oxidized $MoO_x$ species. The XPS spectra were obtained on powders prepared by freeze-drying the dispersions. To analyze the XPS data, we firstly calibrated the spectra using carbon 1s core-level spectra at 284.8 eV. Then we used Shirley background subtraction followed by fitting the Mo 3d core-level with Gaussian-Lorentzian line shapes using the constrains summarized in Table 4.1. All of the spectra were fitted with a residual less than 1.5 except the one obtained from LiOH/air/light/Day 7 (residual = 2.3) which could due to the high content of oxidized Mo content. One may notice that we did not set the FWHM of each spin-orbital splitting coupling to be equal. This is because in Scanlon D. *et al.*'s study of electronic structure of $MoO_2$ and $MoO_3$, they showed that Mo $3d_{5/2}$ has smaller FWHM value than Mo $3d_{3/2}$.[155] In fact, this rule is also found in the XPS analysis of other transition metal compounds.[156] Hence, we decided to apply this rule to our analysis as well.

**Table 4.1 Summary of fitting constrains for XPS analysis.**

| | |
|---|---|
| position constraint | A: 1T Mo $3d_{5/2}$: (228.2, 228.4)<br>B: 1T Mo $3d_{3/2}$: B = A + 3.15 eV<br>C: 2H Mo $3d_{5/2}$: C = A + 0.7 eV<br>D: 2H Mo $3d_{3/2}$: D = A + 0.7 + 3.15 eV<br>E: Mo (VI) $3d_{5/2}$: (232.5, 232.6)<br>F: Mo (VI) $3d_{3/2}$: (235, 236)<br>G: $MoO_2$ Mo $3d_{5/2}$: (230.0, 232.2)<br>H: $MoO_2$ Mo $3d_{3/2}$: (233.1, 233.5) |
| fwhm constraint | A: 1T Mo $3d_{5/2}$: (0.8, 1)<br>B: 1T Mo $3d_{3/2}$: (0.85, 1.1); B≥A<br>C: 2H Mo $3d_{5/2}$: (0.8, 1)<br>D: 2H Mo $3d_{3/2}$: (0.85, 1.2); D≥C<br>E: Mo (VI) $3d_{5/2}$: (0.7, 2)<br>F: Mo (VI) $3d_{3/2}$: (0.7, 2); F≥E<br>G: $MoO_2$ Mo $3d_{5/2}$: (0.7, 2)<br>H: $MoO_2$ Mo $3d_{3/2}$: (0.7, 2); H≥G |
| area constraint | A: 1T Mo $3d_{5/2}$: N/A |

| | |
|---|---|
| | B: 1T Mo $3d_{3/2}$: A * 2/3<br>C: 2H Mo $3d_{5/2}$: N/A<br>D: 2H Mo $3d_{3/2}$: C * 2/3<br>E: Mo (VI) $3d_{5/2}$: N/A<br>F: Mo (VI) $3d_{3/2}$: E * 2/3<br>G: $MoO_2$ Mo $3d_{5/2}$: N/A<br>H: $MoO_2$ Mo $3d_{3/2}$: G * 2/3 |

## 4.3 Results and Discussion

The fresh stock dispersions resulting from the chemical exfoliation of $MoS_2$ in water initially appeared black in color.[104,108,154] Our procedure results in a mixture of ~68% 1T-$MoS_2$ with the remainder in the more thermodynamically stable 2H polymorph as is typically reported by others.[68,72] The pH of the resulting solution is ~11.5 due to the generation of LiOH (and $H_2$) which results when lithium intercalated $MoS_2$ is exposed to water. This is the typical starting point for most reports which use chemical exfoliation procedures in the literature[91,92,104] and the following sections will explore the chemical changes occurring with time upon exposure of the resulting $MoS_2$ to different environments.

### 4.3.1 Effect of pH on 1T-$MoS_2$ stability.

As shown in Figure 4.1, by storing freshly prepared 1T-$MoS_2$ (pH ~ 11.5) on the lab with constant exposure to ambient air and ambient light, we noticed that after several weeks of storage, these initially dark samples became a translucent yellowish color. To create a more controlled environment, in the first case to be discussed, all samples were stored under controlled ambient light (two florescence lamps in a closed cabinet). Also, no special precautions were used to eliminate dissolved oxygen from the samples as they were processed under ambient conditions initially (i.e., exposed to air). Analysis by UV-Vis spectroscopy (Figure 4.1b) indicates a sharp increase in the absorbance at 209 nm (with a shoulder peak at ~230 nm) in the alkaline (LiOH, pH ~ 11.5) samples after 7 days, while only a slight increase of absorbance at this wavelength was observed in samples which had been washed and stored in Milli-Q water (neutral samples) over the same time period. This distinct absorbance peak at 209 nm is near the peak known to be associated with aqueous solutions of molybdates ($MoO_4^{2-}$).[157] This suggests that part of the observed degradation may be associated with the oxidation of molybdenum (from Mo(IV) to Mo(VI)) where $MoS_2$ forms soluble molybdate ions. The formation of soluble Mo is confirmed using XPS and the results are shown in the later discussion. The oxidation and oxygen substitution in $MoS_2$ were confirmed by performing FTIR on the aged samples. The spectra of fresh and 7-day-aged Milli-Q samples (orange curves in Figure 4.1c) were largely the same, while significant features were observed in the basic samples (blue curves in Figure 4.1c) at 820 $cm^{-1}$, 995 $cm^{-1}$,

which indicates the formation of O–Mo–O and Mo=O bonds, respectively.[158,159] In addition, the absorption band at 1120 $cm^{-1}$ indicates the formation of S=O bonds. In fact, Sugioka *et al.* suggested this FTIR absorption band (1120 $cm^{-1}$) could also indicate the formation of sulfate ($SO_4^{2-}$).[160] This suggests that dissolution of sulfur could be part of the degradation result and this is in an agreement with Zhang *et al.*'s observation that sulfate ions are produced when bulk $MoS_2$ is directly exposed to water. Raman spectroscopy was also performed on the samples. However, we did not observe any significant features in the 7-days-aged alkaline (LiOH, pH ~ 11.5) samples (Figure 4.1d); this is in line with the conclusion by Zhang *et al.* that Raman spectroscopy is not a sensitive detection method for identifying oxidation in $MoS_2$.[151] Nonetheless, Raman results show strong evidence of 1T polymorph remaining in the one-week-aged alkaline (LiOH, pH ~ 11.5) samples (orange curve). The changes in the 2H/1T ratio are shown in Table 4.2. The ratio was estimated using the method based on UV-Vis result presented by Knirsch *et al.*[108] This method estimates an increase in 2H content of only 2-3% for both the alkaline and neutral cases over the course of 7 days.

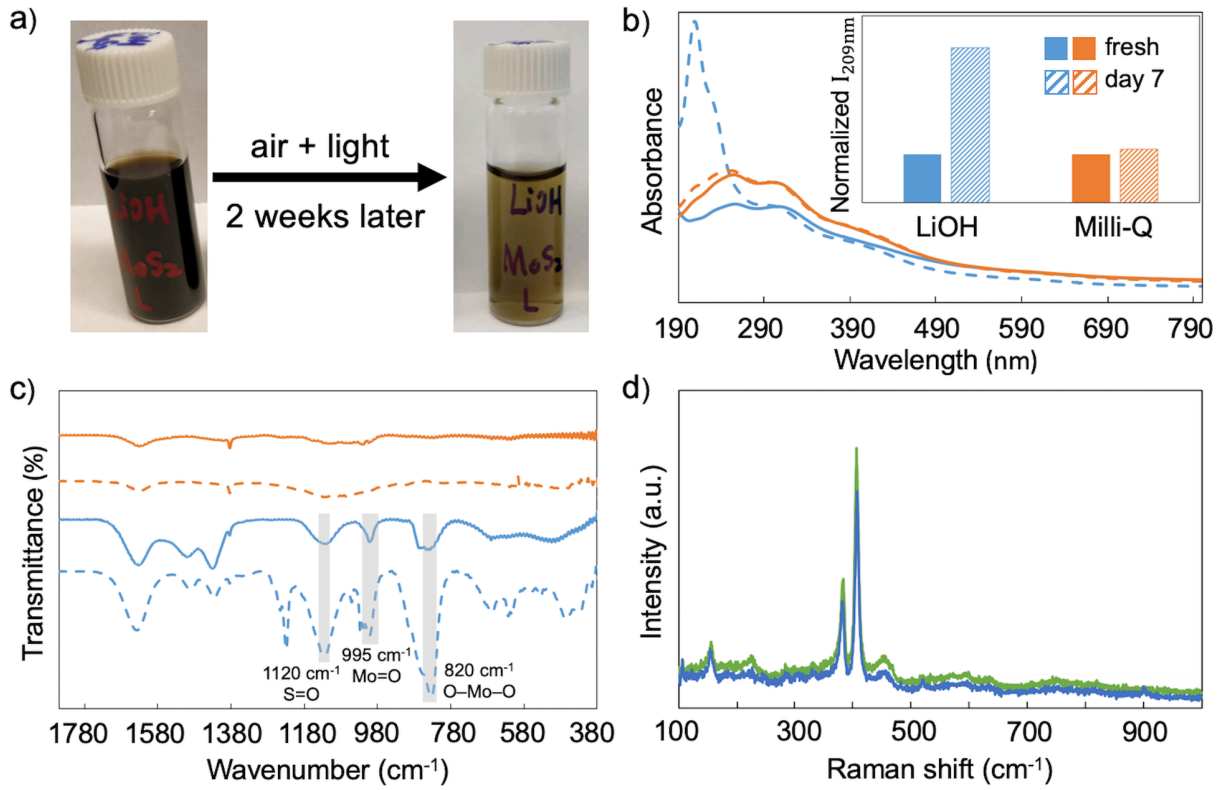



**Figure 4.1 Study of pH effect**. (a) Photograph of color changes in 1T-$MoS_2$ alkaline dispersion after storing on the lab bench with constant exposure to ambient light and air for two weeks. (b) UV-Vis spectra and (c) FTIR spectra of 1T-$MoS_2$ dispersion stored in LiOH (blue curves) and Milli-Q water (orange curves) that were freshly made (solid

lines) and stored under light (dashed line) for 7 days. Inset in (b) shows normalized absorbance at 209 nm for LiOH and Milli-Q samples. Note that all UV-Vis curves are normalized to 305 nm of the corresponding fresh samples and all samples are stored in an ambient air environment. (d) Raman spectra of LiOH samples that were freshly made (light green) and stored under light, had been exposed to air and aged under these conditions for 7-days (navy blue).

**Table 4.2 Changes in 2H/(2H+1T) with time estimated by UV-Vis (and XPS)**

| Sample | LiOH/light/air | Milli-Q/light/air |
|---|---|---|
| Fresh | 32% (32%) | 32% |
| Day 7 | 34% (33%, after filtration) | 35% |

Continued degradation was observed in alkaline (LiOH, pH ~ 11.5) samples, while precipitation of $MoS_2$ nanosheets (Figure 4.2 inset) were found in neutral (Milli-Q) cases with the supernatant displaying a light-yellow color which later on turned blue. The precipitation phenomenon was observed and studied by Nurdiwijayanto *et al*.[154] It is also worth to point out that strong absorption was detected in the blue supernatant in the UV region (Figure 4.2).

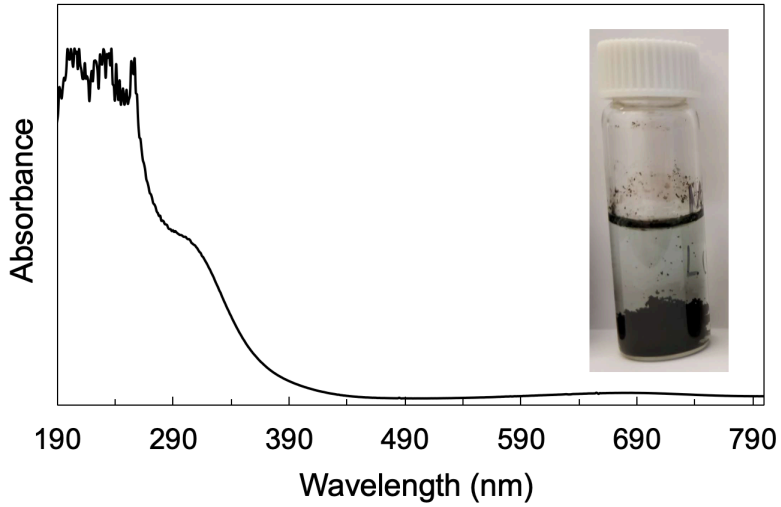



**Figure 4.2 UV-Vis spectra of two-weeks aged Milli-Q samples when stored in air and under light.** The inset shows an image of an aged Milli-Q sample (with starting concentration of 1.5 mg/mL) with precipitated sheets and light blue supernatant after two weeks.

Simply by preparing the fresh sample at a more diluted concentration, the precipitation effect can be reduced. Figure 4.3 shows the absorbance changes of diluted samples (~ 0.7 mg/mL) in neutral and alkaline cases. With exposure to ambient light and air for 12 days, neutral (Milli-Q) samples began to show noticeable degradation indicated by the increase in absorbance at 209 nm in the UV-Vis spectra, while steady and stronger degradation was observed in alkaline (LiOH, pH ~ 11.5) samples. The overall degradation rate is summarized as a histogram in the Figure 4.1b inset

and Figure 4.3 inset. It is clear that alkaline media can enhance the degradation in 1T-$MoS_2$ aqueous dispersion when samples are directly exposed to ambient air and light.

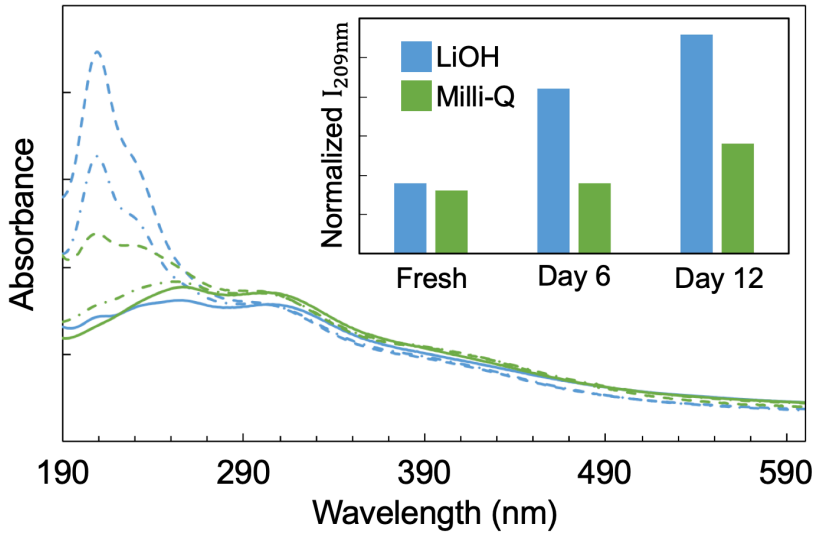



**Figure 4.3 Impact of dispersion concentration of the fresh samples**. UV-Vis spectra of diluted 1T-$MoS_2$ dispersion (~ 0.7 mg/mL) in LiOH (blue curves) and Milli-Q water (green curves) that were freshly made (solid lines) and were stored under light and air for 6 days (dash dotted line) and 12 days (dashed line). Note that all UV-Vis results are normalized to 305 nm of the corresponding fresh sample. Inset shows the corresponding normalized absorbance changes at 209 nm for LiOH and Milli-Q samples.

### 4.3.2 Ambient light-accelerated degradation

After observing significant degradation under alkaline conditions, we then looked at the effect of ambient light (two florescence lamps in a closed cabinet). To the naked eye, while the 7-day old samples stored under illumination appeared the same as those stored in the dark, there was a significant fading in the color of the dispersion for samples stored under illumination were diluted with the same amount of Milli-Q water (Figure 4.4a). The effect was the same irrespective of whether the pH was adjusted using LiOH or KOH even though it was shown by Nurdiwijayanto *et al.* that Li-ion concentration has impact on restacking behavior of 1T-$MoS_2$ in aqueous dispersion.[154] The UV-Vis spectra shown in Figure 4.4b and 4.4c, indicate an increase in the peak absorbance around 209 nm after 7 and 14 days for both LiOH (pH = 11.54) and KOH (pH = 11.60) cases, regardless of whether the samples were stored under light (blue and brown curves), or in the dark (purple and dark red curves). However, it was obvious that illumination induces a two-fold absorbance increase in alkaline samples compared to those stored in darkness (see the insets in Figure 4.4b and 4.4c). Furthermore, we observed a slightly faster degradation in LiOH compared

to KOH regardless of the illumination condition, suggesting that the cation of the base also has some effect. The exact nature of this effect is left for future work.

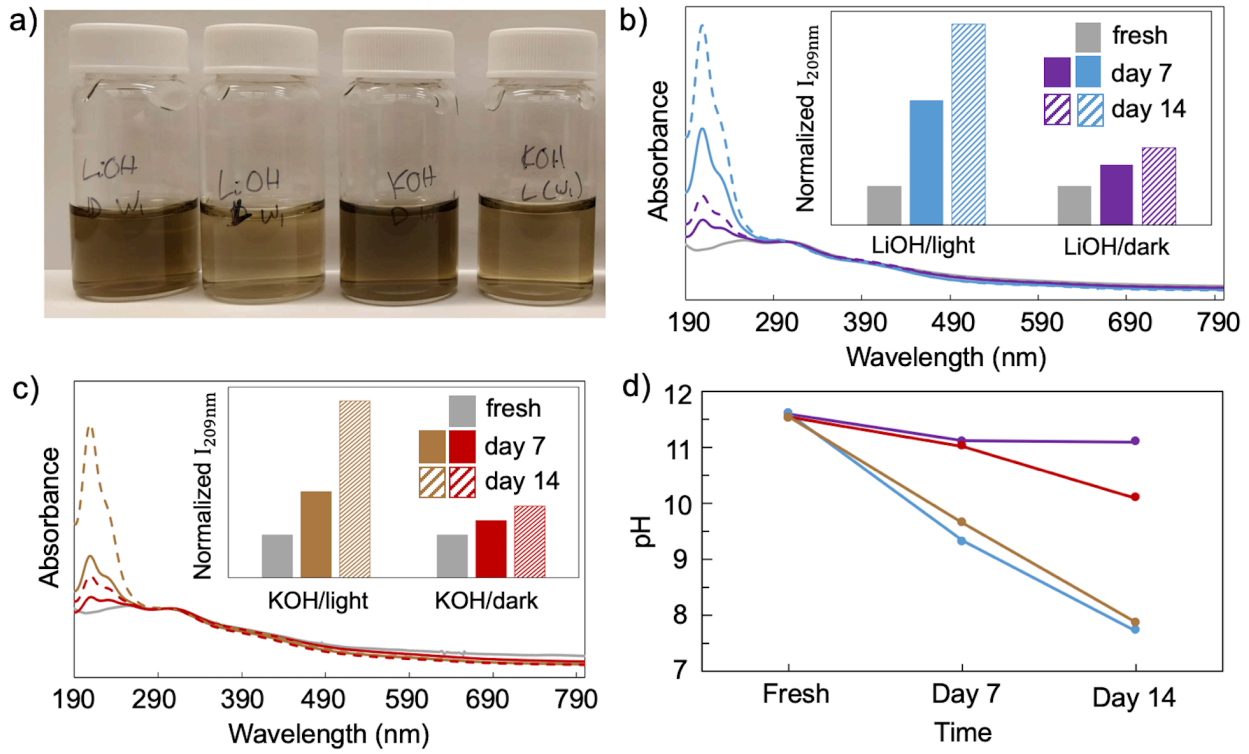



**Figure 4.4 Light-induced rapid degradation of 1T dominated $MoS_2$ in basic aqueous dispersion.** (a) Photograph of color changes in basic samples after being stored with and without light illumination for one week. All four samples were dilute with the same amount of Milli-Q water on the 7th day. The four samples were (from left to right) LiOH samples under dark (LiOH/dark) and light (LiOH/light) and KOH samples under dark (KOH/dark) and light (KOH/light). (b) UV-Vis spectra of 1T-$MoS_2$ dispersion in LiOH (pH ~ 11.5) that were freshly made (grey lines) and stored under light (blue) and dark (purple) for 7 days (solid line) and 14 days (dashed line). (c) UV-Vis spectra of 1T-$MoS_2$ dispersion in KOH (pH ~ 11.6) that were freshly made (grey lines) and were stored under light (brown) and dark (dark red) for 7 days (solid line) and 14 days (dashed line). Insets in both (b) and (c) indicate the normalized absorbance at 209 nm for the various samples. (d) Corresponding pH changes for LiOH/dark (purple), KOH/dark (dark red), KOH/light (brown) and LiOH/light (blue). Note that all UV-Vis results were normalized to 305 nm of the corresponding fresh sample and all samples were stored after exposure to air

A more quantitative investigation of chemical changes involved in the aging process was conducted using X-ray photoelectron spectroscopy (XPS). The result, with corresponding fitted curves, of freshly prepared vs. 7-days-degraded (light-accelerated) 1T-$MoS_2$ samples is shown in Figure 4.5. Compared to the 2H polymorph $MoS_2$ (green curve) obtained from the bulk $MoS_2$ powder (Figure 4.6), the fitted result of Mo 3d core level spectra obtained in freshly prepared 1T-$MoS_2$ shows that the binding energy of Mo(IV) $3d_{5/2}$ and Mo(IV) $3d_{3/2}$ shifts to a lower value by ~0.7 eV for the 1T polymorph $MoS_2$ (red curve). This is very close to what has been observed

previously.[91,104,108] As for the aged sample, the fitted results, summarized in Table 4.3, show close to two-fold increase of total detected Mo(VI) and Mo(IV)$O_2$ species in the light-illuminated samples (~34%) than the one in the dark samples (~18%). As expected, the formation of these species was accompanied by the depletion of peaks corresponding to $MoS_2$ (1T and 2H). We also measured significant pH drops (Figure 4.4d) in all of the basic samples, where samples under illumination had more severe pH decreases (blue and brown dots in Figure 4.4d). This suggested that the degradation must form acidic species which consumes $OH^-$ ions leading to a dramatic decrease in dispersion pH.

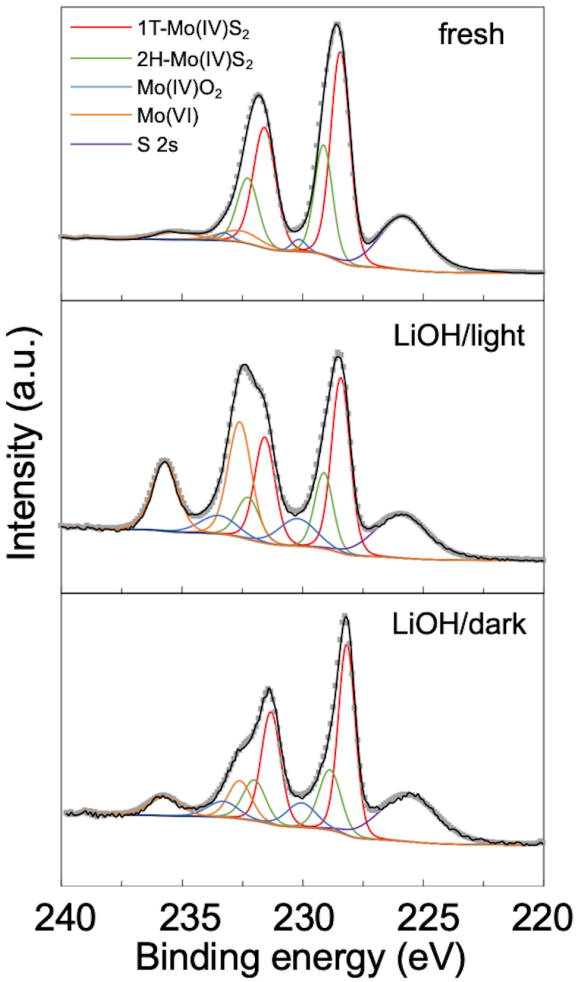



**Figure 4.5 XPS results of fresh, LiOH/light and LiOH/dark samples**. XPS Mo 3d core level spectra (black curve) and corresponding fitted curves for individual components including 1T polymorph Mo(IV)$S_2$ (red), 2H polymorph Mo(IV)$S_2$ (green), Mo(IV)$O_2$ (blue) and Mo(VI) (orange) for freshly prepared 1T-$MoS_2$ samples as well as 7 days aged LiOH samples stored under light (LiOH/light) and under dark (LiOH/dark). Note that the black curve shows raw data and grey squares show the overall fitted curve.

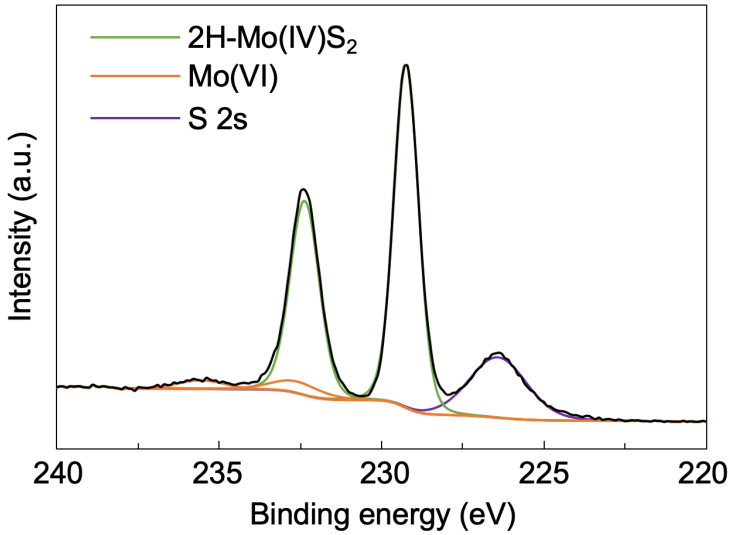



**Figure 4.6 XPS results of bulk $MoS_2$ powder.** XPS Mo3d core level spectra of 2H $MoS_2$ bulk powder (black curve) and corresponding fitted curves for individual components including 2H polymorph Mo(IV)$S_2$ (green), Mo(VI) (orange).

**Table 4.3 Percentage of the individual component estimated by the integrated areas of the fitted Mo 3d core level spectra.**

| Sample | 1T-$MoS_2$ | 2H-$MoS_2$ | Mo(VI) | Mo(IV)$O_2$ | 2H/(1T+2H) ratio | Mo(VI)+ Mo(IV)$O_2$ |
|---|---|---|---|---|---|---|
| $MoS_2$ powder | 0% | 93% | 7% | 0% | 1 | 7% |
| Fresh 1T-$MoS_2$ | 61% | 29% | 7% | 3% | 0.32 | 10% |
| LiOH/light/Day 7 | 39% | 17% | 32% | 12% | 0.30 | 44% |
| LiOH/dark/Day 7 | 52% | 22% | 14% | 12% | 0.30 | 28% |
| LiOH/light/Day 7 (after filtration) | 58% | 29% | 4% | 9% | 0.33 | 17% |
| LiOH/dark/Day 7 (after filtration) | 60% | 29% | 4% | 7% | 0.33 | 11% |

With regards to the Milli-Q samples, the chemical changes due to degradation are slower and aggregation of the dispersion dominates the long-term aging process. By preparing the fresh sample in a more dilute concentration (~ 0.7 mg/mL), we observed faster precipitation and the supernatant appears transparent in Milli-Q samples when stored under light. After storing the Milli-Q samples under light for 18 days, precipitation was observed near the bottom of the vial. By recording the UV-Vis spectra of the supernatant, a strong absorption in the UV region was obtained while significant decrease was observed after 305 nm (see the red curve in Figure 4.7a). This confirmed that majority of the $MoS_2$ sheets were settled out from the solution. By contrast,

the samples stored in the dark remain partially dispersed with nearly no absorption peak shown at 209 nm. Thus, when samples are stored in the ambient air, light irradiation can result in more degradation as well as faster precipitation of 1T-$MoS_2$ sheets in the Milli-Q water. Currently, the reason for this remains unknown. However, the mechanism behind this enhanced precipitation under light irradiation remains unknown.

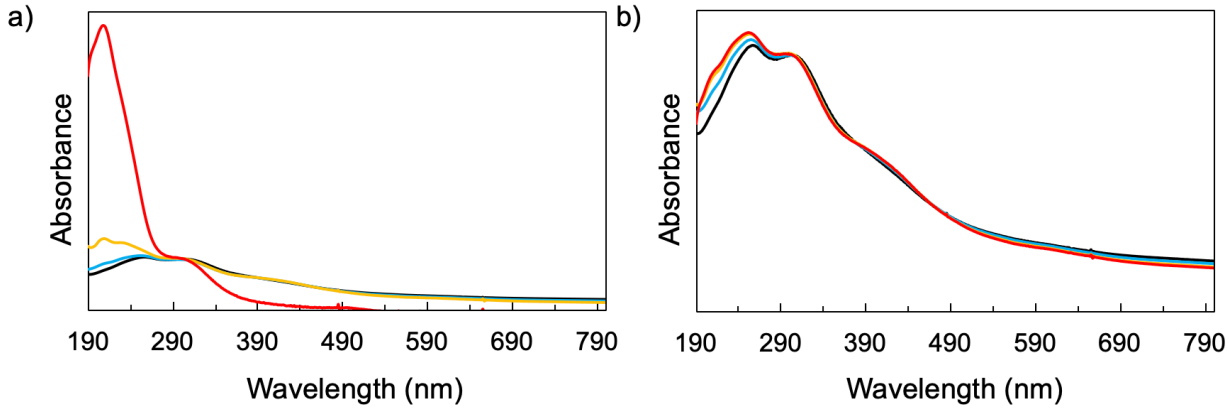



**Figure 4.7 Settlement of nanosheets in diluted 1T-$MoS_2$ dispersion facilitated by light exposure**. UV-Vis spectra of diluted 1T-$MoS_2$ dispersion (~ 0.7 mg/mL) in Milli-Q water with (a) and without (b) light exposure that were freshly made (black lines) and were stored for 6 days (blue lines), 12 days (yellow lines) and 18 days (red lines). Note that all UV-Vis results are normalized to 305 nm of the corresponding fresh sample and all of the samples were stored in the air environment.

### 4.3.3 Influence of oxygen on degradation process.

As oxidized $MoS_2$ was detected as one of the major degradation products, we suspected that dissolved $O_2$ plays a crucial role in the degradation process. Therefore, we studied the aging of deoxygenated dispersions in both basic and neutral condition as well as with and without light exposure. The experiment was carried out by purging freshly prepared stock dispersions with $N_2$ followed by distributing the dispersion into separated vials which were tightly sealed until the day they were set to be analyzed (one sample per desired day in each case). The UV-Vis spectra and the inset plot in Figure 4.8 show that deoxygenating the dispersion significantly suppresses the degradation compared to the results discussed above where dispersions were exposed to air (Figure 4.1b and Figure 4.4b).

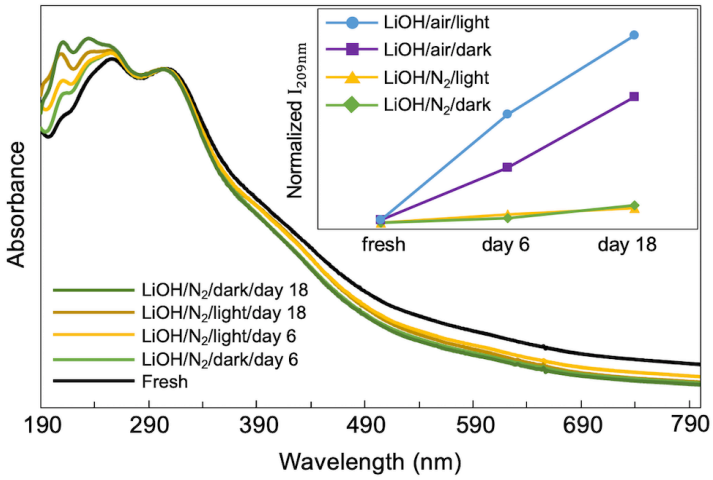



**Figure 4.8 Influence of oxygen on degradation process – $O_2$ environment**. UV-Vis spectra of deoxygenated, 1T-$MoS_2$ alkaline dispersions that were: freshly made (black curve), stored under $N_2$ with light irradiation for 6 days (yellow curve), 18 days (darker yellow curve) and others stored in the dark for 6 days (green curve) and 18 days (darker green curve). Inset shows the normalized absorbance at 209 nm for 1T-$MoS_2$ dispersions in alkaline media. Note that all of the UV-Vis results were normalized to the absorbance at 305 nm of the corresponding fresh samples.

However, even after inert gas purging, the aging effect cannot be completely eliminated under basic conditions even in the absence of light. On the other hand, as shown in Figure 4.9, an inert gas environment led to negligible changes in the Milli-Q samples (at a concentration of ~0.7 mg/mL). Furthermore, deoxygenated Milli-Q samples remained dispersed in the water. Thus, we conclude that oxygen is the main driving force for the degradation and even when the oxygen content is low, alkaline conditions can still have an impact even over the course of a few weeks.

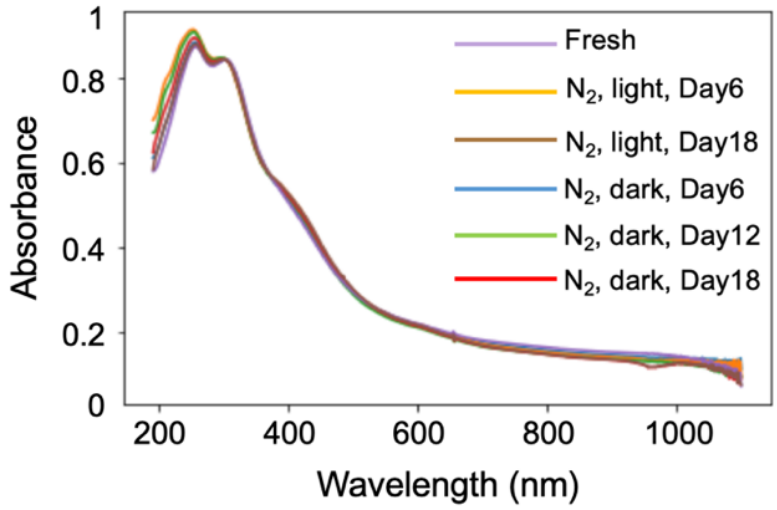



**Figure 4.9 Influence of oxygen on degradation process – $N_2$ environment.** Negligible changes in UV-Vis spectra of diluted 1T-$MoS_2$ dispersion (~ 0.7 mg/mL) in Milli-Q water under corresponding storage

conditions indicated in the graph. Note that all of the UV-Vis results were normalized to 305 nm of the fresh sample.

### 4.3.4 Insights on the enhanced degradation of 1T-$MoS_2$ dispersion by alkaline media and ambient light irradiation.

Thus far, we have demonstrated the degradation products including: 1). Oxidation and dissolution of Mo, forming $MoO_4^{2-}$ indicated by the distinct absorption peak at 209 nm; 2). Oxygen substitution indicated by FTIR and XPS likely forming $MoO_2$ and other Mo(VI) species. To further confirm that the dissolution of Mo is the majority degradation/oxidation product from the 1T-$MoS_2$ dispersion, the aged 1T-$MoS_2$ dispersion was filtered through a 0.1 μm polyvinylidene fluoride membrane. The UV-Vis spectra of original degraded dispersion, filtrate and rinsed and re-dispersed filter cake are shown in Figure 4.10a. It is clear that the distinct absorption peak at 209 nm, which is associated with molybdate ions ($MoO_4^{2-}$),[157] is only observed in the filtrate (green curve) but not in the filtered dispersion (blue curve). Furthermore, the XPS spectra were recorded on the filtered $MoS_2$ samples and the fitted results of Mo 3d core level spectra on the corresponding samples aged under light and in the dark are shown in Figure 4.10b and 4.10c, respectively, with the fitted results summarized in Table 4.3. Compared to the entire degradation product of $MoS_2$ discussed above with regards to Figure 4.5, the calculated Mo(VI) content, which should mostly be $MoO_3$ after the filtration, is reduced from 32% to 4% with light and from 14% to 4% without light. This, together with the distinct absorption peak at 209 nm in the UV region, confirms that majority of the degradation/oxidation product are molybdate ions.

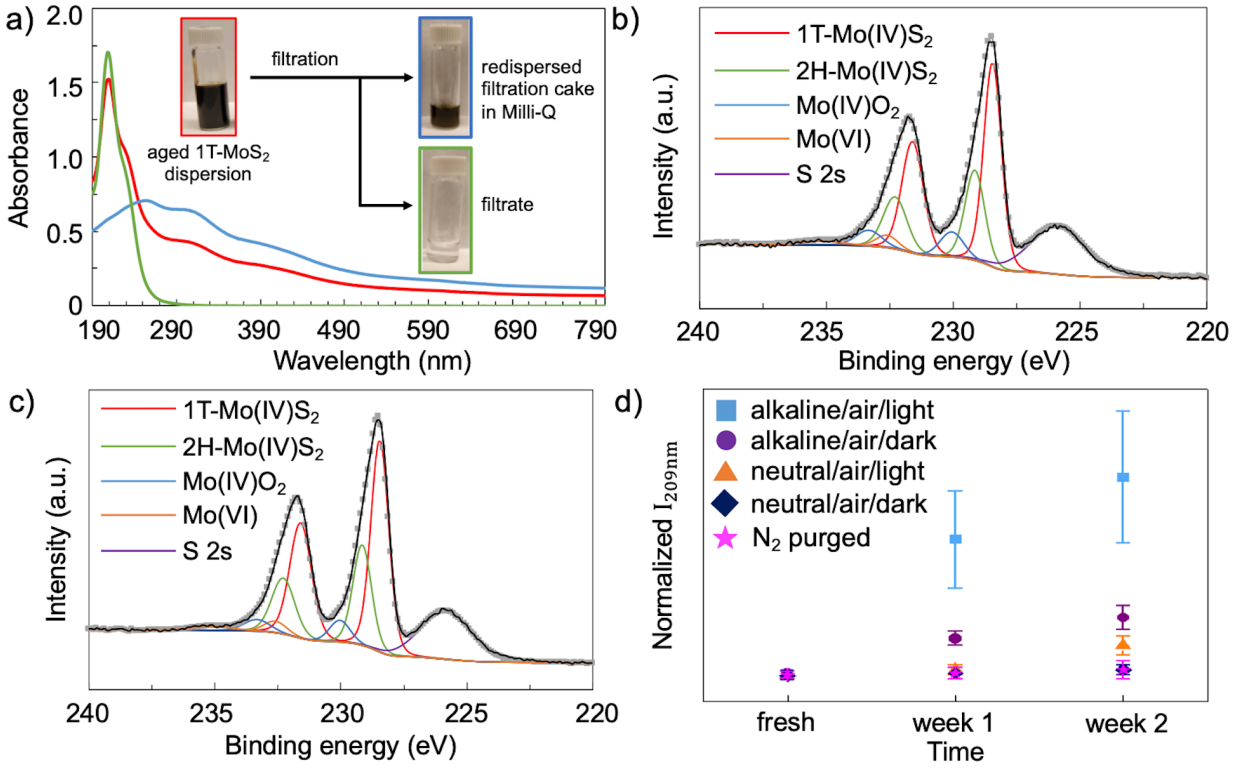



**Figure 4.10 Analysis of the solid and soluble degradation products and comparison of degradation rates.** (a) Absorption spectra of 7-days-aged 1T-$MoS_2$ basic dispersion (red curve), its filtrate (green curve) and re-dispersed filter cake (blue curve) with the photos of these three samples shown in the inset. XPS Mo 3d core level spectra (black curve) and corresponding fitted curves for individual components including 1T polymorph $Mo(IV)S_2$ (red), 2H polymorph $Mo(IV)S_2$ (green), $Mo(IV)O_2$ (blue) and Mo(VI) (orange) for re-dispersed filter cake of 1T-$MoS_2$/LiOH samples stored under light (b) and in darkness (c) after 7 days. Note that the black curve shows raw date and grey squares show the overall fitted curve. (d) Overview of relative degradation rates as indicated by the normalized absorbance at 209 nm under various conditions. Error bars indicate the standard deviation of measurements taken from samples prepared from at least 3 separate batches.

The morphology changes were investigated by obtaining atomic force microscopy (AFM) images of freshly prepared 1T-$MoS_2$ and aged products in the alkaline dispersion stored in air with ambient light exposure over 3 weeks. As shown in Figure 4.11a and 4.11b, two dimensional sheets were observed in the freshly prepared dispersion while fragments and aggregates were observed in the aged dispersion.

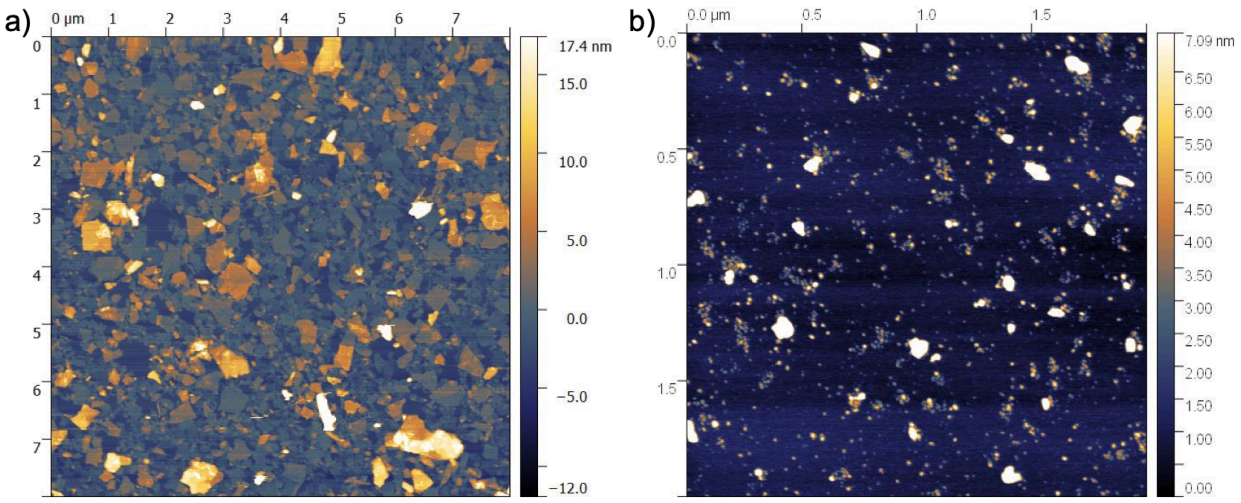



**Figure 4.11 Morphology changes in 1T-$MoS_2$ sheets after degradation.** Contact mode AFM images of (a) Langmuir film of freshly prepared 1T-$MoS_2$ dispersion and (b) aged dispersion stored in alkaline media (LiOH, pH ~ 11.5) with exposure to ambient air and light over 3 weeks. The method for preparing the Langmuir film of freshly made 1T-$MoS_2$ dispersion can be found in ref.[61] and spin-coating was used to prepare the AFM sample of degraded dispersion. Both samples were prepared on atomically flat muscovite mica (SPI) substrates.

Even though the degradation results in oxidation and oxygen substitution regardless of the conditions, the degradation rate of 1T-$MoS_2$ dispersion in water varies depending on the environment. Figure 4.10d summarizes the degradation rate indicated by the growth of normalized absorption at 209 nm under all of the cases studied in this work. As shown in the previous discussion, by degassing the dispersion using $N_2$, one could effectively slow down the degradation. This, again, indicates that oxygen is the main criteria for the degradation to happen but once oxygen is introduced to the system, light irradiation and alkaline media are able to significantly accelerate the degradation effect. Here, we attempt to propose the mechanism behind this enhanced degradation induced by these two factors.

As shown in the Figure 4.10d, even when samples were stored under dark, the degradation of 1T-$MoS_2$ can be enhanced noticeably under the alkaline condition. This suggests that alkaline condition favors the oxidation and in fact alkaline media is commonly used to accelerate oxidation of $MoS_2$ in pressure oxidative leaching (high pressure, high temperature) of molybdenite ($MoS_2$) and when $MoS_2$ is exposed to basic media, where $OH^-$ ions can directly react with $MoS_2$ forming thermally stable $MoO_4^{2-}$.[161] This process can be expressed by:

**Scheme 4.1 Oxidation under alkaline conditions:**

$$MoS_2 + 6OH^- + 4.5O_2 \rightarrow MoO_4^{2-} + 2SO_4^{2-} + 3H_2O \quad (4.1)$$

Even though the degradation in our case is observed under ambient temperature and pressure, enhanced oxidation by $OH^-$ ions could still happen considering that it results in forming the most stable molybdenum species, $MoO_4^{2-}$ in the aqueous solution. In addition to that, a significant drop in pH was observed in the alkaline case which can be attributed to this reaction.

On the other hand, as shown in Figure 4.10d, light exposure dramatically accelerated the degradation in both alkaline (comparing blue squares with purple circles) and neutral (comparing orange triangles with navy rhombuses) cases. This enhanced oxidation effect could be due to the formation of reactive oxygen species (ROS) such as superoxide which has been reported previously in both 2H and 1T $MoS_2$.[162,163] The generation of ROS upon exposure to light and their effect on $MoS_2$ can be expressed by (only oxidized Mo is presented as the degradation product):

**Scheme 4.2 Photo-induced generation of superoxide**

$$2H\ MoS_2 + h\nu \rightarrow 2H\ MoS_2\ (h^+/e^-) \quad (4.2)$$

$$1T\ MoS_2 + h\nu \rightarrow 1T\ MoS_2\ (e^-) \quad (4.3)$$

$$O_2 + e^- \rightarrow O_2^{\bullet-} \quad (4.4)$$

$$H_2O + h^+ \rightarrow 2H^+ + 1/2\ O_2 \quad (4.5)$$

To prove that the degradation involves the formation of the superoxide radical, benzoquinone (BQ) was chosen as the superoxide scavenger, which is one of the most commonly used molecules for this purpose.[164] The reduction of BQ to hydroquinone (HQ) has a potential at vacuum level of -5.2 eV which is sufficient to accept an electron from superoxide. To carry out the experiment, a solution of 10 mmol/L BQ was mixed with freshly prepared 1T-$MoS_2$ dispersion at a volume ratio of 1:1 and then distributed into individual vials followed by storing under the condition of LiOH-based alkaline/air/light. As shown in Figure 4.12a, the strong absorbance from BQ with a maximum at 244 nm was observed in the freshly prepared sample. Within the first 24 hrs, the intensity decreased at 244 nm indicating the reduction of BQ and meanwhile an increase in HQ was measured according to the absorption band around 296 nm (Figure 4.12a inset). In addition, the amount of remaining $MoS_2$ can be monitored by following the intensity at 350 nm (strong contribution from 1T $MoS_2$ with local minimum in 2H [108]), considering that both BQ and HQ do not contribute to significant changes of the absorption above 300 nm. Unfortunately, the high absorbance of BQ in the UV region prohibited accurate monitoring of molybdate generation

at 209 nm and thus this was not followed. Figure 4.12b demonstrates that while a significant amount of $MoS_2$ degraded under the condition alkaline/air/light over one week, only a very small amount of degradation was measured in the BQ 'protected' sample. This provides strong evidence to support our conclusion that photo-induced superoxide is formed and is largely responsible for the degradation observed. Note that the result remains the same when 410 nm (strong contribution from 2H $MoS_2$ [108]) was used to trace the amount of remaining $MoS_2$. In fact, we have noticed that the degradation rates are very similar for 1T and 2H polymorph $MoS_2$.

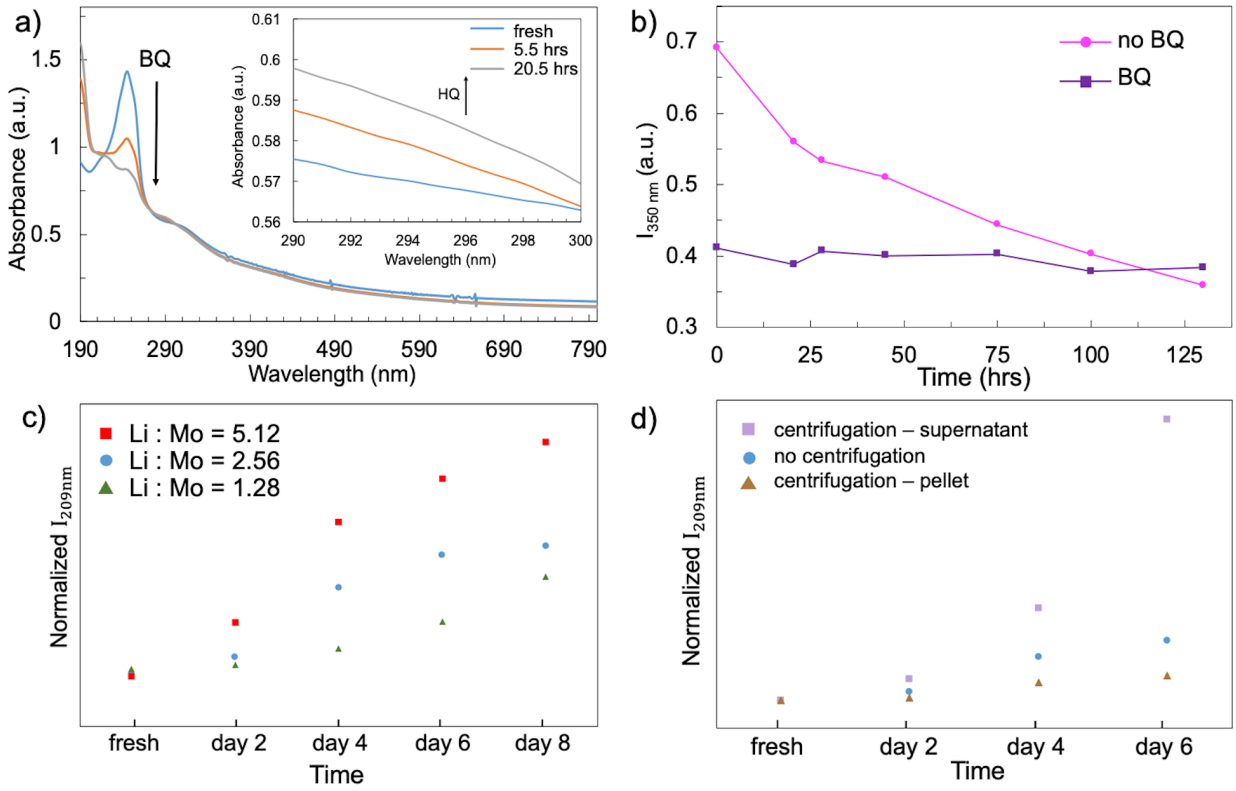



**Figure 4.12 Mechanism study of light-accelerated degradation of 1T-$MoS_2$ aqueous dispersion**. (a) UV-Vis spectra of 1T-$MoS_2$ in LiOH that were freshly prepared followed by addition of 10 mmol/L BQ at volume ratio of 1:1. The sample was stored under light after exposed to air. The measurement was conducted using the corresponding time intervals. Due to the difference in absorption coefficients, the absorption of hydroquinone is much weaker than that of benzoquinone. A magnification of the same spectra is shown in the inset in (a). (b) A plot of degradation resulted absorbance changes at 350 nm over the course of the first 130 hrs for the corresponding cases. Note that the two samples in (b) were prepared with different dilution factors resulting in difference in the initial absorbance. (c) Plot of normalized absorbance changes at 209 nm for 1T-$MoS_2$ dispersion preparing using various $MoS_2$/Li molar ratios in the intercalation step. The investigated ratios were indicated by the legends. (d) Plot of normalized absorbance changes at 209 nm for dispersions containing supernatant and pellet prepared by centrifugation at 3000 rpm as well as regular dispersion without centrifugation process. Defect studies in (c) and (d) were carried out under the condition of LiOH-based alkaline/air/light.

#### 4.3.4.1 *Degradation rate comparison for 2H and 1T $MoS_2$*

As shown in Table 4.3, XPS analysis shows similar degradation rate for 1T and 2H $MoS_2$ (comparing fresh and filtrated aged sample). In fact, in all cases we observe little to no change in the 1T/2H ratio which suggests that the oxidation process affects each polymorph in a similar way. In addition to that, the UV-vis results lead us to the same conclusion. Figure 4.13a shows the absorbance changes at 350 nm (strong contribution from 1T $MoS_2$ with local minimum in 2H) and 410 nm (strong contribution from 2H $MoS_2$) for 1T-$MoS_2$ dispersions stored in the LiOH based alkaline solution while also being exposed to air and light irradiation. It is shown that the intensities of these two representative wavelengths is reduced at a very similar rate. Based on first-order reaction kinetics (see detailed discussion in the next session), the calculated rate constants turn out to be nearly the same (0.0046 $hr^{-1}$ for 350 nm vs. 0.0047 $hr^{-1}$ for 410 nm) regardless of the representative absorbance we chose for analysis, as shown in the inset in Figure 4.13a. The degradation of supernatant samples (under the same condition of LiOH/air/light) were also analyzed and the absorbance changes at 350 nm and 410 nm were plotted in the Figure 4.13b with the corresponding natural logarithm of which shown in the inset. In this case, a slightly higher rate constant was observed for 1T vs. 2H (0.0171 $hr^{-1}$ for 350 nm vs. 0.0162 $hr^{-1}$ for 410 nm). However, the change was small and likely not significant. Thus, it seems that the degradation rates are constant between the polymorphs (at least within the time period we investigated) which suggests that the chemical attack is not dependent on the $MoS_2$ electronic properties. It also suggests that the superoxide is likely being generated at both material/solution interfaces as one might expect the concentration of high energy species to be higher locally, near the source.

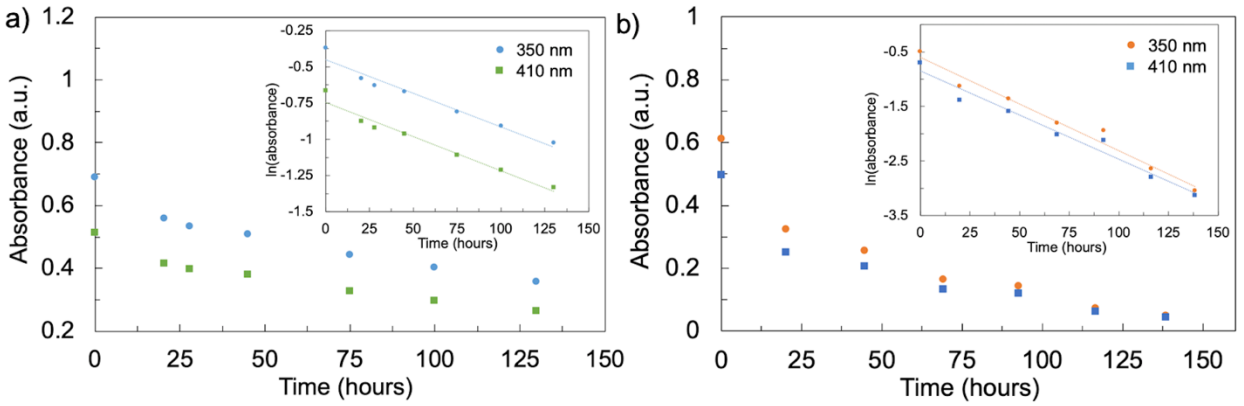



**Figure 4.13 Degradation of supernatant samples**. Absorbance at 350 and 410 nm over the course of the first 150 hrs: (a) regular/LiOH/air/light samples and (b) supernatant/LiOH/air/light samples. Insets in both (a) and (b) show the

natural logarithm of corresponding optical intensity against time. The $R^2$ in (a) equals to 0.96 for both cases and the $R^2$ in (b) equals to 0.97 and 0.98 for analysis based on 350 nm and 410 nm, respectively.

#### **4.3.4.2** *Kinetic study of 1T-$MoS_2$ aqueous degradation in air*

A more detailed kinetic study was carried out by tracing the absorption changes of the dispersions for several cases including LiOH/air/light, LiOH/air/dark, neutral/air/light and supernatant/LiOH/air/light over a shorter and more frequent time interval. Within the studied time period (about a week), only supernatant samples degraded almost completely where we observed dramatic color change from black to pale yellow. As shown in Figure 4.10a, the shape of UV-Vis spectra of remaining $MoS_2$ in water barely changes during degradation, we are able to trace the aging of $MoS_2$ by recording the intensity changes at a representative wavelength such as 410 nm (strong contribution from 2H $MoS_2$). Note that analysis based on 350 (strong contribution from 1T $MoS_2$ with local minimum in 2H) results in the same conclusion. The absorption changes at 410 nm over the course of 6 days, when the color of dispersion faded to pale yellow were plotted in Figure 4.14a. The exponential reduction over time indicates that the degradation is not a $0^{th}$ order reaction. The natural logarithm and the reciprocal of the optical intensity at 410 nm against time were presented in Figure 4.14b and 4.14c, respectively. The linearity of the results plotted as $ln(Abs)_t$ vs. $t$ strongly indicates that the degradation follows a (pseudo) first-order reaction rate law. The first-order rate law was also applied to other cases and the natural logarithm of absorbance against time for each case were plotted in Figure 4.14d. The $R^2$ of fitting, the calculated rate constants and half-lives for each case are summarized in Table 4.4. It is worth pointing out that the difference in the rate constant matches the trend we observed in the generation of molybdates as discussed in the main text (by following the normalized 209 nm peak). Note that the initial dispersion for all cases in this study were prepared at a concentration of ~ 0.5 mg/mL (the concentration of freshly prepared 1T-$MoS_2$ remains the same as all of the other batches, which is 1.5 mg/mL) and sediment was not observed in all cases over the course of one week. In addition to that, a replication with a different initial concentration (~ 0.7 mg/mL) of $MoS_2$ for the LiOH/air/light case showed a similar rate constant of 0.0048 $hr^{-1}$ ($R^2$ = 0.98).

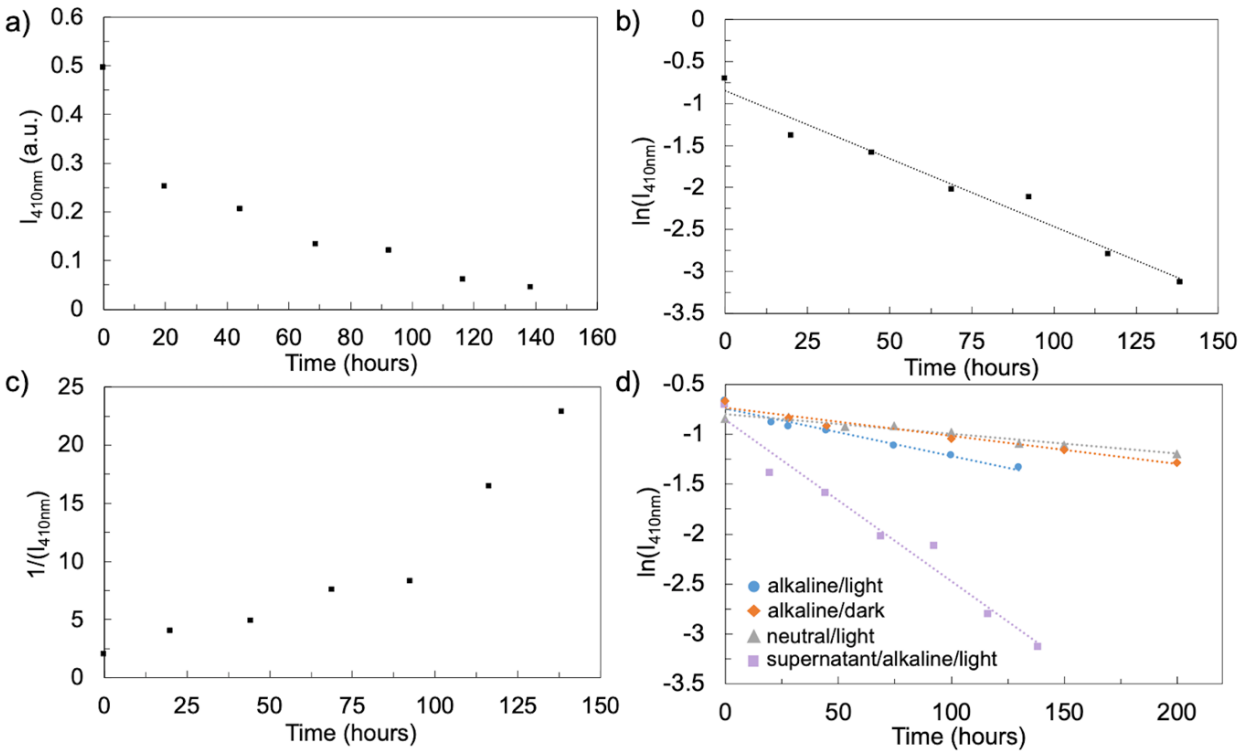



**Figure 4.14 Kinetic study of 1T-$MoS_2$ aqueous degradation in air.** (a) The decay behavior, (b) the natural logarithm and (c) the reciprocal of optical intensity at 410 nm versus time of 1T-$MoS_2$ supernatant samples stored in LiOH-based alkaline dispersion and under light irradiation. (d) Plot of natural logarithm of absorbance at 410 nm against time in cases indicated by the legend. Note that the time intervals are only approximately similar due to the limited access to characterization instruments. All of the samples were store in sealed vials after exposure to air.

**Table 4.4 Kinetic parameters extracted from first-order rate law**

| Condition | Half-life (hr) | Rate constant ($hr^{-1}$) | $R^2$ of fit |
|---|---|---|---|
| supernatant/LiOH/air/light | 43 | 0.0162 | 0.97 |
| LiOH/air/light | 147 | 0.0047 | 0.96 |
| LiOH/air/dark | 248 | 0.0028 | 0.96 |
| neutral/air/light | 347 | 0.002 | 0.96 |

The influence of sulfur vacancies and edge defects on the degradation was also investigated. The relative amount of sulfur vacancies was altered by varying the Li/$MoS_2$ molar ratio during chemical reduction[108] while the edge-defects were probed by selecting $MoS_2$ of different lateral size via centrifugation. The study was carried out under the condition of LiOH-based alkaline/air/light on 1T-$MoS_2$ dispersions. Figure 4.12c shows the changes of normalized absorbance at 209 nm over the course of the first 8 days for each case. Molybdate generation was

enhanced with higher Li/$MoS_2$ molar ratio which suggests that sulfur vacancies (naturally occurring after chemical exfoliation[165]) promote degradation. Figure 4.12d shows how the sheet size qualitatively affects the degradation rate. The supernatant sample which contained the smaller and thinner sheets was found to degrade the fastest followed by the non-sorted sample and with the pellet containing the larger and thicker sheets degrading the slowest. Since the smaller sheets have a higher ratio of edge-sites to basal plane-sites, these results suggest that degradation is also favored at higher energy edge-sites.

In order to determine the kinetics of $MoS_2$ degradation under various conditions, we followed the absorbance at 410 nm which was outside the range of the interfering molybdate peak at 209 nm. In all cases, the degradation over the course of the first week follows a pseudo first-order rate law (see Figure 4.14 and associated discussion). The rate constants and half-life of the $MoS_2$ under the various conditions are summarized in Table 4.4 above.

Figure 4.15 and eqn 4.1-4.8 illustrate the proposed mechanism for photo-accelerated oxidation of $MoS_2$ in alkaline aqueous solution for 1T-dominated $MoS_2$ dispersion. It is necessary to discuss both polymorphs since our 1T-dominated $MoS_2$ has ~ 30 % of 2H $MoS_2$ according to the estimation based on UV-Vis and XPS results. In 2H $MoS_2$, as the material absorbs light, an electron-hole pair is generated. The free electron can react with oxygen forming superoxide ($O_2^{\bullet-}$) as the conduction band of 2H $MoS_2$ is higher than the redox potential associated with the $O_2$/ $O_2^{\bullet-}$ reaction. On the other side, the redox potential of the $O_2/H_2O$ reaction is higher than the valance band of $MoS_2$ indicating that, thermodynamically, water can be oxidized by photo-generated holes ($h^+$). As the pH increases, the energy difference between the $O_2/H_2O$ half-cell reaction and the valance band energy of $MoS_2$ increases as well. This will enhance the possibility of water being oxidized by the free hole and thus favors the formation of superoxide. In 1T-$MoS_2$, which is the metallic polymorph, it is known that free electrons could be created via the photoelectric effect,[166] which could also result in generation of superoxide. The resulting superoxide from either of these processes could then form hydrogen peroxide which is a strong oxidizing agent (eqn 4.6). As mentioned, besides generating oxygen, the oxidation of water also creates protons (eqn 4.5) which could be involved in the reduction of superoxide to form hydrogen peroxide. Furthermore, as illustrated in eqn 4.7 and 4.8, the oxidation of $MoS_2$ forms soluble molybdate species under basic condition while acidic conditions (pH < 6) would form insoluble $MoO_3$.[151] This solubility may

explain why faster degradation is observed in alkaline conditions; while $MoS_2$ is being oxidized and dissolving into the solution, new vacancies and edge-like defect sites are created and exposed to $H_2O_2$ or related reactive oxygen species. In contrast, under conditions of neutral or slightly acidic pH, the degradation results in $MoO_3$ which remains bound to the $MoS_2$ surface.[151] This could act as a passivation layer which slows further degradation.

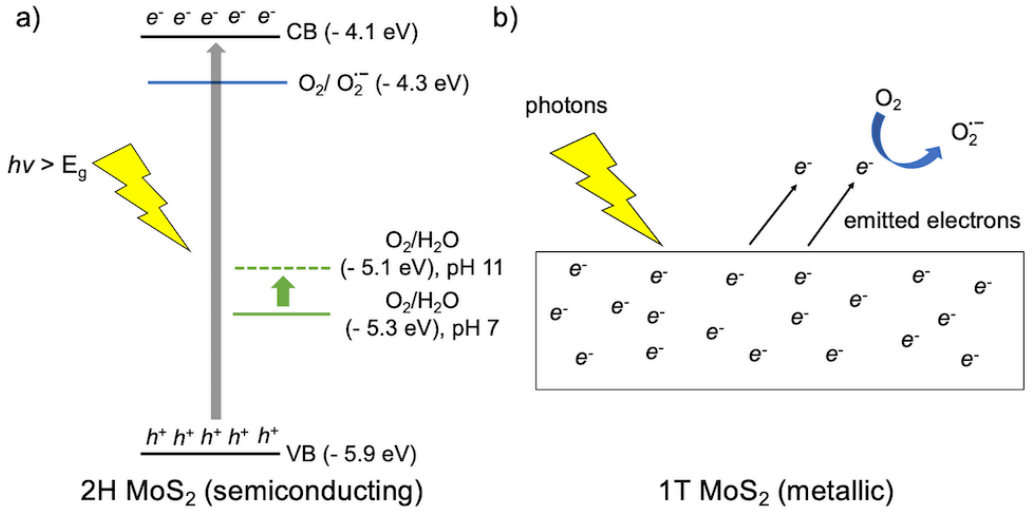



**Figure 4.15 Proposed mechanism of photo accelerated degradation in 1T dominated $MoS_2$ aqueous dispersion**. (a) Band alignment of single layer 2H $MoS_2$ (semiconducting) with redox potential of $O_2/O_2^{\bullet-}$ and $O_2/H_2O$ with specified pH condition. Note that the potential value is with respect to the absolute vacuum scale and 'CB' denotes conduction band and 'VB' denotes valence band. (b) Illustration of photoelectronic effect in metallic 1T-$MoS_2$.

**Scheme 4.3 Oxidation of $MoS_2$ by $H_2O_2$**

$$O_2^{\bullet-} + 2H^+ + e^- \rightarrow H_2O_2 \quad (4.6)$$

$$H_2O_2 + MoS_2 \rightarrow MoO_4^{2-} \quad (pH > 8) \quad (4.7)$$

$$MoO_4^{2-} + 2H^+ \rightarrow MoO_3{\cdot}H_2O \quad (pH < 6) \quad (4.8)$$

### 4.3.5 The improved spreading dispersion of *ce*-$MoS_2$ – Maximizing yields of monolayer sheets and 1T polymorph contents

To formulate the final spreading dispersion, the aqueous *ce*-$MoS_2$ (1T-$MoS_2$) has to be transferred into an organic solvent before mixing with DCE. Therefore, it is of great importance to investigate the optimal procedure to carry out this solvent exchange process. We first investigated the neutralization methods including using a dilute hydrochloride (HCl) solution vs. dialysis ($N_2$ purging, under dark). Figure 4.16a presents the UV-Vis spectra of aqueous dispersions prepared via both approaches. The sample prepared by mixing in dilute HCl solution showed

negligible degradation product – molydebates, detected at ~210 nm. The one that underwent dialysis showed a slightly increased absorbance at ~210 nm. However, this 7% increase is ten to twenty times lower that of *ce*-$MoS_2$ alkaline dispersions stored in the air with (156%) or without (80%) light exposure. Additionally, both neutralization methods retained maximum amount of 1T content (~70%). Therefore, both methods were used in further investigations.

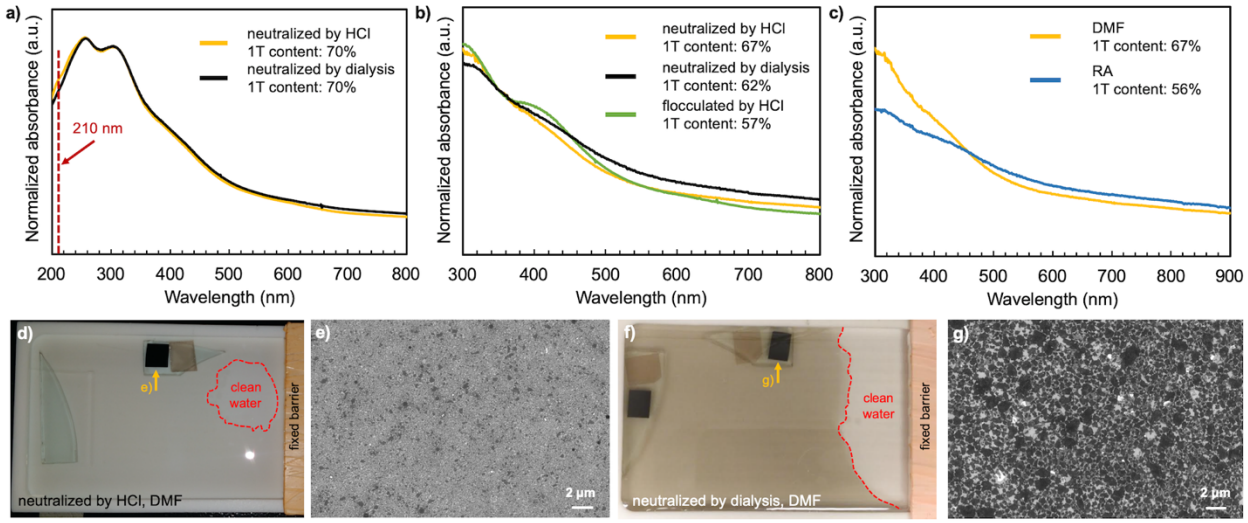



**Figure 4.16 Improved spreading dispersion of *ce*-$MoS_2$.** UV-Vis Spectra of (a) neutralized *ce*-$MoS_2$ dispersion by a diluted HCl solution vs. by three-days dialysis. (b) spreading dispersion in DMF prepared from neutralized *ce*-$MoS_2$ dispersion using 10% HCl solution vs. neutralized *ce*-$MoS_2$ dispersion via three-days dialysis vs. from flocculated *ce*-$MoS_2$ dispersion using 10% HCl solution. (c) spreading dispersion in DMF vs. RA of *ce*-$MoS_2$ prepared from neutralized *ce*-$MoS_2$ dispersion using 10% HCl solution. Photos taken from the top of the trough at the end of a deposition using the spreading dispersion in DMF prepared from neutralized *ce*-$MoS_2$ dispersion (d) by a diluted HCl solution vs. (f) by three-days dialysis. (e) and (g) SEM images of the film located in (d) and (f), respectively, with the scale bars labelled in the images

Figure 4.16b displays the UV-Vis spectra of DMF dispersion of *ce*-$MoS_2$ prepared from nanosheets collected via vacuum filtration from 1). Neutralized aqueous dispersion by a dilute HCl solution; 2). Neutralized aqueous dispersion via dialysis; 3). Flocculated nanosheets by adding a dilute HCl solution until pH~2. Note that the third method was used in some of our previous works.[42,61] All three methods resulted in reduction in 1T content, with the most impact – 13% decrease shown in Method 3. We also investigated the impact of the final organic solvents used. Figure 4.16c shown DMF vs. reagent alcohol (RA) dispersion of *ce*-$MoS_2$ prepared from nanosheets collected via Method 1. Even though alcohols, such as ethanol and isopropanol have been often used to disperse $MoS_2$ nanosheets,[23,24] it is clear that these solvents should be avoid for metallic *ce*-$MoS_2$ due to significant loss (~ 14%) in 1T content.

Since both Method 1 and 2 result in a final DMF dispersion of *ce*-$MoS_2$ with minimal degradation product and adequate amount of metallic properties, we prepared and evaluated films prepared by *SSaL* method from both dispersions. Photos of a trough containing the resulting films were presented in Figure 4.16d and 4.16f together with SEM images of corresponding films displayed in Figure 4.16e and 4.16g, respectively. The significantly darker color shown in Figure 4.16f suggests that dialysis may have caused the exfoliated nanosheets to restack. This is confirmed by the bigger and darker aggregates seen in the SEM images (Figure 4.16g). Therefore, the optimal process to prepare the final dispersions of *ce*-$MoS_2$ should be first to neutralize the aqueous *ce*-$MoS_2$ dispersion using a dilute HCl solution, and then collect the nanosheets via vacuum filtration followed by re-dispersing the filter cake in DMF. This method was used to prepared the DMF dispersion of *ce*-$MoS_2$ for all studies including cluster structure (**Chapter 5)**, solvent spreading (**Chapter 6**) and Langmuir film application (**Chapter 7**).

When using the old method reported in our previous work (Flocculation + DMF),[42,61] we could only obtain 40-50% single-layer sheets. In contrast, new method yields almost 64% monolayers with better consistencies between batches. Details regarding the distribution analysis of sheet layer-numbers obtained from old vs. new methods can found in the work by Zhang (Xu) *et al.*[141] and in **Chapter 5 section 5.3.2**, respectively.

## 4.4 Conclusions

In this work, we systematically investigated the chemical instability of aqueous dispersions prepared by chemical exfoliation under the effects of alkaline pH, ambient light irradiation and ambient air environment. It was found that both dispersed 1T-$MoS_2$ and 2H-$MoS_2$ rapidly degrade over a one-week time period when exposed to ambient air/oxygen, alkaline media and ambient light. As the result, 34% of the molybdenum was either oxidized (converted from Mo (IV) to Mo (VI)) or bonded to oxygen via substitution of sulfur and the resulting half-life was less than a week. Soluble molybdates were observed to be the strongest indicator of the degradation process which was shown as a distinct characteristic absorption peak in the UV-Vis spectra. The dissolution of Mo from 1T-$MoS_2$ was also confirmed by the morphological changes observed by AFM where small fragments were observed after a few weeks of aging. We found that both sulfur vacancies and edge defects can result in faster degradation and that the formation of superoxide was the main

cause of the degradation which likely formed oxidizing $H_2O_2$. While one might expect this mechanism to degrade $MoS_2$ over a wide pH range, we suggest that it is accelerated due to the high solubility of molybdates under alkaline conditions that would otherwise passivate the surface with insoluble $MoO_3$. We believe that this work will provide a much-needed foundation to assist researchers in choosing suitable conditions for storing and utilizing $MoS_2$ (1T and 2H) aqueous dispersions in a practical environment.

Furthermore, we also optimized the procedure for producing the spreading dispersion of 1T-$MoS_2$ (*ce*-$MoS_2$) in DMF, which preserves almost 100% of metallic (1T) $MoS_2$ and leads to ~40% increase in single-layer content. This procedure was used in later studies in this thesis and denoted as *ce*-$MoS_2$.

# Chapter 5: Spontaneous Clustering of Exfoliated Two-dimensional Materials at the Air-Water Interface *

## 5.1 Introduction

Manipulating Langmuir films using Langmuir troughs and transferring the resulting barrier-compressed films to solid substrates using the Langmuir-Blodgett or Langmuir-Schaeffer techniques remain among the few approaches to assemble one-molecule thick films from a liquid dispersed phase.[49,51,52,167]. While historically used to produce films of insoluble amphiphiles such as fatty acids, nanomaterials or colloids can also be trapped at the air-water interface, held up by surface tension, and manipulated using the same tools.[54–59,168,169]

To form a Langmuir film composed of nanomaterials, a liquid dispersion or ink is transferred onto the surface of water via pipette or syringe pump. In the ideal case, the impinging dispersion spreads on the water sub-phase and the solvent evaporates. However, due to the lower dispersion concentrations for many nanomaterials, tens or even hundreds of successive droplets are frequently needed to form a film, opposed to the case of amphiphilic molecules where only a few droplets of more concentrated solutions are used. Therefore, how the floating nanomaterials arrange themselves during this process becomes crucial, as they are the building blocks for the final film. Previous studies, focused on zero- (0D) or one-dimensional (1D) materials, have observed spontaneous clustering and associated this with the complex process of solvent spreading and evaporation.[26,27,55,113,116,170,171] For example, Cheng *et al*. presented that cetyltrimethylammonium bromide (CTAB)-capped gold nanoparticles formed fractal clusters with a fractal dimension of ~ 1.8 immediately after the chloroform-based dispersion spread over the water. Additionally, these clusters retained their fractal shape even after compression under intermediate surface pressures of 13 – 30 mN/m.[26]

In the case of two-dimensional (2D) nanomaterials, in **Chapter 3** we have presented that single-layer graphene oxide (GO) can form both island-like domains and fractal clusters

* This chapter is adapted from my published paper: "**Xu, L.**; Chekini, M.; Wilson, N. D.; Zamperoni, R. J.; Pope, M. A. Spontaneous Clustering of Exfoliated Two-Dimensional Materials at the Air-Water Interface. *J Colloid Interface Sci* **2023**, *648*, 129–140. https://doi.org/10.1016/j.jcis.2023.05.157."

immediately after solvent evaporation and the cluster structure can be tuned by the concentration of the dispersion.[67] However, this spontaneous aggregation is not widely reported for GO nanosheets, instead they often appear as individual sheets, and even after compression, the GO sheets remain apart by considerable spacing.[9,25,37,66,117] One exception was reported by Zhang *et al*. who observed that GO aggregated into close-packed islands, whose sizes can be tuned by changing the pH value of the subphase water.[118] This underreporting is likely due to the substantial loss of GO into the water after spreading, attributed to the use of alcohol solution as dispersing solvent (typically alcohol > 80%). It has been proven that almost 99% of GO is lost in the water[25] and to complicate things further, the actual transfer efficiency is dependent on the affinity of materials to water. Gravelle and Botto recently demonstrated that even slight changes in GO's chemical structure and hydrophobicity can lead to significant differences in the possibilities of whether or not sheets would move back to the air-water interface,[172] despite the fact that GO is known to preferentially remain in the subphase water.[173] This explains why there are more reports on 2D clustering of hydrophobic nanosheets such as reduced graphene oxide (rGO)[28] and liquid-exfoliated 2H molybdenum disulfide ($MoS_2$) nanosheets.[22]

In **Chapter 3 and Chapter 4**, we presented a solution to significantly enhance the material transfer efficiency for hydrophilic materials like GO and chemically-exfoliated $MoS_2$ (*ce*-$MoS_2$).[42,61,67] The new formulation requires a polar organic solvent such as alcohol or dimethylformamide (DMF) to prepare a stock dispersion, followed by mixing with a considerable amount of volatile, water-immiscible organic solvent such as 1,2-dichloroethane (DCE) or chloroform to produce the final spreading dispersion. This new formulation can effectively reduce the possibilities of material being mixed into sub-phase water and prevent the nanosheets from restacking in a poor solvent (e.g., DCE and chloroform which are not good solvents for these materials).[67] In this Chapter, we proceed with a similar strategy and conducted detailed studies on spontaneous clustering phenomena of various 2D nanosheets at the air-water interface. We reveal a nearly universal concentration effect which is better quantified by sheet number density ($A/V$) which directly controls the cluster fractal dimension ($d_f$). Furthermore, we uncovered the impact of these tunable cluster structures on the final Langmuir film prepared by both the traditional method using compression of physical barriers (Barrier-compressed Langmuir film, *BCL*) and a modified method using the spreading force from solvent spreading (Solvent-spreading assisted Langmuir film, *SSaL*). Finally, we discuss possible aggregation mechanisms in the context of

reaction vs. diffusion limited cluster aggregation and various interparticle forces acting on the floating sheets at an interface. We believe that this study will not only contribute to the fundamental knowledge of nanomaterial clustering behaviors at fluid interfaces and build a solid foundation before we move onto study the impact of the spreading pressure/force, but also provide insights for assembling new nanomaterials at the air-water interface.

## 5.2 Materials and Methods

### 5.2.1 Materials

$MoS_2$ powder (~6 μm particle size, #69860), hexane (HPLC, ≥ 98.5%, #293253), dimethylformamide (DMF, ACS, ≥99.8%, #319937), sulphuric acid ($H_2SO_4$, ACS, 95.0 – 98.0%, #258105-PC), phosphoric acid ($H_3PO_4$, ACS, ≥85 wt. % in $H_2O$, #438081), hydrogen peroxide ($H_2O_2$, ACS, 30 wt. % in $H_2O$, #216763), hydrochloric acid (HCl, ACS, 37%, #258148-GL), reagent alcohol (RA, HPLC, #270741) were purchased from Sigma Aldrich. Reduced graphene oxide powder (rGO) was from Global Graphene Group (Gi-PW-B050 (N002-PDR)). 1.6 M n-butyllithium (n-BuLi) in hexane (100 mL) was purchased from Fisher Scientific Acros (AC181271000). 2-propanol (IPA, ACS Grade, #A416P), potassium permanganate ($KMnO_4$) were purchased from Fisher Chemical or Fisherbrand (#351268). Graphite flake (metals basis, -10 mesh, #43319) was from Alfa Aesar. Ethanol, absolute was from Greenfield. 1,2-dichloroethane (DCE, ≤0.002% evaporation residue) was from Fisher Chemical (#E175) and Sigma Aldrich (#319929). Deionized water (MilliQ) was used in this work. All chemicals were used as received without any further treatment. Note that ethanol (absolute) was only used in GO synthesis and reagent alcohol was used in formulating dispersions.

### 5.2.2 Experimental methods

#### 5.2.2.1 *Chemically exfoliated molybdenum disulfide (*ce-*$MoS_2$)*

**Intercalation of $MoS_2$ powder by n-butyllithium** 500 mg $MoS_2$ powder was measured out and loaded into a 10 mL round bottom reaction flask with a magnetic stir bar. The flask was covered by aluminum foil and poked with a few holes. A secondary beaker was used to contain the reaction flask and both were placed in an oven at 75 °C overnight to remove any moisture. The

next day, after removing the reaction flask and secondary beaker from the oven, they were cooled down to room temperature before being transferred into an Argon (Ar)-filled glove box together with a 20 mL disposable plastic syringe, a 12 in. long disposable needle (14 Gauge) and a 20 mL vial containing hexane. The needle was secured onto the syringe via luer lock, and purged with Ar gas a few times. Then, it was used to carefully take out 5 mL of 1.6 M n-butyllithium (n-BuLi) in hexane which was slowly injected into the reaction flask. The reaction flask was capped and secured with a clamp. The needle and syringe were carefully flushed with pure hexane at least twice to remove n-BuLi residues. Finally, the reaction flask was placed onto a stir plate operating at 800 rpm for adequate mixing. This reaction took 62 – 65 hrs at room temperature inside the Ar-filled glove box. The contaminated hexane was transferred out of the glove box and quenched following the procedure in *Quenching method of n-BuLi residues*. Note that heat should be avoided around this reaction with the setup demonstrated here due to safety concerns.

**Quenching of n-butyllithium (n-BuLi) residues** n-BuLi is pyrophoric. Thus, a recommended guideline was followed to quench n-BuLi residues.[174] The procedure was carried out in a well-ventilated fume hood. Prior to the intercalation step, all heating elements and flammable solvents/residues were removed from the fume hood. A beaker containing 200 mL isopropanol (IPA), the main quenching agent, was then stirred at a moderate speed on a stirring plate. A glass cover was placed on the beaker to diminish any possibility of ignition. Once the contaminated hexane was taken out of the glove box, it was carefully poured into the IPA followed by placing the glass cover back on top immediately. After waiting for a couple of minutes, a few millilitres of methanol was slowly added into the mixture to carry out the quenching reaction further. Lastly, water was added dropwise until bubbling ceased, which indicated the completion of the quenching reaction. White powder – lithium hydroxide formed during the quenching procedure. The glass cover needed to be placed over the beaker between each quenching stage. This procedure was also used for quenching n-BuLi contaminated filtrate generated in the exfoliation procedure. Note that this quenching procedure is only applicable for quenching small quantities of n-BuLi. More information on quenching guidelines for large quantity as well as on other types of butyllithium can be found in Gau and Zdilla's work.[174]

**Exfoliation of $Li_xMoS_2$ in water** Once the intercalation was completed, the excess n-BuLi was removed before exfoliating the intercalated powder in water. These two steps were carried out in a nitrogen ($N_2$) gas filled glove bag (Aldrich® AtmosBag, Z530212) which contained the

reaction flask, a prepared filtration unit, a stirring plate, a beaker filled with 500 mL MilliQ water, a squeeze bottle filled with hexane and a pair of tweezers. The glove bag was set up in a fume hood. The entire filtration unit was dried to eliminate the chance of n-BuLi reacting with water. A mixed cellulose esters membrane (Millipore, 0.22 pore size, GSWP04700) was then loaded into the filtration unit, followed by pre-rinsing it with ~60 mL hexane which was kept in the bottom of the filtration flask. Once the prepared reaction flask was transferred into glove bag together with items mentioned above, the bag was evacuated and then refilled with $N_2$ (99.99% purity, dry). This step was repeated three time to eliminate oxygen and moisture. Then, the reaction dispersion was carefully poured into the filtration unit and the excess n-BuLi was diluted with hexane in the bottom of the flask. The reaction flask and the filter cake were rinsed with ~60 mL hexane twice. Once the filter cake was free of solvent, it was carefully transferred along with the membrane into the water. Once a moderate stirring speed was applied, the powder immediately dispersed into the water and generates bubbles. A layer of metallic looking film was observed at the water surface, which was easily removed during centrifugation in later steps. After the aqueous dispersion was stirred in the glove bag for 5 min, it was removed from the glove bag and 1 h of bath sonication (VEVOR DIGITAL PRO$^+$, 360 W) was applied to complete the exfoliation process. The n-BuLi contaminated filtrate was quenched according to the procedure described in section: *Quenching method of n-BuLi residues*. After bath sonication, unexfoliated flakes and the metallic-like surface film were removed by centrifuging the dispersion at 3800 rpm for 30 min (Fisher Scientific accuSpin$^{TM}$ 3). Because the original machine became inoperable in the middle of the project, we switched to centrifuging the dispersion at 3100 rpm for 60 min using an alternative machine (KOKUSAN, H-103N SERIES) and we observed no significant difference in the results. Note that degradation of *ce*-$MoS_2$/LiOH aqueous dispersion can be accelerated due to light exposure,[175] thus it was always kept in the dark during processing.

**5.2.2.2** *Synthesis method of graphene oxide (GO)*

Please refer to **Chapter 3 section 3.2.1** for details

**5.2.2.3** *Preparation of stock dispersions*

***ce*-$MoS_2$ in dimethylformamide (DMF) and reagent alcohol (RA)**: Immediately after exfoliation, on the same day, every 50 mL of *ce*-$MoS_2$/LiOH aqueous solution was filtered through

a nylon membrane (Millipore, GNWP04700, 0.2 μm pore size) using vacuum filtration. When there was about 5 mL remaining over the filter cake, the remaining dispersion was discarded and the wet filter cake along with the membrane were transferred into 15 mL of dimethylformamide (DMF). The *ce*-$MoS_2$ could be easily redispersed in DMF by shaking the container gently. Then, 6-10 min of bath sonication (VEVOR DIGITAL PRO$^+$, 360 W) was applied to remove material stuck to the filtration membrane, followed by 2 min of probe-sonication (BioLogics, Model 150V/T Ultrasonic Homogenizer 460 W, at 70% max power) to ensure recovery of *ce*-$MoS_2$ monolayers in DMF. For the RA-based dispersions, DMF was simply replaced by RA with the same volume but 6 min of probe-sonication (BioLogics, Model 150V/T Ultrasonic Homogenizer 460 W, at 70% max power) was used instead. Note that we found it difficult to recover single layer sheets from fully dried filter cakes. This is why, wet/moist cakes were used in this work. Note that *ce*-$MoS_2$ stock dispersions in DMF (or RA) were stored at concentration less than 0.8 mg/mL and new batches were prepared every 1-2 months to limit the impact of aging.

**GO in reagent alcohol (RA)** The weight percentage of GO in GO/ethanol stock was measured by weighing the dry mass of GO after evaporating the solvent in a vacuum oven. Three replicates were averaged to obtain the stock concentration. Then, 10 mL of GO in RA at a concentration of 1.4 mg/mL was prepared by diluting the GO stock with RA followed by 5 min probe-sonication (BioLogics, Model 150V/T Ultrasonic Homogenizer 460 W, at 60% max power) to obtain monolayer GO sheets. Note that GO stock dispersion in RA was stored at concentration equal to or less than 0.35 mg/mL under moderate stirring for no longer than two weeks, after which a fresh stock dispersion would be prepared from the GO/ethanol stock.

**rGO in 1,2-dichloroethane (DCE)** A stock dispersion of rGO in DCE was prepared at a concentration of ~1.75 mg/mL. Since the rGO is fluffy nanomaterial, a nano-powder enclosure was used for handling it. In a typical procedure, 40 mL (50.02 g) of DCE was first added into a glass jar together with a stir bar. Then the jar was sealed and transferred into the nano-powder enclosure. An aluminum foil weighing boat was used to measure out 104.7 mg of rGO powder. A funnel made from aluminum foil was placed at the mouth of the glass jar which will help guide the fluffy powder directly into the liquid. Then, the mixture was taken out of the enclosure and the remaining 20 ml (24.92 g) DCE was added. Then, 90 min of probe-sonication was applied (BioLogics, Model 150V/T Ultrasonic Homogenizer 460 W, at 70% max power) while moderate magnetic stirring was used at the same time to obtain exfoliated sheets. An ice bath was also used

to prevent over-heating and minimize solvent evaporation. After sonication, the concentration would typically increase to ~1.91 mg/mL from 1.75 mg/mL. Lastly, the dispersion was centrifuged at 3000 rpm (KOKUSAN, H-103N SERIES) for 45 min to sediment the unexfoliated aggregates. The final stock dispersion was obtained by collecting 25 – 30 mL of the supernatant. rGO stock dispersion in DCE was stored at 0.2 mg/mL and a new batch was prepared every two months.

**5.2.2.4** *Preparation of spreading dispersions*

Note that the spreading dispersions, no matter containing *ce*-$MoS_2$ GO, or rGO, were prepared freshly before each cluster or film deposition, and they were used right after mixing without any further treatments.

***ce*-$MoS_2$ in DMF/DCE and RA/DCE** The final spreading dispersion of *ce*-$MoS_2$ was prepared by mixing stock dispersion of *ce*-$MoS_2$/DMF or *ce*-$MoS_2$/RA with DCE at a desired concentration with a volume ratio ($V_{DMF/RA}/V_{DCE}$) of 1:6. For example, to prepare 1.4 mL of a final spreading dispersion of *ce*-$MoS_2$ in DMF/DCE (v:v=1:6) at 0.057 mg/mL, 200 µL of 0.4 mg/mL *ce*-$MoS_2$/DMF was diluted by 1.5 g of DCE (the density of DCE is 1.246 g/mL). Table 5.1 provides recipes for various dispersions used in this work.

**Table 5.1 Recipes of spreading dispersion of *ce*-$MoS_2$ used in this work in an example of 1.4 mL spreading dispersion**

| $V$, mL | $c$*, mg/mL | $c$, mg/mL | $V_{DMF}/V_{DCE}$ | $V_{RA}/V_{DCE}$ | $V_1$ of $c$, µL | $m_{DCE}$, g | Primary solvent |
|---|---|---|---|---|---|---|---|
| 1.4 | 0.057 | 0.4 | 1:6 | - | 200 | 1.5 | DMF |
| 1.4 | 0.028 | 0.2 | 1:6 | - | 200 | 1.5 | DMF |
| 1.4 | 0.019 | 0.13 | 1:6 | - | 200 | 1.5 | DMF |
| 1.4 | 0.014 | 0.1 | 1:6 | - | 200 | 1.5 | DMF |
| 1.4 | 0.011 | 0.08 | 1:6 | - | 200 | 1.5 | DMF |
| 1.4 | 0.128 | 0.9 | - | 1:6 | 200 | 1.5 | RA |

**GO in RA/DCE** GO/RA dispersion at desired concentration was first prepared from the stock dispersion (1.4 mg/mL) by diluting it with RA. Then, the spreading dispersion was obtained by mixing it with DCE. A volume ratio of reagent alcohol/DCE = 1:13 was used at the target concentration. For example, to prepare 10 mL of a final dispersion at 0.014 mg/mL, the GO/RA stock dispersion was first diluted with RA to prepare a dispersion at 0.2 mg/mL. Then 714 µL of this dispersion was diluted with 11.57 grams of DCE (the density of DCE is 1.246 mg/mL) to prepare the final spreading dispersion. Table 5.2 provides more details.

**Table 5.2 Recipes of spreading dispersion of GO used in this work in an example of 1.4 mL spreading dispersion**

| $V$, mL | $c$*, mg/mL | $c$, mg/mL | $V_{RA}/V_{DCE}$ | $V_1$ of $c$, µL | $m_{DCE}$, g | Primary solvent |
|---|---|---|---|---|---|---|
| 1.4 | 0.014 | 0.2 | 1:13 | 100 | 1.62 | RA |
| 1.4 | 0.006 | 0.09 | 1:13 | 100 | 1.62 | RA |

**rGO in RA/DCE** The stock concentration of rGO in DCE was measured to be 0.2 mg/mL. The final spreading dispersion was prepared at desired concentration by diluting the rGO/DCE stock dispersion slightly with RA to obtain a volume ratio of RA/DCE at 1:13. Table 5.3 provides recipes for various dispersions used in this work.

**Table 5.3 Recipes of spreading dispersion of rGO used in this work in an example of 1.4 mL spreading dispersion**

| $V$, mL | $c$*, mg/mL | $c$, mg/mL | $V_{RA}/V_{DCE}$ | $V_{RA}$, µL | $m$ of $c$, g | Primary solvent |
|---|---|---|---|---|---|---|
| 1.4 | 0.186 | 0.2 | 1:13 | 100 | 1.62 | DCE |
| 1.4 | 0.093 | 0.1 | 1:13 | 100 | 1.62 | DCE |
| 1.4 | 0.046 | 0.05 | 1:13 | 100 | 1.62 | DCE |
| 1.4 | 0.018 | 0.02 | 1:13 | 100 | 1.62 | DCE |
| 1.4 | 0.009 | 0.01 | 1:13 | 100 | 1.62 | DCE |

### **5.2.2.5** *Deposition methods*

Regardless of the deposition methods, here we summarize some general procedure:

1. The deposition was carried out in a well-ventilated area to ensure that solvent would spread and evaporate sufficiently.
2. The initially available surface area was 6.5 cm × 10 cm and defined by trough edges and a movable barrier. This barrier was only moving lengthwise from right to left as shown in the schematic below.
3. To prepare the deposition, the trough was first cleaned by wiping it with ethanol, then substrates were placed underneath the water prior to the deposition, after filling the trough with MilliQ water, the barrier were used to reduce the water surface and thus any contaminates would be confined and then removed by vacuuming away the top layer of water. Lastly, the barrier was moved back to its initial position (10 cm away from the other edge) and the trough was refilled with MilliQ water until the water surface meniscus was almost at its maximum.
4. The dripping position was placed in the middle widthwise and 1 cm away from the right edge lengthwise (aka. the movable barrier)

5. In the experiments where surface pressure was monitored, the Wilhelmy plate was placed to the left of the trough so that the solvent spreading would not directly touch the sensor. And only one side of barrier moved to compress and expand the film.

**Substrate preparation** $SiO_2$/Si wafer (300 nm wet thermal oxide, University Wafer, #1433) were first cut into small pieces, then cleaned in IPA and acetone sequentially by bath-sonicating (VEVOR DIGITAL PRO+, 360 W) for 5 min. After the substrates were dried by $N_2$ gas (99.99% purity, dry), 20 min of UV/ozone-cleaning (homemade) or 25 min of air plasma cleaning (HARRICK PLASMA, PDC-001-HP, HI power setting) was applied. Atomically flat muscovite mica (SPI) substrates were cleaned by removing the surface layers (top and bottom) using pieces of Scotch® tape.

**Deposition of nanosheets clusters** A deposition area of 6.5 cm × 10 cm was set up using a movable barrier in a custom-made Teflon trough. The as-prepared spreading dispersion was added onto the air-water interface through a glass syringe with a Teflon tubing (Hamilton™ PTFE Tubing 30G, # HAM90630) attached at the end. The dripping position is in the middle widthwise and 1 cm away from the movable barrier to the left of the trough. Unless it was mentioned otherwise in the paper, a dripping rate of 0.1 mL/min was used for DMF/DCE (v:v = 1:6) based dispersions and 0.13 mL/min was used for RA/DCE (v:v = 1:13) based ones. This was to allow for complete evaporation between drops. The droplet was placed right above the water surface before it naturally fell off the tubing and touched the water surface. Pre-treated $SiO_2$/Si substrates were placed under water just prior to the depositions. After adding 6-12 droplets, the water surface where clusters float around was reduced by slowly moving the barrier until it was ~2 cm away from the trough edge on the right. With minimal amount of material added to the interface, the changes of surface pressure were measured to be approximately zero and typical graphs of surface pressure vs. area are shown in Figure 5.1. Then, the horizontal-precipitation method was used to deposit samples onto the substrates. This was carried out by slowly removing the water from the region to the right of the movable barrier.[67,176] The samples were dried in the air for at least 5 h and then in an oven at 65 ºC overnight.

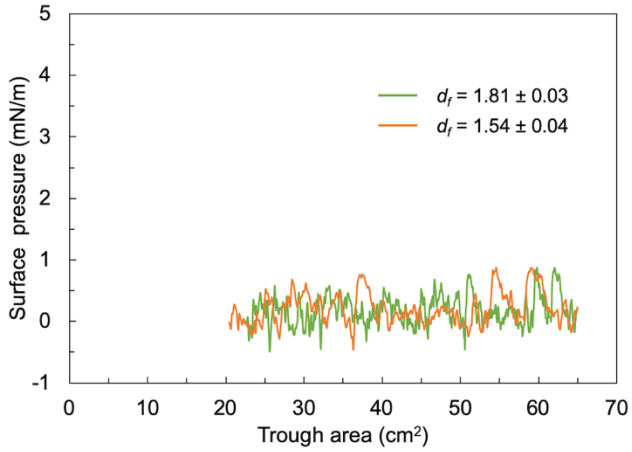



**Figure 5.1 Surface pressure measurement during cluster deposition of *ce*-$MoS_2$.** Surface pressure was monitored by a Wilhelmy plate (platinum).

**Solvent-spreading assisted Langmuir (*SSaL*) film assembly** A similar method has been reported elsewhere previously.[42,61,67] In this work, the trough, barrier and dripper were set the same way described in the cluster deposition method, but the barrier was fixed throughout the whole process. Pre-treated $SiO_2$/Si and clean mica substrates were pre-loaded at desired spots. The as-prepared dispersion was added dropwise onto the defined area as the film forming from the other edge to the barrier. The same dripping speed was used as the one in cluster deposition. The deposition ended when evaporation was no longer achieved and a lens of dispersion solvent accumulated under the dripping position. The horizontal-precipitation method (Figure 2.2c) was used to transfer the film onto substrates and dried as discussed above. Note that as demonstrated in previous reports, surface pressure was not monitored in this case but this method results in solid films.[42,61,67,135,177]

**Barrier-compressed Langmuir (*BCL*) film assembly** A Langmuir trough system (NIMA Langmuir Trough Model 312D) was used to carry out the experiment, except the trough was replaced with the same custom-made one used in all the other depositions. The barrier was set up at the same location to confine the deposition area. A clean platinum plate (i.e., Wilhelmy plate) was used to measure surface tension and was placed close to the left edge of the trough. Note that the plate was oriented to be parallel to the barrier in all experiments and the sensor was calibrated before each experiment. The cleanliness of the air-water interface was checked by ensuring that the measured surface tension deviated by less than 0.1 mN/m when the surface area was fully reduced. Similar to the deposition process demonstrated above, pre-treated $SiO_2$/Si substrates were

placed under water prior to the depositions. Once the setup was ready, the as-prepared spreading dispersion was added to the air-water interface as discussed above. Once the desired volume of dispersion was transferred, compression started after 10 min of equilibration. Note that the same amount of materials (~0.02 mg) was transferred onto the water surface for both concentration cases before compression. The surface pressure was monitored while movable barriers compressed at a rate of 10 mm/min until the target surface pressure of 5 or 10 mN/m was achieved. Once the target pressure was achieved, the barrier movement was paused, and horizontal-precipitation method was used to collect the resulting films. The same drying method was used as the other cases.

**Compression/expansion isotherms** We followed the procedures described in *BCL* film assembly. However, instead of stopping the barrier movement and holding the surface pressure at target value, a compression-expansion cycle was performed. For example, as for *ce*-$MoS_2$, the films were compressed to 10 mN/m at a rate of 10 mm/min, and then the barrier was retreated at the same rate until it reached its initial position. The surface pressure was recorded throughout the cycle. Note that the same amount of materials (~0.02 mg) was transferred onto the water surface for both concentration cases before compression and the resulting film was not collected in this experiment.

**High compression *BCL*** We followed the procedures described in *BCL* film assembly. However, the compression was not stopped until the surface pressure reached a plateau, which appeared to be ~39 mN/m in both cases. This plateau was obtained with ~0.03 mg being transferred onto the water surface in the case of low $d_f$ cluster but with ~0.04 mg in the case of high $d_f$ cluster. Films collected on pre-treated $SiO_2$/Si substrates at ~26 mN/m and ~39 mN/m followed the procedure described in *BCL* film assembly. Note that a Savitzky-Golay filter was applied to the compressional elastic modulus *K* vs. surface pressure curves by fitting linear least squares on successive sub-sets of adjacent data points. The purpose of this filter is to smooth the data without distorting the original signal. This was achieved by using the scipy.signal.savgol_filter() function in python.

### 5.2.3 Characterization methods

**Scanning electron microscopy (SEM)** SEM was carried out using a Zeiss Leo 1530 scanning electron microscope with a 10 kV accelerating voltage on clusters and films transferred

onto pre-treated $SiO_2$/Si substrates. In some cases, the brightness and contrast of the entire image was adjusted using ImageJ software.

**Atomic force microscope (AFM)** Contact mode AFM was used on films prepared by *SSaL* and deposited on pre-cleaned atomically flat muscovite mica (SPI) substrates. A Nanoscope MultiMode AFM (Veeco) and NP-STT10 tips (Bruker) were used. AFM images were analyzed using Gwyddion software to extract the height profiles. More details can be found in '*Height profile (AFM) with Multi-Gaussian fit*' in the **section 5.2.4.4**.

**Brewster angle microscopy (BAM)** Brewster angle microscopy (BAM, KSV NIMA Techniques) was used to capture photos and videos of GO clusters at the air-water interface. Note that the imaging resolution limit is ~2 μm. Note that the trough equipped with BAM has a much larger water surface area than our custom-made Teflon trough does.

**Surface tension measurement** Surface tension measurements were carried out using a Platinum Wilhelmy plate equipped to a Langmuir trough system (NIMA Langmuir Trough Model 312D).

### 5.2.4 Data analysis methods

#### **5.2.4.1** *Calculation of fractal dimension ($d_f$) based on SEM images*

Fractal dimension ($d_f$) was estimated using box counting method. In our case, it is a mathematical method that describes how area of a pattern scales with its radius and the equation is shown here:

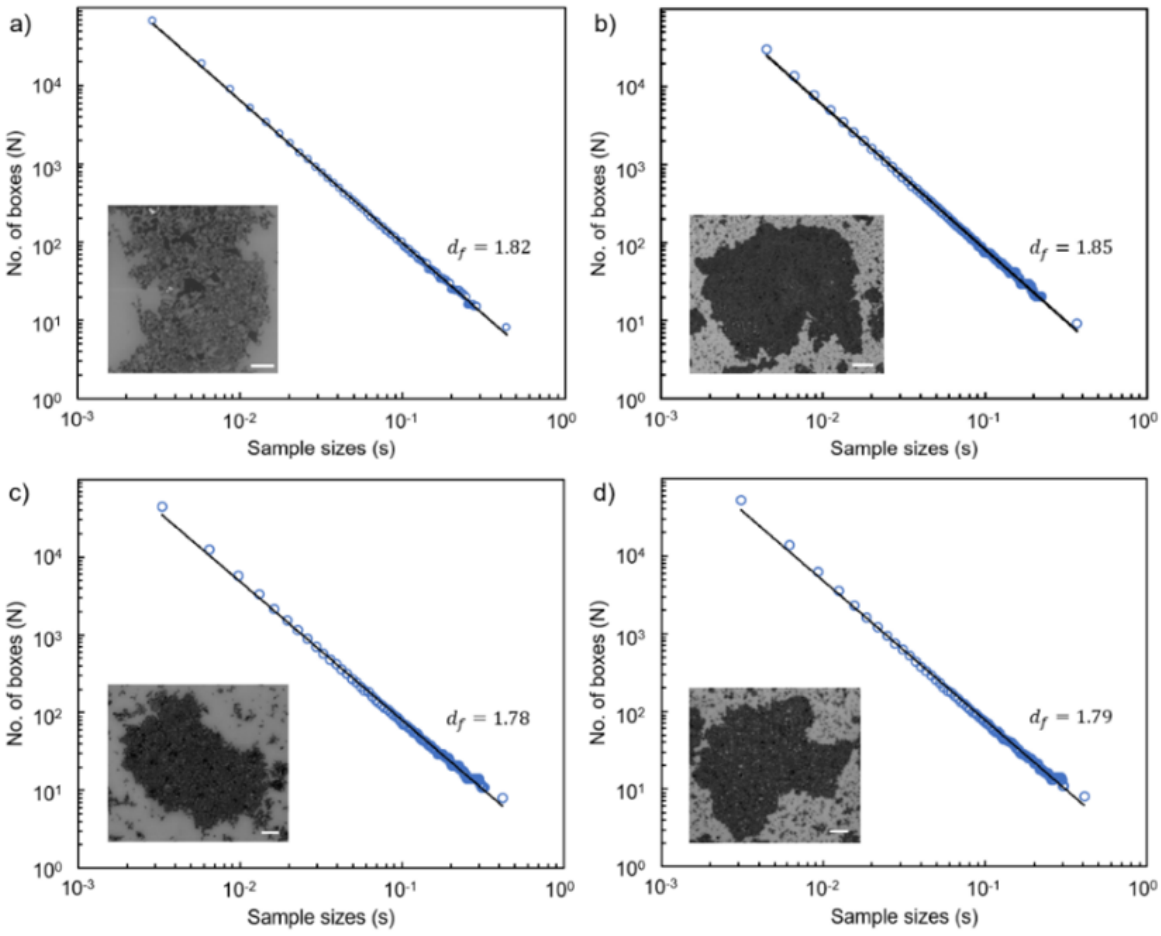
$$\frac{m_k}{m_1} = \left(\frac{a_k}{a_1}\right)^{d_f}$$

where $a_1$ and $m_1$ are radius and mass of primary pattern; $a_k$ and $m_k$ are radius and mass after scaling and $d_f$ is the fractal dimension. FracLac is a free-of-charge open-source plugin for ImageJ that was developed and maintained to perform box-counting algorithm. Based on its manual and other online tutorials, here are the steps and settings we applied to each cluster SEM image:

1. Select and duplicate the area containing the cluster
2. Apply 'Smooth' and 'Sharpen' process to the image

3. Adjust ‘Threshold’ to highlight areas of nanosheets
4. Apply the threshold and create binary image
5. Manually remove the ‘dirt’
6. In the FracLac ‘BC’ settings: Select ‘Lock White Background’; Set 4 initial box location and minimum box size to be 2 pixels and maximum to be 45 % of image; select ‘Draw grid’ for graphic options and then select ‘Metrics’ and ‘Convex hull’ for hull and circle.
7. Then click ‘Scan’ in the FracLac manual bar.

Figure 5.2 presents some examples of the results obtained by the method described above:



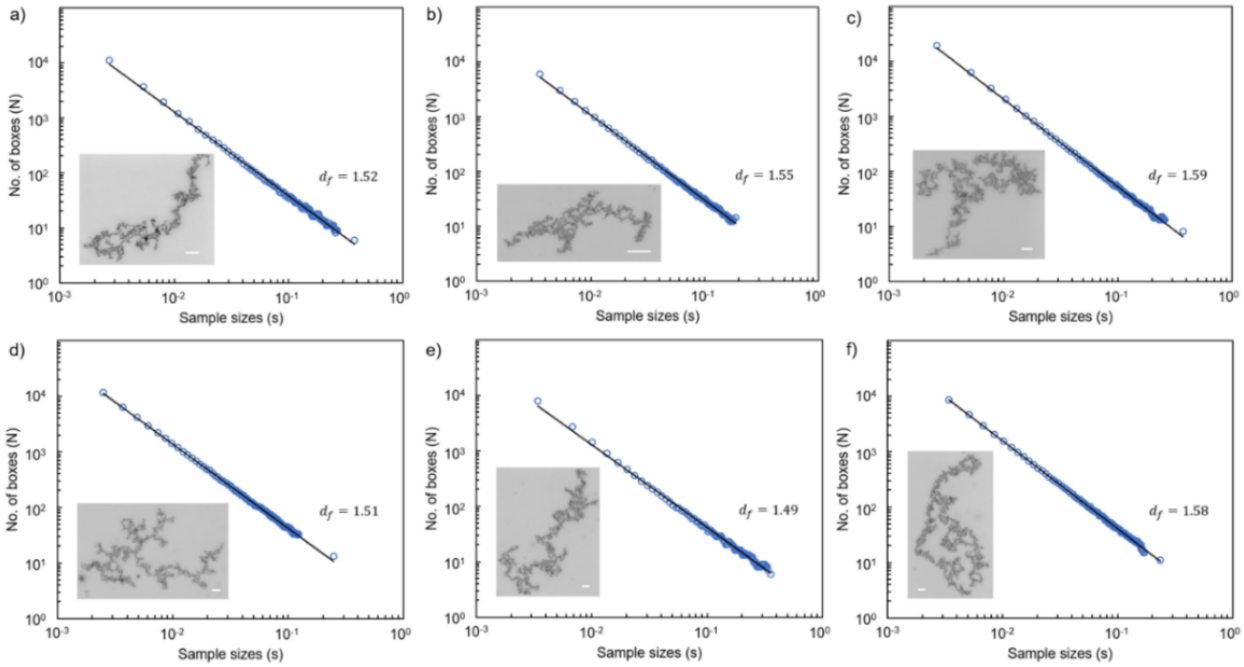



**Figure 5.2 Examples of fractal dimension characterization**. Top panel (a-d): Plot of number of boxes vs. samples sizes for highest concentration case (0.057 mg/mL) forming *ce*-$MoS_2$ with the corresponding SEM images shown in the insets. Bottom panel (a-f): Plot of number of boxes vs. samples sizes for lowest concentration case (0.011 mg/mL) forming *ce*-$MoS_2$ clusters with the corresponding SEM images shown in the insets. The scale bars are not included for these images but the scales of the clusters can be found out in images presented in **Result & Discussion**.

### **5.2.4.2** *Calculation of microscopic interfacial coverage (C) based on SEM images*

The microscopic interfacial coverage was calculated using the 'Area fraction measurement' function in Image J. Here are the steps:

1. Set the scale based on the given scale bar in the SEM image
2. Select the region and duplicate the image

   Adjust 'Threshold' to only highlight the area that are not covered by nanosheets
3. Apply the threshold
4. Take the measurement of 'Area fraction', denoted as $C_0$ (%), and $C$ *(%)* = 100 - $C_0$

Note that for each case at least 4 SEM images were analyzed and they were randomly picked from a pool of images.

### **5.2.4.3** *Calculation of Langmuir specific surface area (LSSA*)

*LSSA* is calculated via this formula: $LSSA = A/m$, where $A$ (in the unit of $m^2$) is the Langmuir surface area that is covered by the nanosheets to naked eyes; $m$ represents the mass of

the floating materials (in the unit of g). Unlike what was defined in our previous work, we did not include the factor of 2, therefore when comparing it to Specific surface area (*SSA*), we need to multiply the *LSSA* by 2, indicating two sides of 2D nanosheets.

**5.2.4.4** *Height profile (AFM) with Multi-Gaussian fit*

The AFM images first underwent the following image corrections using Gwyddion:

1. Align rows – Median difference
2. Remove scars
3. Plane level or Facet Level or both

Then the height profile (distribution of heights) was generated in the same software using Statistical functions tool. A custom made python code (scipy.optimize module) was written to perform the multi-Gaussian fit and here are the equation and settings we used:

1. $f(x) = a \times \exp\left(-\frac{(x-b)^2}{2c^2}\right)$ This equation represents one single Gaussian curve, where a is the amplitude, b is the center and c is the width of the normal distribution.
2. The first gaussian curve (substrate) has an upper and lower bound of amplitude equaling to half and one tenth of the maximum y value of the raw data. The rest of the curves (layer 1, layer 2 …) have an upper amplitude boundary equaling to the maximum y value of the raw data and a lower boundary of 0.
3. The first gaussian curve (substrate) has an upper and lower bound of center equaling to the guess value of substrate plus and minus 0.1. The rest of the curves (layer 1, layer 2 …) have an upper and lower center bound equaling to the guess value of the sum of substrate and total thickness of corresponding layers plus and minus 0.2.
4. The first gaussian curve (substrate) has an upper and lower bound of width equaling to 1 and 0. The rest of the curves (layer 1, layer 2 …) have an upper and lower center bound equaling to the 0 and 1.5

**5.2.4.5** *Calculation of interparticle attractive forces*

The attractive van der Waals (vdW) potential between the nanosheets was estimated according to Silverberg *et al.* [25] who presented a model for the potential between edge-to-edge

facing geometries of disk-like nanosheets. The full interaction pair potential is presented in the following equation:[29]

$$vdW(L,R_1,R_2) = -A_H\delta^2\left[\frac{{R_1}^2{R_2}^2\left({R_1}^4 - 2L^4 + L^2{R_2}^2 + {R_2}^4 + {R_1}^2\left(L^2 - 2{R_2}^2\right)\right)}{2\left({R_1}^4 + \left(L^2 - {R_2}^2\right)^2 - 2{R_1}^2\left(L^2 + {R_2}^2\right)\right)^{5/2}}\right] \quad (5.1)$$

where $L$ is the center-to-center separation distance and $L = D + R_1 + R_2$, where $D$ is the separation distance between the edge surfaces of two disks; $R_1 = R_2$ are the radius of circular nanosheets. $A_H$ represents the Hamaker constant. We used Hamaker constant estimated for monolayer graphene as the Hamaker constant for rGO.[178] The Hamaker constants of pure materials ($A_{H(mGr-mGr)}$) can be estimated from the interfacial component of the Hamaker constant ($\mathrm{A_{mGr-SiO_2}}$) using the following approximation:[178]

$$A_{H(mGr-SiO_2)} \approx \sqrt{A_{H(mGr-mGr)}A_{H(SiO_2-SiO_2)}}$$

where $A_{mGr-SiO_2} = 7.1 \times 10^{-20}$ and $A_{SiO_2-SiO_2} = 6.5 \times 10^{-20}$. It yields $A_{mGr-mGr} = 7.8 \times 10^{-20}$. Table 5.4 summarized values for all parameters used in the calculation based on equation (5.1).

**Table 5.4 Parameters for estimating van der Waals (vdW) potential.**

| Material | $R_1 = R_2$ = ½ diameter, nm | $A_H$, J | $\delta$, thickness, nm |
|---|---|---|---|
| **GO** | 1000 | $2.37 \times 10^{-21}$ [25,179] | 1 |
| ***ce*-$\mathbf{MoS_2}$** | 150 | $9.38 \times 10^{-20}$ [180] | 2 |
| **rGO** | 300 | $7.8 \times 10^{-20}$ [178] | 10 |

Unlike vdW forces, capillary force is often longer range. When particles float at the air-water interface, they can cause deformation of the interface which is known to cause attraction between similar materials. The mass of the particle and the associated deformation due to gravity is a typical cause for capillary forces between micron-sized particles (e.g. polystyrene particle, PS). However, once a PS particle radius reduces to ~500 nm (weighing ~17.8 fg), the gravity-induced capillary attraction is expected to decrease to below $kT$, which becomes insufficient to cause aggregation.[181] In our case, if we model our 2D materials as circular disks with a diameter of 2 μm for GO, 600 nm for rGO and 300 nm for *ce*-$MoS_2$, the flakes only weigh approximately 4.3, 5.7 and 0.7 fg, respectively. Therefore, a gravity-induced capillary force is expected to be negligible in our system. However, a long-range capillary force resulting from an irregular meniscus (e.g.

surface roughness, shape anisotropy, etc.) could still play a role. In the PS case presented by Stamou *et al*., the meniscus was pinned to heterogeneities on the particle surface and the resulting capillary interaction between two light-weight particles ($\delta E_{AB}$) can be estimated using the following equations:[181]

$$\delta E_{AB} \approx -12\, cos[2(\varphi_A+\varphi_B)]\, \frac{{r_c}^4}{L^4}\, \delta E \tag{5.2}$$

$$\delta E = \pi \gamma_w h^2 \tag{5.3}$$

where $\gamma_w$ is the water surface tension; $L$ is a center-of-mass separation between two particles and $L = 2R + D$, where $R$ is the particle radius and $D$ is separation distance between the edge surfaces of two particles; $\varphi_A$ and $\varphi_B$ are the orientations of two particles and can be simplified as $\varphi_A = \varphi_B = 0$; $r_c$ is the contact radius which is very close to particle radius, $R$; The prefactor $h$ can be estimated from a typical value of contact angle hysteresis: $\Delta\theta \approx 10°$. A typical value for pinning-induced deviation from the ideal contact line is $h \approx \frac{1}{2} R \times \Delta\theta$. For PS particles with diameter of 1 μm, the pinning-induced deviation from contact line is about 50 nm, which is ~10% of particle radius, and at an interparticle distance of 2 μm, the $\delta E_{AB}$ can be as high as ~$5 \times 10^4$ $kT$, which explains the experimental aggregations observed between two lightweight PS particles. However, considering that the thickness of our nanosheets (1-10 nm) is only one hundredth to one thousandth of the lateral size (300-2000 nm), it will not be appropriate to assume $h$ being 10% of (circular) nanosheet radius. Therefore, we instead chose 20% of thickness as $h$ to explore the possible impact of capillary force in our cases. Table 5.5 summarized values for all parameters used in the calculation based on equation (5.2) & (5.3). The resulting capillary potential takes place when nanosheets are a few hundreds of nanometers apart and when the distance reduces to 20 nm, it provides ~2 $kT$ attractive potential for GO, ~ 5 $kT$ for *ce*-$MoS_2$ and ~160 $kT$ for rGO. The magnitude of capillarity is likely comparable to the overall negative potential resulted from electrical double layer repulsion and vdW attraction, which is around 2.5 $kT$ for GO.[25]

**Table 5.5 Parameters for estimating long-range capillary potential.**

| Material | $\gamma_w$, J/m$^2$ | Thickness, nm | $R$ = ½ Diameter, nm | $\Delta\theta$, degree | *h, nm* | $\delta E$, J |
|---|---|---|---|---|---|---|
| **GO** | 0.0728 | 1 | 1000 | 0.025 | 0.22 | $1 \times 10^{-20}$ |
| ***ce*-$MoS_2$** | 0.0728 | 2 | 150 | 0.3 | 0.39 | $4 \times 10^{-20}$ |
| **rGO** | 0.0728 | 10 | 300 | 0.8 | 2.09 | $1 \times 10^{-18}$ |

Another possible interparticle force – hydrophobic attraction is greatly dependent on the material properties. The hydrophobic force is found to cause aggregation at the air-water interface because water molecules have limited orientations to bond on hydrophobic surfaces and thus a net attractive force forms as a result of reducing the total entropy.[182] One can estimate the normalized hydrophobic force (*F/R*) and the corresponding interfacial energy per unit area (*W*) using the following equations:[183]

$$W = -2\gamma_i H_y e^{-D/D_H} \tag{5.4}$$

$$H_y = 1 - \frac{a_0}{a} \tag{5.5}$$

$$F/R = 2\pi W \tag{5.6}$$

where $\gamma_i$ is the hydrophobic-water interfacial tension ($\gamma_i \approx 50\, mJ/m^2$ for rGO)[37]; $H_y$ is the Hydra parameter, where $a_0$ is the hydrophilic area and $a$ is the hydrophobic area at a given interface; $D$ represents the separation distance between two the edge surfaces of two particles; $D_H$ is the decay length, and a typical value of 1 nm is used in our case; We assume that our rGO is fully hydrophobic, thus $H_y \approx 1$. This will not overestimate the resulting hydrophobic force since the reported surface energy of rGO ranges from 50 – 90 mJ/m$^2$ and we chose $\gamma_i$ on the lower end.[184] Table 5.6 summarized values for all parameters used in the calculation based on equation (5.4)-(5.6). On the other hand, Lu *et al*. has reported that hydrophobic force was not detected at the edge surface of the $MoS_2$.[185] The hydrophobic interaction also unlikely takes place between GO sheets, since GO contains abundant oxygen-functioning groups at the edges which can easily bond with water molecules. The results show that hydrophobic force takes place within the same range where vdW and electrical double layer forces occur. It is reported that the hydrophobic force is usually significantly stronger than vdW.[183]

**Table 5.6 Parameters for estimating hydrophobic potential/area.**

| Material | $\gamma_i$, mJ/m$^2$ | $H_y$ | $D_H$, nm |
|---|---|---|---|
| **rGO** | 50 [184] | 1 | 1 |

## 5.3 Results and Discussion

### 5.3.1 Surface tension measurements of various solvents

Table 5.7 summarize the surface tension measurement of pure and mixed solvents used in this Chapter. The values for pure solvents are in line with literature values. As for the mixtures, the measured value is in-between those of the pure ones, ranging from 31 – 34 mN/m.

**Table 5.7 Surface tension of pure and mixed solvents used in this work.**

| **Pure solvent** | | **Solvent mixture** | |
|---|---|---|---|
| **Type** | Surface tension (mN/m) | Type | Surface tension (mN/m) |
| Reagent alcohol (RA) | 22.4 ± 0.2 | RA/DCE (v:v = 1:6) | 31.3 ± 0.1 |
| pure ethanol | 22.5 ± 0.2 | RA/DCE (v:v = 1:13) | 32.1 ± 0.1 |
| DMF | 36.2 ± 0.8 | DMF/DCE (v:v = 1:6) | 34.0 ± 0.1 |
| DCE | 32.0 ± 0.2 | | |

Note that the reagent alcohol we used is a specific type of denatured ethanol, containing 5% isopropanol and 5% methanol. Compared to pure ethanol, the denatured components do not have any impact on surface tension. This is supported by the evidence of negligible increases in surface pressure as shown in Figure 5.3.

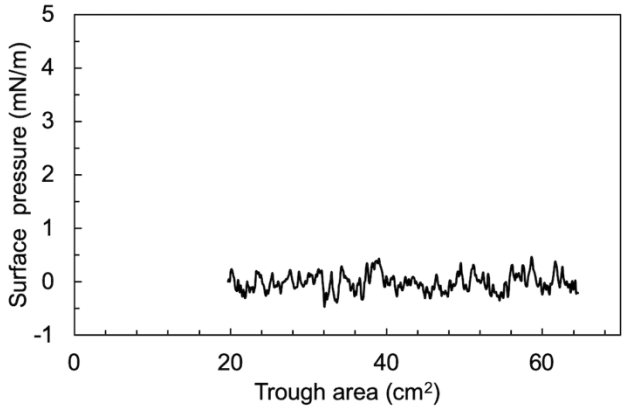
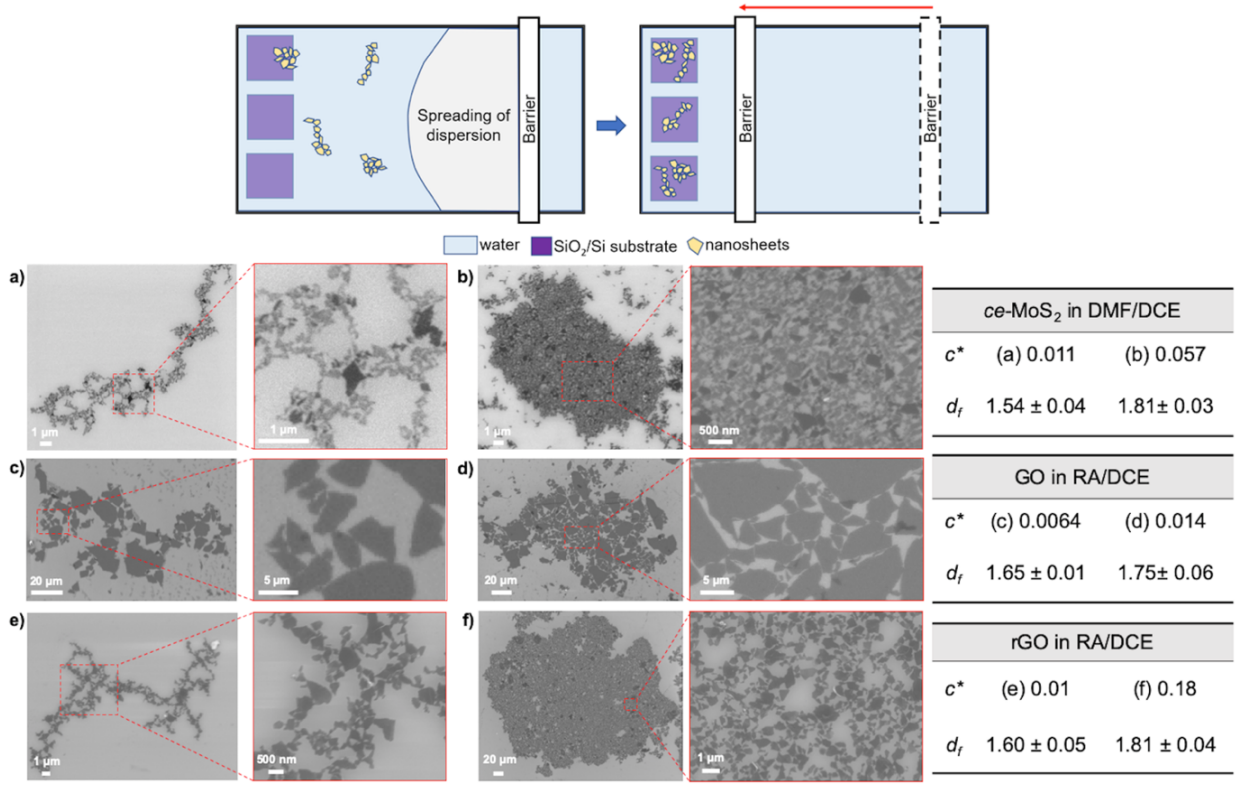



**Figure 5.3 Investigation on the purity of reagent alcohol**. Surface pressure vs. trough area plot of compressing the water surface where 3.2 mL RA/DCE (v:v = 1:13) were deposited. Negligible increases in surface pressure suggest that the maximum amount of surface-active impurities that could be introduced into the system is insignificant.

### 5.3.2 Spontaneous cluster formation and concentration effect

To isolate the morphology of clusters formed from individual drops of dispersion, we only added several drops to a large Langmuir trough. This was to avoid spreading-induced compression.[67] As the schematic illustrated in Figure 5.4, these sparse structures were then slowly

compressed to an extent that adjacent domains of floating nanomaterials did not overlap, and were still in the gas phase (negligible change in surface pressure after compression). Then the clusters were collected on pre-treated $SiO_2$/Si substrates by the horizontal-precipitation method. Figure 5.4a and 5.4b show scanning electron microscope (SEM) images of the resulting clusters for *ce*-$MoS_2$ deposited with low (0.011 mg/mL) and high (0.057 mg/mL) concentrations, respectively. SEM images for films deposited using low and high concentration dispersions of GO (Figure 5.4c and 5.4d, respectively) and rGO (Figure 5.4e and 5.4f, respectively) are also shown. The corresponding concentrations are summarized in the tables to the right.




| *ce*-$MoS_2$ in DMF/DCE | | |
|---|---|---|
| $c^*$ | (a) 0.011 | (b) 0.057 |
| $d_f$ | 1.54 ± 0.04 | 1.81± 0.03 |

| GO in RA/DCE | | |
|---|---|---|
| $c^*$ | (c) 0.0064 | (d) 0.014 |
| $d_f$ | 1.65 ± 0.01 | 1.75± 0.06 |

| rGO in RA/DCE | | |
|---|---|---|
| $c^*$ | (e) 0.01 | (f) 0.18 |
| $d_f$ | 1.60 ± 0.05 | 1.81 ± 0.04 |

**Figure 5.4 Fractal clusters and island-like domains formed by various nanosheets**: Top: Schematic illustration of deposition method of clustered 2D nanosheets. Bottom: SEM images of cluster structures composed of (a-b) *ce*-$MoS_2$; (c-d) GO; (e-f) rGO. Concentrations of spreading dispersions and corresponding cluster fractal dimension were summarized in the table to the right. Clusters are deposited on pre-treated $SiO_2$/Si substrates. Scale bars are labelled in the images. The average and error values were calculated based on 4-8 other clusters prepared at the same conditions. Tables to the right: $c^*$ (in mg/mL): concentration of spreading dispersion (aka. stock diluted by DCE); $d_f$: fractal dimension at corresponding $c^*$.

As for GO and *ce*-$MoS_2$, each cluster is comprised of mostly monolayer sheets: GO sheets have an average thickness of 0.8 ± 0.2 nm as reported in our previous work.[24] The *ce*-$MoS_2$ monolayers were measured to be 1.2 nm by AFM (Figure 5.5a and 5.5b), which is in line with the

literature value[61,186] but larger than the theoretical value of 0.65 nm, likely due to absorbed solvent.[187] On the other hand, the commercial rGO is composed of multilayer graphene sheets as thin as 3-4 nm (Figure 5.5d-f). Its wrinkled nature was captured in the AFM images shown in Figure 5.5d and 5.5e. Despite the differences in nanosheet thickness, lateral sizes and material properties, as the dispersion concentration ($c^*$) increases, identical clustering transitions appears to emerge from fractal networks (Figure 5.4a, 5.4c, 5.4e) to compact island-like domains (Figure 5.4b, 5.4d, 5.4f).

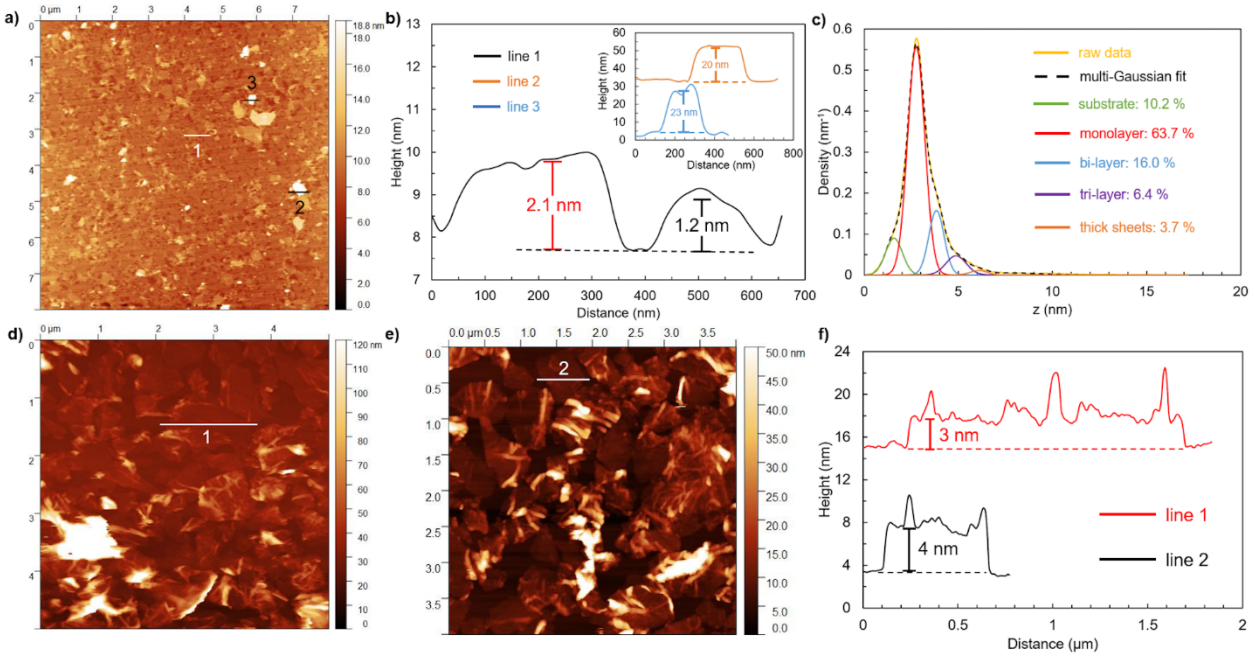



**Figure 5.5 Material characterization of *ce*-$MoS_2$ and rGO nanosheets**: (a) AFM image of *ce*-$MoS_2$ Langmuir film with locations for height profiles measurements indicated by lines. (b) Height profiles of *ce*-$MoS_2$ nanosheets with locations indicated in (a) accordingly. (c) Height distribution of *ce*-$MoS_2$ Langmuir film with multi-Gaussian fit. The resulting percentages of each component were listed in the graph. (d) and (e) AFM images of rGO Langmuir film with locations for height profiles measurements indicated by lines. (f) Corresponding height profiles of measurements taken in (d) and (e). Note that the Langmuir film were prepared by *SSaL* method and clean mica substrates were used for collecting the resulting films.

Even though this concentration effect is reported for the first time for 2D nanosheets, it has been observed for nanoparticles of lower dimensionality previously. Santhanam *et al*. showed a densely packed monolayer array of 5 nm gold nanoparticles formed at an optimized concentration of ~1 μM. However, reducing this concentration by half resulted in an array that was instead separated by fractal aggregates.[188] Sear *et al*. revealed that silver quantum nanodots can form densely packed circular islands or linear stripes immediately after the evaporation of carrier

solution at the water surface and an increase in concentration was responsible for the transition from island shapes to linear stripes.[27] Similar stripe-like patterns were also observed by Bai *et al*. at relatively high concentrations, while a network structure was shown in the dilute case.[116] Ge *et al*. presented the aggregation patterns of CdSe nanoparticles after spreading from chloroform on a smooth highly ordered pyrolytic graphite (HOPG) substrate, where surface mobility is higher than other rough substrates, like quartz, and thus is more comparable to the surface of water. The results showed that as the particle coverage decreased from 60% - 20%, the cluster structure changed from a spinodal pattern composed of small linear 'worms' to a honeycomb like network, then to a continuous film with holes.[189] In summary, these previous works have all suggested that a reduction in concentration tends to result in a more linear, network fractal structure in nanoparticle aggregation which is in line with the observations we presented for 2D nanosheets.

### 5.3.3 Global trend in 2D materials

To quantify the differences in cluster shapes, we used the fractal dimension ($d_f$) to describe the 2D packing density of each cluster or domain. The $d_f$ value represents how the area of a pattern scales with its radius and can be quantified using a simple box counting method.[114,190] In general, 2D aggregates reach a maximum density when the particles or sheets are packed as a dense disk with $d_f = 2$, while hitting a minimum when the arrangement is a line and $d_f = 1$. In the case of relatively low concentrations (~0.01 mg/mL for *ce*-$MoS_2$; ~0.006 mg/mL for GO, ~0.01 mg/mL for rGO), sheets are found to arrange into more linear 2D aggregates, with very few short branches resulting in a $d_f = 1.54 \pm 0.04$ for *ce*-$MoS_2$, $d_f = 1.65 \pm 0.01$ for GO and $d_f = 1.60 \pm 0.05$ for rGO. While in the case of relatively high concentrations, the corresponding $d_f$ increased to $1.81 \pm 0.03$ , $1.75 \pm 0.06$ and $1.81 \pm 0.04$ , respectively. The higher magnification views beside each of the original SEM images (Figure 5.4a-f) suggest that both cluster structures are composed of tiled sheets which are associated edge-to-edge and, generally, are not overlapping. In the domains, GO and *ce*-$MoS_2$ nanosheets pack relatively densely whereas in some cases the edge of one sheet was parallel to its neighbors', while rGO domains have much more void area. This could be explained by increased thickness in rGO nanosheets (Figure 5.5f), resulting in larger cross-sectional areas and mass leading to stronger attractive van der Waals forces and the increase in magnitude of attractive floatation forces.[191] In all cases, the attractive forces at edge-to-edge

contacts appears quite strong. For example, in the linear structure (Figure 5.4a, 5.4c & 5.4d), the sheets 'connect' to their neighbors via very limited points. Despite this, these clusters retain their shape under the disturbance of air convection, when monitored under a Brewster angle microscope (BAM).

Since all three materials show a similar trend, we used *ce*-$MoS_2$ to conduct more detailed studies on the concentration effect. Figure 5.6a-e displays SEM images of examples of clusters formed with increasing concentrations with smaller intervals and their corresponding fractal dimensions were listed under each image. As the cluster transformed from a chain structure to a densely packed island, the void space within the cluster decreased significantly and the fractal dimension of *ce*-$MoS_2$ clusters increased with concentration from $d_f \approx 1.54$ to $d_f \approx 1.81$.

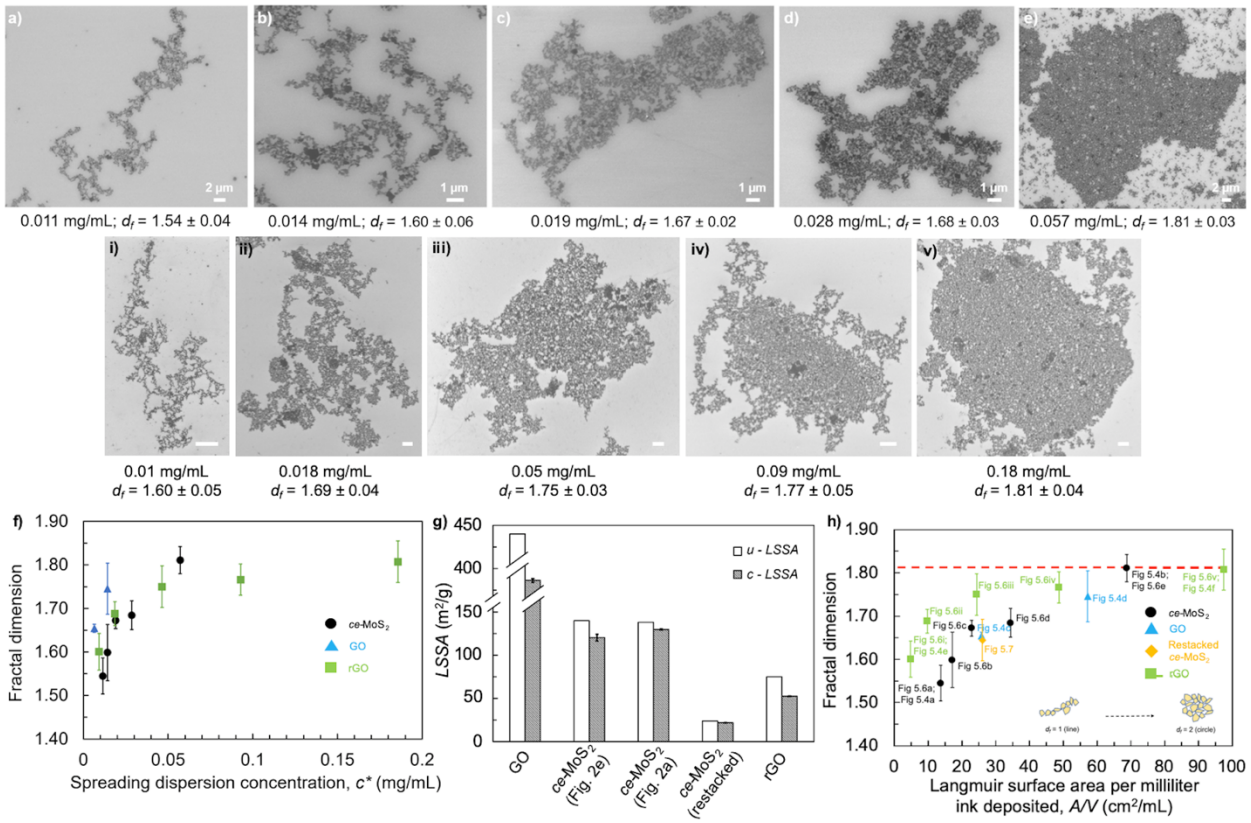



**Figure 5.6 Global trend of 2D nanosheets clustering at the air-water interface**: Concentration effect: (a-e) SEM images of cluster structures composed of *ce*-$MoS_2$ nanosheets prepared from increased concentrations of spreading dispersions (after mixing with DCE). Scale bars are labelled in the images. (i-v) SEM image of cluster formed from rGO dispersion in RA/DCE. Scale bars in (i) - (v) are 10 µm. Corresponding fractal dimensions were listed below each image. Clusters were collected on pre-treated $SiO_2$/Si substrates. (f) cluster fractal dimension as the function of concentration of spreading dispersion ($c^*$): *ce*-$MoS_2$ (●, black); GO (▲, blue); rGO (■, green). (g) Histogram of uncorrected (u-*LSSA*) and corrected *LSSA* (c-*LSSA*) for GO; *ce*-$MoS_2$ prepared at $c^*$ of 0.057 mg/mL and 0.011

mg/mL; re-stacked *ce*-$MoS_2$ (RA) and rGO (h) Universal trend in cluster structure transition across 4 different nanomaterials: cluster fractal dimension as the function of Langmuir surface area per milliliter (*A/V*): *ce*-$MoS_2$ (●, black); GO (▲, blue); restacked *ce*-$MoS_2$ (◆, yellow); rGO (■, green). Red line indicates the maximum value of fractal dimension obtained. The average and error values were calculated based on 4-8 other clusters prepared at the same conditions.

There is a continuous, nearly linear increase in $d_f$ with $c^*$ for *ce*-$MoS_2$ (●, black) as shown in Figure 5.6f which also compares the behavior of all materials studied. While the same general trends are apparent, the transitions are considerably shifted on the concentration axis. This is because, for the same mass of 2D material, each material has a different theoretical specific surface area (in $m^2/g$) due to differences in molecular weights and, more practically, each dispersion is exfoliated to various degrees leading to changes in the actual specific surface area of the 2D material in the dispersion. In other words, less exfoliated or restacked nanosheets will cover less water surface area per mass than monolayers. To quantify this, we define a Langmuir specific surface area (*LSSA*).[17,61,67] It describes the amount of water surface area ($A$, in the unit of $m^2$) that one gram of a nanomaterial can cover. The *LSSA* is calculated as:

$$LSSA = \frac{A}{c \times V} \tag{5.7}$$

where $c$ is the concentration (mg/mL) of nanomaterial in a dispersion and $V$ is the volume of dispersion (mL) needed to cover an area, $A$ ($m^2$).

**Table 5.8 Uncorrected vs. corrected *LSSA* using microscopic packing density.**

| Stock | $c^*$ (mg/mL) | $d_f$ | *u-LSSA* ($m^2/g$) | *C* (%) | *c-LSSA* ($m^2/g$) |
|---|---|---|---|---|---|
| ***ce*-$MoS_2$ in DMF** | 0.057 | 1.81 ± 0.03 | 140 | 85.9 ± 2.7 | 120 ± 3.8 |
| ***ce*-$MoS_2$ in DMF** | 0.011 | 1.54 ± 0.04 | 138 | 94.00 ± 0.4 | 130 ± 0.5 |
| ***ce*-$MoS_2$ in RA** | 0.129 | 1.64 ± 0.05 | 24 | 91.8 ± 1.2 | 22 ± 0.3 |
| **GO in RA** | 0.0064 | 1.65 ± 0.01 | 440 | 87.8 ± 0.5 | 386 ± 2.2 |
| **rGO in DCE** | 0.018 | 1.69 ± 0.04 | 75 | 70.2 ± 0.4 | 53 ± 0.3 |

$c^*$: concentration of spreading dispersion (aka. stock diluted by DCE)
$d_f$: fractal dimension at corresponding $c^*$
*u-LSSA*: uncorrected *LSSA* where interfacial coverage is assumed to be 100%.
*C*: Microscopic interfacial coverage estimated via analyzing SEM images of Langmuir films
*c*-LSSA: corrected LSSA where microscopic void space was considered.

Figure 5.6g and Table 5.8 summarize the *LSSA* measured for each type of nanosheets used in this work before and after correcting for film coverage, including an alternative exfoliation approach for *ce*-$MoS_2$, denoted as *ce*-$MoS_2$ (RA), which led to restacking and thus a lower specific surface area for the same material. The films used to estimate this parameter were formed by

solvent-spreading assisted Langmuir (*SSaL*) film deposition where material is dripped onto the air-water interface until a solid Langmuir film forms nearly across the entire Langmuir trough.[67] The volume deposited, area covered and coverage (as estimated by SEM) were used to calculate the *LSSA*. A larger difference between the uncorrected *LSSA* (*u-LSSA*) and corrected LSSA (*c-LSSA*) was observed in films formed by the packing of island-like domains ($d_f \sim 1.8$) where the film coverage was found to be relatively low. Moreover, particle jamming phenomenon became an obstacle for achieving higher packing density even at relatively low concentrations for rGO films. Dividing the theoretical specific surface area (*SSA*) by the c-*LSSA* can provide an estimate of the average layer number of the nanosheets (*N*). Using *ce*-$MoS_2$ as an example, the theoretical *SSA* of monolayer $MoS_2$ is 318 $m^2/g$ (one-sided),[61] by dividing its *c-LSSA* shown in Table 5.8, we can obtain 318/130 = 2.4 layers on average. After fitting multiple Gaussian curves in the AFM height profiles of a typical scan of 8 μm by 8 μm, we can determine the distribution of layer numbers. The result suggests that as-prepared *ce*-$MoS_2$ dispersions in DMF contain 63.7% monolayer sheets, 16.0% bi-layer sheets, 6.4% tri-layer sheets., with rest being ~20 nm thick sheets/aggregates (Figure 5.5a and 5.5b). Since the thickness between layers equals to the difference between bi-layer and monolayer (Figure 5.5b): 2.1 – 1.2 = 0.9 nm, we can assume that the thick sheets contain approximately 20/0.9 = 22 layers. As a result, we can calculate the average layer number $N = 1 \times 63.7\% + 2 \times 16.0\% + 3 \times 6.4\% + 22 \times 3.7\% = 2.0$, which is on par with the 2.4 layers obtained from our *c-LSSA* method. The difference is within the error of concentration measurements. Thus, it confirms the accuracy of our *c-LSSA* and suggests negligible loss of *ce*-$MoS_2$ into the subphase water. Detailed discussion around *LSSA* of GO can be found in our previous report.[67] Unfortunately, since rGO nanosheets are normally wrinkled, the method mentioned above cannot be used to estimate their layer number.

We then normalize the concentration by multiplying the *LSSA* with $c^*$ to obtain *A/V* which represents the total covered water surface area by floating nanomaterials (Langmuir surface area, *A*) per volume of a dispersion added. By plotting $d_f$ against *A/V*, as shown in Figure 5.6h, cases of *ce*-$MoS_2$ (●, black) and GO (▲, blue) presented in previous discussion roughly fall on the same curve, irrespective of nanomaterial used and surface area (i.e., aggregation state in the 3D dispersion). The increase in $d_f$ suggests that nanosheets were arranged with increasing density as *A/V* increases (see schematic illustrated in Figure 5.6h). To verify whether this trend also applies

to cases where sheets restack in the solvent, we also prepared a *ce*-$MoS_2$ dispersion in reagent alcohol (RA) instead of dimethylformamide (DMF). The SEM images of resulting cluster structures are presented in Figure 5.7, and it is clear that there is a larger density of sheets with higher contrast which are presumably restacked sheets that block the secondary electron emission from the substrate.[192] This restacking reduces the *c-LSSA* to be ~ 22 $m^2/g$ (Table 5.8), which is almost five times less than what *ce*-$MoS_2$ in DMF is. Even though with a dispersion concentration as high as 0.13 mg/mL we could only obtained clusters of $d_f = 1.64 \pm 0.05$, and this data set labelled as ◆, yellow in Figure 5.6h clearly follows the same trend. On the other hand, clusters of rGO nanosheets (■, green in Figure 5.6h) exhibit the same $d_f$ values at higher *A/V*. However, the reduction in *A/V* has less effect in transforming densely aggregated clusters to linear fractal ones. The potential underlying reason regarding the deviation of rGO case from the trend is discussed in the latter part of next section.

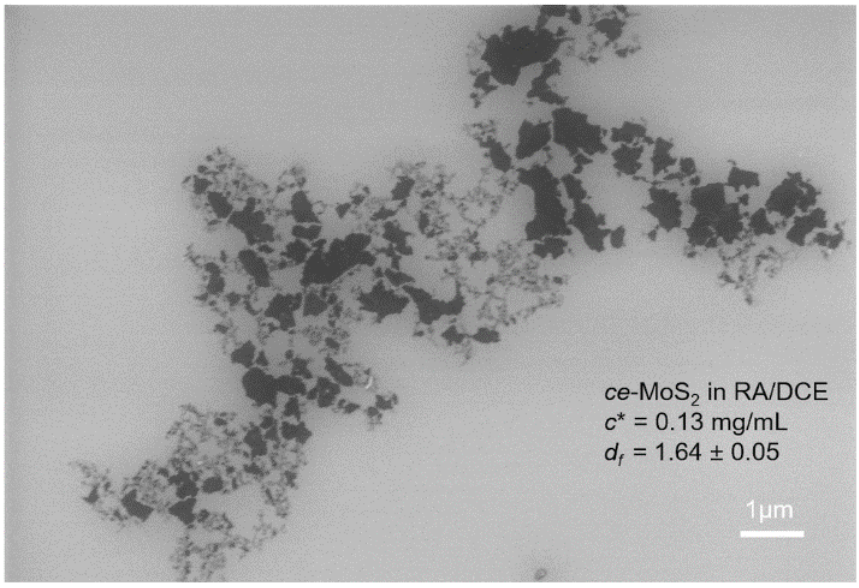



**Figure 5.7 SEM image of cluster formed from re-stacked *ce*-$MoS_2$ dispersion in RA/DCE**. The final concentration ($c^*$) and corresponding fractal dimension ($d_f$) are indicated in the image. The scale bar is 1 μm. Large dark flakes were formed by re-stacking of single-layer sheets which resulted 5 times reduction in the *c-LSSA*. Clusters were collected on pre-treated $SiO_2$/Si substrates. The average and error values were calculated based on 4-8 other clusters prepared at the same conditions.

### 5.3.4 Clustering mechanism

In this section, we attempt to shed light on the clustering mechanism. Starting from the assumption that the 2D material is well-dispersed before injection on the air-water interface, we

hypothesized that the 2D clusters could form in one of several ways: i) accumulating and clustering on the surface of the dispersion droplet during syringe pump injection; ii) gathering in the thin liquid film of spread dispersion during the spreading process and then aggregation either outside of the spreading area or during the drying (evaporation) process or iii) during film transfer to a substrate. To investigate i), since rapid evaporation can result in the migration and accumulation of nanosheets at the interface of the droplet, as illustrated in the schematic in Figure 5.8c, the dripping speed of the spreading dispersion was modulated as we have previously observed large aggregates of rGO accumulating at the bottom of droplet surface if it was left to evaporate for too long before dropping onto the water surface. In the SEM images shown in Figure 5.8a and 5.8b, we see that when the dripping speed was reduced to half, the *ce*-$MoS_2$ sheets packed into denser clusters, resulting in the average $d_f$ increasing from ~1.54 to ~1.63.

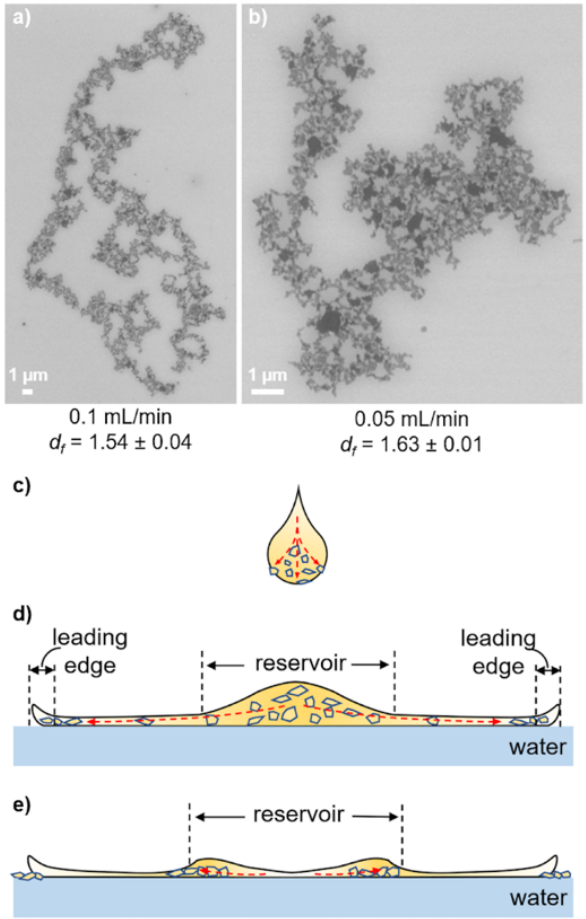



**Figure 5.8 Study of clustering mechanism stage 1 – Gathering of nanosheets**: SEM images of cluster structure as a function of spreading dispersion dripping speed: (a) 0.1 mL/min vs. (b) 0.05 mL/min. Scale bars are labelled in the images. Clusters were collected on pre-treated $SiO_2$/Si substrates. The average and error values were calculated based

on 4-8 other clusters prepared at the same conditions. Schematic illustration of sheets migration (red dashed-line arrows) during the process of (c) droplet formation and (d-e) solvent spreading at the air-water interface.

Slowing down the dripping rate had little effect on the concentrations within the droplet since we measured negligible difference in UV-vis absorbance of *ce*-$MoS_2$ dispersions collected at these two rates. Droplets of dispersion were collected in 7 mL scintillation vials. At a dripping rate of 0.1 mL/min, about 25 drops formed. For both cases, ~130 droplets were collected. Each droplet formed above the vial and these experiments were carried out in fume hoods, as did all the depositions in this work. The vial was sealed immediately once the desired number of droplets were collected. Then UV-Vis spectroscopy was used to compare concentrations after diluting both sample with the same factor. As shown in Figure 5.9 half the dripping speed barely impact the concentration of the droplet. Therefore, the resulting increase in cluster density (Figure 5.8b vs. 5.8a) is not due to the concentration effect.

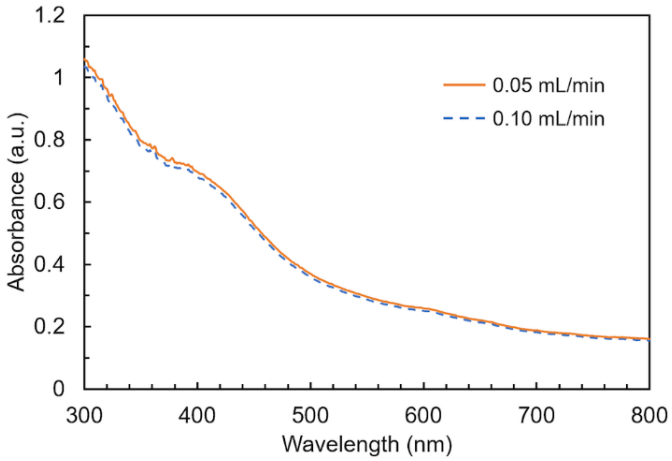



**Figure 5.9 Impact of dipping rate on concentration of droplet**. UV-Vis spectra of dispersion collected from dispensing the same spreading dispersion at two different dripping rates: 0.1 mL/min (dash line, blue) vs. 0.05 mL/min (solid line, orange). The overlapping curves implies concentration barely changes when dispensing rate reduced to half.

At a typical dripping rate, the surface area of a 4 µL droplet is ~13.8 $mm^2$ (assuming a spherical geometry). Based on the estimated *LSSA* of each Langmuir film, we can estimate the surface area of dispersed 2D material per drop ($A$/drop). For the case of $d_f$~1.54, $A$/drop ~ 6.5 $mm^2$ and for $d_f$~1.8, $A$/drop ~ 36 $mm^2$. For the $d_f$ ~ 1.8 case, the 2D material surface area exceeds the droplet surface area and thus cannot account for the cluster formation in this case. Therefore, even

though some nanosheets may gather at the droplet-air interface, explanation i) is unlikely the dominant factor for the clustering mechanism.

To investigate hypothesis ii), we need to first understand how liquid spreads on the water surface. The known profile of a single droplet of volatile organic solvent spreading at the air-water interface is shown in Figure 5.8d.[125] The reservoir retains the majority of dispersion/nanosheets while the rim spreads into a monolayer of liquid with an advancing leading edge. A continuous flow from the center, outward across the spreading area, occurs due to the Marangoni effect.[130] This leads to materials leaving the reservoir, traveling to, and accumulating at the leading edge, indicated by red dashed-line arrows in Figure 5.8d. Thus, this could provide opportunity for materials to gather and form clusters at the edge. In fact, Hurd and Schaefer have observed that silica microspheres (300 nm) would aggregate into fractal clusters right outside the edge where methanol spreading ended.[193] With slower dripping rate, increased local population of nanosheets can result in more materials gathering at the edge, thus boosting the possibility to form denser clusters. The surface tension of pure solvents and mixture combinations used in this work were measured using a Wilhelmy plate (platinum) and the results were summarized in Table 5.7. The surface tension of mixed solvents lies between the values of pure solvents and is within 2 mN/m of pure DCE. While spreading, the composition of solvents starts changing not only because DCE evaporates much faster than RA and DMF but also due to the non-uniform evaporation rate from the center reservoir to the edge rim. Therefore, additional Marangoni effect could occur within the reservoir region due to the gradient of surface tension resulting from compositional changes alongside the temperature-induced surface tension changes caused by varying evaporation rates.[194,195] Thus, initial gathering of nanomaterials could also happen within the reservoir, as illustrated in Figure 5.8e. To verify this hypothesis, we prepared a RA/DCE ($V_{RA}/V_{DCE}$ = 1:13) dispersion saturated with Sudan III dye, which will allow visualization of moving particles in the reservoir region. Then we recorded videos of it spreading at the water surface using the slow-motion feature on a cell phone. Snapshots of video taken are presented in Figure 5.10. A continuous outward flow was observed in the reservoir, as indicated by the green arrows in Figure 5.10e, forcing the dye particles to accumulate at the edge of the reservoir followed by rapid aggregation after the solvent had evaporated. Therefore, it is convincible that hypothesis ii) is the mechanism of the spontaneous clustering of 2D nanosheets at the air-water interface studied in

this work. Unfortunately, due to detection limits of the camera, it is not suitable for monitoring clustering at the leading edge, neither could it capture dye motion in other solvent combinations that exhibit much faster spreading and evaporation.

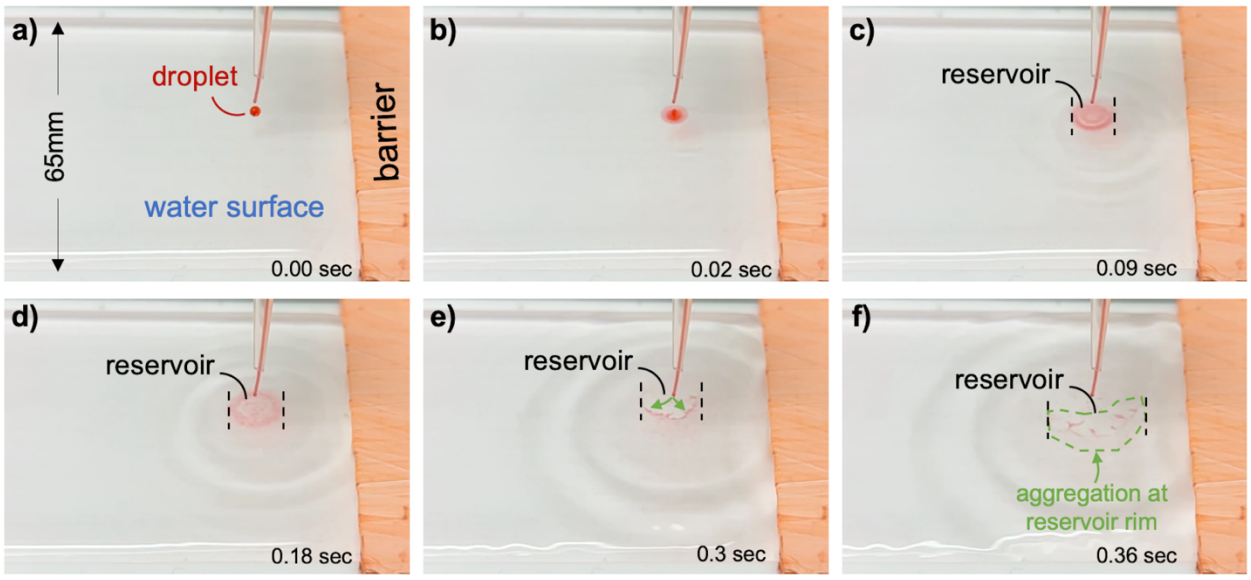



**Figure 5.10 2D materials gathering in the spreading reservoir**. (a-d) Time-lapse of snapshots showing the spreading of RA/DCE dispersion saturated with Sudan III dye. The outwards flow was indicated by green arrows in (e) and further aggregation at the rim of reservoir were circled out by green dashed line in (f). The time stamps were indicated at the bottom right of each photo. An iPhone 13 pro was used to take the video with slow motion function switched on. QuickTime was used to trim videos and take snapshots.

To rule out iii), we have captured GO clusters directly on the surface of water by using BAM, and similar clustered structures were observed (Figure 5.13 insets). However, we were unable to obtain clear BAM images of *ce*-$MoS_2$ nor rGO because with the fixed laser power both materials reflect too much light. Additionally, since the average lateral size of *ce*-$MoS_2$ nanosheets is a few hundred nanometers, which is much smaller than the resolution of BAM (2 μm), it will be impossible to resolve these sheets. Thus, depositing the clusters directly on the substrate was used in this work as an alternative.

As nanosheets gather at the spreading boundaries according to hypothesis ii), clusters should form either outside (scenario 1, Figure 5.11a) or inside (scenario 2, Figure 5.11b) of the spreading area. The former could be explained by an aggregation mechanism such as diffusion-limited cluster aggregation (DLCA) or reaction-limited cluster aggregation (RLCA) theory while the latter scenario is more similar to evaporation-induced aggregation on a solid support, except it occurs at the low-friction water surface. We hypothesize that a RLCA dominated aggregation

mechanism governs the formation of low-density cluster ($d_f$~1.54) while evaporation-induced aggregation results in dense cluster ($d_f$~1.8). To our knowledge, researchers commonly conclude that fractal clusters with $d_f$ > 1.5 represent a RLCA system. However, several studies have suggested that both structure (fractal dimension) and dynamics of clusters need to be considered to provide conclusive evidence with regards to the nature of the aggregation process.[120–122] In the RLCA theory, attractive forces dominate the overall interparticle potential while repulsive forces still play a crucial role to allow necessary rearrangement for dense structures to form.[123] To prove that aggregation could occur at the air-water interface after nanosheets leave the spreading area, we focus the analysis on possible attractive forces and estimated van der Waals (vdW) (Figure 5.11c), capillary (Figure 5.11d), and hydrophobic forces (Figure 5.11e) for all three materials and then compared them with the electrical double-layer repulsion (EDL) reported in the literature. The parameters used in calculations are provided in **Material and Methods** (**Section 5.2.4.5**). Even though the vdW potential increases exponentially as nanosheets become a few nanometers apart (less than 5 nm), it acts against EDL which occurs within a similar range. It has been reported that when only competing with vdW, EDL can result in an overall repulsive potential for nanosheets, e.g. Silverberg *et al*. have presented that as for GO exhibiting as much vdW potential as shown in Figure 5.11c, the estimated EDL can result in an energy barrier of ~2.5 $kT$.[25] However, we found out that this energy barrier could be overcome by long-range interparticle force such as irregular wetting-induced capillarity, kinetic energy and additional hydrophobic force.[28,181] As shown in Figure 5.11d, the capillarity comes into effect when nanosheets are a few hundreds of nanometers apart and at a distance of 20 nm, it provides ~2 $kT$ attractive potential for GO, ~ 5 $kT$ for *ce*-$MoS_2$ and ~160 $kT$ for rGO. Moreover, nanosheets should still retain kinetic energy generated from hydrodynamic forces as the solvent spreads. As for rGO, additional short-range attractive hydrophobic force is also identified as displayed in Figure 5.11e. It takes place in the same range when vdW and EDL occur and it is reported to provide significantly stronger attraction than vdW.[183] Therefore, the total attractive energy (i.e. vdW, capillarity and hydrophobic force) will likely suppress the EDL repulsion and result in sheets colliding with each other to form a cluster. Since the repulsive EDL force could still allow rearrangement of sheets in some orientations while the total attractive forces secure the final aggregations, RLCA theory is applicable for GO and *ce*-$MoS_2$ clusters (network-like, $d_f$~1.54) formed outside of the spreading

area. However, it cannot be used for rGO because even if rGO has similar EDL compared to *ce*-$MoS_2$ it exhibits $10^2$-$10^3$ stronger vdW and capillarity as well as additional hydrophobic force (Figure 5.11c-e), suggesting a very low possibility of rearrangements. Therefore, rGO clusters formed at low concentration are more likely to follow the DLCA (particle stick upon first contact). Since fewer rGO sheets would manage to leave the spreading solvent – a rather thermodynamically favorable region for rGO, this could explain why rGO has a delayed concentration effect. In conclusion, we suggest that RLCA dominated clustering mechanism can result in the formation of low-density cluster ($d_f$~1.54).

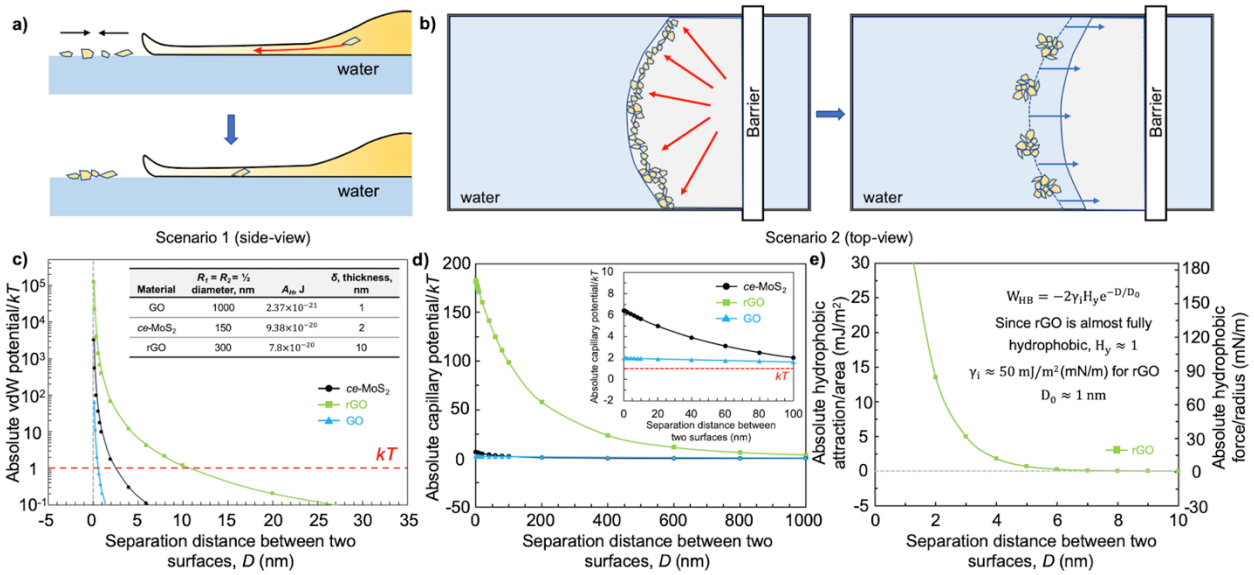



**Figure 5.11 Study of clustering mechanism stage 2 – Final aggregation of nanosheets**: Schematic illustration of two proposed aggregation scenarios: (a) network-like clusters assembled at the air-water interface after nanosheets leaves the spreading area; (b) island-like cluster formed at the spreading edges due to evaporation-induced aggregation. Estimated absolute values of interparticle attractive potential vs. separation distance between two surfaces for GO, *ce*-$MoS_2$ and rGO, resulted from (c) Van der Waals (vdW) force, (d) long-range capillary force and (e) hydrophobic force. Calculation in details can be found in **section 5.2.4.5**

On the other hand, traditionally, it takes at least hours or even days for sheets to rearrange and form a cluster with $d_f$ as high as ~1.8,[196] while in our case the spreading and evaporation takes about 2 sec and the cluster deposition process takes no longer than 10 min. Therefore, RLCA-dominated aggregation theory is unlikely the theory for the formation of denser clusters (island-like, $d_f$~1.8). Furthermore, according to RLCA, formation of dense cluster relies upon sufficient repulsive energy to provide possibility of particle rearrangement, which is in conflict with our observation that rGO has overpowering attractive forces but still formed dense clusters (Figure

5.6ii-v). Therefore, we proposed that denser clusters ($d_f$~1.7-1.8) may instead form within the spreading area, similar to evaporation-induced aggregation. Figure 5.11b shows a schematic illustration of the second scenario. We suggest that as nanosheets being brought together at the spreading boundaries by hydrodynamic forces, nanosheets could be 'pinned' at the boundaries. The laminar flow will result in two-dimensional assembly as presented in a previous report.[197] As more and more materials accumulate at the boundary (Figure 5.11b left), dense clusters form due to capillary immersion force once solvent evaporates (Figure 5.11b right). With an increase in dispersion concentration, material will accumulate faster and form denser clusters. This theory could further explain why rGO shows a delayed concentration effect (Figure 5.6h). Since it is hydrophobic and prefers to stay within the spreading solvent, rGO sheets will likely retreat with the solvent causing additional accumulation of materials which facilitates formation of dense cluster at a relatively lower concentration (*A/V*) as shown in Figure 5.6h. This solvophobic attraction induced aggregation at the air-water interface has been reported for 1D nanoparticles previously. [26,198,199] Due to the lack of existing studies on dynamics of binary solvent spreading and evaporation-induced aggregation at the air-water interface, we are unable to provide quantitative analysis to further support the second scenario.

### 5.3.5 Impact of cluster structure on Langmuir film assembly

In the following, we discuss the impact of the aggregate morphology on the quality of the final Langmuir film. Langmuir film formation involves transferring sequential drops of the dispersion onto the air-water interface, with each drop leaving behind an aggregate/cluster with a given $d_f$. These aggregates become building blocks and are assembled into a film either by the spreading force from solvent spreading (Solvent-spreading assisted Langmuir film, *SSaL*, introduced in **Chapter 3**) or by physically compressing the barriers (traditional barrier-compressed Langmuir film, *BCL*). Figure 5.12a-d displays SEM images of the resulting film assembled from two types of building blocks: island-like domains ($d_f \sim 1.8$) and network clusters ($d_f \sim 1.54$), respectively. The compression of films in Figure 5.12a and 5.12b was provided by the spreading force of the deposited solvent. Black and grey spots are thick and thin *ce*-$MoS_2$ nanosheets while light grey spots are void spaces. Examples of uncovered spots are pointed out by red arrows in Figure 5.12a. To ensure a fair comparison, the samples examined were collected at a constant

distance (4 cm) from the dripping location. By implementing pixel threshold analysis on the SEM images, a coverage as high as 94% was measured for $d_f \sim 1.54$ while the island-like domains resulted in a much lower coverage – 85.9 ± 2.7 %. The insets in Figure 5.12a and 5.12b are processed SEM images providing visualized evidence that linear clusters pack denser in the final film. This implies that clusters with high $d_f$ are less efficient in achieving higher coverage density microscopically, considering that the initial packing density of the domain structure (for example, see Figure 5.4b and Figure 5.6e) within one island cluster is measured to be 80.1 ± 3.8%, only ~5.8% less than that of the film. We additionally examined the morphology of films prepared by the more traditional *BCL* method. Note that a target surface pressure of 10 mN/m was chosen for both cases and it is below the collapse pressure. Figure 5.12c shows SEM images of the film prepared from high-density building blocks. The image shows a lack of clear boundaries between individual sheets and no apparent void space under this magnification. This suggests that the film could be over-compressed. In contrast, a maximum surface pressure of 10 mN/m is not sufficient to fully compress the film composed of low-density building blocks (Figure 5.12d). This could suggest that the linear clusters have stronger repulsive forces. To verify this hypothesis, Figure 5.12e and 5.12f present the compression and expansion isotherms of the two cases. The overlaps between the cycles of the isotherms in Figure 5.12f indicate that the interaction between sheets is more reversible when the building blocks are lower-density, branched-like clusters. This may also explain why a higher packing density is possible when using *SSaL* assembly (Figure 5.12b), since repetitive dripping act as hundreds of these cycles where the sheets are directed to reorient themselves to minimize void spaces.

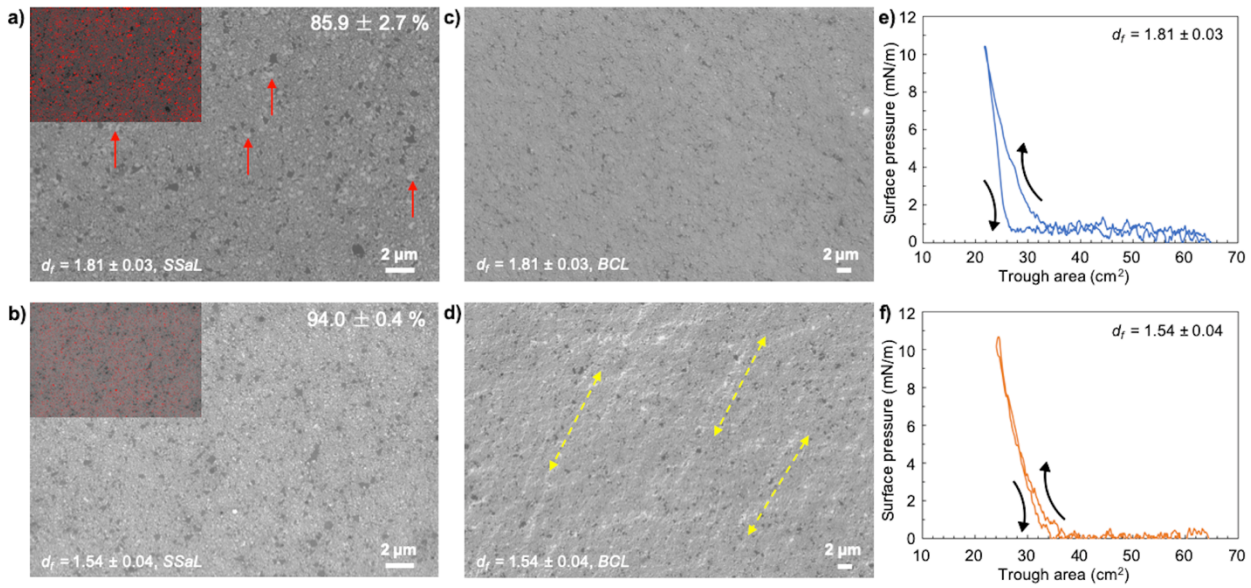



**Figure 5.12 Impact of cluster structure on packing density in the final Langmuir film of *ce*-$MoS_2$**: SEM images of the final film prepared by Solvent-spreading assisted Langmuir (*SSaL*) film method from cluster of (a) high and (b) low $d_f$. SEM images of the final film prepared by traditional barrier-compressed Langmuir (*BCL*) film method from cluster of (c) high and (d) low $d_f$. The films were deposited onto pre-treated $SiO_2$/Si substrates. Scale bars are labelled in the images. Compression and expansion isotherm of Langmuir film prepared from cluster of (e) high and (f) low $d_f$. Upwards and downwards arrows indicate compression and expansion cycle, respectively.

Similar phenomena were observed in the case of GO monolayers. Figure 5.13a and 5.13b presented compression-expansion isotherms of GO nanosheets and corresponding cluster structures captured by BAM. The insets are images of snapshots of BAM videos. The floating objects are GO monolayers on water reflecting incoming light (laser) and are shown as white region. It is clear that significantly less hysteresis phenomena were shown in the case of network-like 2D domains.

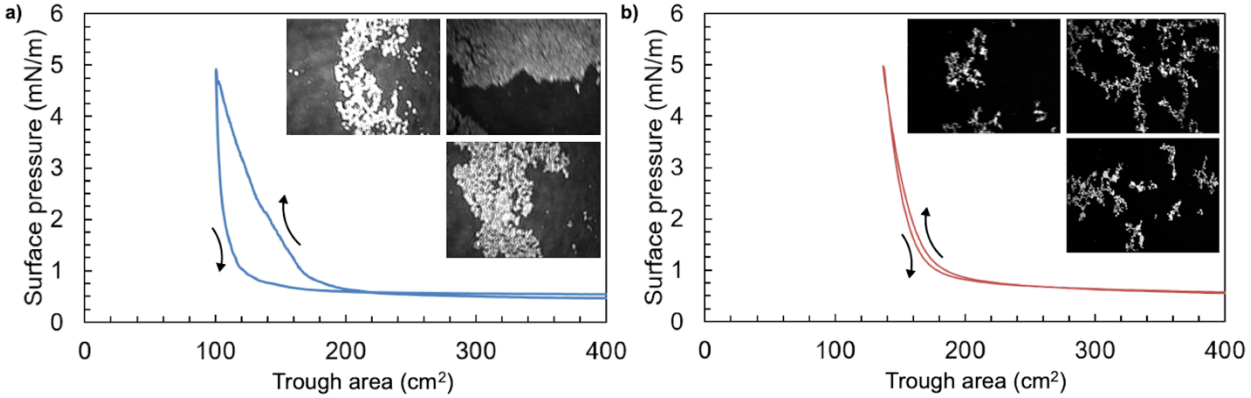



**Figure 5.13 Compression-expansion isotherms of GO nanosheets prepared from clusters of (a) island-like domains (0.025 mg/mL) and (b) linear networks (0.00625 mg/mL)**. Insets: corresponding cluster structures captured by BAM.

When comparing the two Langmuir film assembly methods, it is apparent that the linear void spaces (labelled by yellow arrows in Figure 5.12d) observed in *BCL* method are absent in *SSaL* films. This likely resulted from the unidirectional compression by the barrier, and thus suggests that our modified method has the advantage of allowing enough time for nanosheets to re-orientate themselves to achieve more uniform coverage.

We then investigated how films formed from different cluster shapes in response to over-compression. Figure 5.14a presents the surface pressure vs. area curves of Langmuir films prepared by the traditional *BCL* method from clusters of island-like domains ($d_f \sim 1.8$) and network clusters ($d_f \sim 1.54$). A plateau of ~ 39 mN/m was reached in both cases but with high $d_f$ clusters showing slightly earlier percolation of a rigid phase. This is likely because we transferred ~0.01 mg more material in this case. The compressional elastic modulus *K* (in the unit of mN/m) was extracted from surface pressure ($\pi$, in the unit of mN/m) vs. trough area ($A^*$, in the unit of $cm^2$) curves using the following equation: [28,200]

$$K = -A^* \frac{d\pi}{dA^*} \tag{5.8}$$

The plots of *K* vs. surface pressure are shown in the inset of Figure 5.14a. Langmuir films prepared from high $d_f$ clusters showed a sharper increase in elastic modulus *K* and yielded at a higher value (*K* ~ 90 mN/m vs. ~ 75 mN/m). This indicates that island-like clusters ($d_f \sim 1.8$) result in stiffer films during compression, likely due to inter-island jamming caused by the densely aggregated sheets. In other words, network clusters ($d_f \sim 1.54$) were more prone to rearrangement during compression, which is in line with the absence of hysteresis in the isotherm shown in Figure 5.12f. Furthermore, before the *K* value underwent a significant decrease above a surface pressure of ~30 mN/m, it exhibited a period of slow reduction in both cases. However, the changes in morphology appeared to be different. Films were collected when surface pressure was about 26 mN/m in both cases. The ones composed of island-like clusters ($d_f \sim 1.8$) displayed striations of darker regions in SEM where sheets collapsed to form thicker films (Figure 5.14b). These features are identified as buckling and folding. They appear in Langmuir films when compressed beyond their mechanical stability limit. The resulting transition from 2D to 3D usually marks the beginning of film collapse.[28,201] These buckling defects became more apparent when surface pressure was increased from ~30 mN/m to ~40 mN/m, showing as continuous 'long lines' in SEM

images that were parallel to the direction of compression (Figure 5.14c). The defects were examined under various magnifications and are presented in Figure 5.15a. On the other hand, films of low $d_f$, exhibited minimal buckling with much more scattered 'lines' of darker contrast perpendicular to the direction of compression (Figure 5.14e). More macroscopic features were visible only when the surface pressure exceeded ~30 mN/m and could be observed by the naked eye (Figure 5.15b). In summary, in the slowly decreasing region of *K*, rearrangement may continue to occur in the case of network clusters ($d_f \sim 1.54$), while film collapse has already started in films of island-like clusters ($d_f \sim 1.8$), resulting in buckling and 3D aggregations in the film. These results highlight the necessity of controlling the cluster structures in forming Langmuir films using traditional *BCL* method, as different cluster shapes respond to compression differently.

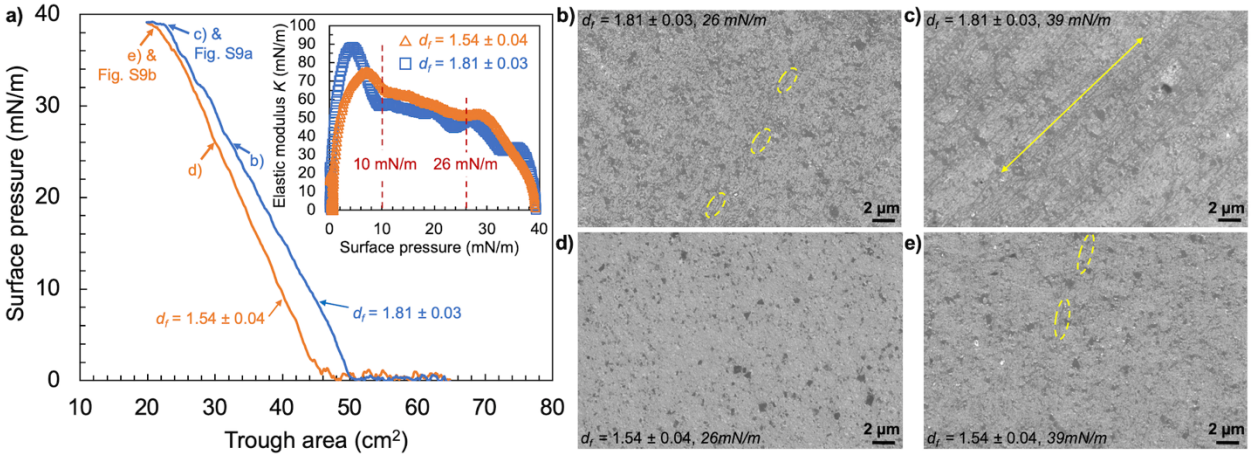



**Figure 5.14 Impact of cluster structure on the final Langmuir film of *ce*-$MoS_2$ (high compression)**: (a) Surface pressure vs. trough area curves of *ce*-$MoS_2$ films prepared by traditional barrier-compressed Langmuir (*BCL*) film method from cluster of high (blue line) and low (orange line) $d_f$. Inset: Compressional elastic modulus *K* as a function of the surface pressure obtained from the surface pressure vs. area curves of high (blue, ☐) vs. low (orange, △) $d_f$. The curves were smoothed (described in Methods Section) to show the overall trends better. SEM images of the Langmuir film prepared by *BCL* method from cluster of (b-c) high and (d-e) low $d_f$ at various targeted surface pressure indicated in (a). The films were deposited onto pre-treated $SiO_2$/Si substrates. Scale bars are labelled in the images. The yellow arrowed line in (c) highlights the direction of the buckling and yellow dashed-line circles in (b) and (e) pointed out examples of aggregations caused by buckling.

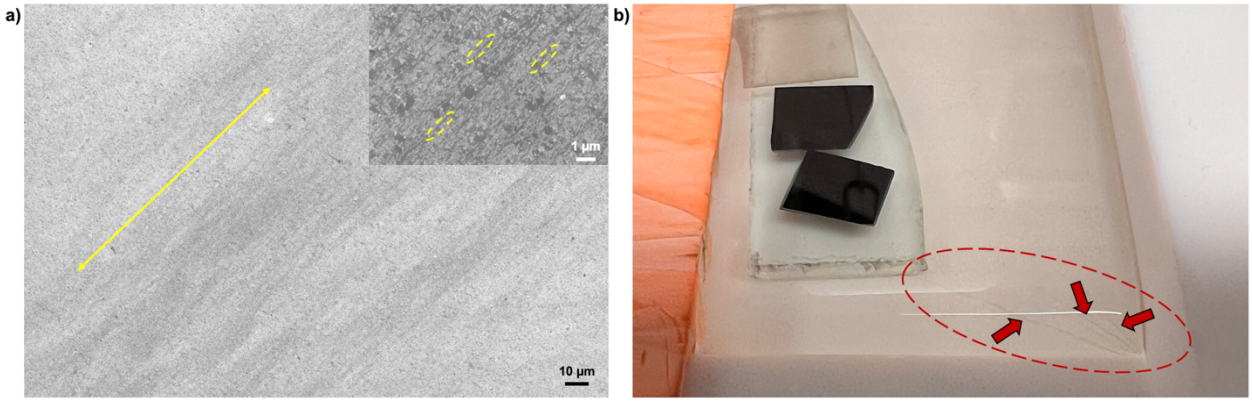



**Figure 5.15 Buckling shown in Langmuir films of *ce*-$MoS_2$ nanosheets when surface pressure reaches plateau**. (a) SEM images at low and high (inset) magnifications of films assembled from island-like cluster ($d_f$~1.8) under maximum compression (surface pressure: ~39 mN/m). The films were deposited onto pre-treated $SiO_2$/Si substrates. Scale bars are labelled in the images. The yellow arrowed line highlights the direction of the buckling and yellow dashed-line circles pointed out examples of aggregations caused by buckling shown in high magnification. (b) Macroscopic buckling captured in films prepared from network cluster ($d_f$~1.55) under maximum compression (surface pressure: ~39 mN/m). The red dashed-line circle and red arrows are used to guide readers' eyes to spot the buckling (grey lines).

## 5.4 Conclusions

In this work, we unveiled the spontaneous clustering behavior of various types of two-dimensional nanomaterials and the impact of these cluster structures on forming dense, uniform Langmuir films. A transition from island-like domains ($d_f$ ~ 1.8) to linear networks ($d_f$ ~ 1.54) can be easily achieved by tuning the dispersion concentrations and we proved that this concentration effect, which is better determined as sheet number density ($A/V$) in the spreading dispersion, is nearly universal regardless of material hydrophobicity and morphology. When preparing Langmuir film using the traditional barrier compression method, we unveiled that low-density clusters ($d_f$ ~ 1.54) required significantly higher target surface pressures for complete densification, likely due to the stronger repulsions between the linear clusters. On the other hand, by taking advantage of hundreds of compression and expansion cycles in a solvent-spreading assisted Langmuir film method, the low-density clusters ($d_f$ ~ 1.54) achieved a final coverage as high as 94%, which was almost 10% higher than what high density clusters ($d_f$ ~ 1.8) achieved. As for the clustering mechanism, previous reports have lacked any detailed discussion on this aspect. [26,27,115,116] Therefore, this is the first time a two-stage aggregation mechanism is proposed where the nanosheets first gather during the process of liquid spreading, resulting from the directional Marangoni flow. This creates favorable conditions for cluster formation. Then, nanosheets self-

assembled into network-like clusters at the air-water interface after leaving the spreading area while dense clusters (island-like) likely form within the spreading area due to drying (evaporation) processes. Even though a few previous reports have presented clustering of two-dimensional nanosheets into island-like domains and network structures,[22,28,118] this work expands the understanding of spontaneous clustering at the air-water interface and highlights impact on Langmuir film formation from zero-dimensional and one-dimensional nanomaterials to the two-dimensional sector.[7,18–23] As more work, including our own, has started modifying the traditional Langmuir-Blodgett assembly method to achieve large-area coatings,[32,36,67,176,202–205] it is crucial to identify and control the structures of the 'building blocks' (i.e., clusters) for continuous assembly of uniform, high-coverage films.

# Chapter 6: Study of Solvent Spreading and its Application in Roll-to-roll processing of 2D Langmuir film

## 6.1 Introduction

In **Chapter 3**, we showcased the potential of transforming a batch deposition using Solvent-spreading assisted Langmuir (*SSaL*) assembly approach into a roll-to-roll (R2R) processing to produce continuous coatings of densely tiled, 2D material films. Even though considerable efforts have been demonstrated in previous reports to convert LB or LS methods into R2R depositions (**Chapter 2, section 2.2.5**),[30–36] our method will lead to a simpler system with no requirements on external compression mechanism as well as eliminating the possibility of aggregations and overlaps due to over-compression. In **Chapter 3**, we hypothesized that the lateral force (pressure) exerted by solvent spreading is the driving force for film densification in the *SSaL* method and suggested that this spreading assisted in transferring the film to a substrate upon withdrawal from the coating bath. In this chapter, we carry out a more detailed investigation on how to control the spreading pressure using solvent mixtures and attempt to identify key factors involving solvent spreading that control film quality, consistency and ability to scale-up to wider coatings in the R2R manufacturing system.

The dynamics of solvent spreading have been historically studied by determining the location and speed of the leading edge. In the case of an infinite liquid source, previous literatures confirmed that for a non-volatile and immiscible spreading film, the location of the leading edge $L$(t) (in the unit of length) was found to follow the following scaling equation:

$$L(t) = K\frac{S^{1/2}}{(\mu\rho)^{1/4}}t^{3/4} \tag{6.1}$$

where $S$ is the spreading coefficient of upper liquid; $\mu$ and $\rho$ represent the subphase viscosity and density, respectively and $K$ is the dimensionless prefactor. The advancing speed of the leading edge, $KS^{1/2}/(\mu\rho)^{1/4}$, is controlled by $S$, which is solvent-dependent, and $K$ ranging from 0.665 to 1.52.[125] As for volatile, water-immiscible solvents, Dussaud *et al*. uncovered that the leading edge velocity increases with increasing spreading coefficient ($S$) whereas the speed of the reservoir

boundary showed negative correlation with vapor pressure of the solvent.[125] Kim *et al*. carried out a dynamic study of isopropanol (IPA) – a volatile, water-miscible solvent at the air-water interface and concluded that the spreading speed is not constant within the profile.[130] The results presented that the speed of the interface flow increases rapidly to the maximum followed by a rapid decrease until it reaches the edge of the static centurial lens where the IPA starts leaching out (Figure 2.16). The spreading was induced by Marangoni-driven mixing and the maximum spreading rate is suggested to be proportional to the surface tension difference between the spreading liquid and water and inversely proportional to the dynamic viscosity of the subphase liquid. When water-immiscible solvents like 1,2-dichloroethane (DCE) and chloroform spread at the water surface, a puddle forms which swirls rapidly around the water surface until the evaporation is complete. After being mixed with polar solvents like alcohol, a uniform, circular spreading behavior is observed. We presumed the spreading behavior could be similar to the pure solvent cases discussed earlier. However, there are no studies on the spreading of solvent mixtures at the air-water interface. Therefore, we determined the spreading profiles of solvent mixtures by using a custom-made Langmuir-Adam balance to directly measure the spreading pressures.

In this chapter, we first evaluate the spreading pressures of various combinations of solvents and investigated several potential factors that could tune the resulting pressures. Then, we study the impact of spreading pressure on film formation and quality. Additionally, we present the macroscopic flow patterns of single and multi-dripper systems and demonstrate the capability of producing wider coatings. Finally, we unveil that the wettability of substrate is the dominate factor that leads to a successful transfer of uniform, continuous, large-scale 2D Langmuir film via a roll-to-roll processing and that the role of solvent spreading is largely to macroscopically transport and densify the floating 2D materials at the location of substrate withdrawal from the coating bath.

## 6.2 Materials and Methods

### 6.2.1 Materials and spreading dispersions

1-butanol (Sigma Aldrich #34867, suitable for HPLC, ⩾99.7%); chloroform (Sigma Aldrich #34854, HPLC grade, amylene stabilized, evaporation residue ⩽0.0005%); t-butanol (Sigma Aldrich #19460, ACS reagent, evaporation residue ⩽ 0.001%); dichloromethane

(Honeywell # 494453, Biotech Grade, 99.9%, contains 40-150 ppm amylene as stabilizer); nylon substrate (GVS, 0.1 μm pore size); PES substrate (GVS, 0.1 μm pore size). Deionized water (MilliQ) was used in this work. All chemicals were used as received without any further treatment.

Please refer to **Chapter 5, section 5.2.1** for the rest of materials and to **Chapter 5, section 5.2.2** for experimental methods on material synthesis and spreading dispersion preparations.

Stock dispersion and spreading dispersion of graphene nanosheet used for R2R deposition can be found in previous literature.[4]

### 6.2.2 Instrumentation

#### **6.2.2.1** *Custom-made Langmuir-Adam balance*

The trough was filled with MilliQ water with the float naturally resting on the water surface. An Arduino breadboard was connected to a computer for power supply and custom-written source codes. Data were collected using CoolTerm software. The calibration curve was first generated by placing standard incremental weights on the calibration hook (Figure 6.1a) and recording the corresponding voltage values. A new calibration curve was collected every time when the subphase water was replaced. The schematic shown in Figure 6.1b illustrates the layout on the water surface. A movable barrier was placed at the starting position which is 10 cm away from the float. Multiple droplets were deployed at 1 cm away from the barrier at a slow rate to ensure that the voltage reading had enough time to return to the baseline between spreading. The barrier and dripper were then moved 1 cm closer to the float and spreading pressure was measured by repeating the dripping process. Final valves were obtained by averaging measurements obtained from at least 8-10 droplets and from experiments carried out on different days. Note that the measurements were carried out in a covered, dark but ventilated enclosure to eliminate the interference of the ambient light on the photodetector.

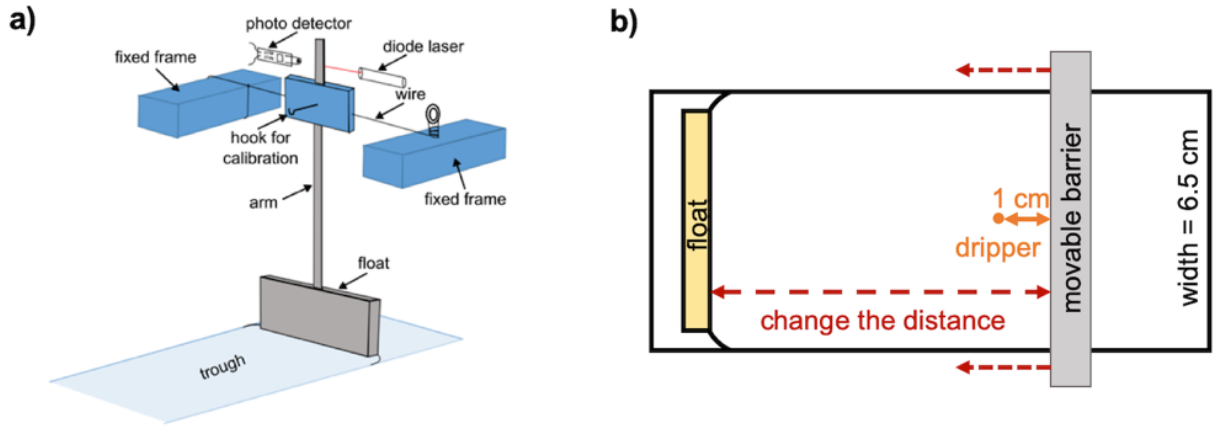



**Figure 6.1 Custom-made Langmuir-Adam balance**. Schematic illustration of (a) custom-made Langmuir-Adam balance and (b) the top view layout of float, dripper, barrier on a 6.5 cm wide trough.

#### **6.2.2.2** *Scanning electron microscopy (SEM)*

SEM was carried out using a Zeiss Leo 1530 scanning electron microscope with a 10 kV accelerating voltage on clusters and films transferred onto pre-treated $SiO_2$/Si substrates. In some cases, the brightness and contrast of the entire image was adjusted using ImageJ software.

#### **6.2.2.3** *Surface tension measurement*

Surface tension measurements were carried out using a flame cleaned, platinum Wilhelmy plate equipped to a Langmuir trough system (NIMA Langmuir Trough Model 312D).

## 6.3 Results and Discussion

### 6.3.1 Upgrade of Custom-designed Langmuir-Adam Balance

Figure 6.2a displays a schematic illustration of the original Langmuir balance. The measurement of surface tension was realized by placing incrementally increased weights in the pan (P) to counteract the surface tension difference between the pure water (H) and the contaminated water surface between A and D. In my MASc thesis, we detailed the original design with the aim to capture the dynamics of the spreading solvents.[206] The combination of a photo detector and diode laser allow sensitive detection captured as voltage changes caused by rapid deflections on the float resulting from droplet spreading and evaporation. However, the old setup was unable to obtain a linear calibration curve from 0 to 30 mN/m. Therefore, in my PhD work, the setup was upgraded to a circular laser source equipped with an adjustable filter to increase the

illumination area. A square shaped hole was used in front of the photo diode to ensure a focused laser signal which permits improved sensitivity. The wooden frames were also replaced with metal ones to eliminate the influence of solvent absorption. Figure 6.2b presents a photo of the upgraded setup when placed in the enclosure and the inset is a photo showing the key components. Compared to the old calibration curve (Figure 6.2c inset), the updated one (Figure 6.2c) showed significantly improved linearity between spreading pressure and the measured voltage. Note that since a narrow trough is used in this work to create a linear spreading front, a spreading pressure acting at the contacting line, in the unit of mN/m, is used to characterize the spreading profile which can be readily estimated by dividing the lateral force by the trough width (6.5 cm).

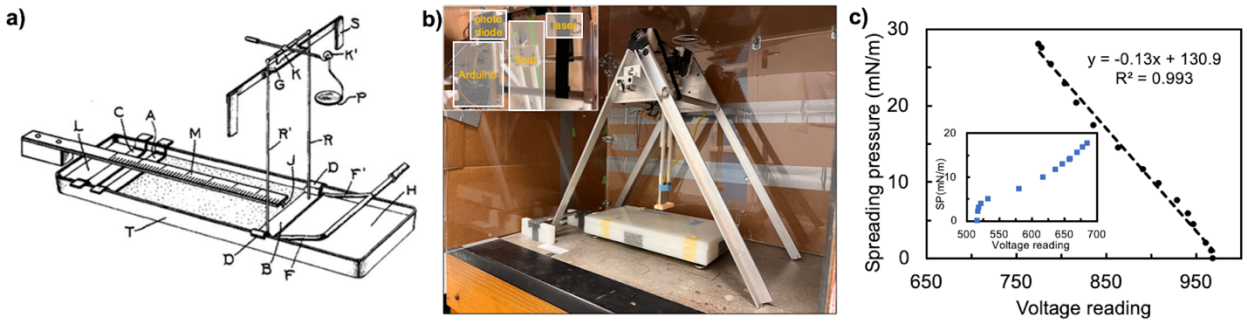



**Figure 6.2 Upgraded Custom-designed Langmuir-Adam Balance**. (a) A schematic of original design of Langmuir trough; (b) A photo of the upgraded custom-designed Langmuir-Adam balance. The inset is a photo taken from the left side of the apparatus showing the layout of Arduino circuit board, photo diode, top part of the float and laser. (c) A typical calibration curve obtained from the upgraded apparatus. The inset shows the old calibration curve

### 6.3.2 Study of the driving force of solvent spreading-assisted Langmuir film assembly (*SSaL*)

#### 6.3.2.1 *Physical properties of solvent mixtures*

Table 6.1 summarizes vapor pressures and surface tensions of the mixed solvents investigated in this work. These solvents were chosen based on our previous investigations and the known fact that alcohols and dimethylformamide (DMF) are common solvents for dispersing a variety of 2D materials while 1,2-dichloroethane (DCE), dichloromethane (DCM) and chloroform are common water-immiscible spreading solvents traditionally used to spread Langmuir films. The vapor pressures of the mixtures are estimated using Raoult's Law. Since the water-immiscible solvents are the dominant component in the mixture, the vapor pressure of the final solvent is largely impacted by the type of water-immiscible solvent used. We also measured the surface tension of some of the pure solvents and their mixtures. The surface tensions of the

various mixtures were found to lie intermediate to the two component values. The following section demonstrates our attempt to correlate the physical properties of the mixtures to the spreading pressures.

**Table 6.1 Physical properties of pure solvents and their mixtures**

| $V_A$:$V_B$ | A: dispersing 2D materials | B: water-immiscible | Vapor pressure (Pa) | Surface tension (mN/m) |
|---|---|---|---|---|
| - | Reagent alcohol (RA) | - | 5945 | 22.4 ± 0.2 |
| - | 1-butanol (BtOH) | - | 965 | 24.6 ± 0.3 |
| - | t-butanol (t-BtOH) | - | 5426 | n/a |
| - | DMF | - | 490 | 36.2 ± 0.8 |
| - | - | DCE | 11597 | 32.0 ± 0.2 |
| - | - | dichloromethane (DCM) | 21328 | n/a |
| - | - | chloroform | 47400 | n/a |
| **1 to 6** | RA | DCE | 10559 | 31.3 ± 0.1 |
| **1 to 6** | BtOH | DCE | 10263 | n/a |
| **1 to 6** | t-BtOH | DCE | 10823 | n/a |
| **1 to 6** | DMF | DCE | 9984 | 34.0 ± 0.1 |
| **1 to 13** | RA | DCE | 11066 | 32.1 ± 0.1 |
| **1 to 13** | BtOH | DCE | 10937 | n/a |
| **1 to 13** | t-BtOH | DCE | 11214 | n/a |
| **1 to 13** | DMF | DCE | 10789 | n/a |
| **1 to 13** | BtOH | DCM | 45034 | n/a |
| **1 to 13** | BtOH | chloroform | 20044 | n/a |

#### **6.3.2.2** *Spreading pressure profile of polar and water-immiscible organic solvent mixture*

The spreading pressures were evaluated as a function of available spreading distance by adjusting the location of the movable barrier, as the schematic illustrates in Figure 6.3a. We first recorded measurements for solvent mixtures used for GO and *ce*-$MoS_2$ films: RA/DCE and DMF/DCE. As the spreading distance is reduced, pure RA shows a gradual increase in spreading pressure until reaching the maximum value of 7.6 mN/m (Figure 6.3b). In contrast, after being mixed with DCE, a rapid increase is observed at 4-5 cm, which could indicate how far the mixture spreads out. By adding more RA into the mixture, the profile shape remains unchanged but with a ~12% greater maximum spreading pressure measured, yielding $20.9 \pm 0.3$ mN/m for RA/DCE (v:v = 1:6) vs. $18.7 \pm 0.2$ mN/m for RA/DCE (v:v = 1:13). As shown in Figure 6.3c, DMF/DCE

showed almost the same profile as RA/DCE does with a sudden increase from negligible pressure to the maximum, yielding 22-23 mN/m when approaching the droplet location. Compared to the RA/DCE cases, the onset of pressure increase occurs at a relatively further distance (7 vs. 5 cm), implying that DMF/DCE spreads over a larger area. The profile of DMF/DCE (v:v = 1:9) is also examined and the result lies perfectly in-between the curves of the other two ratios, indicating that higher spreading pressure can be generated from increasing the amount of the more polar solvent in the mixture. Furthermore, similar profiles are also observed from 1-butanol (BtOH)/DCE mixtures (Figure 6.3d). The mixture containing a volume ratio of $V_{BtOH}$:$V_{DCE}$ = 1:6 showed significant extension in spreading distance and force, showing ~4 mN/m as far as 9 cm away from the dripping position, where the edge of the trough is located.

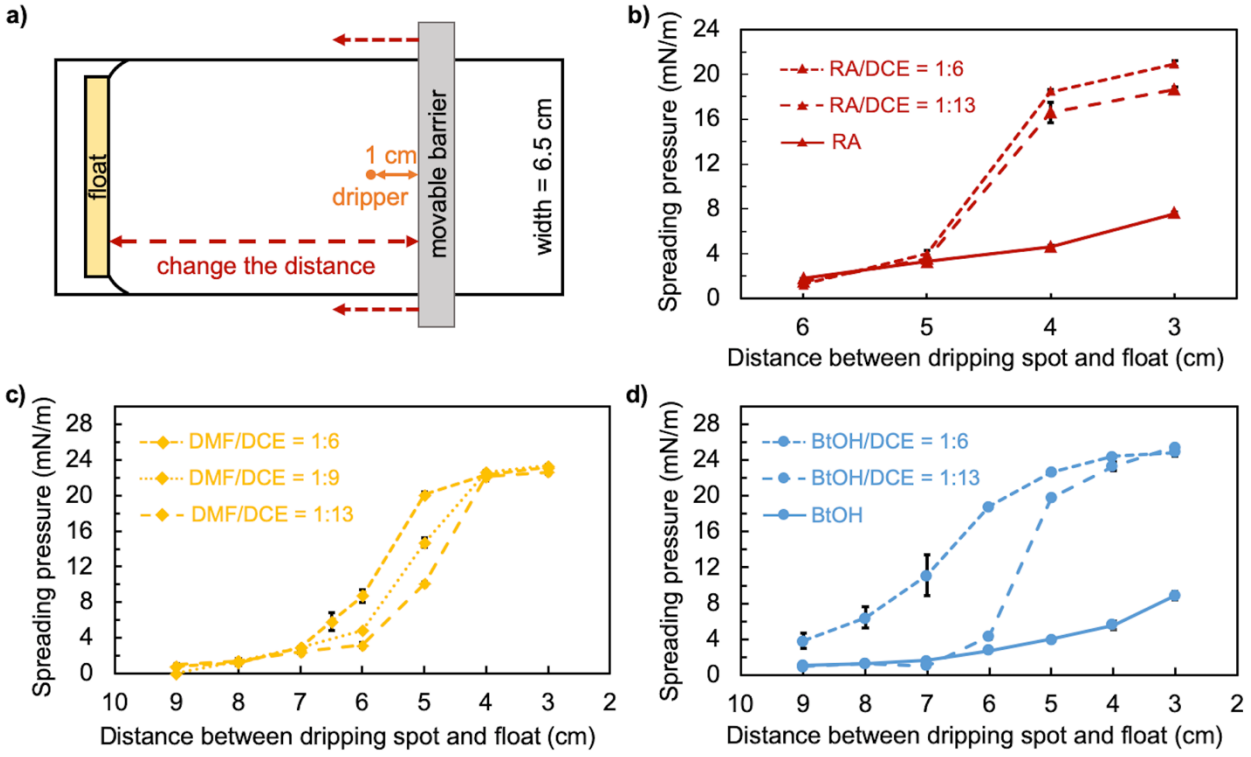



**Figure 6.3 Spreading profile of various polar and water-immiscible solvent mixtures**. (a) Schematic illustration of the layout of float, dripper, barrier on a 6.5 cm wide trough (top-view). Spreading pressure vs. distance between dripping spot and floater plots of (a) RA and RA/DCE mixture, (b) DMF/DCE mixture and (c) BtOH and BtOH/DCE mixture. The volume ratio between two components are indicated in the legends. Error bars are presented for each data point however some of them are too small to be visible.

Figure 6.4a summarizes the profiles of all mixtures containing volume ratios of v:$v_{DCE}$ =1:13 as well as corresponding pure solvents. Note that pure DMF is excluded in this study as it

is difficult to obtain accurate measurements, likely due to the changes in water surface tension cause by its high boiling point and water-miscibility. Compared to the mixtures, both pure RA and BtOH show only subtle changes in spreading pressure with distance confirming that the unique spreading behavior only occurs after mixing with the less polar, water-immiscible solvents. By comparing the scenarios of RA, DMF and BtOH, BtOH shows more rapid increase in spreading pressure vs. distance, achieving the highest maximum spreading pressure. We hypothesized that the higher spreading pressure is due to the immiscibility of BtOH with water. To test this, we compare DCE mixtures of 1-BtOH and t-BtOH. Unlike 1-BtOH which is only sparingly soluble in water, t-BtOH is highly water-miscible. However, as shown in Figure 6.4b we observe negligible difference in spreading profiles regardless of the dilution factors with DCE. This indicates that the water miscibility of polar solvents unlikely plays a dominate role on shaping the spreading profile.

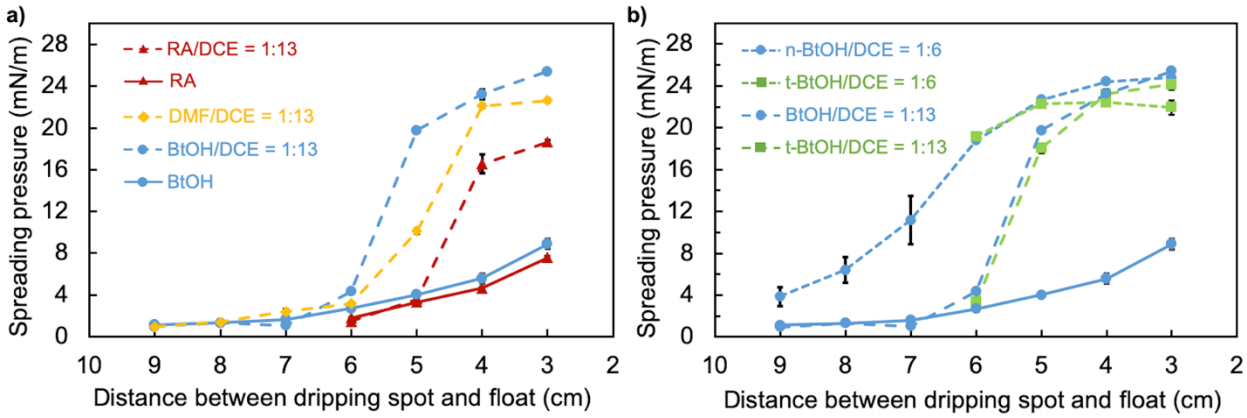



**Figure 6.4 Impact of polar solvent on spreading profile**. Spreading pressure vs. distance between dripping spot and floater plots of (a) RA, BtOH and DCE mixture with RA, DMF and BtOH at volume ratio of v:$v_{DCE}$ =1:13. (b) DCE mixture with n-BtOH and t-BtOH. The volume ratio between two components are indicated in the legends. Error bars are presented for each data point however some of them are too small to be visible.

We then investigated the impact of less polar, water-immiscible solvents while keeping 1-butanol (BtOH) as the minority component. DCE, chloroform and DCM, all have limited miscibility with water but their volatility varies considerably. As shown in Figure 6.5, mixtures with DCE exhibit a significantly higher spreading pressure at small distances compared to the other solvents which show only a small increase compared to pure BtOH. In contrast to DCE, chloroform and DCM exhibit two-fold and four-fold higher vapor pressure, respectively (Table

6.1). By using a more volatile non-polar solvent, the profiles show similar shape to those of pure solvents, which indicates that higher volatility reduces spreading pressure.

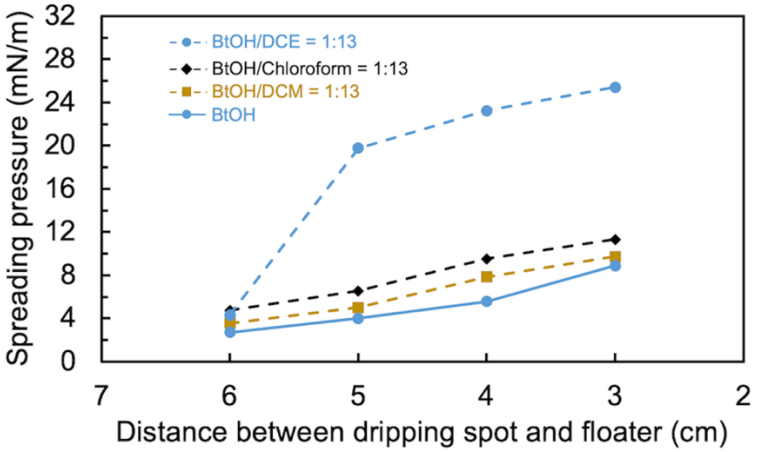



**Figure 6.5 Impact of water-immiscible solvent on spreading profile**. Spreading pressure vs. distance between dripping spot and floater plots of (a) BtOH and BtOH mixture with DCE, DCM and chloroform at volume ratio of $V_{BtOH}$:V =1:13. Error bars are presented for each data point. However, some of them are too small to be visible.

The spreading pressures measured within the range of 4-6 cm are summarized in Figure 6.6. In almost all scenarios presented above, a position of 4 cm away from the dripping position is where solvent mixtures spread to exert the maximum lateral pressure, while beyond 6 cm the lateral pressure is barely detected.

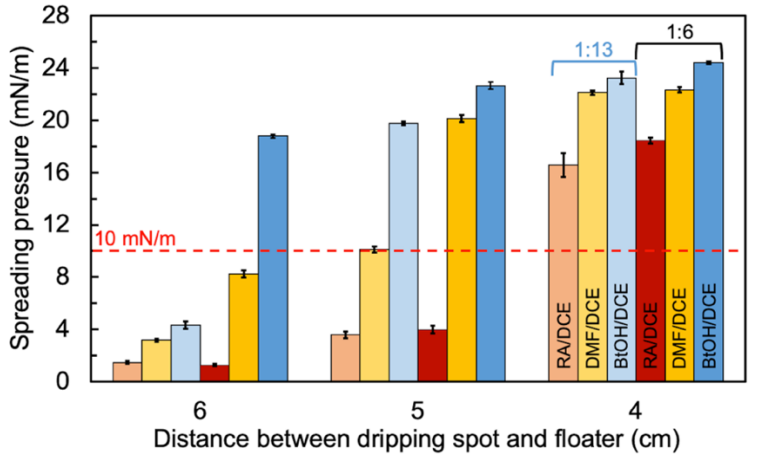



**Figure 6.6 Summary plot of spreading pressure measured at 4-6 cm away from the dripping position**.

Figure 6.7a and 6.7b plot the correlation of measured spreading pressures at 4 and 6 cm, respectively, with the calculated vapor pressure of the mixture. There is no apparent correlation between spreading pressure (*SP*) at 6 cm and vapor pressure ($P_v$). On the other hand, a clear

correlation of *SP* at 4 cm with $P_v$ is observed which we fit to the form of $SP \sim P_V^{-0.75}$. However, DCE-only mixtures do not show clear correlations (Figure 6.7a inset). Dussaud *et al*. presented that the spreading prefatory (*K*) (eqn. 6.1) of the reservoir region shows a power law correlation with vapor pressure. However, the referred reservoir region is much smaller than a radius of 4 cm.[125] The discrepancy is likely because our system is more complicated where the spreading is driven by various types of Marangoni effects including surface tension gradients, temperature gradients and solutal mixing. Thus, we are unable to perform a direct comparison to a pure solvent system.

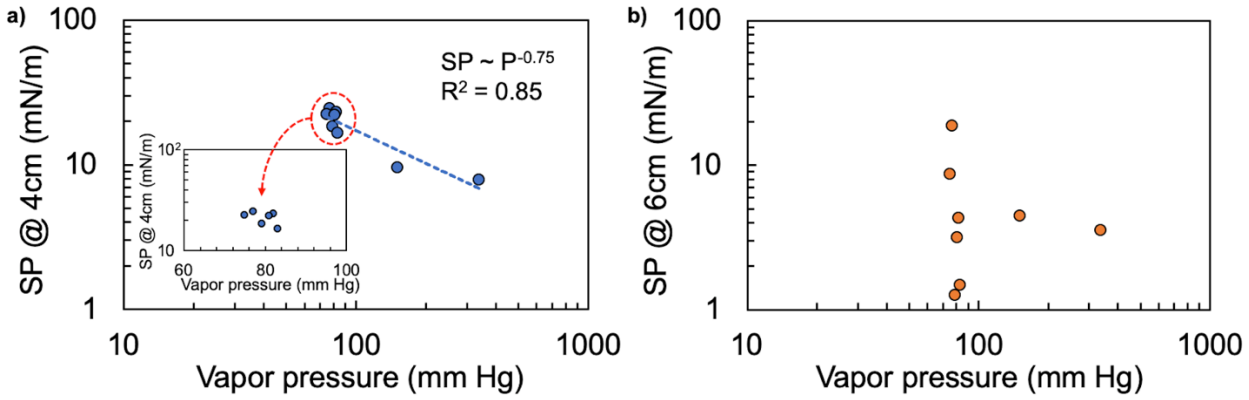



**Figure 6.7 Correlation between spreading profile and mixture physical properties**. Correlation of calculated vapor pressures of the mixtures and measured spreading pressures at (a) 4 and (b) 6 cm, respectively. The inset in (a) shows correlations from DCE mixtures only.

Since previous reports have also presented correlations between spreading profile and spreading coefficient (*S*), we attempt the same investigation in our mixture system. To estimate *S*, interfacial tension between the mixture and water is required. The pendant drop method is commonly used to determine the interfacial tension between two liquids. However, it cannot be used for our mixtures due to mixing between water and the polar solvents. Therefore, an alternative method is attempted where the interfacial tension is estimated using the Hansen solubility parameters (HSP). Unfortunately, based on the existing models and known parameters, we were unable to obtain satisfactory interfacial tension estimations between water and pure solvents within a reasonable difference compared to experimental results reported by others. Therefore, we decided to exclude this study from the scope of this thesis.

### 6.3.3 Impact of spreading profile on film assembly

When spreading lipids on a water surface, volatile, water-immiscible organic solvents such as chloroform and toluene are typically used. Since amphiphilic lipids are surface active, they can modify the surface tension and thus result in Marangoni flow during solvent evaporation that help chloroform and toluene to create a more uniform spreading and even distribution of lipids on water surface. However, 2D materials are unable to generate the same effect. Thankfully, our solvent mixture can result in uniform spreading by themselves besides providing high-yield transfer rate of 2D sheets. In the following section, we will investigate the impact of spreading pressure from the solvent mixtures on films formed by clusters with various densities.

#### **6.3.3.1** *Impact on Langmuir film packing density*

Film coverage of the resulting Langmuir film can be of great importance in the final application. As demonstrated in **Chapter 5 section 5.3.5**, cluster structure can play a crucial role on the final packing density. Since the spreading profile shows a decrease in lateral pressure along the spreading direction, it is important to investigate how the spreading force will assist the film densification as film grows from the edge of the trough to the dripping location. In other words, a uniform packing density across the film will imply sufficient compression which could be more ideal in R2R processing. Figure 6.8a-b and 6.8c-d present SEM images of the final film of *ce*-$MoS_2$ prepared using spreading solvents of DMF/DCE (v:v = 1:6), with samples examined at 9 cm (trough edge, *SP* ~0 mN/m) and 4 cm away (*SP* ~22.3 mN/m) from the dripper. Figure 6.8a-b are films prepared from linear clusters ($d_f$ ~1.54) whereas Figure 6.8c-d are from island-like clusters ($d_f$ ~1.8). A schematic illustration of sample locations is displayed in Figure 6.8g and the resulting film coverages are plotted in Figure 6.8h. In the case of high-density clusters ($d_f$ ~1.8), the film located at the edge of the trough has a packing density of 82.6 ± 0.4%, which is only 2% higher than that of island-like clusters themselves. As the film approaches closer to the dripper, an increase of 4% in coverage is observed (Figure 6.8d vs. 6.8c), suggesting that the maximum spreading pressure can densify the nanosheets located close to the spreading center. However, it is unable to penetrate through the solid *ce*-$MoS_2$ film composed of island-like clusters, likely due to the jamming effect. Similar phenomenon is also observed with rGO nanosheets, as presented in Figures 6.8e and 6.8f with the coverages summarized in Figure 6.8h. An increase of 4.5% in

packing density is obtained by *SP* ~16.6 mN/m. On the other hand, as for network-like clusters, by applying the same lateral pressure, i.e. using the same spreading solvents, the resulting films achieve a final coverage as high as ~94% regardless of the locations, which is ~9.3% denser than what can be achieved by high-density clusters (Figure 6.8d). This suggests that the maximum spreading pressure (16-22 mN/m) is sufficient for films composed of low-density clusters ($d_f$ ~1.54) but is not enough force to compress or restructure island-like cluster ($d_f$ ~1.8) into a dense film. However, in R2R processing, one may have to settle with relatively lower surface coverage (80-85%) to achieve a reasonable throughput since the coating speed is proportional to the dispersion concentration which increases cluster density. Discussion around the coating speed can be found in **section 6.3.4.2**.

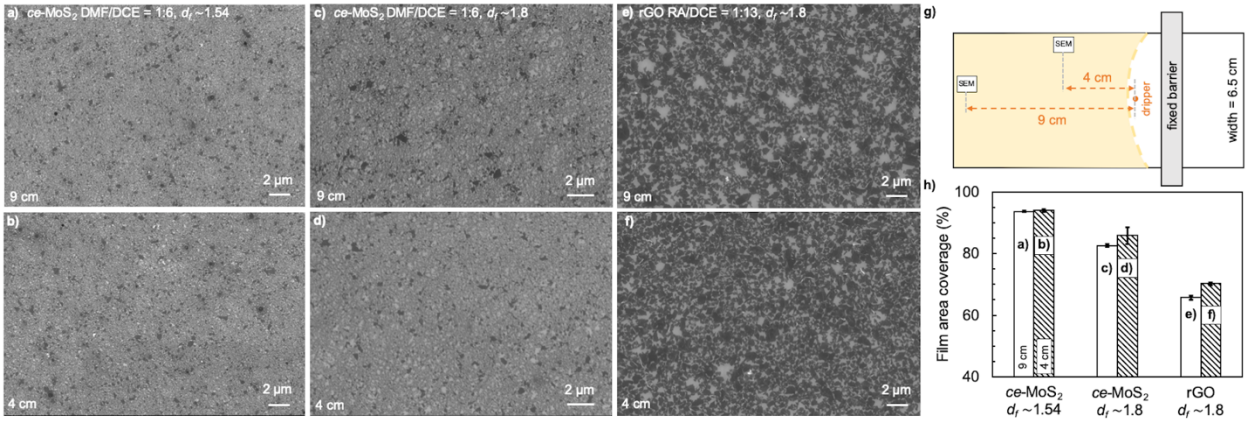



**Figure 6.8 Impact of spreading pressure on film packing density**. SEM images of the resulting film located at 9 and 4 cm away from the dripper and prepared from dispersion of (a) and (b) *ce*-$MoS_2$, $d_f$ ~1.54; (c) and (d) *ce*-$MoS_2$, $d_f$ ~1.8; (e) and (f) rGO, $d_f$ ~1.54. The scale bar is labelled in the images. (g) Schematic illustration of the sample locations in the resulting film (top-view) (h) Histogram summarizes the surface coverage of samples presented in (a-f) and the error bars are calculated from at least 3 samples.

### **6.3.3.2** *Impact on Langmuir film phase transition*

Even though the spreading pressure may not be sufficient to obtain dense coverage (> 90%), it is crucial to determine how fast the clusters will assemble into a solid film, which dictates when the floating film is Eventj. Figure 6.9 presents the formation of *SSaL* film of rGO using RA/DCE (Figure 6.9a-b) vs. BtOH/DCE (Figure 6.9c-d) with the volume ratio of $v:v_{DCE}$ = 1:13. Since BtOH/DCE provides higher spreading pressure and extended spreading distance, a macroscopically dense, solid film is obtained at a very early stage of the deposition (Figure 6.9c), while the island-like clusters from RA/DCE remain scattered for a significantly longer time period

(Figure 6.9a). As the solid films form in both cases, a curved growth in the case of RA/DCE while BtOH/DCE results in a linear boundary line, which would be more beneficial for R2R coatings as it indicates a uniform pushing force across the trough width. Note that since RA/DCE results in nearly linear spreading front in our regular trough (6.5 cm), an 8 cm wide trough was used in this experiment to magnify the impact of spreading solvents on the linearity of the growing boundary.

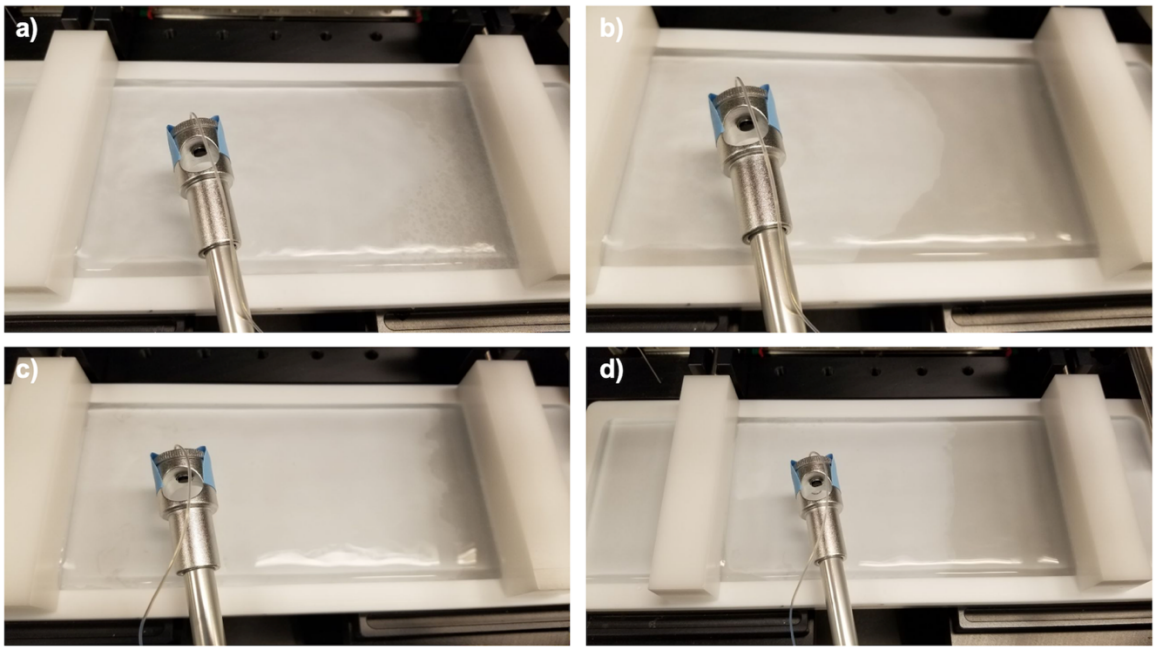



**Figure 6.9 Impact of spreading pressure on Langmuir film phase transition**. Snapshots of video taken through *SSaL* deposition of rGO using (a) and (b) RA/DCE vs. (c) and (d) BtOH/DCE with the volume ratio of $v:v_{DCE} = 1:13$. Note that an 8 cm wide trough was used in these experiments.

When forming the film using different cluster structures, we observed that low-density clusters delay the film solidification process on the water surface, in which case the floating film remains elastic (i.e., the floating film is reversibly compressed and expanded with every drop of spreading dispersion added to the coating bath) for an extensive time and in some cases never transforms into a solid film. This may not be an issue in batch deposition since movable barriers can be used for compression. However, it will significantly hinder continuous, R2R transfer processes. Therefore, we use relatively denser clusters to assemble R2R films even though the resulting spreading pressure is not sufficient for a high packing density (> 90%). Fortunately, we can easily conduct multiple depositions to fill remaining voids and achieve 100% surface coverage at the expense of slightly thicker films and longer processing times.

### **6.3.3.3** *Impact of number of drippers on wider film assembly*

Figure 6.10 presents snapshots of videos taken through rGO film formation on a wider trough using both a single-, double- and triple-dripper. Spreading dispersions containing RA/DCE (v/v = 1:13) were used. This formulation can result in a linear growth front of densely aggregated, edge-to-edge tiled 2D material on a 6.5 cm wide trough (Figure 3.9b). However, when the width is doubled, the growth front becomes circular (Figure 6.10b-d) which is incompatible with R2R coating since: 1) material accumulates and is wasted at the two sides; 2) the material cannot be pushed along the trough edges onto the substrate due to film jamming and insufficient spreading pressure to advance the floating film to the substrate. On the other hand, when double drippers are used, we observe that the overlaps of two spreading profiles creates a linear-like spreading boundary (Figure 6.10e-g). As for the RA/DCE and DMF/DCE formulations presented in this thesis, each dripper can adequately cover a 6.5 cm wide water surface. This can be verified by the scenario presented in Figure 6.10i-k where three dippers result in a linear growing boundary of rGO films on a 21 cm wide trough. Note that the distance between the drippers and front edge of the trough was kept at 9 cm in all the cases.

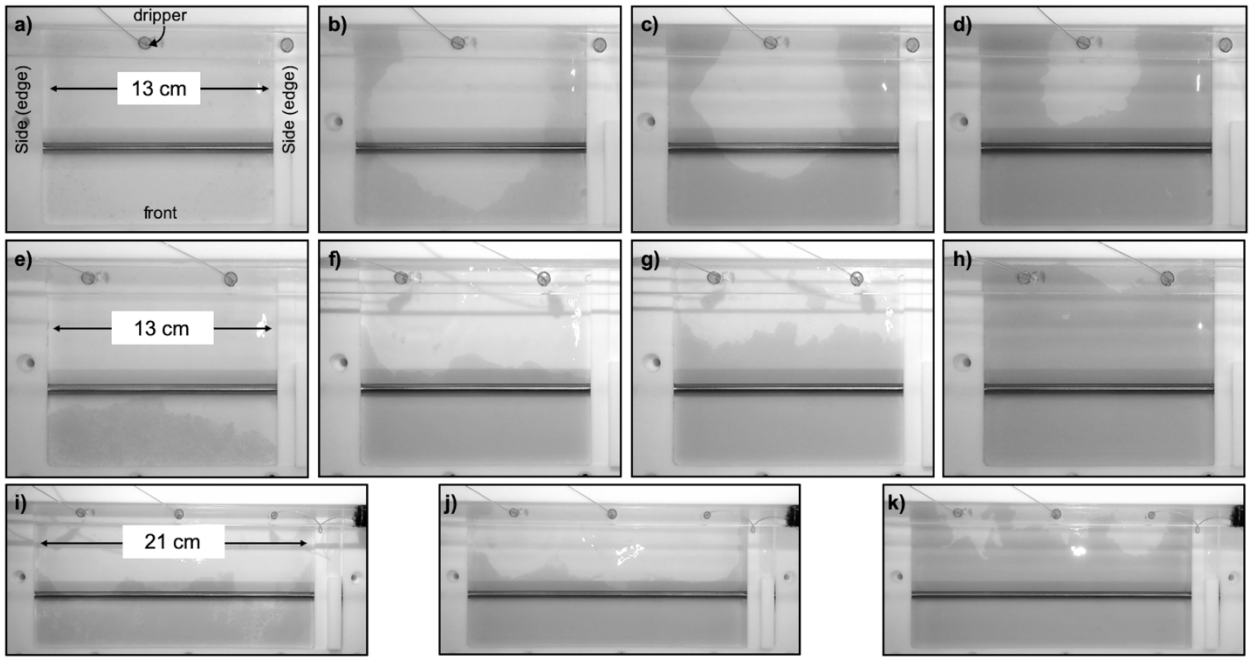



**Figure 6.10 Impact of number of drippers on wider film assembly**. Snapshots of video recorded through single- and multi-dripper depositions of rGO using *SSaL* method from RA/DCE (v/v = 1:13): (a-d) single-dripper, 13 cm wide trough; (e-h) double-dripper, 13 cm wide trough and (i-k) triple-dripper, 21 cm wide trough. The brightness and contrast of the images were adjusted.

### 6.3.4 R2R Coatings of 2D Langmuir films

The R2R processing can be divided into three sections: 1) Formation of solid film at the air-water interface; 2) Transfer of the resulting film onto the substrate and 3) Film Drying. As for traditional coating methods such as slot-die and roll coatings, the coating qualities are typically evaluated by three criteria: coating dry weight, cross-web (substrate) uniformity and coating adhesion. Economically speaking, it is also important to achieve high coating speed (>10 m/min) and flexible coating width. Since traditional coating methods have yet able to deliver single-layer deposition of 2D sheets, our development will focus more on overcoming obstacles that prevent continuous film formation and transferring and less on achieving ultimate film quality. In previous discussions, we have highlighted the importance of using solvent mixtures as spreading solvents to boost spreading pressure which will benefit faster transition into solid floating films and provide as much pushing force as possible for continuous film transfer. Here, we uncover the importance of substrate wettability by water for continuous film transfer.

#### **6.3.4.1** *Importance of substrate wettability*

Regardless of cluster structure and spreading profile, wettability of substrate by water is found to be a more dominant factor for obtaining macroscopically uniform film in the R2R coating process. Figure 6.11a-c present snapshots of videos recorded through R2R deposition of *ce*-$MoS_2$ film on a hydrophobic polyethylene terephthalate (PET) substrate. The concentration of *ce*-$MoS_2$ spreading dispersion in DMF/DCE (v:v = 1:6) was 0.057 mg/mL and the coating speed was 1 cm/min. The yellow arrows in Figure 6.11a indicate the growth front of the film and the black arrow represents the direction of rewinding PET (web). As R2R coating proceeds, a crack starts to form at the corner of the floating film and then extends towards the center, highlighted by the red dashed-line circle in Figure 6.11b. The crack eventually caused the floating film to break off (Figure 6.11c) and force the continuous deposition to cease. Fortunately, this issue can be easily resolved by using a hydrophilic substrate instead. Figure 6.11d displays a resulting R2R film of *ce*-$MoS_2$ on nylon substrate. Since water can easily wet the nylon completely, a uniform coating was obtained over a length of over 12 inches without changing any other parameters such as spreading dispersion formulation and coating speed. The same impact was also obtained in the case of hydrophobic materials. Figure 6.11d presented R2R film of graphene nanosheets on

plasma-treated and non-treated PET. Before treatment, water will easily break into droplets and roll off PET surface resulting in a patchy film (Figure 6.11e right). After the surface treatment via air plasma, water can easily spread into a layer of thin film on PET and the resulting film is free of macroscopic defects (Figure 6.11e left). The small crack observed along the two sides were likely due to insufficient wettability of the treated PET and can possibly be resolved by using a double-dripper to provide enough spreading force to move the solid film which eventually gets jammed on the sides of the trough.




**Figure 6.11 Impact of substrate wettability by water on film quality prepared using R2R processing**. (a-c) Snapshots of video taken through R2R deposition from *ce*-$MoS_2$ dispersion (DMF/DCE, v:v = 1:6) on hydrophobic PET substrate. The yellow arrows point at the growing front of the film and the black arrow indicates the direction of rewinding PET. (d) R2R deposition from *ce*-$MoS_2$ dispersion (DMF/DCE, v:v = 1:6) on nylon substrate. (e) R2R deposition from graphene dispersion (DMF/DCE, v:v = 1:3) on plasma-treated and non-treated PET substrate.

### **6.3.4.2** *Coating speed of SSaL-R2R processing*

By using the uncorrected *LSSA*, *u-LSSA* (Figure 5.6g and Table 5.8), a concentration of $c^*$, a dripping rate of $r$ in the unit of mg/mL and a width of the continuous coating bath as $d$ = 6.5 cm, the film growth speed can be utilized to estimate the R2R coating speed according to:

$$v = \frac{LSSA \cdot c^* \cdot r}{d} \tag{6.2}$$

**Table 6.2 Summary of *SSaL*-R2R coating speed**

| Stock | *c** (mg/mL) | *u-LSSA* ($m^2$/g) | Batch coverage (%) | *r* (mL/min) | *d (cm)* | *v (cm/min)* |
|---|---|---|---|---|---|---|
| ***ce*-$MoS_2$ in DMF** | 0.057 | 140 | 85.9 ± 2.7 | 0.1 | 6.5 | 1.2 |
| ***ce*-$MoS_2$ in DMF** | 0.011 | 138 | 94.00 ± 0.4 | 0.1 | 6.5 | 0.2 |
| **GO in RA** | 0.025 | 440 | ~ 88% | 0.13 | 6.5 | 2.2 |
| **rGO in DCE** | 0.18 | 75 | ~ 70% | 0.13 | 6.5 | 2.7 |

Table 6.2 summarize the estimated coating speed for inks used in this thesis. The coating speed could foreseeably be increased by enhancing the evaporation rate of the solvent through increased temperature or gas flow as well as by using a second dripper (double the speed) or more. Furthermore, the system requires only a water bath which means that many coating baths could be operated in parallel at negligible capital cost if increased throughput is necessary. The coating velocity is comparable to other LB-based R2R deposition that yields monolayer coating of 1D materials (maximum of 6 cm/min).[35,36] It can also be compared to high temperature (~ 1000 °C), high capital cost R2R CVD growth and transfer systems. By this method, maximum coating velocities of 10 cm/min have been achieved with graphene and the resulting film consisted of sub-micron crystallite size yielding a sheet resistance of 500 Ω/sq before doping.[207]

**6.3.4.3** *Resulting R2R films*

Figure 6.12a shows a photo of Evercloak's R2R setup (Generation 2) with labeling of the unwind and rewind rolls. Tension can be applied manually on the unwind roll. A computer-controlled motor is used to drive the collection of coated substrates. The initial drying of the coating is carried out by using an infrared lamp. Figure 6.12b illustrates a top-down view of the crucial components for carrying out R2R coating. As for R2R coatings of GO, a double-dripper is used to provide sufficient spreading pressure to overcome resistance along the trough edges and prevent accumulation along the two sides and a coating speed of 4 – 4.5 cm/min is used. This resulted in a successful continuous transfer of GO films from the water surface to the substrate. Polyethersulfone (PES) membrane was chosen due to their flat surface and moderate pore size (< 2 μm), which is smaller than the average GO size. Figure 6.12c presents a photo of PES coated with ten depositions of GO Langmuir films in comparison to a bare substrate. A slight tint in color appears in the coated sample. SEM images of bare PES and GO coated PES (10 depositions) are

displayed in Figure 6.12d and Figure 6.12d-g, respectively. The majority of holes are covered by GO monolayers and the surface texture of PES substrate remain apparent. This suggests that the double drippers did not result in any 3D aggregations and the flexible GO monolayers are able to conform to the substrate surface texture. Examples of remaining holes are indicated by yellow dashed-line circles in Figure 6.12e and 6.12g, likely because the local pore size is significantly larger than the GO sheet size causing the sheets to fall through the holes. We attempted to use the resulting films for water-vapor selective membrane applications. However, ten depositions of atomically thin GO are not sufficient to hinder air permeation and leads to undesirable selectivity.

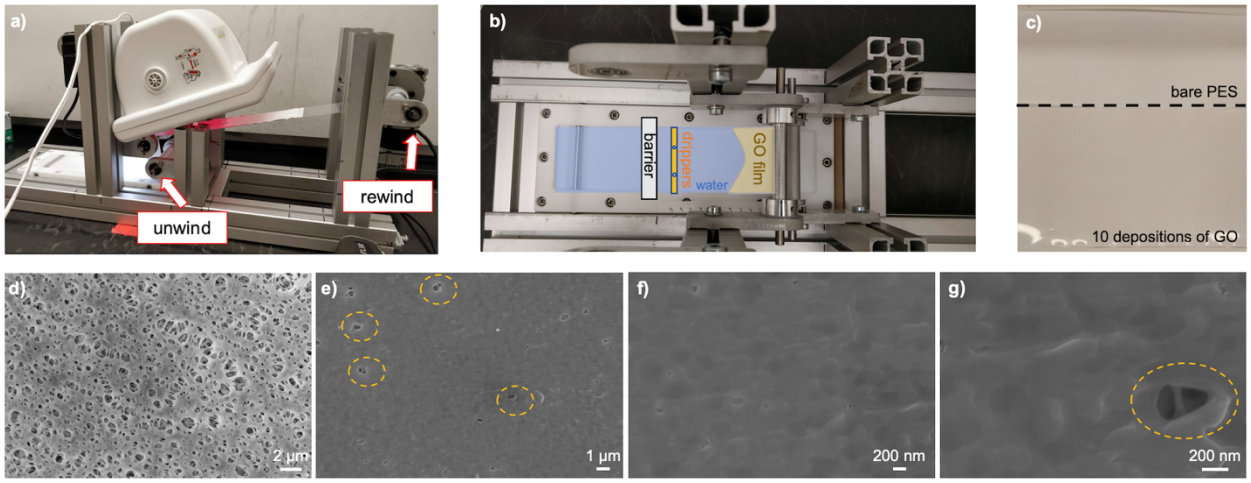



**Figure 6.12 Resulting 2D films by *SSaL*-R2R processing**. (a) A photo of Everlcoak's R2R setup (Generation 2) (b) Layout of the critical components for R2R deposition from the top view. (c) A photo of a portion of GO coated and non-coated PES substrates. SEM images of (d) bare and (e-g) GO coated PES substrates shown in (c). Scale bars are labelled in the images.

Figure 6.13 shows a R2R processing of wider coating realized by using a multi-dripper setup. The demonstration is carried out by using rGO nanosheets (RA/DCE, v/v = 1:6) for the best visualization. With a double-dripper setup, a coating as wide as 7.8 inches was achieved, as the resulting film shown in Figure 6.13b. Cracks/defects along the two sides of the film are likely due to insufficient spreading pressure at the far trough edges and can be easily resolved by adding more drippers as demonstrated in Figure 6.10i-k.

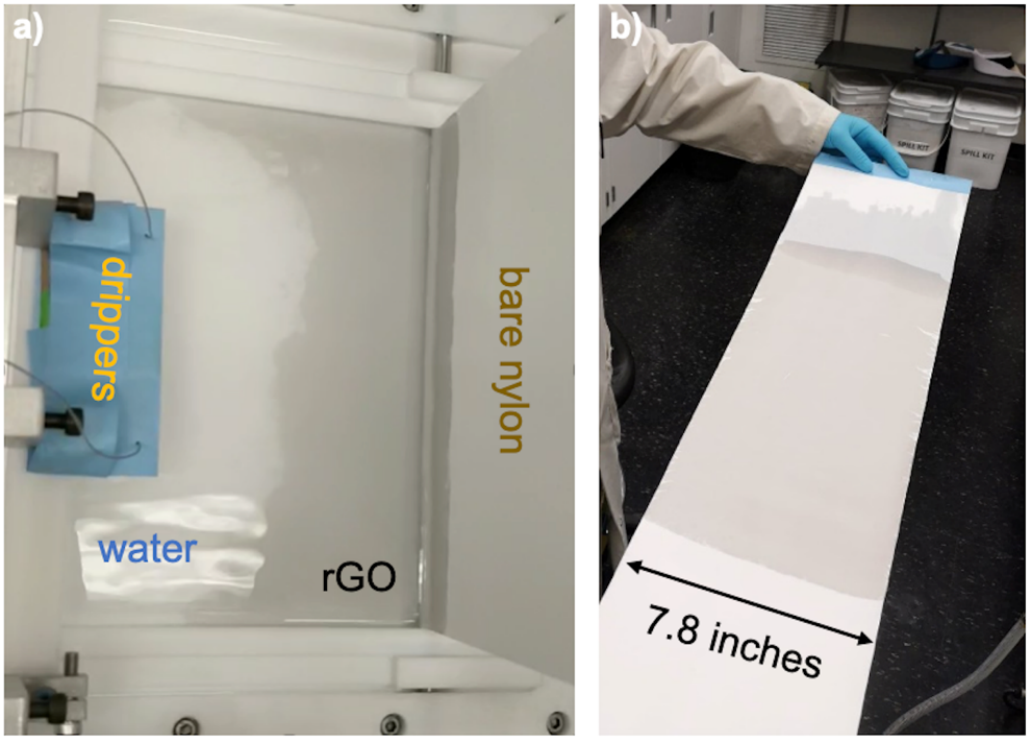



**Figure 6.13 Resulting 2D films by *SSaL*-R2R processing on wider trough**. (a) Snapshots of video taken through deposition of rGO using a double-dipper setup to obtain wider coatings on nylon substrate (b) A photo of the resulting rGO coatings on a 7.8 inches wide nylon substrate via R2R processing shown in (a).

## 6.4 Conclusion

In this chapter, we examined the spreading profiles of various solvent mixtures and investigated the impact of solvent spreading on film assembly. A spreading distance dependent spreading pressure is observed in all the polar and water-immiscible solvent mixtures investigated which is absent in the pure solvents. Compared to RA/DCE mixtures, both DMF/DCE and BtOH/DCE exhibit extended spreading distance and larger spreading pressures which are beneficial in the R2R deposition to achieve continuous, crack-free films. As for a certain mixture, increasing the amount of the more polar solvent results in an increase in the maximum spreading pressure and increases the spreading pressure at further distances. By investigating the macroscopic flow of the multi-dripper system, wider coatings can be enabled by overlapping the spreading patterns from several single spreading drippers. The resulting directional flow forms a linear film growing front which is beneficial for R2R deposition. Even though the spreading pressure can lead to significantly higher packing density in the resulting films assembled from low-density clusters, but not from high-density clusters, the latter ones are used for R2R processing

because they form solid film early and provide five times higher throughput (see Table 6.2). In a R2R deposition, the wettability of substrate by water is proven to be more important in achieving continuous coating with minimal macroscopic defects. Our *SSaL* based R2R processing is capable of assembling large-scale films of various exfoliated 2D materials including graphene, GO, rGO and *ce*-$MoS_2$ at nearly any coating width. Since this method only requires a syringe pump and glass/Teflon trough, we expect the procedures described can help researchers explore deposition of ultra-thin films of various emerging nanomaterials to engineer both monolayer and heterostructure devices based on unique properties of 2D materials which are typically only exhibited when they are one or few-layer in thickness.

# Chapter 7: $MoS_2$ Langmuir film for perovskite solar cell

## 7.1 Introduction

Perovskite solar cells (PSCs) have emerged as the next-gen solar harvesting devices which capture renewable energy more efficiently thanks to the superior material nature and low-cost, solution-based fabrication process. During the past decade, PSCs have broken the power conversion efficiency (PCE) record several times, achieving up to 25.5% for a single junction device.[111] The high efficiency is contributed by the direct bandgap (~1.5 eV), high carrier mobilities, and long carrier diffusion length of perovskite materials. Despite promising performance, long-term stability and scalability remain as the major constraints that prevents PSCs from entering the everyday market.

PSC is usually constructed by several layers of functional solids and the two most common configurations are n-i-p (conventional) and p-i-n (inverted). In both configurations, a transparent conducting oxide (TCO) substrate and metal electrodes are on the bottom and top, respectively. The perovskite layer is located in the middle and sandwiched between two carrier-transport layers. In a n-i-p based device, an electron-transport layer (ETL) is laid right above the TCO with a hole-transport layer (HTL) located underneath the metal contacts, whereas an inverted device (p-i-n) has an opposite layout. No matter which configuration is used, perovskite layer absorbs the light and generates electron-hole pairs. The ETL and HTL play crucial roles to extract the corresponding carriers which flow in the circuits to generate electricity. In a p-i-n based PSC, poly(3,4-ethylenedioxythiophene):polystyrene-sulfonate (PEDOT:PSS), has been widely used as HTL, attributed to its high hole mobility and facile solution-based processability. However, its intrinsic acidity and hygroscopic effect can cause degradation on TCO electrodes and perovskite layer, resulting in significant reduction in device lifetime.

Inorganic TMD material such as $MoS_2$ has good hole mobility and broad, tunable band gap that can be compatible with valence bands of perovskite and commonly used organic hole transport materials (HTM) such as spiro-OMeTAD, PEDOT:PSS and poly(triaryl amine) (PTAA). Therefore, it has emerged as a popular HTL and interfacial layer in PSC. Compared to organic HTM-based devices, researchers have unveiled that by implementing 1T or 2H $MoS_2$ the resulting

PSC devices demonstrated not only 2-3% improvement on PCE, but also significant enhancement in stability and long life-time.[44–46,48] A simulation work carried out by Kohnehpoushi *et al*. uncovered that the thickness of $MoS_2$ layer has a critical impact on the device performance, suggesting an optimum thickness ranging from 0.67 – 5.36 nm.[47] However, so far researchers have only reported studies based on $MoS_2$ film prepared by spray- and spin-coating – methods that lack such a sophisticated level of control over film thickness and uniformity. In this chapter, we attempt to implement large-area Langmuir films of *ce*-$MoS_2$ monolayers as HTL in p-i-n type perovskite solar cell. The coating thickness will be precisely engineered via layer-by-layer deposition. By taking advantage of the work conducted in previous chapters, we expect that the resulting HTL can be easily fabricated via R2R processing on a flexible substrate which would advance large-scale manufacturing of the perovskite solar cells.

## 7.2 Experimental Methods

### 7.2.1 Preparation of FTO substrate

Prepatterned fluorine-doped tin oxide (FTO) was first cleaned by detergent and then bath-sonicated (Fisher Scientific Ultrasonic Bath, 110 W 40 kHz ± 6%) in acetone (ACS reagent, Sigma-Aldrich), isopropanol (ACS reagent, Sigma-Aldrich), and DI water for 10 mins, respectively. After bath sonication, the substrates were dried using a nitrogen gun ($N_2$ gas, 99.99%) followed by 20 min of air plasma cleaning (HARRICK PLASMA, PDC-001-HP, HI power setting).

### 7.2.2 *SSaL* deposition of *ce*-$MoS_2$ and annealing treatment

Please refer to **Chapter 5 section 5.2.2.3 and 5.2.2.4** for experimental details on the preparation of stock and spreading dispersion. Please refer to **Chapter 5 section 5.2.2.5** for experimental details on the preparation of deposition methods. Two coatings of *ce*-$MoS_2$ film were deposited in this work and note that before depositing the 2$^{nd}$ layer of *ce*-$MoS_2$ film, the sample was dried in 75 °C oven overnight to ensure that the 1$^{st}$ layer would not come off after placing it back underneath the water of the coating bath.

**Annealing treatment** After depositing the 2$^{nd}$ layer of *ce*-$MoS_2$ film and the film was air-dried for 3-5 hours. The sample were transferred into a tube furnace (Thermo Scientific™ Lindberg/Blue M™ Mini-Mite™ Tube Furnace) for annealing treatment. Ar gas (99.999%) was

flew through the tube at 1.5 LPM for 20 min and the flow was maintained at the same rate throughout the annealing and cool-down process. Then the furnace was ramped to 200 °C at 10 °C/min rate and held at 200 °C for 2 hours. After the furnace being naturally cooled, the samples were collected for further depositions.

### 7.2.3 Fabrication of perovskite solar cells

Inverted (p-i-n) perovskite solar cell were fabricated with the structure of FTO/$MoS_2$/ MAPbI3/$PC_{61}BM$/BCP/Ag. Annealed FTO/$MoS_2$ were transferred into a nitrogen-filled glove box for depositing other layers. Inside the glove box, a mixture of N, N-dimethylformamide (DMF, Sigma Aldrich, HPLC grade, ⩽0.030% water)/dimethyl sulfoxide (DMSO, Sigma Aldrich, HPLC grade, ⩽0.2% water) was first prepared by mixing DMF and DMSO in a volume ratio of 9:1. Then, 1 M $PbI_2$ solution was prepared by dissolving $PbI_2$ powder (Alfa Asear, 99.99%, ultra-dry) in the pre-mixed DMF/DMSO solution. The dispersion was kept stirring at 70 °C overnight. 1 M MAI (Great Solar) was dissolved in IPA and stirred for 1 h at room temperature. The perovskite thin film was prepared by a two-step spin-coating technique carried out over the course of 60 sec at 4000 rpm, with 40 μL of $PbI_2$ dispersion being dropped at the $10^{th}$ sec of spinning followed by MAI (40ul) being added after 30 sec of spinning. Then, the FTO/$MoS_2$/ MAPbI3 was annealed at 65°C for 2 min and 100°C for 3 mins. To deposit ETL, 20 mg/ml of $PC_{61}BM$ in chlorobenzene (Xi'an Polymer Light Technology Corp) was spin-coated onto the $MAPbI_3$ thin film at 1500rpm for 30 sec, followed by heating at 100 °C for 8 min. Subsequently, 0.75mg/ml of bathocuproine (BCP) in IPA (Xi'an Polymer Light Technology Corp) was spin-coated onto PCBM at 5000 rpm for 20 sec. Lastly, the 100 nm silver layer was deposited via a thermal evaporation process.

### 7.2.4 Characterization

**Characterization of photovoltaic performance of the cell** The current density–voltage ($J-V$) curves of the devices were measured using a Keysight 3458A Digital multimeter under the AM 1.5 G (one sun illumination, 100 mW $cm^{-2}$), generated from a Xenon lamp-based solar simulator (Newport Oriel Instrument 67005, 150 W Solar Simulator). The light intensity was calibrated by an NREL-calibrated KG5 silicon reference cell to minimize spectral mismatch. All $J-V$ measurements were recorded with a scan rate of 100 mV $s^{-1}$.

## 7.3 Results and Discussion

Figure 7.1 presented the forward-bias $J - V$ curves of $MAPbI_3$ devices with and without $MoS_2$ film as HTL. The device structure is shown as the inset in the figure. Compared to a device without HTL, our two-layers thick $MoS_2$ Langmuir film achieved doubled open-circuit voltage ($V_{oc}$), which is in line with the prediction presented by Kohnehpoushi *et al.*[47] This suggests that a fair amount of light-generated electron and hole pairs have been separated and collected successfully. However, in this initial trail, the resulting $J_{SC}$ is much lower than literature values, which can be explained by two dominant causes: 1). The thickness of the perovskite layer is yet optimized – too thin of a coating limits the current generation whereas too thick of coating leads to high recombination rate which also hinder current generation. 2). The interface between layers is not yet optimized – defects, particularly at the surface of $MoS_2$, can favor recombination of electron and hole pairs resulting in loss of current density. A previous report has recommended to anneal $MoS_2$ films in the presence of sulfur powder to heal defects which could potentially yield higher performance.[149]

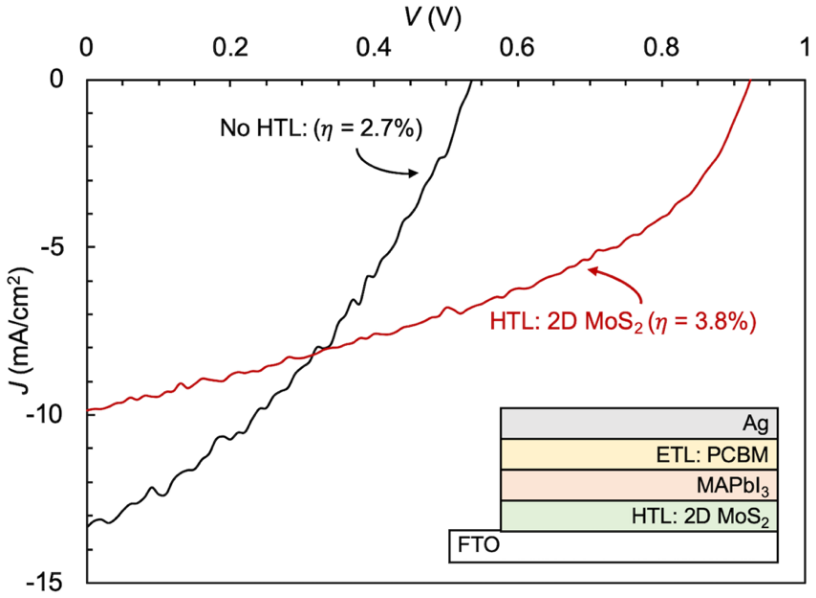



**Figure 7.1 Forward-bias $J - V$ characteristics of PSC with and without $MoS_2$ film as HTL**. The inset is a schematic illustration shows the configuration of the perovskite solar cell.

## 7.4 Conclusion

In this chapter, we showcased the potential of using the $MoS_2$ Langmuir film as HTL in perovskite solar cell (PSC) and the preliminary result showed promising enhancement in $V_{oc}$ which suggested successful separation of light-generated electrons and holes. Further work is required in various aspects, including optimization on the thickness and polymorph of $MoS_2$, optimization on the perovskite layer and study of long-term stability. We expect that this $MoS_2$-based HTL layer can be easily implemented into large-scale manufacturing of flexible PSC by using the R2R processing demonstrated in **Chapter 6**.

# Chapter 8: Summary and Recommendations for Future Studies

## 8.1 Summary of Main Conclusions

In this thesis, we presented a LB-modified coating method – Spreading-solvent assisted Langmuir (*SSaL*) assembly, that is capable of depositing single layers of exfoliated 2D materials onto large-area substrates with finely tuned material (ink formulation), building block (cluster structure) and driving force (spreading pressure). We demonstrated the benefit of using a mixture of polar and water-immiscible solvent to form 2D materials ink which permits high-yield delivery of 2D materials for Langmuir film assembly regardless of the material hydrophobicity. During the systematically investigation of aqueous dispersions of *ce*-$MoS_2$, we unveiled a light-accelerated, rapid degradation behavior for both dispersed 1T $MoS_2$ and 2H $MoS_2$ when exposed to ambient air/oxygen and alkaline media. Soluble molybdates were observed to be the main degradation product in alkaline solution which resulted in morphology changes in sheets to small fragments. This study facilitates the development of an improved *ce*-$MoS_2$ spreading ink which retains almost 100% of metallic $MoS_2$ along with ~40% increase in single-layer content. The Langmuir film prepared from this new ink showed potential usage as hole transport layer in perovskite solar cell. To obtain better control on the building block structure, we proved that 2D materials form clusters spontaneously after being transferred onto water surface via solvent spreading and evaporation. As for all three materials investigated – *ce*-$MoS_2$, GO and rGO, the density of cluster structure can be easily increased by increasing the concentration of spreading dispersion. Note that this concentration is better described as the Langmuir surface area per volume deposited. We also revealed that cluster structure can impact the attainable density of transferred Langmuir films. When using *SSaL* method, low-density, net-work like clusters exhibit higher packing efficiency, yielding film coverage as high as 94%. On the other hand, these clusters can also withstand higher compression pressure without collapsing after being compressed by movable barriers. During our analysis of the driving force for film formation and transfer to substrate, we found out the spreading pressure of polar and water-immiscible solvent mixtures is distance-dependent, showing a rapid increase with reduced distance from the dripping position. As for DCE mixtures, both DMF and BtOH presented extended spreading distance and larger spreading pressures which are beneficial for R2R processing. Within the same composition, the maximum spreading pressure and spreading

distances can be increased by using more of a more polar solvent in the mixture. With directional flow provided by solvent spreading and implementation of a multi-dripper system, we can easily widen the coating width at a rate of 6.5 cm per dripper. By using the water-wettable substrate, our *SSaL*-R2R processing is capable of assembling large-scale films of various exfoliated 2D materials including graphene, GO, rGO and *ce*-$MoS_2$ at arbitrary width. The coating speed of our R2R processing largely depends on the ink concentration. When a single dripper system is used, the coating speed is optimized at 1, 2 and 3 cm/min for single layer deposition of *ce*-$MoS_2$, GO and rGO inks, respectively, but this can be enhanced by increasing the number of drippers and evaporation rate of the solvent.

## 8.2 Recommendations for Future Studies

### 8.2.1 $MoS_2$ HTL based large-area PSC

Based on the preliminary results presented in Chapter 7, one can further optimize the coating thickness of perovskite layer and the number of $MoS_2$ Langmuir film depositions to improve the PCE of PSC. Additionally, it is also important to study the impact of $MoS_2$ polymorph and material defects and evaluating the stability of $MoS_2$ based PSC. The ultimate goal is to produce large-area PSC on flexible substrate by using $MoS_2$ HTL prepared by *SSaL*-R2R processing.

### 8.2.2 Expanding the ink library

So far, the Langmuir film of 2D materials still predominately focus on GO with some recent work expanding to TMD materials such as $MoS_2$, even though there has been considerable material development on other 2D materials such as Mxene, silicene and germanene. When we are developing spreading inks for different materials, we have noticed that some inks could only produce an 'elastic' film which resulted in patchy coverage even after high compression. Based on existing evidence, we hypothesized that this is caused by inefficient dispersion concentration (i.e. Langmuir surface area per volume). However, further work is required to determining a universal concentration threshold that can be easily implemented for developing unexplored 2D materials.

### 8.2.3 Developing method to 'connect' sheets

We have mentioned in this thesis that even though the film composed of tiled sheets, they are not electronically connected laterally, in other words, the contact resistance is significantly high. Thus far, improvement of lateral connection has relied on sheets sliding over each other. This method is only applicable for flexible, monolayer GO sheets but bit for rigid sheets like rGO and $MoS_2$. Therefore, it could be interesting to introduce functional groups at the sheet edges or insert molecules between sheets where after-treatment such as light or chemical exposure could induce connections and improve electrical conductivity between sheets. The resulting film could possibly provide better performance in laterally structured devices such as conductor or sensor.

### 8.2.4 Further investigation: Aggregation mechanism of 2D sheets at the air-water interface

As demonstrated in Chapter 5, capillary interactions between the 2D sheets show critical impact on their aggregation at the air-water interface when they are free from spreading solvents, which is in line with previous reports. We used wetting hysteresis to estimate the capillary interactions. However, one could further investigate other mechanisms that results in capillarity between flat sheets at the air-water interface. Moreover, by using high speed camera and other unique imaging techniques, one could aim to collect direct evidence by tracing the particle movements to unveil the aggregation mechanism.

# References


(1) Fiori, G.; Bonaccorso, F.; Iannaccone, G.; Palacios, T.; Neumaier, D.; Seabaugh, A.; Banerjee, S. K.; Colombo, L. Electronics Based on Two-Dimensional Materials. *Nature Nanotechnology*. Nature Publishing Group January 1, 2014, pp 768–779. https://doi.org/10.1038/nnano.2014.207.

(2) Lemme, M. C.; Akinwande, D.; Huyghebaert, C.; Stampfer, C. 2D Materials for Future Heterogeneous Electronics. *Nature Communications*. Nature Research December 1, 2022. https://doi.org/10.1038/s41467-022-29001-4.

(3) Stephenson, T.; Li, Z.; Olsen, B.; Mitlin, D. Lithium Ion Battery Applications of Molybdenum Disulfide (MoS2) Nanocomposites. *Energy Environ Sci* **2014**, *7* (1), 209–231. https://doi.org/10.1039/C3EE42591F.

(4) Pahlevaninezhad, M.; Miller, E. E.; Yang, L.; Prophet, L. S.; Singh, A.; Storwick, T.; Pahlevani, M.; Pope, M. A.; Roberts, E. P. L. Exfoliated Graphene Composite Membrane for the All-Vanadium Redox Flow Battery. *ACS Appl Energy Mater* **2023**. https://doi.org/10.1021/acsaem.3c00428.

(5) Zhang, X.; Hou, L.; Ciesielski, A.; Samorì, P. 2D Materials Beyond Graphene for High-Performance Energy Storage Applications. *Adv Energy Mater* **2016**, *6* (23), 1600671. https://doi.org/10.1002/aenm.201600671.

(6) Dervin, S.; Dionysiou, D. D.; Pillai, S. C. 2D Nanostructures for Water Purification: Graphene and Beyond. *Nanoscale* **2016**, *8* (33), 15115–15131. https://doi.org/10.1039/c6nr04508a.

(7) Huang, H.; Sheng, X.; Tian, Y.; Zhang, L.; Chen, Y.; Zhang, X. Two-Dimensional Nanomaterials for Anticorrosive Polymeric Coatings: A Review. *Industrial and Engineering Chemistry Research*. American Chemical Society September 2, 2020, pp 15424–15446. https://doi.org/10.1021/acs.iecr.0c02876.

(8) Gokce, C.; Gurcan, C.; Besbinar, O.; Unal, M. A.; Yilmazer, A. Emerging 2D Materials for Antimicrobial Applications in the Pre- and Post-Pandemic Era. *Nanoscale*. Royal Society of Chemistry 2022, pp 239–249. https://doi.org/10.1039/d1nr06476b.

(9) Cote, L. J.; Kim, F.; Huang, J. Langmuir−Blodgett Assembly of Graphite Oxide Single Layers. *J Am Chem Soc* **2009**, *131* (3), 1043–1049. https://doi.org/10.1021/ja806262m.

(10) Zheng, Q.; Ip, W. H.; Lin, X.; Yousefi, N.; Yeung, K. K.; Li, Z.; Kim, J. K. Transparent Conductive Films Consisting of Ultralarge Graphene Sheets Produced by Langmuir-Blodgett Assembly. In *ACS Nano*; 2011; Vol. 5, pp 6039–6051. https://doi.org/10.1021/nn2018683.

(11) Sutar, D. S.; Narayanam, P. K.; Singh, G.; Botcha, V. D.; Talwar, S. S.; Srinivasa, R. S.; Major, S. S. Spectroscopic Studies of Large Sheets of Graphene Oxide and Reduced Graphene Oxide Monolayers Prepared by Langmuir-Blodgett Technique. *Thin Solid Films* **2012**, *520* (18), 5991–5996. https://doi.org/10.1016/j.tsf.2012.05.018.

(12) Yin, Z.; He, Q.; Huang, X.; Zhang, J.; Wu, S.; Chen, P.; Lu, G.; Chen, P.; Zhang, Q.; Yan, Q.; Zhang, H. Real-Time DNA Detection Using Pt Nanoparticle-Decorated Reduced Graphene Oxide Field-Effect Transistors. *Nanoscale* **2012**, *4* (1), 293–297. https://doi.org/10.1039/C1NR11149C.

(13) Wang, X.; Bai, H.; Shi, G. Size Fractionation of Graphene Oxide Sheets by PH-Assisted Selective Sedimentation. *J Am Chem Soc* **2011**, *133* (16), 6338–6342. https://doi.org/10.1021/ja200218y.

(14) Han, F.; Yang, S.; Jing, W.; Jiang, Z.; Liu, H.; Li, L. A Study on Near-UV Blue Photoluminescence in Graphene Oxide Prepared by Langmuir-Blodgett Method. *Appl Surf Sci* **2015**, *345*, 18–23. https://doi.org/10.1016/j.apsusc.2015.01.214.

(15) Kumar, V.; Bahadur, N.; Sachdev, D.; Gupta, S.; Reddy, G. B.; Pasricha, R. Restructural Confirmation and Photocatalytic Applications of Graphene Oxide-Gold Composites Synthesized by Langmuir-Blodgett Method. *Carbon N Y* **2014**, *80* (1), 290–304. https://doi.org/10.1016/j.carbon.2014.08.067.

(16) Mangadlao, J. D.; Santos, C. M.; Felipe, M. J. L.; de Leon, a C. C.; Rodrigues, D. F.; Advincula, R. C. On the Antibacterial Mechanism of Graphene Oxide (GO) Langmuir–Blodgett Films. *Chem. Commun.* **2015**, *51* (14), 2886–2889. https://doi.org/10.1039/C4CC07836E.

(17) Nasr Esfahani, A.; Malcolm, A. J.; Xu, L.; Yang, H. B.; Storwick, T.; Kim, N. Y.; Pope, M. A. Ultra-Thin Films of Solution-Exfoliated Hexagonal Boron Nitride by Langmuir Deposition. *J Mater Chem C Mater* **2020**, *8* (39), 13695–13704. https://doi.org/10.1039/d0tc02933e.

(18) Ogilvie, S. P.; Large, M. J.; Wood, H. J.; Amorim Graf, A.; Lee, F.; Salvage, J. P.; King, A. A. K.; Dalton, A. B. Size Selection and Thin-Film Assembly of MoS2elucidates Thousandfold Conductivity Enhancement in Few-Layer Nanosheet Networks. *Nanoscale* **2022**, *14* (2), 320–324. https://doi.org/10.1039/d1nr05815k.

(19) Norton, K.; Jacobs, J.; Neilson, J.; Hopkinson, D.; Mokhtar, M. Z.; Curry, R. J.; Lewis, D. J. Preparation of Solution Processed Photodetectors Comprised of Two-Dimensional Tin(Ii) Sulfide Nanosheet Thin Films Assembledviathe Langmuir-Blodgett Method. *RSC Adv* **2021**, *11* (43), 26813–26819. https://doi.org/10.1039/d1ra04470b.

(20) Zheng, Q.; Wang, J.; Wang, Y.; Chen, Z. Novel Molybdenum Disulfide Langmuir Blodgett Thin Film as a Saturable Absorber for a Passively Q-Switched Nd:$GdVO_4$ Laser. *Opt Mater Express* **2018**, *8* (10), 3176. https://doi.org/10.1364/OME.8.003176.

(21) Kouloumpis, A.; Chatzikonstantinou, A. V.; Chalmpes, N.; Giousis, T.; Potsi, G.; Katapodis, P.; Stamatis, H.; Gournis, D.; Rudolf, P. Germanane Monolayer Films as Antibacterial Coatings. *ACS Appl Nano Mater* **2021**, *4* (3), 2333–2338. https://doi.org/10.1021/acsanm.0c03149.

(22) Kalosi, A.; Demydenko, M.; Bodik, M.; Hagara, J.; Kotlar, M.; Kostiuk, D.; Halahovets, Y.; Vegso, K.; Marin Roldan, A.; Maurya, G. S.; Angus, M.; Veis, P.; Jergel, M.; Majkova, E.; Siffalovic, P. Tailored Langmuir-Schaefer Deposition of Few-Layer MoS2 Nanosheet Films for Electronic Applications. *Langmuir* **2019**, *35* (30), 9802–9808. https://doi.org/10.1021/acs.langmuir.9b01000.

(23) Tang, Z.; Wei, Q.; Guo, B. A Generic Solvent Exchange Method to Disperse MoS2 in Organic Solvents to Ease the Solution Process. *Chemical Communications* **2014**, *50* (30), 3934–3937. https://doi.org/10.1039/c4cc00425f.

(24) Song, O.; Rhee, D.; Kim, J.; Jeon, Y.; Mazánek, V.; Söll, A.; Kwon, Y. A.; Cho, J. H.; Kim, Y. H.; Sofer, Z.; Kang, J. All Inkjet-Printed Electronics Based on Electrochemically Exfoliated Two-Dimensional Metal, Semiconductor, and Dielectric. *NPJ 2D Mater Appl* **2022**, *6* (1). https://doi.org/10.1038/s41699-022-00337-1.

(25) Silverberg, G. J.; Pearce, P.; Vecitis, C. D. Controlling Self-Assembly of Reduced Graphene Oxide at the Air-Water Interface: Quantitative Evidence for Long-Range Attractive and Many-Body Interactions. *ACS Appl Mater Interfaces* **2015**, *7* (6), 3807–3815. https://doi.org/10.1021/am5087984.

(26) Cheng, W.; Dong, S.; Wang, E. Spontaneous Fractal Aggregation of Gold Nanoparticles and Controlled Generation of Aggregate-Based Fractal Networks at Air/Water Interface. *Journal of Physical Chemistry B* **2005**, *109* (41), 19213–19218. https://doi.org/10.1021/jp052255a.

(27) Sear, R.; Chung, S.-W.; Markovich, G.; Gelbart, W.; Heath, J. Spontaneous Patterning of Quantum Dots at the Air-Water Interface. *Phys Rev E* **1999**, *59* (6), R6255–R6258. https://doi.org/10.1103/PhysRevE.59.R6255.

(28) Imperiali, L.; Liao, K. H.; Clasen, C.; Fransaer, J.; MacOsko, C. W.; Vermant, J. Interfacial Rheology and Structure of Tiled Graphene Oxide Sheets. *Langmuir* **2012**, *28* (21), 7990–8000. https://doi.org/10.1021/la300597n.

(29) Zheng, Q.; Ip, W. H.; Lin, X.; Yousefi, N.; Yeung, K. K.; Li, Z.; Kim, J. K. Transparent Conductive Films Consisting of Ultralarge Graphene Sheets Produced by Langmuir-Blodgett Assembly. *ACS Nano* **2011**, *5* (7), 6039–6051. https://doi.org/10.1021/nn2018683.

(30) Wells, R. A.; Johnson, H.; Lhermitte, C. R.; Kinge, S.; Sivula, K. Roll-to-Roll Deposition of Semiconducting 2D Nanoflake Films of Transition Metal Dichalcogenides for Optoelectronic Applications. *ACS Appl Nano Mater* **2019**, *2* (12), 7705–7712. https://doi.org/10.1021/acsanm.9b01774.

(31) Hayes, T. R.; Lang, E. N.; Shi, A.; Claridge, S. A. Large-Scale Noncovalent Functionalization of 2D Materials through Thermally Controlled Rotary Langmuir-Schaefer Conversion. *Langmuir* **2020**, *36* (35), 10577–10586. https://doi.org/10.1021/acs.langmuir.0c01914.

(32) Parchine, M.; McGrath, J.; Bardosova, M.; Pemble, M. E. Large Area 2D and 3D Colloidal Photonic Crystals Fabricated by a Roll-to-Roll Langmuir–Blodgett Method. *Langmuir* **2016**, *32* (23), 5862–5869. https://doi.org/10.1021/acs.langmuir.6b01242.

(33) Parchine, M.; Kohoutek, T.; Bardosova, M.; Pemble, M. E. Large Area Colloidal Photonic Crystals for Light Trapping in Flexible Organic Photovoltaic Modules Applied Using a Roll-to-Roll Langmuir-Blodgett Method. *Solar Energy Materials and Solar Cells* **2018**, *185* (May), 158–165. https://doi.org/10.1016/j.solmat.2018.05.026.

(34) Zhavnerko, G.; Marletta, G. Developing Langmuir-Blodgett Strategies towards Practical Devices. *Mater Sci Eng B Solid State Mater Adv Technol* **2010**, *169* (1–3), 43–48. https://doi.org/10.1016/j.mseb.2009.12.005.

(35) Chen, I. Te; Schappell, E.; Zhang, X.; Chang, C. H. Continuous Roll-to-Roll Patterning of Three-Dimensional Periodic Nanostructures. *Microsyst Nanoeng* **2020**, *6* (1). https://doi.org/10.1038/s41378-020-0133-7.

(36) Li, X.; Gilchrist, J. F. Large-Area Nanoparticle Films by Continuous Automated Langmuir-Blodgett Assembly and Deposition. *Langmuir* **2016**, *32* (5), 1220–1226. https://doi.org/10.1021/acs.langmuir.5b03760.

(37) Zheng, Q.; Ip, W. H.; Lin, X.; Yousefi, N.; Yeung, K. K.; Li, Z.; Kim, J.-K. Transparent Conductive Films Consisting of Ultralarge Graphene Sheets Produced by Langmuir–Blodgett Assembly. *ACS Nano* **2011**, *5* (7), 6039–6051. https://doi.org/10.1021/nn2018683.

(38) Khaligh, H. H.; Xu, L.; Khosropour, A.; Madeira, A.; Romano, M.; Pradére, C.; Tréguer-Delapierre, M.; Servant, L.; Pope, M. A.; Goldthorpe, I. A. The Joule Heating Problem in Silver Nanowire Transparent Electrodes. *Nanotechnology* **2017**, *28* (42). https://doi.org/10.1088/1361-6528/aa7f34.

(39) Wells, R. A.; Johnson, H.; Lhermitte, C. R.; Kinge, S.; Sivula, K. Roll-to-Roll Deposition of Semiconducting 2D Nanoflake Films of Transition Metal Dichalcogenides for Optoelectronic Applications. *ACS Appl Nano Mater* **2019**, *2* (12), 7705–7712. https://doi.org/10.1021/acsanm.9b01774.

(40) Kim, M. S.; Ma, L.; Choudhury, S.; Moganty, S. S.; Wei, S.; Archer, L. A. Fabricating Multifunctional Nanoparticle Membranes by a Fast Layer-by-Layer Langmuir–Blodgett Process: Application in Lithium–Sulfur Batteries. *J Mater Chem A Mater* **2016**, *4* (38), 14709–14719. https://doi.org/10.1039/C6TA06018H.

(41) Harries, R. W.; Brown, C. J.; Ogilvie, S. P.; Large, M. J.; Amorim Graf, A.; Clifford, K.; Simon, T.; Giamas, G.; Dalton, A. B.; King, A. A. K. Langmuir Films of Layered Nanomaterials: Edge Interactions and Cell Culture Applications. *Journal of Physical Chemistry B* **2020**, *124* (33), 7184–7193. https://doi.org/10.1021/acs.jpcb.0c05573.

(42) Chen, J.; Walker, W. R.; Xu, L.; Krysiak, O.; She, Z.; Pope, M. A. Intrinsic Capacitance of Molybdenum Disulfide. *ACS Nano* **2020**, *14* (5), 5636–5648. https://doi.org/10.1021/acsnano.9b10182.

(43) Agresti, A.; Pescetelli, S.; Palma, A. L.; Martín-García, B.; Najafi, L.; Bellani, S.; Moreels, I.; Prato, M.; Bonaccorso, F.; Di Carlo, A. Two-Dimensional Material Interface Engineering for Efficient Perovskite Large-Area Modules. *ACS Energy Lett* **2019**, *4* (8), 1862–1871. https://doi.org/10.1021/acsenergylett.9b01151.

(44) Kim, Y. G.; Kwon, K. C.; Le, Q. Van; Hong, K.; Jang, H. W.; Kim, S. Y. Atomically Thin Two-Dimensional Materials as Hole Extraction Layers in Organolead Halide Perovskite Photovoltaic Cells. *J Power Sources* **2016**, *319*, 1–8. https://doi.org/10.1016/j.jpowsour.2016.04.032.

(45) Kakavelakis, G.; Paradisanos, I.; Paci, B.; Generosi, A.; Papachatzakis, M.; Maksudov, T.; Najafi, L.; Del Rio Castillo, A. E.; Kioseoglou, G.; Stratakis, E.; Bonaccorso, F.; Kymakis, E. Extending the Continuous Operating Lifetime of Perovskite Solar Cells with a Molybdenum Disulfide Hole Extraction Interlayer. *Adv Energy Mater* **2018**, *8* (12), 1–15. https://doi.org/10.1002/aenm.201702287.

(46) Capasso, A.; Matteocci, F.; Najafi, L.; Prato, M.; Buha, J.; Cinà, L.; Pellegrini, V.; Carlo, A. Di; Bonaccorso, F. Few-Layer MoS2 Flakes as Active Buffer Layer for Stable Perovskite Solar Cells. *Adv Energy Mater* **2016**, *6* (16), 1–12. https://doi.org/10.1002/aenm.201600920.

(47) Kohnehpoushi, S.; Nazari, P.; Nejand, B. A.; Eskandari, M. MoS2: A Two-Dimensional Hole-Transporting Material for High-Efficiency, Low-Cost Perovskite Solar Cells. *Nanotechnology* **2018**, *29* (20), 205201. https://doi.org/10.1088/1361-6528/aab1d4.

(48) Huang, P.; Wang, Z.; Liu, Y.; Zhang, K.; Yuan, L.; Zhou, Y.; Song, B.; Li, Y. Water-Soluble 2D Transition Metal Dichalcogenides as the Hole-Transport Layer for Highly Efficient and Stable p-i-n Perovskite Solar Cells. *ACS Appl Mater Interfaces* **2017**, *9* (30), 25323–25331. https://doi.org/10.1021/acsami.7b06403.

(49) Franklin, B. XLIV. Of the Stilling of Waves by Means of Oil. Extracted from Sundry Letters between Benjamin Franklin, LL. D. F. R. S. William Brownrigg, M. D. F. R. S. and the Reverend Mr. Farish. *Philos Trans R Soc Lond* **1774**, *64*, 445–460. https://doi.org/10.1098/rstl.1774.0044.

(50) Giles, C. H. Franklin s Teaspoonful of Oil. Studies in the Early History of Surface Chemistry, Part 1. *Chem Ind* **1969**.

(51) Langmuir, I. THE CONSTITUTION AND FUNDAMENTAL PROPERTIES OF SOLIDS AND LIQUIDS. II. LIQUIDS. [1]. *J Am Chem Soc* **1917**, *39* (9), 1848–1906. https://doi.org/10.1021/ja02254a006.

(52) Blodgett, K. B. Films Built by Depositing Successive Monomolecular Layers on a Solid Surface. *J Am Chem Soc* **1935**, *57* (6), 1007–1022. https://doi.org/10.1021/ja01309a011.

(53) Le Roux, S.; Roché, M.; Cantat, I.; Saint-Jalmes, A. Soluble Surfactant Spreading: How the Amphiphilicity Sets the Marangoni Hydrodynamics. *Phys Rev E* **2016**, *93* (1), 1–13. https://doi.org/10.1103/PhysRevE.93.013107.

(54) Collier, C. P.; Saykally, R. J.; Shiang, J. J.; Henrichs, S. E.; Heath, J. R. Reversible Tuning of Silver Quantum Dot Monolayers Through the Metal-Insulator Transition. *Science (1979)* **1997**, *277* (5334), 1978–1981. https://doi.org/10.1126/science.277.5334.1978.

(55) Kim, F.; Kwan, S.; Akana, J.; Yang, P. Langmuir−Blodgett Nanorod Assembly. *J Am Chem Soc* **2001**, *123* (18), 4360–4361. https://doi.org/10.1021/ja0059138.

(56) Paul, S.; Pearson, C.; Molloy, A.; Cousins, M. A.; Green, M.; Kolliopoulou, S.; Dimitrakis, P.; Normand, P.; Tsoukalas, D.; Petty, M. C. Langmuir−Blodgett Film Deposition of Metallic Nanoparticles and Their Application to Electronic Memory Structures. *Nano Lett* **2003**, *3* (4), 533–536. https://doi.org/10.1021/nl034008t.

(57) Tao, A.; Kim, F.; Hess, C.; Goldberger, J.; He, R.; Sun, Y.; Xia, Y.; Yang, P. Langmuir−Blodgett Silver Nanowire Monolayers for Molecular Sensing Using Surface-Enhanced Raman Spectroscopy. *Nano Lett* **2003**, *3* (9), 1229–1233. https://doi.org/10.1021/nl0344209.

(58) Li, X.; Zhang, L.; Wang, X.; Shimoyama, I.; Sun, X.; Seo, W. K.; Dai, H. Langmuir-Blodgett Assembly of Densely Aligned Single-Walled Carbon Nanotubes from Bulk Materials. *J Am Chem Soc* **2007**, *129* (16), 4890–4891. https://doi.org/10.1021/ja071114e.

(59) Wang, D.; Chang, Y.-L.; Liu, Z.; Dai, H. Oxidation Resistant Germanium Nanowires: Bulk Synthesis, Long Chain Alkanethiol Functionalization, and Langmuir−Blodgett Assembly. *J Am Chem Soc* **2005**, *127* (33), 11871–11875. https://doi.org/10.1021/ja053836g.

(60) Zheng, Q.; Shi, L.; Yang, J. Langmuir-Blodgett Assembly of Ultra-Large Graphene Oxide Films for Transparent Electrodes. *Transactions of Nonferrous Metals Society of China* **2012**, *22* (10), 2504–2511. https://doi.org/10.1016/S1003-6326(11)61492-1.

(61) Zhang, Y.; Xu, L.; Walker, W. R.; Tittle, C. M.; Backhouse, C. J.; Pope, M. A. Langmuir Films and Uniform, Large Area, Transparent Coatings of Chemically Exfoliated MoS 2 Single Layers. *J Mater Chem C Mater* **2017**, *5* (43), 11275–11287. https://doi.org/10.1039/C7TC02637D.

(62) Oliveira, O. N.; Caseli, L.; Ariga, K. The Past and the Future of Langmuir and Langmuir-Blodgett Films. *Chemical Reviews*. American Chemical Society March 23, 2022, pp 6459–6513. https://doi.org/10.1021/acs.chemrev.1c00754.

(63) He, P.; Fang, K.; Zou, G.; Peltonen, J. P. K.; Rosenholm, J. B. *Elasticity of Langmuir Monolayer Detected by Dynamic Oscillation Method*; 2002; Vol. 201. www.elsevier.com/locate/colsurfa.

(64) Ładniak, A.; Jurak, M.; Wiącek, A. E. Langmuir Monolayer Study of Phospholipid DPPC on the Titanium Dioxide–Chitosan–Hyaluronic Acid Subphases. *Adsorption* **2019**, *25* (3), 469–476. https://doi.org/10.1007/s10450-019-00037-1.

(65) Poonia, M.; Gupta, R. K.; Manjuladevi, V.; Gupta, S. K.; Akhtar, J. Supramolecular Assembly of Single-Walled Carbon Nanotubes at Air-Solid Interface. *Journal of Nanoparticle Research* **2014**, *16* (8). https://doi.org/10.1007/s11051-014-2572-2.

(66) López-Díaz, D.; Mercedes Velázquez, M.; Blanco de La Torre, S.; Pérez-Pisonero, A.; Trujillano, R.; Fierro, J. L. G.; Claramunt, S.; Cirera, A. The Role of Oxidative Debris on Graphene Oxide Films. *ChemPhysChem* **2013**, *14* (17), 4002–4009. https://doi.org/10.1002/cphc.201300620.

(67) Xu, L.; Tetreault, A. R.; Khaligh, H. H.; Goldthorpe, I. A.; Wettig, S. D.; Pope, M. A. Continuous Langmuir–Blodgett Deposition and Transfer by Controlled Edge-to-Edge Assembly of Floating 2D Materials. *Langmuir* **2019**, *35* (1), 51–59. https://doi.org/10.1021/acs.langmuir.8b03173.

(68) Geim, A. K.; Novoselov, K. S. The Rise of Graphene. *Nat Mater* **2007**, *6* (3), 183–191. https://doi.org/10.1038/nmat1849.

(69) Drnovšek, N. The Translation of the Seat of Metropolitanate of Kiev from Kiev to Moscow. *Bogoslovni Vestnik* **2018**, *78* (1), 135–146. https://doi.org/10.1126/science.1102896.

(70) Zhang, Y.; Zhang, L.; Zhou, C. Review of Chemical Vapor Deposition of Graphene and Related Applications. *Acc Chem Res* **2013**, *46* (10), 2329–2339. https://doi.org/10.1021/ar300203n.

(71) Marcano, D. C.; Kosynkin, D. V.; Berlin, J. M.; Sinitskii, A.; Sun, Z.; Slesarev, A.; Alemany, L. B.; Lu, W.; Tour, J. M. Improved Synthesis of Graphene Oxide. *ACS Nano* **2010**, *4* (8), 4806–4814. https://doi.org/10.1021/nn1006368.

(72) Higginbotham, A. L.; Lomeda, J. R.; Morgan, A. B.; Tour, J. M. Graphite Oxide Flame-Retardant Polymer Nanocomposites. *ACS Appl Mater Interfaces* **2009**, *1* (10), 2256–2261. https://doi.org/10.1021/am900419m.

(73) Stankovich, S.; Dikin, D. A.; Piner, R. D.; Kohlhaas, K. A.; Kleinhammes, A.; Jia, Y.; Wu, Y.; Nguyen, S. B. T.; Ruoff, R. S. Synthesis of Graphene-Based Nanosheets via Chemical Reduction of Exfoliated Graphite Oxide. *Carbon N Y* **2007**, *45* (7), 1558–1565. https://doi.org/10.1016/j.carbon.2007.02.034.

(74) Dreyer, D. R.; Park, S.; Bielawski, C. W.; Ruoff, R. S. The Chemistry of Graphene Oxide. *Chem. Soc. Rev.* **2010**, *39* (1), 228–240. https://doi.org/10.1039/B917103G.

(75) He, P.; Sun, J.; Tian, S.; Yang, S.; Ding, S.; Ding, G.; Xie, X.; Jiang, M. Processable Aqueous Dispersions of Graphene Stabilized by Graphene Quantum Dots. *Chemistry of Materials* **2015**, *27* (1), 218–226. https://doi.org/10.1021/cm503782p.

(76) Jalili, R.; Aboutalebi, S. H.; Esrafilzadeh, D.; Konstantinov, K.; Moulton, S. E.; Razal, J. M.; Wallace, G. G. Organic Solvent-Based Graphene Oxide Liquid Crystals: A Facile Route toward the Next Generation of Self-Assembled Layer-by-Layer Multifunctional 3D Architectures. *ACS Nano* **2013**, *7* (5), 3981–3990. https://doi.org/10.1021/nn305906z.

(77) Gudarzi, M. M. Colloidal Stability of Graphene Oxide: Aggregation in Two Dimensions. *Langmuir* **2016**, *32* (20), 5058–5068. https://doi.org/10.1021/acs.langmuir.6b01012.

(78) Konkena, B.; Vasudevan, S. Understanding Aqueous Dispersibility of Graphene Oxide and Reduced Graphene Oxide through PKa Measurements. *J Phys Chem Lett* **2012**, *3* (7), 867–872. https://doi.org/10.1021/jz300236w.

(79) Mkhoyan, K. A.; Contryman, A. W.; Silcox, J.; Stewart, D. A.; Eda, G.; Mattevi, C.; Miller, S.; Chhowalla, M. Atomic and Electronic Structure of Graphene-Oxide. *Nano Lett* **2009**, *9* (3), 1058–1063. https://doi.org/10.1021/nl8034256.

(80) Large, M. J.; Ogilvie, S. P.; King, A. A. K.; Dalton, A. B. Understanding Solvent Spreading for Langmuir Deposition of Nanomaterial Films: A Hansen Solubility Parameter Approach. *Langmuir* **2017**, acs.langmuir.7b03867. https://doi.org/10.1021/acs.langmuir.7b03867.

(81) Bagri, A.; Mattevi, C.; Acik, M.; Chabal, Y. J.; Chhowalla, M.; Shenoy, V. B. Structural Evolution during the Reduction of Chemically Derived Graphene Oxide. *Nat Chem* **2010**, *2* (7), 581–587. https://doi.org/10.1038/nchem.686.

(82) Hontoria-Lucas, C.; López-Peinado, A. J.; López-González, J. de D.; Rojas-Cervantes, M. L.; Martín-Aranda, R. M. Study of Oxygen-Containing Groups in a Series of Graphite Oxides: Physical and Chemical Characterization. *Carbon N Y* **1995**, *33* (11), 1585–1592. https://doi.org/10.1016/0008-6223(95)00120-3.

(83) Yang, D.; Velamakanni, A.; Bozoklu, G.; Park, S.; Stoller, M.; Piner, R. D.; Stankovich, S.; Jung, I.; Field, D. A.; Ventrice, C. A.; Ruoff, R. S. Chemical Analysis of Graphene Oxide Films after Heat and Chemical Treatments by X-Ray Photoelectron and Micro-Raman Spectroscopy. *Carbon N Y* **2009**, *47* (1), 145–152. https://doi.org/10.1016/j.carbon.2008.09.045.

(84) Pope, M. Electrochemical Double-Layer Capacitors Based on Functionalized Graphene. **2013**, *7354*.

(85) Tarcan, R.; Todor-Boer, O.; Petrovai, I.; Leordean, C.; Astilean, S.; Botiz, I. Reduced Graphene Oxide Today. *Journal of Materials Chemistry C*. Royal Society of Chemistry 2020, pp 1198–1224. https://doi.org/10.1039/c9tc04916a.

(86) Molina-Sánchez, A.; Hummer, K.; Wirtz, L. Vibrational and Optical Properties of MoS2: From Monolayer to Bulk. *Surf Sci Rep* **2015**, *70* (4), 554–586. https://doi.org/https://doi.org/10.1016/j.surfrep.2015.10.001.

(87) Newaz, A. K. M.; Prasai, D.; Ziegler, J. I.; Caudel, D.; Robinson, S.; Haglund Jr., R. F.; Bolotin, K. I. Electrical Control of Optical Properties of Monolayer MoS2. *Solid State Commun* **2013**, *155*, 49–52. https://doi.org/https://doi.org/10.1016/j.ssc.2012.11.010.

(88) Li, X.; Zhu, H. Two-Dimensional MoS2: Properties, Preparation, and Applications. *Journal of Materiomics* **2015**, *1* (1), 33–44. https://doi.org/10.1016/j.jmat.2015.03.003.

(89) Baugher, B. W. H.; Churchill, H. O. H.; Yang, Y.; Jarillo-Herrero, P. Intrinsic Electronic Transport Properties of High-Quality Monolayer and Bilayer MoS 2. *Nano Lett* **2013**, *13* (9), 4212–4216. https://doi.org/10.1021/nl401916s.

(90) Winchester, A.; Ghosh, S.; Feng, S.; Elias, A. L.; Mallouk, T.; Terrones, M.; Talapatra, S. Electrochemical Characterization of Liquid Phase Exfoliated Two-Dimensional Layers of Molybdenum Disulfide. *ACS Appl Mater Interfaces* **2014**, *6* (3), 2125–2130. https://doi.org/10.1021/am4051316.

(91) Acerce, M.; Voiry, D.; Chhowalla, M. Metallic 1T Phase MoS2 Nanosheets as Supercapacitor Electrode Materials. *Nat Nanotechnol* **2015**, *10* (4), 313–318. https://doi.org/10.1038/nnano.2015.40.

(92) Lukowski, M. A.; Daniel, A. S.; Meng, F.; Forticaux, A.; Li, L.; Jin, S. Enhanced Hydrogen Evolution Catalysis from Chemically Exfoliated Metallic MoS2 Nanosheets. *J Am Chem Soc* **2013**, *135* (28), 10274–10277. https://doi.org/10.1021/ja404523s.

(93) Rowley-Neale, S. J.; Brownson, D. A. C.; Smith, G. C.; Sawtell, D. A. G.; Kelly, P. J.; Banks, C. E. 2D Nanosheet Molybdenum Disulphide (MoS 2 ) Modified Electrodes Explored towards the Hydrogen Evolution Reaction. *Nanoscale* **2015**, *7* (43), 18152–18168. https://doi.org/10.1039/C5NR05164A.

(94) Mehmood, F.; Pachter, R.; Back, T. C.; Boeckl, J. J.; Busch, R. T.; Stevenson, P. R. Two-Dimensional MoS 2 2H, 1T, and 1T ′ Crystalline Phases with Incorporated Adatoms: Theoretical Investigation of Electronic and Optical Properties. *Appl Opt* **2021**, *60* (25), G232. https://doi.org/10.1364/ao.433239.

(95) *Gmelin Handbook of Inorganic and Organometallic Chemistry*, 8th ed.; Springer-Verlag: Vol. B7, 1995.

(96) Benavente, E.; Santa Ana, M. A.; Mendizábal, F.; González, G. Intercalation Chemistry of Molybdenum Disulfide. *Coord Chem Rev* **2002**, *224* (1–2), 87–109. https://doi.org/10.1016/S0010-8545(01)00392-7.

(97) Li, T.; Galli, G. Electronic Properties of MoS2 Nanoparticles. *The Journal of Physical Chemistry C* **2007**, *111* (44), 16192–16196. https://doi.org/10.1021/jp075424v.

(98) Splendiani, A.; Sun, L.; Zhang, Y.; Li, T.; Kim, J.; Chim, C. Y.; Galli, G.; Wang, F. Emerging Photoluminescence in Monolayer MoS2. *Nano Lett* **2010**, *10* (4), 1271–1275. https://doi.org/10.1021/nl903868w.

(99) Jariwala, D.; Davoyan, A. R.; Wong, J.; Atwater, H. A. Van Der Waals Materials for Atomically-Thin Photovoltaics: Promise and Outlook. *ACS Photonics* **2017**, *4* (12), 2962–2970. https://doi.org/10.1021/acsphotonics.7b01103.

(100) Yin, Z.; Li, H. H.; Li, H. H.; Jiang, L.; Shi, Y.; Sun, Y.; Lu, G.; Zhang, Q.; Chen, X.; Zhang, H. Single-Layer MoS2 Phototransistors. *ACS Nano* **2012**, *6* (1), 74–80. https://doi.org/10.1021/nn2024557.

(101) Cai, Z.; Liu, B.; Zou, X.; Cheng, H.-M. Chemical Vapor Deposition Growth and Applications of Two-Dimensional Materials and Their Heterostructures. *Chem Rev* **2018**, *118* (13), 6091–6133. https://doi.org/10.1021/acs.chemrev.7b00536.

(102) Coleman, J. N.; Lotya, M.; Oâ€™Neill, A.; Bergin, S. D.; King, P. J.; Khan, U.; Young, K.; Gaucher, A.; De, S.; Smith, R. J. Two-Dimensional Nanosheets Produced by Liquid Exfoliation of Layered Materials. *Science (1979)* **2011**, *331* (6017), 568–571.

(103) Nicolosi, V.; Chhowalla, M.; Kanatzidis, M. G.; Strano, M. S.; Coleman, J. N. Liquid Exfoliation of Layered Materials. *Science (1979)* **2013**, *340* (6139), 1226419. https://doi.org/10.1126/science.1226419.

(104) Eda, G.; Yamaguchi, H.; Voiry, D.; Fujita, T.; Chen, M.; Chhowalla, M. Photoluminescence from Chemically Exfoliated MoS2. *Nano Lett* **2011**, *11* (12), 5111–5116. https://doi.org/10.1021/nl201874w.

(105) Joensen, P.; Frindt, R. F.; Morrison, S. R. Single-Layer MoS2. *Mater Res Bull* **1986**, *21* (4), 457–461. https://doi.org/10.1016/0025-5408(86)90011-5.

(106) Ambrosi, A.; Pumera, M. Exfoliation of Layered Materials Using Electrochemistry. *Chem Soc Rev* **2018**, 7213–7224. https://doi.org/10.1039/C7CS00811B.

(107) Liu, N.; Kim, P.; Kim, J. H.; Ye, J. H.; Kim, S.; Lee, C. J. Large-Area Atomically Thin MoS2 Nanosheets Prepared Using Electrochemical Exfoliation. *ACS Nano* **2014**, *8* (7), 6902–6910. https://doi.org/10.1021/nn5016242.

(108) Knirsch, K. C.; Berner, N. C.; Nerl, H. C.; Cucinotta, C. S.; Gholamvand, Z.; McEvoy, N.; Wang, Z.; Abramovic, I.; Vecera, P.; Halik, M.; Sanvito, S.; Duesberg, G. S.; Nicolosi, V.; Hauke, F.; Hirsch, A.; Coleman, J. N.; Backes, C. Basal-Plane Functionalization of Chemically Exfoliated Molybdenum Disulfide by Diazonium Salts. *ACS Nano* **2015**, *9* (6), 6018–6030. https://doi.org/10.1021/acsnano.5b00965.

(109) Wi, S.; Kim, H.; Chen, M.; Nam, H.; Guo, L. J.; Meyhofer, E.; Liang, X. Enhancement of Photovoltaic Response in Multilayer MoS2 Induced by Plasma Doping. *ACS Nano* **2014**, *8* (5), 5270–5281. https://doi.org/10.1021/nn5013429.

(110) Jeong, J.; Kim, M.; Seo, J.; Lu, H.; Ahlawat, P.; Mishra, A.; Yang, Y.; Hope, M. A.; Eickemeyer, F. T.; Kim, M.; Yoon, Y. J.; Choi, I. W.; Darwich, B. P.; Choi, S. J.; Jo, Y.; Lee, J. H.; Walker, B.; Zakeeruddin, S. M.; Emsley, L.; Rothlisberger, U.; Hagfeldt, A.; Kim, D. S.; Grätzel, M.; Kim, J. Y. Pseudo-Halide Anion Engineering for α-FAPbI3 Perovskite Solar Cells. *Nature* **2021**, *592* (7854), 381–385. https://doi.org/10.1038/s41586-021-03406-5.

(111) Min, H.; Lee, D. Y.; Kim, J.; Kim, G.; Lee, K. S.; Kim, J.; Paik, M. J.; Kim, Y. K.; Kim, K. S.; Kim, M. G.; Shin, T. J.; Il Seok, S. Perovskite Solar Cells with Atomically Coherent Interlayers on SnO2 Electrodes. *Nature* **2021**, *598* (7881), 444–450. https://doi.org/10.1038/s41586-021-03964-8.

(112) Yoo, J. J.; Seo, G.; Chua, M. R.; Park, T. G.; Lu, Y.; Rotermund, F.; Kim, Y. K.; Moon, C. S.; Jeon, N. J.; Correa-Baena, J. P.; Bulović, V.; Shin, S. S.; Bawendi, M. G.; Seo, J. Efficient Perovskite Solar Cells via Improved Carrier Management. *Nature* **2021**, *590* (7847), 587–593. https://doi.org/10.1038/s41586-021-03285-w.

(113) Hu, J.; Zhao, B.; Xu, W.; Fan, Y.; Li, B.; Ozaki, Y. Aggregation of Silver Particles Trapped at an Air-Water Interface for Preparing New SERS Active Substrates. *Journal of Physical Chemistry B* **2002**, *106* (25), 6500–6506. https://doi.org/10.1021/jp0143286.

(114) Flores-Tandy, L. M.; García-Monjaraz, A. V.; van Nierop, E. A.; Vázquez-Martínez, E. A.; Ruiz-Garcia, J.; Mejía-Rosales, S. Fractal Aggregates Formed by Ellipsoidal Colloidal Particles at the Air/Water Interface. *Colloids Surf A Physicochem Eng Asp* **2020**, *590*, 124477. https://doi.org/10.1016/j.colsurfa.2020.124477.

(115) Yang, P.; Kim, F. Langmuir - Blodgett Assembly of One-Dimensional Nanostructures. *ChemPhysChem* **2002**, *3* (6), 503–506. https://doi.org/10.1002/1439-7641(20020617)3:6<503::AID-CPHC503>3.0.CO;2-U.

(116) Bai, X.; Ma, H.; Li, X.; Dong, B.; Zheng, L. Patterns of Gold Nanoparticles Formed at the Air/Water Interface: Effects of Capping Agents. *Langmuir* **2010**, *26* (18), 14970–14974. https://doi.org/10.1021/la102674f.

(117) Zheng, Q.; Shi, L.; Ma, P.-C.; Xue, Q.; Li, J.; Tang, Z.; Yang, J. Structure Control of Ultra-Large Graphene Oxide Sheets by the Langmuir–Blodgett Method. *RSC Adv.* **2013**, *3* (14), 4680–4691. https://doi.org/10.1039/C3RA22367A.

(118) Zhang, X.; Sun, H.; Yang, S. Self-Limiting Assembly of Two-Dimensional Domains from Graphene Oxide at the Air/Water Interface. *Journal of Physical Chemistry C* **2012**, *116* (35), 19018–19024. https://doi.org/10.1021/jp3051005.

(119) Li, Q.; Jonas, U.; Zhao, X. S.; Kappl, M. The Forces at Work in Colloidal Self-Assembly: A Review on Fundamental Interactions between Colloidal Particles. *Asia-Pacific Journal of Chemical Engineering* **2008**, *3* (3), 255–268. https://doi.org/10.1002/apj.144.

(120) Robinson, D. J.; Earnshaw, J. C. Experimental Study of Colloidal Aggregation in Two Dimensions. III. Structural Dynamics. *Phys Rev A (Coll Park)* **1992**, *46* (4), 2065–2071. https://doi.org/10.1103/PhysRevA.46.2065.

(121) Robinson, D. J.; Earnshaw, J. C. Experimental Study of Colloidal Aggregation in Two Dimensions. I. Structural Aspects. *Phys Rev A (Coll Park)* **1992**, *46* (4), 2045–2054. https://doi.org/10.1103/PhysRevA.46.2045.

(122) Robinson, D. J.; Earnshaw, J. C. Experimental Study of Colloidal Aggregation in Two Dimensions. II. Kinetic Aspects. *Phys Rev A (Coll Park)* **1992**, *46* (4), 2055–2064. https://doi.org/10.1103/PhysRevA.46.2055.

(123) Xiao, L.; Zhou, R.; He, Y.; Li, Y.; Yeung, E. S. Direct Observation of Nanoparticle Self-Assembly Dynamics at the Water−Air Interface Using Differential Interference Contrast Microscopy. *The Journal of Physical Chemistry C* **2009**, *113* (4), 1209–1216. https://doi.org/10.1021/jp807776w.

(124) Harkins, W. D.; Feldman, A. FILMS. THE SPREADING OF LIQUIDS AND THE SPREADING COEFFICIENT. *J Am Chem Soc* **1922**, *44* (12), 2665–2685. https://doi.org/10.1021/ja01433a001.

(125) Dussaud, A. D.; Troian, S. M. Dynamics of Spontaneous Spreading with Evaporation on a Deep Fluid Layer. *Physics of Fluids* **1998**, *10* (1), 23–38. https://doi.org/10.1063/1.869546.

(126) Huh, C.; Inoue, M.; Mason, S. Uni-Directional Spreading of One Liquid on the Surface of Another. *Can J Chem Eng* **1975**, *53*, 367–371. https://doi.org/10.1002/cjce.5450530402.

(127) McDowell, R. S.; McCutchen, C. W. The Thoreau-Reynolds Ridge, a Lost and Found Phenomenon. *Science (1979)* **1971**, *172* (3986), 973–973. https://doi.org/10.1126/science.172.3986.973.

(128) Kim, H.; Lee, J.; Kim, T.-H.; Kim, H.-Y. Spontaneous Marangoni Mixing of Miscible Liquids at a Liquid–Liquid–Air Contact Line. *Langmuir* **2015**, *31* (31), 8726–8731. https://doi.org/10.1021/acs.langmuir.5b01897.

(129) Davies, J. T.; Rideal, E. *Interfacial Phenomena*; Academic Press, INC: New York, P. 26, 1963.

(130) Kim, H.; Muller, K.; Shardt, O.; Afkhami, S.; Stone, H. A. Solutal Marangoni Flows of Miscible Liquids Drive Transport without Surface Contamination. *Nat Phys* **2017**, *13* (11), 1105–1110. https://doi.org/10.1038/nphys4214.

(131) Zheng, Q.; Zhang, B.; Lin, X.; Shen, X.; Yousefi, N.; Huang, Zhen. D.; Li, Z.; Kim, Jang. K. Highly Transparent and Conducting Ultralarge Graphene Oxide / Single-Walled Carbon

Nanotube Hybrid Films Produced by Langmuir-Blodgett Assembly. *J Mater Chem* **2012**, *22* (48), 25072. https://doi.org/10.1039/c2jm34870e.

(132) Jia, B.; Zou, L. Langmuir–Blodgett Assembly of Sulphonated Graphene Nanosheets into Single- and Multi-Layered Thin Films. *Chem Phys Lett* **2013**, *568–569*, 101–105. https://doi.org/10.1016/j.cplett.2013.02.073.

(133) Li, X.; Zhang, G.; Bai, X.; Sun, X.; Wang, X.; Wang, E.; Dai, H. Highly Conducting Graphene Sheets and Langmuir-Blodgett Films. *Nature Nanotechnol.* **2008**, *3* (9), 538–542. https://doi.org/10.1038/nnano.2008.210.

(134) Lin, X.; Jia, J.; Yousefi, N.; Shen, X.; Kim, J.-K. Excellent Optoelectrical Properties of Graphene Oxide Thin Films Deposited on a Flexible Substrate by Langmuir-Blodgett Assembly. *J Mater Chem C Mater* **2013**, *1* (41), 6869–6877. https://doi.org/10.1039/c3tc31497a.

(135) Kim, M. S.; Ma, L.; Choudhury, S.; Archer, L. A. Multifunctional Separator Coatings for High-Performance Lithium–Sulfur Batteries. *Adv Mater Interfaces* **2016**, *3* (22). https://doi.org/10.1002/admi.201600450.

(136) Lee, Y. L.; Liu, K. L. Relaxation Behaviors of Monolayers of Octadecylamine and Stearic Acid at the Air/Water Interface. *Langmuir* **2004**, *20* (8), 3180–3187. https://doi.org/10.1021/la030272q.

(137) Bradder, P.; Ling, S. K.; Wang, S.; Liu, S. Dye Adsorption on Layered Graphite Oxide. *J Chem Eng Data* **2011**, *56* (1), 138–141. https://doi.org/10.1021/je101049g.

(138) Montes-Navajas, P.; Asenjo, N. G.; Santamaría, R.; Menéndez, R.; Corma, A.; García, H. Surface Area Measurement of Graphene Oxide in Aqueous Solutions. *Langmuir* **2013**, *29* (44), 13443–13448. https://doi.org/10.1021/la4029904.

(139) Transue, L. F.; Washburn, E. R.; Kahler, F. H. The Direct Measurement of the Spreading Pressures of Volatile Organic Liquids on Water. *J Am Chem Soc* **1942**, *64* (2), 274–276. https://doi.org/10.1021/ja01254a019.

(140) Reid, R. C.; Prausnitz, J. M.; Poling, B. E. *The Properties of Gases and Liquids*, 3rd ed.; McGraw Hill Book Co.,New York, NY: United States, 1977.

(141) Zhang, Y.; Xu, L.; Walker, W. R.; Tittle, C. M.; Backhouse, C. J.; Pope, M. A. Langmuir Films and Uniform, Large Area, Transparent Coatings of Chemically Exfoliated MoS 2 Single Layers. *J. Mater. Chem. C* **2017**. https://doi.org/10.1039/C7TC02637D.

(142) Schniepp, H. C.; Li, J.-L.; McAllister, M. J.; Sai, H.; Herrera-Alonso, M.; Adamson, D. H.; Prud'homme, R. K.; Car, R.; Saville, D. A.; Aksay, I. A. Functionalized Single Graphene Sheets Derived from Splitting Graphite Oxide. *J Phys Chem B* **2006**, *110* (17), 8535–8539. https://doi.org/10.1021/jp060936f.

(143) Pope, M. A.; Aksay, I. A. Four-Fold Increase in the Intrinsic Capacitance of Graphene through Functionalization and Lattice Disorder. *The Journal of Physical Chemistry C* **2015**, *119* (35), 20369–20378. https://doi.org/10.1021/acs.jpcc.5b07521.

(144) Chou, S. S.; Huang, Y. K.; Kim, J.; Kaehr, B.; Foley, B. M.; Lu, P.; Dykstra, C.; Hopkins, P. E.; Brinker, C. J.; Huang, J.; Dravid, V. P. Controlling the Metal to Semiconductor Transition of MoS2 and WS2 in Solution. *J Am Chem Soc* **2015**, *137* (5), 1742–1745. https://doi.org/10.1021/ja5107145.

(145) Mak, K. F.; Lee, C.; Hone, J.; Shan, J.; Heinz, T. F. Atomically Thin MoS2: A New Direct-Gap Semiconductor. *Phys Rev Lett* **2010**, *105* (13), 136805. https://doi.org/10.1103/PhysRevLett.105.136805.

(146) Peng, B.; Ang, P. K.; Loh, K. P. Two-Dimensional Dichalcogenides for Light-Harvesting Applications. *Nano Today* **2015**, *10* (2), 128–137. https://doi.org/10.1016/j.nantod.2015.01.007.

(147) Li, C.; Cao, Q.; Wang, F.; Xiao, Y.; Li, Y.; Delaunay, J. J.; Zhu, H. Engineering Graphene and TMDs Based van Der Waals Heterostructures for Photovoltaic and Photoelectrochemical Solar Energy Conversion. *Chem Soc Rev* **2018**, *47* (13), 4981–5037. https://doi.org/10.1039/c8cs00067k.

(148) Lien, D. H.; Amani, M.; Desai, S. B.; Ahn, G. H.; Han, K.; He, J. H.; Ager, J. W.; Wu, M. C.; Javey, A. Large-Area and Bright Pulsed Electroluminescence in Monolayer Semiconductors. *Nat Commun* **2018**, *9* (1), 1–7. https://doi.org/10.1038/s41467-018-03218-8.

(149) Yin, Y.; Han, J.; Zhang, Y.; Zhang, X.; Xu, P.; Yuan, Q.; Samad, L.; Wang, X.; Wang, Y.; Zhang, Z.; Zhang, P.; Cao, X.; Song, B.; Jin, S. Contributions of Phase, Sulfur Vacancies, and Edges to the Hydrogen Evolution Reaction Catalytic Activity of Porous Molybdenum Disulfide Nanosheets. *J Am Chem Soc* **2016**, *138* (25), 7965–7972. https://doi.org/10.1021/jacs.6b03714.

(150) Gao, J.; Li, B.; Tan, J.; Chow, P.; Lu, T. M.; Koratkar, N. Aging of Transition Metal Dichalcogenide Monolayers. *ACS Nano* **2016**, *10* (2), 2628–2635. https://doi.org/10.1021/acsnano.5b07677.

(151) Zhang, X.; Jia, F.; Yang, B.; Song, S. Oxidation of Molybdenum Disulfide Sheet in Water under in Situ Atomic Force Microscopy Observation. *The Journal of Physical Chemistry C* **2017**, *121* (18), 9938–9943. https://doi.org/10.1021/acs.jpcc.7b01863.

(152) Pető, J.; Ollár, T.; Vancsó, P.; Popov, Z. I.; Magda, G. Z.; Dobrik, G.; Hwang, C.; Sorokin, P. B.; Tapasztó, L. Spontaneous Doping of the Basal Plane of MoS2 Single Layers through Oxygen Substitution under Ambient Conditions. *Nat Chem* **2018**, *10* (12), 1246–1251. https://doi.org/10.1038/s41557-018-0136-2.

(153) Zhang, W.; Matsuda, K.; Miyauchi, Y. Photostability of Monolayer Transition-Metal Dichalcogenides in Ambient Air and Acidic/Basic Aqueous Solutions. *ACS Omega* **2019**, *4* (6), 10322–10327. https://doi.org/10.1021/acsomega.9b01067.

(154) Nurdiwijayanto, L.; Ma, R.; Sakai, N.; Sasaki, T. Insight into the Structural and Electronic Nature of Chemically Exfoliated Molybdenum Disulfide Nanosheets in Aqueous Dispersions. *Dalton Transactions* **2018**, *47* (9), 3014–3021. https://doi.org/10.1039/c7dt03706f.

(155) Scanlon, D. O.; Watson, G. W.; Payne, D. J.; Atkinson, G. R.; Egdell, R. G.; Law, D. S. L. Theoretical and Experimental Study of the Electronic Structures of MoO 3 and MoO2.

*Journal of Physical Chemistry C* **2010**, *114* (10), 4636–4645. https://doi.org/10.1021/jp9093172.

(156) Biesinger, M. C.; Payne, B. P.; Grosvenor, A. P.; Lau, L. W. M.; Gerson, A. R.; Smart, R. S. C. Resolving Surface Chemical States in XPS Analysis of First Row Transition Metals, Oxides and Hydroxides: Cr, Mn, Fe, Co and Ni. *Appl Surf Sci* **2011**, *257* (7), 2717–2730. https://doi.org/10.1016/j.apsusc.2010.10.051.

(157) Ozeki, T.; Kihara, H.; Ikeda, S. Study of Equilibria in 0.03 MM Molybdate Acidic Aqueous Solutions by Factor Analysis Applied to Ultraviolet Spectra. *Anal Chem* **1988**, *60* (19), 2055–2059. https://doi.org/10.1021/ac00170a014.

(158) Weber, Th.; Muijsers, J. C.; van Wolput, J. H. M. C.; Verhagen, C. P. J.; Niemantsverdriet, J. W. Basic Reaction Steps in the Sulfidation of Crystalline MoO 3 to MoS 2 , As Studied by X-Ray Photoelectron and Infrared Emission Spectroscopy. *J Phys Chem* **1996**, *100* (33), 14144–14150. https://doi.org/10.1021/jp961204y.

(159) Hirata, T. In-Situ Observation of Mo-O Stretching Vibrations during the Reduction of MoO3 with Hydrogen by Diffuse Reflectance FTIR Spectroscopy. *Appl Surf Sci* **1989**, *40* (1–2), 179–181. https://doi.org/10.1016/0169-4332(89)90174-8.

(160) SUGIOKA, M.; KIMURA, F. Oxidation and Reduction of Molybdenum Disulfide Catalyst and Their Effects on the Decomposition of 2-Propanol. *Journal of The Japan Petroleum Institute* **1985**, *28* (4), 306–311. https://doi.org/10.1627/jpi1958.28.306.

(161) MIRVALIEV, R.; INOUE, K. Pressure Oxidative Leaching of Molybdenite in Alkaline Media. *Shigen-to-Sozai* **2001**, *117* (1), 72–76. https://doi.org/10.2473/shigentosozai.117.72.

(162) Abinaya, R.; Archana, J.; Harish, S.; Navaneethan, M.; Ponnusamy, S.; Muthamizhchelvan, C.; Shimomura, M.; Hayakawa, Y. Ultrathin Layered MoS2 Nanosheets with Rich Active Sites for Enhanced Visible Light Photocatalytic Activity. *RSC Adv* **2018**, *8* (47), 26664–26675. https://doi.org/10.1039/c8ra02560f.

(163) Yang, X.; Li, J.; Liang, T.; Ma, C.; Zhang, Y.; Chen, H.; Hanagata, N.; Su, H.; Xu, M. Antibacterial Activity of Two-Dimensional MoS2 Sheets. *Nanoscale* **2014**, *6* (17), 10126–10133. https://doi.org/10.1039/C4NR01965B.

(164) Li, F. T.; Wang, Q.; Ran, J.; Hao, Y. J.; Wang, X. J.; Zhao, D.; Qiao, S. Z. Ionic Liquid Self-Combustion Synthesis of BiOBr/Bi24O31Br10 Heterojunctions with Exceptional Visible-Light Photocatalytic Performances. *Nanoscale* **2015**, *7* (3), 1116–1126. https://doi.org/10.1039/c4nr05451b.

(165) Zhou, L.; He, B.; Yang, Y.; He, Y. Facile Approach to Surface Functionalized MoS2 Nanosheets. *RSC Adv* **2014**, *4* (61), 32570–32578. https://doi.org/10.1039/C4RA04682J.

(166) Einstein, A. Concerning an Heuristic Point of View toward the Emission and Transformation of Light. *Am J Phys* **1965**, *33* (5), 367. https://doi.org/10.1119/1.1971542.

(167) RAYLEIGH. Surface Tension. *Nature* **1891**, *43* (1115), 437–439. https://doi.org/10.1038/043437c0.

(168) Jia, L.; Zhang, Y.; Li, J.; You, C.; Xie, E. Aligned Single-Walled Carbon Nanotubes by Langmuir–Blodgett Technique. *J Appl Phys* **2008**, *104* (7), 074318. https://doi.org/10.1063/1.2996033.

(169) Yang, P.; Kim, F. Langmuir–Blodgett Assembly of One-Dimensional Nanostructures. *ChemPhysChem* **2002**, *3* (6), 503. https://doi.org/10.1002/1439-7641(20020617)3:6<503::AID-CPHC503>3.0.CO;2-U.

(170) Min, Younjin; Akbulut, Mustafa; Kristiansen, Kai; Golan, Yuval; Israelachvili, J. The Role of Interparticle and External Forces in Nanoparticle Assembly. *Nat Mater* **2008**, *7*, 527–538. https://doi.org/10.1038/nmat2206.

(171) Vora, S. R.; Bognet, B.; Patanwala, H. S.; Chinesta, F.; Ma, A. W. K. Surface Pressure and Microstructure of Carbon Nanotubes at an Air-Water Interface. *Langmuir* **2015**, *31* (16), 4663–4672. https://doi.org/10.1021/la504934x.

(172) Gravelle, S.; Botto, L. Adsorption of Single and Multiple Graphene-Oxide Nanoparticles at a Water-Vapor Interface. *Langmuir* **2021**, *37* (45), 13322–13330. https://doi.org/10.1021/acs.langmuir.1c01902.

(173) Cote, L. J.; Kim, J.; Zhang, Z.; Sun, C.; Huang, J. Tunable Assembly of Graphene Oxide Surfactant Sheets: Wrinkles, Overlaps and Impacts on Thin Film Properties. *Soft Matter* **2010**, *6* (24), 6096–6101. https://doi.org/10.1039/C0SM00667J.

(174) Gau, M. R.; Zdilla, M. J. A Protocol for Safe Lithiation Reactions Using Organolithium Reagents. *Journal of Visualized Experiments* **2016**, *2016* (117). https://doi.org/10.3791/54705.

(175) Xu, L.; Tetreault, A. R.; Pope, M. A. Chemical Insights into the Rapid, Light-Induced Auto-Oxidation of Molybdenum Disulfide Aqueous Dispersions. *Chemistry of Materials* **2020**, *32* (1), 148–156. https://doi.org/10.1021/acs.chemmater.9b02987.

(176) Zhavnerko, G.; Marletta, G. Developing Langmuir-Blodgett Strategies towards Practical Devices. *Mater Sci Eng B Solid State Mater Adv Technol* **2010**, *169* (1–3), 43–48. https://doi.org/10.1016/j.mseb.2009.12.005.

(177) Kim, M. S.; Ma, L.; Choudhury, S.; Moganty, S. S.; Wei, S.; Lynden, A. Fabricating Multifunctional Nanoparticle Membranes by a Fast Layer-by- Layer Langmuir-Blodgett Process : Application in Lithium-Sulfur Batteries. **2016**. https://doi.org/10.1039/C6TA06018H.

(178) Kocherlakota, L. S.; Krajina, B. A.; Overney, R. M. Communication: Local Energetic Analysis of the Interfacial and Surface Energies of Graphene from the Single Layer to Graphite. *Journal of Chemical Physics* **2015**, *143* (24). https://doi.org/10.1063/1.4939248.

(179) McAllister, M. J.; Li, J. L.; Adamson, D. H.; Schniepp, H. C.; Abdala, A. A.; Liu, J.; Herrera-Alonso, M.; Milius, D. L.; Car, R.; Prud'homme, R. K.; Aksay, I. A. Single Sheet Functionalized Graphene by Oxidation and Thermal Expansion of Graphite. *Chemistry of Materials* **2007**, *19* (18), 4396–4404. https://doi.org/10.1021/cm0630800.

(180) Li, Y.; Yang, X.; Fu, J.; Li, W.; Hu, C. New Insights into the Beneficial Roles of Dispersants in Reducing Negative Influence of Mg2+on Molybdenite Flotation. *RSC Adv* **2020**, *10* (46), 27401–27406. https://doi.org/10.1039/d0ra05556e.

(181) Stamou, D.; Duschl, C.; Johannsmann, D. Long-Range Attraction between Colloidal Spheres at the Air-Water Interface: The Consequence of an Irregular Meniscus. *Phys Rev E* **2000**, *62* (4), 5263–5272. https://doi.org/10.1103/PhysRevE.62.5263.

(182) Israelachvili, J.; Pashley, R. The Hydrophobic Interaction Is Long Range, Decaying Exponentially with Distance. *Nature* **1982**, *300* (5890), 341–342. https://doi.org/10.1038/300341a0.

(183) Donaldson, S. H.; Røyne, A.; Kristiansen, K.; Rapp, M. V.; Das, S.; Gebbie, M. A.; Lee, D. W.; Stock, P.; Valtiner, M.; Israelachvili, J. Developing a General Interaction Potential for Hydrophobic and Hydrophilic Interactions. *Langmuir* **2015**, *31* (7), 2051–2064. https://doi.org/10.1021/la502115g.

(184) Kozbial, A.; Li, Z.; Conaway, C.; McGinley, R.; Dhingra, S.; Vahdat, V.; Zhou, F.; Durso, B.; Liu, H.; Li, L. Study on the Surface Energy of Graphene by Contact Angle Measurements. *Langmuir* **2014**, *30* (28), 8598–8606. https://doi.org/10.1021/la5018328.

(185) Lu, Z.; Liu, Q.; Xu, Z.; Zeng, H. Probing Anisotropic Surface Properties of Molybdenite by Direct Force Measurements. *Langmuir* **2015**, *31* (42), 11409–11418. https://doi.org/10.1021/acs.langmuir.5b02678.

(186) Fan, X.; Xu, P.; Li, Y. C.; Zhou, D.; Sun, Y.; Nguyen, M. A. T.; Terrones, M.; Mallouk, T. E. Controlled Exfoliation of MoS2 Crystals into Trilayer Nanosheets. *J Am Chem Soc* **2016**, *138* (15), 5143–5149. https://doi.org/10.1021/jacs.6b01502.

(187) Backes, C.; Smith, R. J.; McEvoy, N.; Berner, N. C.; McCloskey, D.; Nerl, H. C.; O'Neill, A.; King, P. J.; Higgins, T.; Hanlon, D.; Scheuschner, N.; Maultzsch, J.; Houben, L.; Duesberg, G. S.; Donegan, J. F.; Nicolosi, V.; Coleman, J. N. Edge and Confinement Effects Allow in Situ Measurement of Size and Thickness of Liquid-Exfoliated Nanosheets. *Nat Commun* **2014**, *5* (1), 4576. https://doi.org/10.1038/ncomms5576.

(188) Santhanam, V.; Liu, J.; Agarwal, R.; Andres, R. P. Self-Assembly of Uniform Monolayer Arrays of Nanoparticles. *Langmuir* **2003**, *19* (19), 7881–7887. https://doi.org/10.1021/la0341761.

(189) Ge, G.; Brus, L. Evidence for Spinodal Phase Separation in Two-Dimensional Nanocrystal Self-Assembly. *Journal of Physical Chemistry B* **2000**, *104* (41), 9574–9575. https://doi.org/10.1021/jp002280a.

(190) Smith, T. G.; Lange, G. D.; Marks, W. B. Fractal Methods and Results in Cellular Morphology — Dimensions, Lacunarity and Multifractals. *J Neurosci Methods* **1996**, *69* (2), 123–136. https://doi.org/10.1016/S0165-0270(96)00080-5.

(191) Bresme, F.; Oettel, M. Nanoparticles at Fluid Interfaces. *Journal of Physics: Condensed Matter* **2007**, *19* (41), 413101. https://doi.org/10.1088/0953-8984/19/41/413101.

(192) Pope, M. A.; Punckt, C.; Aksay, I. A. Intrinsic Capacitance and Redox Activity of Functionalized Graphene Sheets. *The Journal of Physical Chemistry C* **2011**, *115* (41), 20326–20334. https://doi.org/10.1021/jp2068667.

(193) Hurd, A. J.; Schaefer, D. W. Diffusion-Limited Aggregation in Two Dimensions. *Phys Rev Lett* **1985**, *54* (10), 1043–1046. https://doi.org/10.1103/PhysRevLett.54.1043.

(194) Kim, H.; Boulogne, F.; Um, E.; Jacobi, I.; Button, E.; Stone, H. A. Controlled Uniform Coating from the Interplay of Marangoni Flows and Surface-Adsorbed Macromolecules. *Phys Rev Lett* **2016**, *116* (12), 1–5. https://doi.org/10.1103/PhysRevLett.116.124501.

(195) Edwards, A. M. J.; Atkinson, P. S.; Cheung, C. S.; Liang, H.; Fairhurst, D. J.; Ouali, F. F. Density-Driven Flows in Evaporating Binary Liquid Droplets. *Phys Rev Lett* **2018**, *121* (18), 184501. https://doi.org/10.1103/PhysRevLett.121.184501.

(196) Flores-Tandy, L. M.; García-Monjaraz, A. V.; van Nierop, E. A.; Vázquez-Martínez, E. A.; Ruiz-Garcia, J.; Mejía-Rosales, S. Fractal Aggregates Formed by Ellipsoidal Colloidal Particles at the Air/Water Interface. *Colloids Surf A Physicochem Eng Asp* **2020**, *590* (November 2019). https://doi.org/10.1016/j.colsurfa.2020.124477.

(197) Zhao, C.; Zhang, P.; Zhou, J.; Qi, S.; Yamauchi, Y.; Shi, R.; Fang, R.; Ishida, Y.; Wang, S.; Tomsia, A. P.; Jiang, L.; Liu, M. Layered Nanocomposites by Shear-Flow-Induced Alignment of Nanosheets. *Nature* **2020**, *580* (7802), 210–215. https://doi.org/10.1038/s41586-020-2161-8.

(198) Rabani, E.; Egorov, S. A. Interactions between Passivated Nanoparticles in Solutions: Beyond the Continuum Model. *Journal of Chemical Physics* **2001**, *115* (8), 3437–3440. https://doi.org/10.1063/1.1395627.

(199) Rabani, E.; Egorov, S. A. Solvophobic and Solvophilic Effects on the Potential of Mean Force between Two Nanoparticles in Binary Mixtures. *Nano Lett* **2002**, *2* (1), 69–72. https://doi.org/10.1021/nl015645r.

(200) Cicuta, P.; Terentjev, E. M. Viscoelasticity of a Protein Monolayer from Anisotropic Surface Pressure Measurements. *European Physical Journal E* **2005**, *16* (2), 147–158. https://doi.org/10.1140/epje/e2005-00016-y.

(201) Milner, S. T.; Joanny, J. F.; Pincus, P. Buckling of Langmuir Monolayers. *Europhysics Letters (EPL)* **1989**, *9* (5), 495–500. https://doi.org/10.1209/0295-5075/9/5/015.

(202) Hayes, T. R.; Lang, E. N.; Shi, A.; Claridge, S. A. Large-Scale Noncovalent Functionalization of 2D Materials through Thermally Controlled Rotary Langmuir-Schaefer Conversion. *Langmuir* **2020**, *36* (35), 10577–10586. https://doi.org/10.1021/acs.langmuir.0c01914.

(203) Chen, I. Te; Schappell, E.; Zhang, X.; Chang, C. H. Continuous Roll-to-Roll Patterning of Three-Dimensional Periodic Nanostructures. *Microsyst Nanoeng* **2020**, *6* (1). https://doi.org/10.1038/s41378-020-0133-7.

(204) Wells, R. A.; Johnson, H.; Lhermitte, C. R.; Kinge, S.; Sivula, K. Roll-to-Roll Deposition of Semiconducting 2D Nanoflake Films of Transition Metal Dichalcogenides for Optoelectronic Applications. *ACS Appl Nano Mater* **2019**, *2* (12), 7705–7712. https://doi.org/10.1021/acsanm.9b01774.

(205) Parchine, M.; Kohoutek, T.; Bardosova, M.; Pemble, M. E. Large Area Colloidal Photonic Crystals for Light Trapping in Flexible Organic Photovoltaic Modules Applied Using a Roll-to-Roll Langmuir-Blodgett Method. *Solar Energy Materials and Solar Cells* **2018**, *185*, 158–165. https://doi.org/10.1016/j.solmat.2018.05.026.

(206) Xu, L. Langmuir Films of Graphene-Based Materials : Towards Large Area Monolayer Deposition. **2017**.

(207) Kobayashi, T.; Bando, M.; Kimura, N.; Shimizu, K.; Kadono, K.; Umezu, N.; Miyahara, K.; Hayazaki, S.; Nagai, S.; Mizuguchi, Y.; Murakami, Y.; Hobara, D. Production of a 100-m-Long High-Quality Graphene Transparent Conductive Film by Roll-to-Roll Chemical Vapor Deposition and Transfer Process. *Appl Phys Lett* **2013**, *102* (2), 023112. https://doi.org/10.1063/1.4776707.